LASL

Controlled Thermonuclear Research Program

January—December 1975

Compiled by

George A. Sawyer
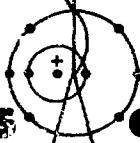
los alamos
scientific laboratory
of the University of California
LOS ALAMOS, NEW MEXICO 87545

An Affirmative Action/Equal Opportunity Employer

MASTER

The four most recent reports in this series, unclassified, are LA-4888-PR,
LA-5250-PR, LA-5656-PR, and LA-6044-PR.

ABSTRACT

This report presents the status of the Controlled Thermonuclear Research
Program at the Los Alamos Scientific Laboratory for calendar year 1975.

CONTENTS

MASTER

I. SCYLLAC DERATED-SECTOR EXPERIMENTS

R. R. Bartsch, C. L. Cantrell, W. R. Ellis, B. L. Freeman, K. B. Freese, R. F. Gribble,
W. D. Gutscher, F. C. Jahoda, K. J. Johnson, R. Kristal, K. J. Kutac, G. Miller,
W. E. Quinn, A. S. Rawcliffe, R. E. Siemon

A. INTRODUCTION AND SUMMARY

The main objective of the Scyllac experiment is to study methods of producing stable high-beta plasma equilibria and confinement in toroidal geometry, with the ultimate goal of developing a fusion reactor. Initial studies of plasma equilibrium and stability were performed in toroidal sectors[1] followed by full torus experiments.[2,3] Presently, experiments are being performed in a 120° sector of the torus with derated parameters to accommodate the capabilities of the feedback system.

Scyllac is a large-aspect-ratio toroidal theta-pinch experiment. In Scyllac a high-beta toroidal equilibrium, Fig. I-1, is achieved by superimposing a small $\ell = 1$ helical field and a small $\ell = 0$ axisymmetric bumpy field on the main theta-pinch field, where ℓ describes the equilibrium fields which vary as $\sin(\ell\theta - hz)$. Plasma distortions, δ_1 and δ_0, are produced by these fields and result in an axially uniform body force, $F_{1,0}$, which equated to the outward toroidal force gives the equilibrium condition, $\delta_1\delta_0 = 2/(3-2\beta)$ h^2aR. The $\ell = 1$ and $\ell = 0$ fields are produced by machining the inner surface of the compression coil to coincide with the appropriate $\ell = 1$, 0 flux surface. Beta is adjusted by plasma filling pressure and/or small trapped field to give equilibrium. The full torus and earlier sector experiments confirm quantitatively the $\ell = 1,0$ plasma equilibrium and its scaling with theory. The results on the full torus without feedback stabilization characterized the confined plasma by the following parameters: $\beta = 0.8$; $a = 1.0$ cm; $n = 2.7 \times 10^{16}$ cm^{-3}; $T_e = 500$ eV; $T_i = 0.8$ keV; $\tau_p = 10$ μs; and $\gamma_{m=1} = 0.7$ MHz. The period of stable plasma confinement, which defines the equilibrium, is terminated by the $m = 1$ motion of the plasma column whose properties in the full torus are those of the theoretically predicted MHD $m = 1$ instability. Higher modes $m \geq 2$, are stabilized by finite-Larmor-radius (FLR) effects as described by the Vlasov equation.[4]

Two methods for stabilizing the $m = 1$ instability in Scyllac have been proposed: feedback (FB) and wall stabilization. In the present Scyllac ex-
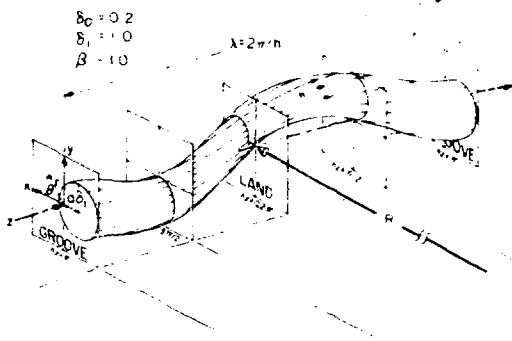
Fig. I-1.

Foreshortened 3-dimensional view of Scyllac $\ell = 1,0$ plasma column.

periments the ratio a/b of plasma to wall radii is too small (~ 0.1) for wall stabilization; therefore feedback control is being used for plasma stabilization. Feedback studies show that the product of the instability growth rate, γ, and the FB delay-rise-time, τ, must satisfy the requirement, $\gamma\tau \leq 0.5$, in order to control the instability, while the Scyllac full torus has $\gamma\tau \approx 1$. In order to reduce γ to a value which is compatible with capabilities of the feedback system the following changes were made in a 120° sector of the torus: (1) compression field reduced from 40 to 17 kG; (2) plasma beta decreased from 0.8 to 0.65; (3) δ_1 increased from 0.7 to 1.4; and (4) $\ell = 1$, 0 wavelength increased from 41.9 to 62.8 cm. Measurements in the derated sector give an $m = 1$ growth rate of 0.3 MHz ($\gamma\tau = 0.4$), reduced from 0.7 MHz in the full torus, and increased plasma confinement times of 15 to 25 μs. An initial outward shift of the plasma equilibrium position occurs because of the longer formative times of the δ_0 and δ_1 plasma distortions with the longer $\ell = 1,0$ wavelengths and lower plasma temperatures. A small reversed bias field (~ 150 G), to fine-tune β, and/or additional $\ell = 0$ "trimming" fields have been used to improve the plasma equilibrium provided by the fields produced by the shaped compression coil.

All Scyllac experiments in 1975 were performed on the derated, or feedback, sector. This sector was brought into operation in February 1975, and initial experiments were concerned with the gross plasma equilibrium and stability properties, and plasma parameters in the new, derated mode. Modest reverse bias fields were used to obtain maximum plasma confinement times of 25 μs.

Computer modeling studies showed that an $\ell = 2$ feedback field is functionally superior to an $\ell = 0$ field for the $\ell = 1,0$ Scyllac configuration. Auxiliary $\ell = 0$ and $\ell = 2$ programmed fields, produced by small capacitor banks, were applied to the feedback sector to study the response of the plasma column to $F_{1,0}$ and $F_{1,2}$ force perturbations of the feedback type and to compare the relative effectiveness of $\ell = 0$ and $\ell = 2$ fields for feedback.[5,6] The presence of the auxiliary field coils, inadvertently shifted the helical magnetic axis slightly in the vertical plane perpendicular to that of the torus. This resulted in an initial displacement, ξ_0, of the plasma column from its equilibrium position, which excited the $m = 1$ instability driving force, $F_1 = \pi a^2 \rho \gamma^2 \xi_0$, for the auxiliary $\ell = 0$ and $\ell = 2$ fields to correct. This initial displacement was later eliminated by shifting the discharge tube so that its axis coincided with the magnetic axis.

In the programmed-field experiments the growth rate of the m = 1 instability was observed to have the predicted value 0.25 $\pm$ 0.05 MHz. The programmed fields were applied either as a half-cycle pulse of 6-μs duration or a crowbarred sustained field. The programmed-field experiments showed: (1) the observed plasma trajectories with applied $\ell = 0$ or $\ell = 2$ field are in good agreement with theoretical predictions. With a peak $\ell = 0$ field of 460 G, the resulting force readily overcame the instability motion and confined the plasma column in the vertical plane until it struck the wall in the horizontal plane. The force from an $\ell = 2$ field of 250 G not only overcame the instability motion, but drove the column through the axis; (2) the $\ell = 2$ field is three times more effective than the $\ell = 0$ field for feedback stabilization as predicted by theory; and (3) the physical mechanism for feedback plasma stabilization of the m = 1 instability works as expected in Scyllac.

In the MHD feedback stabilization system for Scyllac, the feedback force is generated by small controllable $\ell = 2$ fields, which produce plasma perturbations, $\delta_2 = B_{\ell=2}/ha$ $(1-\epsilon/2)B$. This perturbation interacts with the $\ell = 1$ equilibrium plasma distortion δ_1 to produce a feedback restoring force, $F_{1,2}^{FB} = \epsilon(2-\epsilon)B^2 h^2 a^2 \delta_1 \delta_2^{FB}/8$, in opposition to the m = 1 destabilizing force. The feedback stabilization system consists of four basic components: (1) plasma position detectors to detect plasma motion away from the equilibrium position; (2) signal processing units, which produce an output proportional to the sum of plasma position and velocity with separate position and velocity gain controls; (3) power amplifier modules, each of which consists of five separate stages of amplification ending in the push-pull operation of two high-power triodes operating at 35-kV plate voltage; and (4) $\ell = 2$ feedback coils driven by the power modules. The feedback system produces an $\ell = 2$ field of 80 G at a radius of 1 cm with a delay-risetime of 1.3 μs.

Experiments with the closed-loop feedback system applied to the derated sector were begun in December. These experiments involved 4-turn $\ell = 2$ coils wound on forms which were placed over the toroidal discharge tube, end to end. Simple $\ell = 0$ coils, driven by a small capacitor bank, were used in addition to the feedback $\ell = 2$ windings. Vertical plasma drifts could be produced or eliminated by raising or lowering the discharge tube within the compression coil by means of positioning screws. Feedback fields have been successful in controlling plasma motions in the vertical plane, perpendicular to the major radius. Feedback has been less successful in the horizontal plane because plasma motions in the plane parallel to the major radius are apparently influenced by non-equilibrium forces of substantial magnitude.

The m = 1 motion in the horizontal plane of the torus appears to be dominated by loss of equilibrium, and is not yet controllable by feedback. During the initial stable period, 7 to 20 μs, the application of either an $\ell = 0$ field or a programmed $\ell = 2$ feedback field will drive the plasma column inward in the toroidal plane to the inner wall. However, once the onset of the outward motion occurs, a force comparable to an appreciable fraction of the $F_{1,0}$ equilibrating force is required to overcome it. The magnitude of the force behind the outward m = 1

motion indicates a loss of equilibrium $(F_R \neq F_{1.0})$ in the horizontal plane, rather than just the $m=1$ instability. Possible causes of the loss of equilibrium include: (1) a decrease of plasma beta with time owing to too-close proximity of the plasma helix to the wall; (2) axial redistribution of plasma pressure or helical/bumpy distortion; or (3) effects of diffuse-plasma equilibrium, as opposed to sharp-boundary equilibrium.

Present experiments on the equilibrium loss include: electron temperature measurements as function of time; measurements of the equilibrium plasma distortions, δ_1 and δ_0, in time, simultaneous plasma beta measurements in land $(B = B_0 + B_{i=0})$ and groove $(\beta = B_0 - B_{i=0})$ regions; measurements of absolute density profiles in groove regions; observations of possible toroidal plasma structure; and detailed magnetic field probing. A helical tube (see below) will be installed in the present sector experiment to increase the clearance between plasma helix and wall (by the amount of $\delta_1 a$) and to eliminate "hunting" for the equilibrium position.

Recent experiments at Garching in the High-Beta Stellarator, Isar II-B, have successfully utilized a helically shaped discharge tube in producing a high-beta toroidal equilibrium with a large helical plasma distortion, $\delta_1 = 3.$[5,7] With the helically shaped tube, the plasma implodes to its helical magnetic equilibrium axis and is quiescent without any δ_1 helical oscillations. In addition, no detrimental effects of the large δ_1 are observed, in agreement with recent theoretical work of Marder.[3]

A quartz forming device for fabricating toroidal, helical-shaped discharge tubes has been designed and constructed at Los Alamos. Plans call for the installation of a helical tube with r_{helix} = 1.4 cm in the present derated sector field configuration as soon as it can be fabricated.

The utilization of large helical plasma distortions, $\delta_1 \sim 3$, in combination with δ_0 and δ_2 plasma distortions, to achieve high-beta toroidal equilibrium have important advantages in the stabilization of the $m=1$ instability. In feedback stabilization, the larger δ_1 reduces the growth rate of the $m=1$ instability and thereby relaxes both the delay-risetime requirement and the magnitude of the feedback field $(B_{FB} \propto \gamma^2)$. The required feedback field is

further reduced since it also depends inversely on δ_1. In wall stabilization of the $m=1$ mode, the requirement on the a/b ratio of plasma to wall radii is also reduced as δ_1 increases. Sector experiments with $\delta_1 \sim 3$ are planned for the near future.

B. EXPERIMENTAL ARRANGEMENT

The Scyllac derated sector was specifically designed to minimize the $m=1$ growth rate γ_1 and hence to accommodate technological limitations in the existing feedback system. Previous results from the toroidal sectors and the full torus established a relationship between the required specifications of the feedback system and the plasma parameters. An assessment of the feedback system based on this knowledge showed that the time response and the output-current capability of the feedback amplifier system were insufficient to control the unstable motion with the full torus plasma parameters. Computer studies indicate that $\gamma_1 \tau_{FB} < 0.5$ (τ_{FB} is the feedback delay-risetime) is required for controlling the instability, while in the full torus, $\gamma_1 \tau_{FB} \approx 1$. These considerations led to a re-evaluation of the plasma regime in which the initial feedback experiments should be conducted. In order to reduce the instability growth rate to a value which is compatible with the response time of the feedback system, the main compression field was reduced and the plasma parameters derated accordingly. Since the device and plasma parameters were being considerably changed to accommodate the feedback system, the changes were carried out first on an 8-m sector of the full torus, comprising energy storage racks six through ten, with a major radius of 4.0 m and a coil arc length of 8.4 m.

The energy storage capacitors which were feeding the bottom collector plates in racks 6-10, comprising one-half of the available bank, were disconnected, and the average coil bore was increased from 14.2 to 24.0 cm. These changes reduced the magnetic field from ~ 40 kG to ~ 17 kG, and theoretical scalings were used to calculate the expected plasma parameters.[3] Table I-I compares the projected derated parameters with those actually measured, and with those observed in the full torus. Note that the $m=1$ growth rate δ_1 is substantially reduced, and $\gamma_1 \tau_{FB} < 0.5$.

TABLE I-I
SCYLLAC PARAMETERS

Parameters	Full Torus Experiment	Projected Derated Sector Experiment	Derated Sector Experiment
$B(kG)$	40	15	17
$\tau/4(\mu s)$	3.7	3.5	3.5
$a(cm)$	1.0	1.4	1.0
$n \times 10^{-16}(cm^{-3})$	2.7	1.3	2.0
$T_e(eV)$	500	130	120
$T_i(eV)$	800	130	120
β	0.8	0.65	0.65
$\tau_{EL}(\mu s)$	---	89	87
$v_A(cm/\mu s)$	37.6	20	18.5
$\tau_A(\mu s)$	(66.8)	20.9	22.6
$\gamma_{1,0}(cm)$	41.9	62.8	62.8
δ_i	0.71	0.98	1.4
δ_0	0.16	0.21	0.2
$\gamma_1 \times 10^{-5}(s^{-1})$	0.70	0.32	0.3
$\gamma_1 \tau_{FB}$	1.0	0.4	0.4
$B_{\ell=2}(r=1.0\ cm)\ (G)$	163	60	58

The plasma equilibrium in the derated sector was computed using sharp-boundary theory and $\beta = 0.65$, consistent with the lower plasma temperature. The equilibrium $\ell = 1$ helical, $B_{\ell=1}/B = 0.095$, and $\ell = 0$ bumpy, $B_{\ell=0}/B = 0.147$, fields were produced by machining the inner surface of the compression coil to coincide with the computed $\ell = 1,0$ flux surfaces. The theoretical value of the vertical field component, $B_v/B = B_{\ell=1} B_{\ell=0}/B^2$, was also included in the flux surface calculations. Figure I-2 shows a section of the compression coil, and Fig. I-3 shows calculated flux surfaces at $hz = 0$ (a land region, where B is a maximum), $hz = \pi/2$, $hz = \pi$ (a groove region, where B is a minimum), and $hz = 3\pi/2$. The annular cross-hatched areas show the location of the quartz discharge tube, and the origin of the x-y coordinate system is the magnetic axis, which is centered in the discharge tube. Note that the outer flux surfaces, which correspond to the coil-bore cross sections at the indicated z positions, are somewhat eliptical. These surfaces are machined by the profile-tracer method on a lathe, using a master profile produced by a 3-dimensional milling machine from a computer-generated tape.

The discharge tube for the sector consisted of four quartz tube sections, each with an arc length of 2.5 m, and a special short section with polished regions for side-on holographic interferometry. The sections were butted with an outer ceramic ring and o-ring seals similar to the arrangement in the full torus but without the pump-out tees. The sector tube with an inside diameter of 8.8 cm was pumped from the ends, which were electrically isolated from ground. No external path for axial Z currents was provided.

Figure I-4 shows a plan view of the sector with its various diagnostic viewing slots. The following measurements are used to study the high-beta toroidal plasma: (a) as many as seven high-speed streak cameras are used to record the transverse motions of the plasma column at various locations around the torus; (b) a coupled-cavity He-Ne laser interferometer is used to measure the time-history of the plasma electron density along a chord of the plasma cross section; (c) twenty and ten channel luminosity profile apparatuses provide self-luminous profiles of the plasma column. These luminosity profiles give the plasma radius, and in conjunction with the coupled-cavity interferometer data, give absolute density profiles; (d) balanced magnetic loop and probe arrangements measure the magnetic flux excluded by the plasma column. Combined with
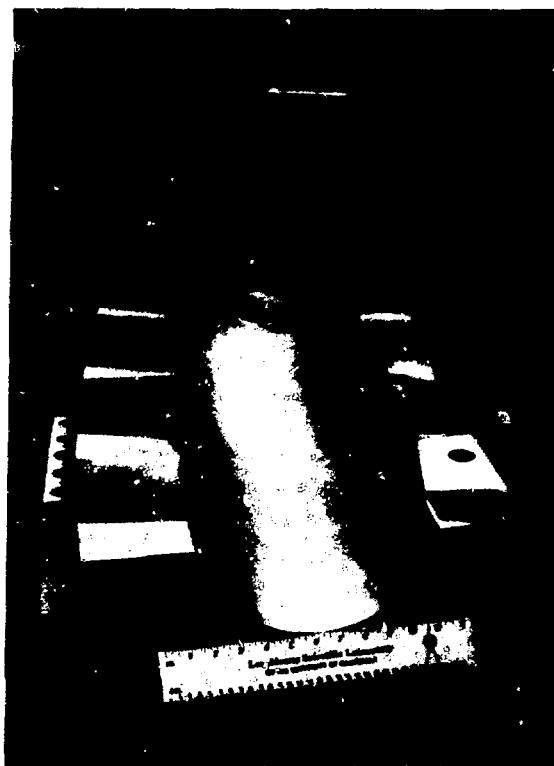
Fig. I-2.

Photograph of a section of the Scyllac compression coil showing the ℓ = 1,0 flux surface.

Fig. I-3.

Plots of the vacuum magnetic flux surfaces generated by the shaped inner surface of the compression coil at four toroidal z positions. The annular cross-hatched areas indicate the discharge tube.

the relative density profiles from the luminosity measurement, the excluded flux can be expressed in terms of the plasma beta; (e) Thomson scattering of laser light is used to determine the plasma electron temperature; (f) a side-on holographic interferometer gives spatially and time resolved absolute plasma electron density profiles; and (g) a fast, 360° optical system ("star" camera) on the torus major axis images ten top coil slits onto a three-frame image-converter camera.

C.   EXPERIMENTAL RESULTS WITHOUT AUXILIARY FIELDS

The first experiments on the sector were performed without feedback to determine the equilibrium and stability properties as well as the parameters of the plasma. With the ℓ = 1 and ℓ = 0 equilibrium fields generated by the shaped inner surface of the compression coil, the plasma equilibrium is normally achieved by adjusting the initial deuterium filling pressure and bank voltage to give a balance between

the $F_{1,0}$ force and the outward toroidal force F_R through their plasma beta dependence. The ratio of $F_{1,0}$ to F_R,

$$\frac{F_{1,0}}{F_R} = \frac{I_1^{'}(\epsilon)I_0^{'}(\epsilon)[1+(1-\beta)I_0(\epsilon)/I_1^{'}(\epsilon)]}{[1+\epsilon\beta I_1(\epsilon)K_1^{'}(\epsilon)][1+\epsilon\beta I_0(\epsilon)K_0^{'}(\epsilon)]}$$
$$\times \frac{R}{a} \frac{B_{\ell=1}B_{\ell=0}}{B^2} , \qquad (1)$$
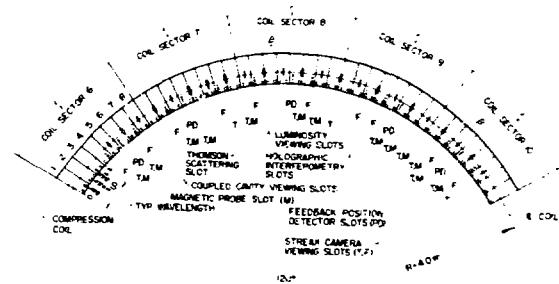
Fig. I-4.

Plan view of the Scyllac derated sector showing the various diagnostic viewing slots and the collector plate current feeds.

5

where I_i and K_i are the modified Bessel functions and $\varepsilon = ha$, is plotted for the parameters of the derated sector as a function of the plasma beta and for various plasma radii in Fig. I-5. The dependence of the force ratio and the equilibrium is not as sensitive to beta at the sector design value of 0.65 as for the higher β values (~ 0.8) in the full torus experiment.

1. *Gross Plasma Motions*. The plasma equilibrium was found to be shifted outward more than usual initially, with the result that the plasma in a land region was quite close to the discharge tube wall. This complicated the data interpretation, particularly the luminosity plasma radius in a land, obtained by viewing perpendicular to the major radius. The usual "knobs" for fine-tuning beta, provided by changing the deuterium filling pressure and/or bank voltage, had less effect in the derated sector. Therefore, in order to create a better toroidal equilibrium, a small antiparallel bias field of 100-200 G was applied and imbedded in the plasma during the preionization phase. A further improvement in plasma uniformity and confinement time was achieved by using slightly different values of the antiparallel bias field in the different racks of the sector.

Figure I-6 shows typical plasma motions for a mixed-bias discharge with a plasma confinement time of 25 μs. The upper streak (L) shows the plasma motion in a land region of rack 9, the center streak (F) shows the motion perpendicular to the plane of the torus in rack 8, and the lower streak (G) the motion in a groove region of rack 7. The structure in F at about 25 μs indicates that the plasma column has collided with the wall in an adjacent land re-

Fig. I-6.

Fig. I-5.

gion. In the land and groove regions (L and G) the upward direction on the streaks corresponds to an outward motion away from the torus major axis in the horizontal plane of the sector.

Following the initial plasma implosion, the column exhibits a stable helical δ_1 oscillation. Figs. I-6 and I-7, i.e., a "breathing" of the helical plasma column with a periodicity corresponding to the $\ell = 1,0$ wavelength. The oscillations damp out in 6-8 μs. In the previous collisionless toroidal experiments at higher plasma temperatures and with shorter $\ell = 1,0$ wavelengths, these helical oscillations were not observed. However, the stable helical oscillations, $\delta_1 = \overline{\delta}_1 \sin \omega_{01} t$, are predicted by MHD sharp-boundary theory where $\omega_{01} = h\, v_A \sqrt{2-\beta}$. The observed frequency of $3.6 \pm 0.5 \times 10^5$ s^{-1} is in agreement with theory.

a. *Comparison of Measured Trajectories with an MHD Model.* In Fig. I-8 measured plasma trajectories (Fig. I-5) are compared with a sharp-boundary MHD model calculation by Miller.[10,11] The model consists of a set of coupled differential equations for the plasma displacement ξ and the plasma distortions δ_0 and δ_{+1}. The calculations used the parameter values of Table I-I with three internal degrees of freedom. Damping terms were included in the δ_0, $\delta_{\pm 1}$ equations to give damping

4510

Fig. I-8.

approximately consistent with the data. The plasma β was a free parameter varied to make the trajectory agree best with the data, resulting in the choice, $\beta = 0.77$. The initial conditions assumed were somewhat unrealistic; they corresponded to a cylindrical constant-pressure plasma column being already present and the $l = 0$ and $l = 1$ fields suddenly switched on at $t = 0$.

Several of the dynamic features of the data find an explanation in the sharp-boundary model. The helical oscillations result from the plasma being initially straight and overshooting its helical equilibrium position as it attempts to conform to the $l = 1$ field. There is an outward shift of the plasma due to the fact that the plasma δ_0 (bumpiness) takes an appreciable time to develop and the $F_{1,0}$ force is not fully operative until this happens. This also accounts for the β value being 0.77 since this value shifts the equilibrium position (the top of the potential hill) out to where the plasma finds itself after its outward shift. The plasma motion for the first 10 μs does not have a simple exponential form. This is due to coupling with the dynamics of δ_0 through the $F_{1,0}$ force. At later times the calculated trajectories, although not shown in Fig. I-8 would go to the inner wall exponentially with a growth rate $\gamma \approx 0.3 \times 10^6 \text{s}^{-1}$. Two possible explanations of the reversing direction of plasma motion observed in the streak photographs are: (1) the

plasma β decreases at later times due to end or other effects causing a shift in the equilibrium position; (2) a decrease in the plasma distortions, δ_0 and/or δ_1.

b. *Plasma Motions with Parallel Bias Field.* A parallel bias field of 100 to 500 G was applied to the plasma in the same manner as the reverse bias. This changed the plasma characteristics considerably. It lowered the plasma temperatures to 50-70 eV and resulted in the development of the $m = 2$ instability. Figure I-9 shows the bifurcation and filamentation of the plasma column which is characteristic of the $m = 2$ instability. This behavior was observed in land regions, at 1/4 wavelength positions midway between land and groove regions, but not in groove regions.

Although the plasma parameters were not studied in detail in the case of parallel bias field, estimates can be made of the parameters which are needed to evaluate the criterion for finite-Larmor-radius (FLR) stabilization of the $l = 1$ driven, $m = 2$ mode given by[4,12]

$$\frac{r_L}{a} \geq g_4 h^2 a^2 \delta^2_1 \quad \text{where} \quad g_4 = 4\beta^2(1-\beta)/(2-\beta), \quad (2)$$

or

$$\frac{T_i(\text{keV})}{B^2(\text{kG})} \geq 2.40 \times 10^{-2} g_4 h^2 a^4 \delta_1^2 \quad . \quad (3)$$

For $B = 17$ kG, $\beta = 0.65$, $h = 0.10 \text{ cm}^{-1}$, $a = 1$ cm, and $\delta_1 = 1.4$, theoretical stability requires $T_i \geq 60$ eV. Measured values of T_i (Table I-1) with parallel

bias field show that the $m = 2$ instability develops for temperature values of ~ 60 eV as predicted by theory. The derated sector experiments without parallel bias field and all the previous Scyllac toroidal experiments confirm the finite-Larmor-radius stabilization of $m \geq 2$ modes as predicted by the Vlasov theory.

2. *Measured Plasma Parameters*. Plasma measurements in the derated sector experiment with the main bank operating at 40 kV ($B \sim 17$ kG) give the following parameters: (1) plasma densities of $1 - 4 \times 10^{16}$ cm^{-3} from both side-on holographic and coupled cavity interferometry; (2) plasma radii of 0.9 - 1.1 cm from luminosity profiles and side-on holographic interferometry; (3) plasma beta at the column center of 0.6 to 0.7 from combined excluded flux and luminosity profiles; (4) plasma electron temperatures of 110-130 eV from Thomson scattering ($T_i = T_e$ in the derated collisional plasma); (5) plasma confinement times of 15-25 μs; (6) $\ell = 0$ plasma distortion, $\delta_0 = 0.2$ from luminosity profiles; (7) $\ell = 1$ plasma distortion, $\delta_1 = 1.4$ determined from streak photographs; and (8) growth rate of $m = 1$ instability, $\gamma \sim 0.2 - 0.3 \times 10^6$s^{-1}. In Table I-I, (third column) these measured parameters are compared with the projected parameters for the sector and also with the parameters in the previous full torus experiments. Although most of the experiments in the derated sector have been performed at bank voltages of 40 kV, measurements were also made at 45 kV ($B = 19$ kG) and 50 kV ($B = 21$ kG). However, the plasma confinement and stability are not significantly improved at the higher bank voltages.

a. *Plasma Electron Temperatures*. The plasma electron temperatures have been measured by Thomson scattering in a groove region of rack 7 (cf. Fig. I-4). A summary of these temperature measurements with initial deuterium filling pressures of 18-19 mTorr, is given in Table I-II.

TABLE I-II
PLASMA ELECTRON TEMPERATURES

V_{Bank} (kV)	Bias Field (G)	No. of Discharges	t (μs)	T_e (eV)
40	0	12	7.0	110 $\pm$ 10
40	~ -140	10	7.0	113 $\pm$ 12
45	0	30	3.4	128 $\pm$ 13
45	~ -160	13	3.4	128 $\pm$ 13
50	0	2	3.4	136 $\pm$ 14
50	~ -190	20	3.4	139 $\pm$ 14
40	$\sim +400$	14	3.4	50 - 70

In these experiments with the derated plasma, the electron-ion equilibration time is the order of a microsecond. Therefore, the measurements give the plasma temperature, $T_i = T_e$. The temperature results given in Table I-II show the following: (1) the plasma temperature is the same with and without reversed bias field; (2) an approximately linear increase occurs in the plasma temperature as the bank voltage is increased, and (3) the application of a parallel bias field decreases the temperature significantly.

b. *Plasma Electron Density and Radius Measurements in Groove Regions*. Side-on holographic interferometry has been used to measure the plasma electron density and radius in a groove region of rack 9 (cf. Fig. I-4). The results are summarized in Table I-III.

TABLE I-III
PLASMA DENSITY AND RADIUS IN GROOVE REGION

P_{D2} (mTorr)	Bias Field (G)	$(n_e)_G$ ($\times 10^{-16}$ cm-3)	a_G (cm)
18.4	0	4.7	1.10
18.1	-120	3.6	1.20
18.4	-136	2.7	1.15

8F-V

|← 8 μs →|

Fig. I-9.

Streak photographs of the plasma column in the horizontal (H) and vertical planes (V) with a parallel bias field of 400 G showing the development of the $m = 2$ instability.

We note that the plasma density decreases in a groove region with increasing reversed bias field, B_i.

c. *Characteristic Sector Times.* The drift time for the outward toroidal force to carry the plasma column to the discharge tube wall in the derated sector is 4.2 µs. The time for an Alfvén wave to propagate from the ends to the center of the sector is 22 µs. The plasma end-loss time scaled with the ratios of coil length to the ion thermal velocity from the Scyllac 5-m linear and Scylla IV-P experiments is 90 µs. The electron thermal conduction time to the ends of the sector is approximately 100 µs.

d. *Plasma Beta and Radius Measurements.* From the experimental curves of luminosity and excluded flux data, the plasma beta at the center of the column, plasma radius, external confining magnetic field, excluded flux, and column internal flux have been computed as functions of time. These parameters have then been combined in appropriate ways to study the plasma equilibrium. The data reported here are from rack 8 of the derated sector (cf. Fig. I-4). Excluded flux and luminosity measurements were made one wavelength (62.8 cm) apart. The discharges were selected on the basis of reliable data, and the machine parameters are characteristic of optimum confinement conditions: $B \sim 17$ kG, bank voltage ~ 40 kV, filling pressure ~ 18 mTorr, reverse bias field ~ -140 G, confinement time = 15-25 µs.

Figure I-10A shows the plasma radius in land, $\bar{a}_L$, and groove, $\bar{a}_G$, regions averaged over four discharges. The mean plasma radius, $<a> = (\bar{a}_G + \bar{a}_L)/2$ is also shown and has a value of approximately 1 cm.

The equilibrium plasma distortion, δ_0, due to the $\ell = 0$ field is, by definition,

$$\delta_0 = \frac{\bar{a}_G - \bar{a}_L}{\bar{a}_G + \bar{a}_L} \quad , \qquad (4)$$

in terms of land and groove radii. The quantity δ_0 is plotted in Fig. I-11 from the radius data of Fig. I-10A. The initial oscillatory nature of δ_0 is characteristic of the axial "sloshing" between land and groove regions. The measured δ_0 approaches the sharp-boundary theoretical value (dashed line),
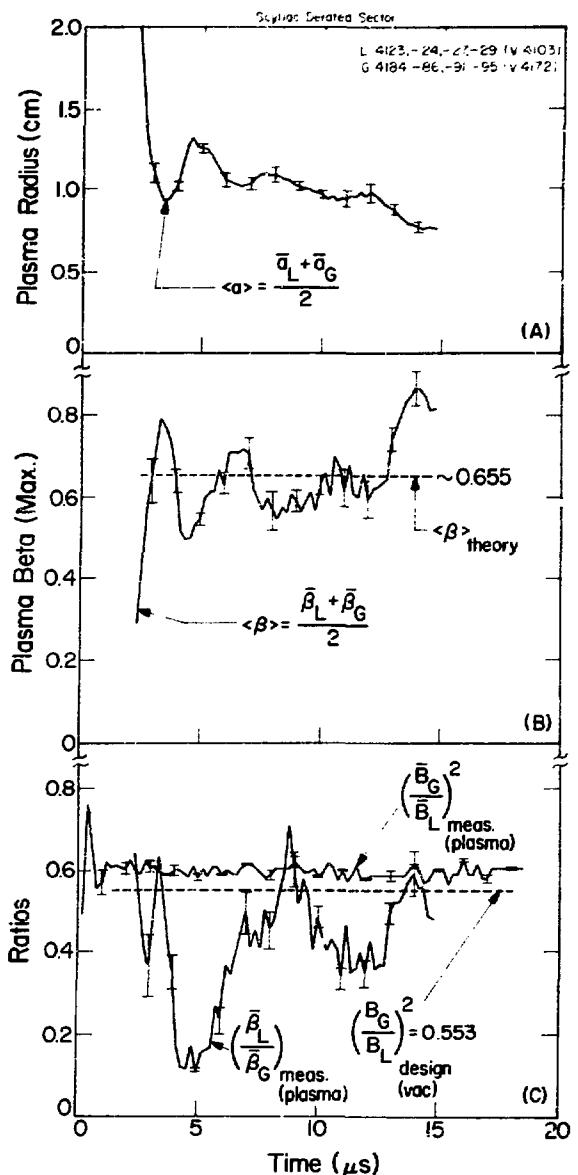
Fig. I-10.

(A) Upper curve: Average plasma radius; (B) center curve: Compares experimentally observed plasma beta with theoretical equilibrium value; (C) lower curve: Shows approach of the plasma column to axial pressure equilibrium.

$$\delta_0 = \frac{B_{\ell=0}/B}{2(1-\beta)} \quad . \qquad (5)$$

Graphs of the plasma betas on axis, determined from the excluded magnetic flux and plasma radius measurements, are shown in Fig. I-10B. Curves

9
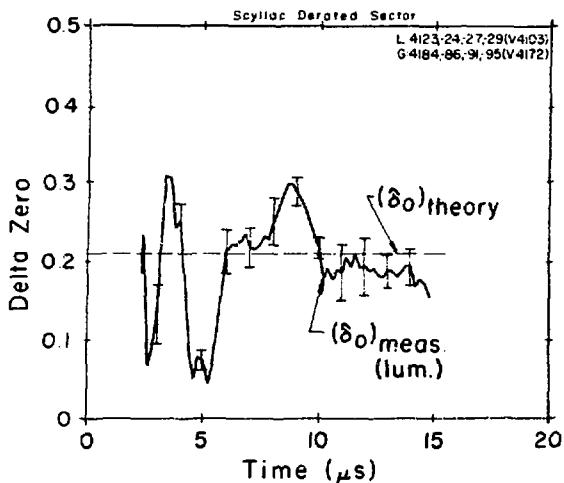
Fig. I-11.

Measured δ_0 compared with predictions of sharp-boundary theory.

labeled $\overline{\beta}_L$ and $\overline{\beta}_G$ refer to beta in land and groove regions, and the mean beta is given by $<\beta> = (\overline{\beta}_G + \overline{\beta}_L)/2$. The dashed curve is the theoretical beta value corresponding to toroidal force balance or equilibrium for the plasma radius and coil design values. The measured β curves show oscillations around the theoretical value with an oscillatory period of approximately 3.5 μs. Agreement between the theoretical and mean experimental beta values is very good, both having a value of ~ 0.65, the design beta value for the derated sector.

Figure I-10C shows the approach of the plasma column to axial pressure equilibrium, i.e., nkT = constant. This condition is equivalent to

$$\frac{\beta_L}{\beta_G} = \left(\frac{B_G}{B_L}\right)^2 = \left[\frac{1 - B_{\ell=0}/B}{1 + B_{\ell=0}/B}\right]^2 \quad . \quad (6)$$

The experimental and theoretical design curves for these parameters are plotted in Fig. 1-10C. The measured plasma beta ratio shows oscillations with a period of ~ 5 μs. The 3.5-μs period, evident in $<\beta(t)>$, does not appear at all in the $\overline{\beta}_L/\overline{\beta}_G$ ratio. The plasma appears to reach pressure equilibrium on a time scale of 15-20 μs, with considerable "sloshing" occurring between land and groove regions. The direction of approach to equilibrium is consistent with an initially too high groove pressure. This direction of pressure equilibration has been

observed in every $\ell = 1,0$ shaped coil experiment done to date. The large oscillations in the beta ratio here may be due to: (a) the relatively large value of $B_{\ell=0}/B$ used, (b) the slower time scale associated with colder plasma, (c) the more collision-dominated (i.e., more truly MHD) regime, and/or (d) the longer $\ell = 1,0$ wavelength.

These measurements show evidence for plasma equilibrium in the derated sector from the measured δ_0, measured plasma $<\beta>$, and measured $\overline{\beta}_G/\overline{\beta}_L$ ratio. A fourth condition can be examined for equilibrium, namely the plasma internal flux ϕ_i, which should be independent of z if the plasma surface is a flux surface. An analysis of the plasma internal flux, ϕ_i, obtained from the measured plasma profile, beta, radius, and external magnetic field shows ϕ_i to be the same in land and groove regions, independent of axial position. The data support the conclusion of a well-defined bumpy plasma column which conserves internal flux, and whose surface therefore coincides with a flux surface, as theory requires.

e. *Measurements of the Plasma Equilibrium Distortion, δ_1.* The plasma distortion, δ_1, has been measured as a function of time on the Scyllac derated sector. This distortion is the helical displacement of the plasma column along its length due to the $\ell = 1$ equilibrium field. For ha $\ll$ 1, sharp-boundary theory gives

$$\delta_1 = \frac{B_{\ell=1}/B}{ha(1 - \beta/2)} \quad , \quad (7)$$

where

$B_{\ell=1}/B = 0.095$, h = 0.1 cm^{-1}, a $\approx$ 1 cm, $\beta = 0.65$, for this experiment. The importance of δ_1 is immediately apparent when one considers that the equilibrium force, $F_{1,0}$, is directly proportional to δ_1. Also, the feedback fields beat against δ_1 in order to control the plasma position. Therefore, if for any reason δ_1 departs significantly from its design value, then one would expect both a loss of equilibrium and a change in the feedback control.

The helical plasma distortion, δ_1, has been determined from streak photographs in planes parallel and perpendicular to that of the torus (horizontal and vertical, respectively). A mirror, beam-splitter arrangement has permitted simultaneous viewing on the same streak camera of the plasma motions at

#6314

#6314
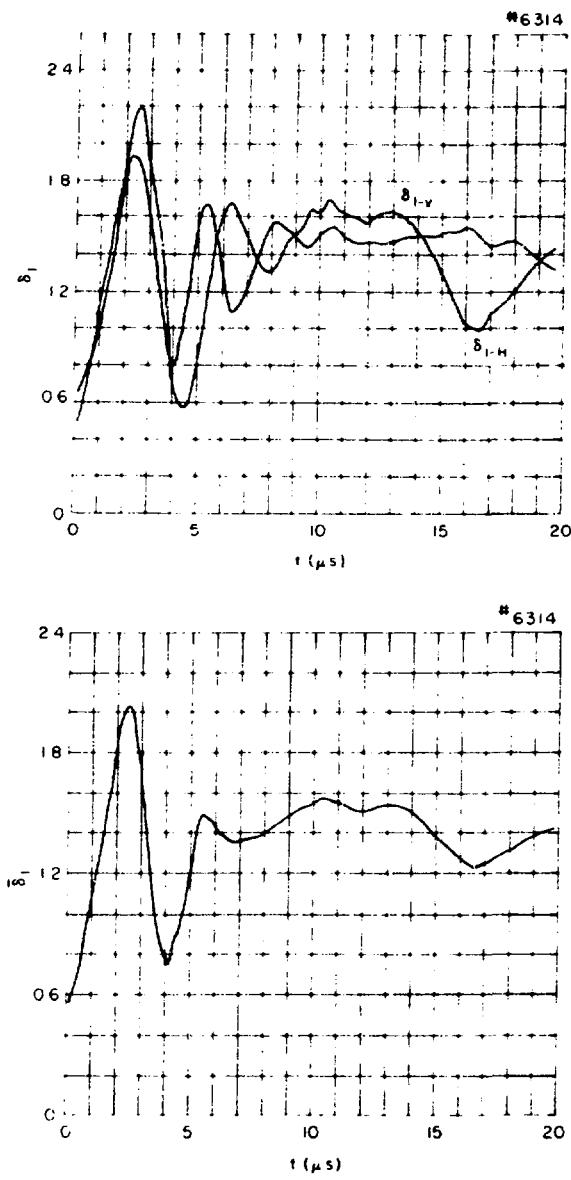
Fig. I-12.

*Plots of the observed δ_1 with an auxiliary $\ell = 0$
field of 470 G applied at 7.0 μs after the initiation of the main discharge $\delta_1 = (\delta_{1V} - \delta_{1H})/2$.*

toroidal locations separated by one-half the periodicity of the $\ell = 1,0$ fields (31.4 cm). Using two streak cameras, one viewing the motion in the horizontal plane in land and groove regions and the other viewing motion in the vertical plane midway between land and groove regions, δ_1 values, associated with the horizontal and vertical planes, are

obtained on each discharge. The spatial separation between simultaneous streak photographs gives

$$2 \delta_1 a = x_1(t) - x_2(t) \quad . \qquad (8)$$

Measurements of δ_1 were made in the feedback sector for the following cases: (1) no feedback coils installed; (2) $\ell = 0$ feedback coils installed (driven and undriven); and (3) $\ell = 2$ feedback coils installed (driven and undriven). Figure I-12 shows plots of δ_{1V} determined from the vertical plane, and δ_{1H} from the horizontal plane in the upper figure, and the average $\delta_1 = (\delta_{1V} + \delta_{1H})/2$ is plotted in the lower figure with an auxiliary $\ell = 0$ field applied. The δ_1 curves are obtained from the $\delta_1 a$ values by using an average value of the plasma radius determined from luminosity profiles in land and groove regions.

The oscillatory structure of δ_1, Fig. I-12, results from the initial δ_1 helical oscillations, owing to implosion of the plasma to the discharge tube axis rather than the helical magnetic axis. The oscillations damp out in 6-8 μs. The decrease in δ_{1H} at later times results because of the outward $m = 1$ motion of the column in the horizontal plane in agreement with theoretical predictions. The increase of δ_{1V} at later times only occurs with the application of the auxiliary $\ell = 2$ field. The average value of the observed δ_1, Fig. I-12 lower, is in agreement with the theoretically predicted value of 1.4 for plasma equilibrium.

The plasma β can also be determined from the $\delta_1 a$ measurement through the theoretical sharp-boundary expression for δ_1 from Eq. (7),

$$\beta = 2 \left[1 - \left(\frac{B_{\ell = 1}}{B} \right) \frac{1}{(ha\delta_1)} \right] \quad , \qquad (8)$$

where the quantity, $2\delta_1 a$, is determined directly from the streak photographs. At present such a β determination is limited by the δ_1 helical oscillations. However, this method can provide an independent check on plasma β with the elimination of the δ_1 oscillations through the use of a helically shaped discharge tube.

3. *Comparison of the $\ell = 1,0$ Toroidal Equilibrium and Its Scaling with Theory.* The observed plasma equilibrium in the feedback sector can be compared with the predictions of sharp-boundary

11

theory. In addition the scaling of the plasma equilibrium between the previous sector (R = 2.4 and 4.0 m) and full torus experiments to the present feedback sector experiment can be compared with theory. In all these experiments the $\ell = 1$ and $\ell = 0$ equilibrium fields were generated by shaping the inner surface of the compression coil giving a fixed ratio of these fields to the main toroidal field for a given experiment. In each experiment the plasma equilibrium was achieved by adjusting the initial deuterium filling pressure to give a balance between the $F_{1,0}$ force and the outward toroidal force through their β dependence. In the earlier sector and full torus experiments the equilibrium was achieved with deuterium filling pressures in the range of 10 to 15 mTorr, while in the feedback sector the filling pressures were 17 to 22 mTorr. In all these experiments the plasma equilibrium has been studied through the use of streak photographs and the measurements of plasma beta, plasma radius and external magnetic field. These measured parameters have been compared with the predictions of theory as a function of time and have confirmed in detail the existence of the high-beta toroidal equilibrium in Scyllac.

The equilibrium parameters measured in the various toroidal sectors and full torus experiments can also be compared directly with theory through the equilibrium relation,

$$\delta_1 \delta_0 = 2/(3-2\beta)h^2 aR \quad . \tag{9}$$

Using the expressions for the equilibrium plasma distortions,

$$\delta_1 = 2B_{\ell = 1}/ha(2-\beta)B \tag{10}$$

and

$$\delta_0 = B_{\ell = 0}/2(1-\beta)B \tag{11}$$

in Eq. (9) gives a relationship between the $\ell = 1,0$ wave number, the torus major radius, the equilibrium magnetic fields and the plasma beta,

$$\frac{hRB_{\ell = 1}B_{\ell = 0}}{B^2} = \frac{2(1-\beta)(2-\beta)}{(3-2\beta)} \quad . \tag{12}$$

This relationship is plotted in Fig. I-13. The solid curve gives the theoretical value of the plasma beta required for toroidal equilibrium as a function of the quantity $hRB_{\ell = 1}B_{\ell = 0}/B^2$.
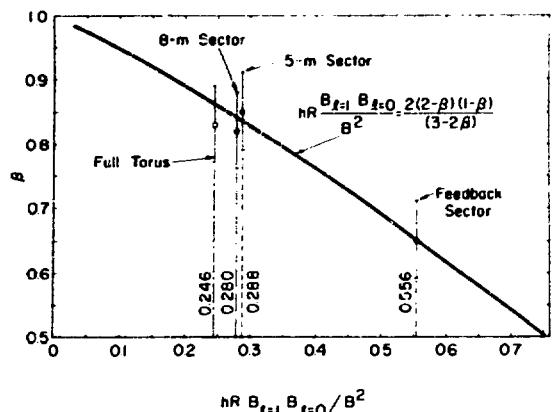
Fig. I-13.

Comparison of the measured plasma beta required experimentally for toroidal plasma equilibrium (experimental points) with that predicted by sharp-boundary theory (solid line).

With the equilibrium fields generated by the shaped inner surface of the compression coil, the quantity $hRB_{\ell = 1}B_{\ell = 0}/B^2$ is fixed for a given experiment as indicated by the vertical dashed lines of Fig. I-13. The experimental points for the average measured plasma beta are plotted together with error bars to indicate the observed variation from discharge to discharge (note the suppressed zero). It can be seen that theory and experiment agree quite well for all four basic Scyllac configurations studied to date. The equilibrium parameters of the feedback sector agree very well with theory and the predicted scaling from the earlier experiments.

These results confirm quantitatively the $\ell = 1,0$ high-beta, toroidal equilibrium and its scaling over a considerable range of parameters.

D. EXPERIMENTS WITH AUXILIARY PROGRAMMED $\ell = 0$ AND $\ell = 2$ FIELDS

A series of experiments with auxiliary $\ell = 0$ and $\ell = 2$ programmed fields was performed in the derated sector to study the response of the plasma column to $F_{1,0}$ and $F_{1,2}$ force perturbations of the feedback type and to compare the relative effectiveness of $\ell = 0$ and $\ell = 2$ fields for feedback. Both $\ell = 0$ and $\ell = 2$ auxiliary magnetic fields can produce a force on the plasma column by interacting with the $\ell = 1$ helical component of the toroidal equilibrium field. An $\ell = 0$ feedback field produces a plasma distortion, $\delta_0^{FB} = B_{\ell = 0}^{FB}/2B(1-\beta)$, and a force on the

plasma column, $F_{1,0}^{FB} = \beta(3-2\beta)B^2h^2a^3\delta_1\delta_0^{FB}/8$. An $\ell = 2$ feedback field produces a plasma distortion, $\delta_2^{FB} = 2 B_{\ell=2}^{FB}/ha(2-\beta)B$, and a force, $F_{1,2}^{FB} = \beta(2-\beta)B^2h^2a^3 \delta_1\delta_2^{FB}/8$. The direction of the $\ell = 0$ and $\ell = 2$ forces depends on their spatial phase relationship with the $\ell = 1$ equilibrium field.

For the parameters of the Scyllac sector experiment, a comparison of the forces in the $\ell = 0$ and $\ell = 2$ feedback systems gives the ratio

$$\frac{F_{1,2}^{FB}}{F_{1,0}^{FB}} = \frac{4(1-\beta)}{ha(3-2\beta)} \frac{B_{\ell=2}^{FB}}{B_{\ell=0}^{FB}} = 8.2 \frac{B_{\ell=2}^{FB}}{B_{\ell=0}^{FB}} . \quad (13)$$

The magnitude of the $\ell = 2$ field can be approximated by $B_{\ell=2} = 3.2 \; rI/d^2 \approx 0.32I$, at a radius $r = 1.0$ cm, and with a coil diameter $d = 10$ cm. The magnitude of the $\ell = 0$ field is given approximately by $B_{\ell=0} \approx 0.06I$. These field magnitudes result in a force ratio

$$\frac{F_{1,2}^{FB}}{F_{1,0}^{FB}} = 4.4 \; I_{\ell=2}^{FB}/I_{\ell=0}^{FB} , \quad (14)$$

which predicts the $\ell = 2$ feedback field to be four times as effective as the $\ell = 0$ field providing the same current can be driven in the $\ell = 2$ windings as in the $\ell = 0$ coils. This greater effectiveness of the $\ell = 2$ feedback field results from its greater efficiency in producing the plasma distortion δ_2, through the dependence of the equilibrium field wave number $h \ll 1$.

The development of the full feedback force requires the formation of the associated plasma distortions. An MHD model of Miller's shows that the $\ell = 0$ plasma distortion has an appreciable formative time of 1-2 μs in contrast to a negligible time for the $\ell = 2$ distortion. Since time delays must be minimized in a feedback system, this is a second advantage of the $\ell = 2$ system.

1. Experimental Arrangement. The auxiliary programmed $\ell = 0$ fields were produced by four $\ell = 0$ coils, Fig. I-14, for each of the thirteen $\ell = 1,0$ wavelengths in the 8.4-m sector. Each coil consisted of twelve parallel windings with an average diameter of 12 cm. Alternate coils were connected in series opposition to null the induced voltage from the main compression field.

The programmed $\ell = 2$ fields were generated by helical windings taped on the outer surface of the

Fig. I-14.

Photograph of $\ell = 0$ coils used in programmed $\ell = 0$ field experiments.

toroidal quartz discharge tube. Each $\ell = 2$ coil was an $\ell = 1,0$ equilibrium wavelength long (62.8 cm) and consisted of a "single-turn" configuration with four helical windings producing a quadrupole field, which rotated in space.

The energy storage bank for the programmed fields consisted of five Scyllac 1.85-μF capacitors and spark gaps with a triggering system which allowed crowbarring the current at either the peak or first zero crossing. This produces time-dependent auxiliary fields shown in Fig. I-15. The risetime to peak value was 2.5 μs and the maximum field for $\ell = 0$ coils was 460 G and with $\ell = 2$ coils, 250 G. Plasma position data was obtained using both streak cameras and a 20-channel luminosity profile apparatus.

The sector compression coil with an arc-length of 8.4 m was energized by one-half the Scyllac bank to produce a peak field of 17 kG with a risetime of 3.5 μs. The crowbarred L/R decay was 250 μs. Deuterium filling pressures of 18 to 22 mTorr were used in these experiments with auxiliary programmed fields. A small reversed bias magnetic field of 130 to 250 G was used, particularly in the end regions of the sector, to increase the plasma beta and improve the plasma equilibrium.

2. Results with Programmed $\ell = 0$ and $\ell = 1$ Fields.

    a. Transverse Plasma Motions with Auxiliary Coils Installed in the Sector Compression Coil.

Fig. I-15.

Magnetic field waveforms: (a) main toroidal theta-pinch field; (b) auxiliary programmed field crow-barred at peak current; (c) auxiliary field crow-barred at end of first half-cycle. Time scale: 2 μs/division.

In both the $\ell = 0$ and $\ell = 2$ programmed-field cases, the initial experiments investigated the toroidal plasma equilibrium with the auxiliary coils installed in the toroidal compression coil but unenergized. Streak photographs and the luminosity profile apparatus showed a vertical motion of the plasma column. This motion developed at 5 to 7 μs after the initiation of the discharge and carried the plasma to the discharge tube wall in 15-20 μs. The vertical motion was essentially the same all around the 8.4-m sector. Figure I-16 shows the range of the plasma column trajectories for twenty-five discharges with no auxiliary fields, but with the $\ell = 2$ windings in place and open-circuited. Identical trajectories were also observed with the $\ell = 0$ coils installed. The trajectories were taken with a 20-channel luminosity apparatus in the vertical plane perpendicular to the plane of the torus. This vertical motion is to be contrasted with the absence of such motion with the same operating conditions without auxiliary coils (cf. Figs. I-16 and I-17).

The vertical motion results from a shift of the magnetic axis in the vertical plane of the torus. The current-feed conductors, which are extensions of the auxiliary coil windings, extend vertically through the top of the main compression coil and produce a perturbation in the $\ell = 1$ field which shifts the helical axis. The plasma implodes initially to the center of the discharge tube and finds that it is not in its equilibrium position about the helical magnetic axis. Consequently, this initial column displacement, ξ_0, excites the m = 1 instability force

VERTICAL POSITION

Range of 30 Discharges
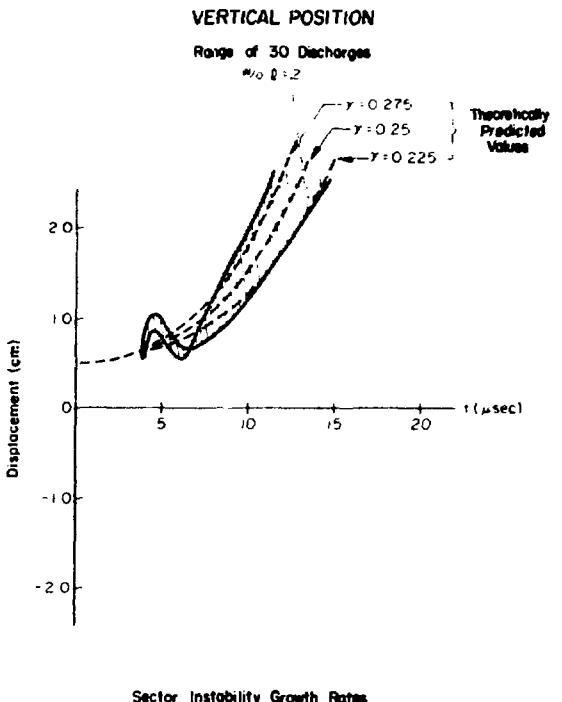
Sector Instability Growth Rates

Fig. I-16.

Plasma column trajectories in vertical plane with $\ell = 2$ coils open-circuited compared with predicted trajectories for a theoretical m = 1 instability growth rate of 0.25 ± 0.025 MHz.

$F_1 \propto \gamma^2 \xi_0$, which accelerates the plasma column farther off the axis and eventually to the discharge tube wall.

This type of plasma behavior was observed previously in the Scylla IV-3 $\ell = 1$ experiments[13] and in previous Scyllac sector experiments with $\ell = 0$ coils.[13]

In the previous experiments it was found that the direction of the m = 1 instability motion of the plasma column could be controlled by varying the position of the discharge tube within the compression coil. A few mm displacement of the tube off the magnetic axis was sufficient to induce the m = 1 instability in a predicted transverse direction. In these experiments, no attempt was made to minimize the vertical motion by shimming the discharge tube, since this initiation of the m = 1 instability provided a reproducible instability motion for the auxiliary fields to correct.

Figure I-16 compares the observed range of plasma trajectories for twenty-five discharges

bounded by the solid curves, with the predictions
of sharp-boundary theory, dashed curves. The pre-
dicted growth rate,

$$\gamma = hv_A$$

$$\left[\frac{\beta(4-3\beta)(2-\beta)}{8(1-\beta)} \; h^2 a^2 \delta_1^2 + \frac{\beta(3-2\beta)(1-\beta)}{(2-\beta)} \; \delta_0^2 \right]^{1/2} ,$$

(15)

is approximately 0.25 MHz. A variation of $\pm$ 10% in
the predicted growth rate covers the calculated
trajectories to span the range of the experimental
data.

     b.   *Transverse Plasma Motions with Auxiliary*
$\ell = 0$ Programmed Fields. In the experiments with the
$\ell = 0$ coils energized by a current pulse, the $\ell = 0$
field was phased with the $\ell = 1$ helical equilibrium
field so as to produce a vertical force on the plas-
ma column to overcome the $m = 1$ unstable motion. The
$\ell = 0$ fields were applied at various times (2 to 10
μs) after the initiation of the main discharge.
However, an application time of 5 to 7 μs provided
the most effective control of the $m = 1$ instability.
Figure I-17 shows typical trajectories of the column
with the programmed field applied 5.5 μs after the
main bank. The dashed line indicates the trajectory
calculated using a simple model where the fully
developed static forces derived from first-order
theory are given the time dependence of the $\ell = 0$
field,

$$m\ddot{x} = \frac{\beta(3-2\beta)}{2(1-\beta)} \; Bh^2 a^3 \delta_1 \; B_{\ell = 0} - \pi a^2 \rho \gamma^2 \xi_0 \; .$$

(16)

No dynamic effects nor formative delays are included
in the model; moreover, no free parameters were uti-
lized. All numerical values are taken directly from
the experimental conditions. Several different on-
set times were explored, and the data fit the simple
model in all cases.

     c.   *Transverse Plasma Motions with Auxiliary*
$\ell = 2$ Programmed Fields. For the $\ell = 2$ experiments,
the impedances of the system were such that the peak
current, risetime, and energy storage were the same
as for the $\ell = 0$ case. Again because of the discharge
tube position relative to the equilibrium field axis,
there was a vertical motion resulting from the $m = 1$
destabilizing force (Fig. I-16). The data shown in
Fig. I-18 were obtained with the $\ell = 2$ field applied
at 6.5 μs and crowbarred at the first zero crossing.
The peak amplitude of the current was the same as

VERTICAL POSITION

With $\ell = 0$ fields
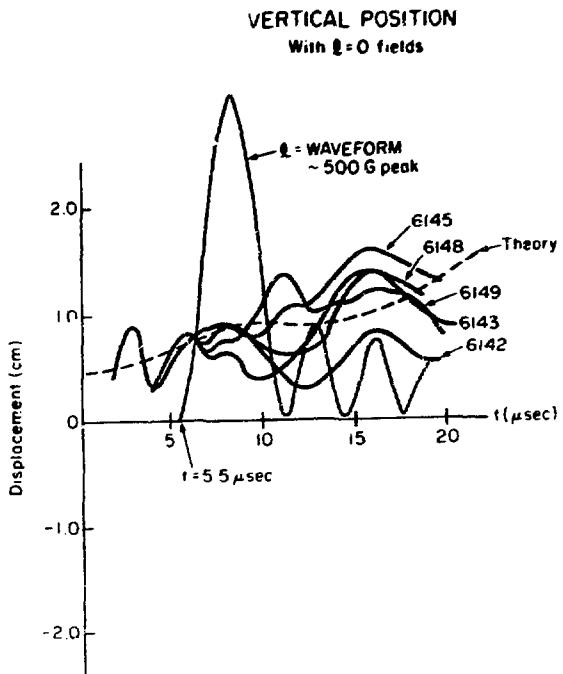
Fig. I-17.

Observed plasma column trajectories in vertical plane
with $\ell = 0$ programmed field crowbarred at end of first
half-cycle compared with theory (dashed line).

in the $\ell = 0$ experiment although the field amplitude
differs due to the differences in the coil geome-
tries. In these and in each of several other cases
the theory, dashed line (Fig. I-18), fits the data
quite well.

     3. Conclusions. In both the $\ell = 0$ and $\ell = 2$
programmed-field cases, the resulting force on the
plasma column overcomes the $m = 1$ unstable motion in
the vertical plane and either confines the column
to the plane of the torus or drives it to the op-
posite wall depending on the magnitude and duration
of the *restoring force.*

     From these experiments with auxiliary pro-
grammed $\ell = 0$ and $\ell = 2$ fields, the following conclu-
sions pertinent to the feedback stabilization of
Scyllac can be drawn: (1) these experiments have
demonstrated that the physical mechanism for feed-
back plasma stabilization of the $m = 1$ instability
in Scyllac works; (2) the comparison of the restor-
ing forces of the $\ell = 0$ and $\ell = 2$ fields, Fig. I-19,
shows that the $\ell = 2$ system is more effective for
feedback stabilization as predicted by theory. In

VERTICAL POSITION
With ℓ = 2

VERTICAL POSITION
ℓ = 2 vs ℓ = 0
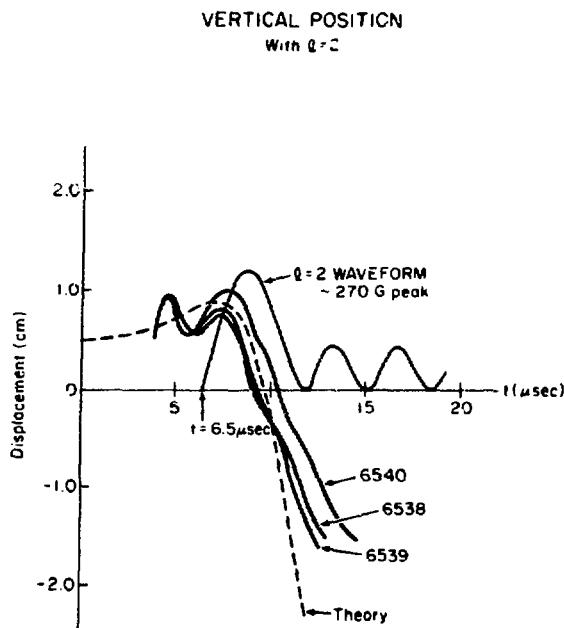
Fig. I-18.

Comparison of observed plasma column trajectories in
vertical plane and theory (dashed line) with ℓ = 2
programmed-field pulse (half-cycle) applied at 6.5 μs.

Instability Control With Programmed Fields

Fig. I-19.

Comparison of observed plasma column trajectories
(solid lines) without and with ℓ = 0 and ℓ = 2 auxil-
iary programmed fields having the same current, rise-
time, and bank energy. The dashed lines are the
theoretically predicted trajectories for an m = 1
instability growth rate of 0.25 MHz.

these experiments with the same coil current, rise-
time, and bank energy, the ℓ = 2 system produces ap-
proximately four times more force than the ℓ = 0 sys-
tem as indicated in Fig. I-19; and (3) the formative
time delay of the ℓ = 0 plasma distortion does not
appear to jeopardize the possibility of a viable
ℓ = 0 feedback system, although it will slow the
response time.

ratio of plasma to wall radii (a/b) less than 0.1.
The second term is driven by the ℓ = 1 equilibrium
field and the third by the ℓ = 0 field. The shortest
unstable wavelength in the full torus experiments
was observed to be greater than 4 m.

In the MHD feedback stabilization system for
Scyllac, the feedback force is generated by small
controllable ℓ = 2 fields which produce plasma per-
turbations,

$$\delta_2 = \frac{B^{FB}_{\ell=2}}{ha(1-\beta/2)B}.$$ (18)

This plasma perturbation interacts with the ℓ = 1
equilibrium plasma distortion to produce a feedback
restoring force,

$$F^{FB}_{1,2} = \beta(2-\beta) B^2 h^2 a^3 \delta_1 \delta^{FB}_2/8,$$ (19)

in opposition to the m = 1 destabilizing force,

E. EXPERIMENTS WITH FEEDBACK STABILIZATION

A feedback stabilization system has been devel-
oped to control the m = 1 instability of the plasma
column in Scyllac. The MHD growth rate of the m = 1,
long wavelength mode is given by,

$$\gamma = hv_A \left[-\beta^2 \left(\frac{a}{b}\right)^4 r^2 + \beta \frac{(4-3\beta)(2-\beta)}{8(1-\beta)} h^2 a^2 \delta^2_1 \right.$$
$$\left. + \frac{\beta(3-2\beta)(1-\beta)}{(2-\beta)} \delta^2_0 \right]^{1/2}.$$ (17)

The first term provides wall stabilization and
arises from the dipole currents induced in the plas-
ma column by the ℓ = 1 field. This term is negligi-
ble in the present Scyllac experiments with the

$$F_1 = \pi a^2 \rho \gamma^2 \, \xi \, , \qquad (20)$$

where ξ is the displacement of the plasma column from its equilibrium position. Equating the feedback force to the destabilizing force gives the feedback field required for stabilizing the $m = 1$ mode,

$$B_{\ell=2}^{FB} = \frac{\gamma^2 \, \xi \, B}{B \, h v_A^2 \, \delta_1} \, . \qquad (21)$$

In addition to the feedback field requirement, feedback control theory requires that the product of the instability growth rate, γ, and the feedback response time, τ, be less than 0.5 for control of the instability.

1. Experimental Arrangement. The feedback stabilization system, Fig. I-20, consists of four basic components: (a) plasma position detectors, silicon photo-detectors, designed to detect plasma motion away from the equilibrium position; (b) the intermediate amplifier contains signal processing units, which produce an output voltage proportional to the sum of plasma position and velocity with separate position and velocity gain controls; (c) power amplifier modules, each of which consists of five separate stages of amplification ending in the push-pull operation of two ML-8618 high-power triodes operating with outputs as high as 1 kA at a plate voltage of 35 kV; and (d) $\ell = 2$ feedback coils located inside the main compression coil and driven by the power modules.

Figure I-21 is a photograph of the derated sector with the feedback stabilization system installed. Three position detector stations are located on the three central compression coil sections of racks 7, 8, and 9 of the five rack sector. Two orthogonal detectors at each station view the plasma at $\pm 45°$ to the horizontal plane of the torus at toroidal positions $hz = 7\pi/8$ and $hz = 9\pi/8$ in a wavelength so that the $\ell = 1$ helical displacement of the plasma column should not be apparent.

These detectors sense the position of the plasma column and feed the analogue processing circuits, which drive the feedback amplifiers. The feedback power modules are located above the Scyllac collector plates on the feedback platform, Fig. I-21. The outputs of the power modules are coupled through

FEEDBACK STABILIZATION SYSTEM
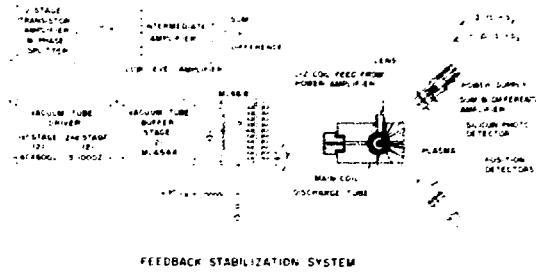
Fig. I-20.

Schematic diagram of Scyllac feedback stabilization system.

output transformers, which are located back of the main compression coil, to the $\ell = 2$ feedback coils.

Thirteen $\ell = 2$ feedback coils, each an $\ell = 1,0$ wavelength long (Fig. I-22), are positioned over the quartz discharge tube inside the main compression coil. Two feedback power modules are used for each $\ell = 1,0$ wavelength; one module drives one of the $\ell = 2$ windings and provides the transverse force in one of the position detector directions while the second module energizes the other $\ell = 2$ winding, which is rotated 45° relative to the first winding, and produces the force in the perpendicular direction. Each position detector controls several power modules.

The feedback power modules require considerable auxiliary equipment: a 480-Vac single-phase power source for the tube filaments, 40-kV capacitor banks

Fig. I-21.

Photograph of the Scyllac derated sector with the feedback apparatus installed.
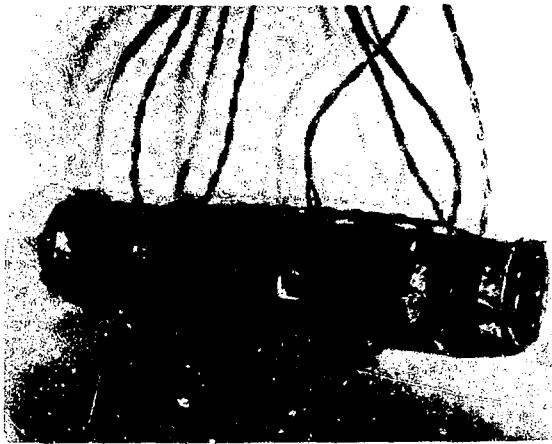
Fig. I-22.

Photograph of ℓ = 2 four-turn feedback coil consisting of a separate coil for each of the two force directions. The four equally spaced, single-turn circular windings are ℓ = 0 trimming coils, which are driven by a small capacitor bank.

for the B + plate supply of the ML-8618 output tubes; 20-kV power supplies for the PFN networks which supply the plate voltage for the ML-6544 driver tubes; lesser plate and bias supply voltages; and an associated control system with various built-in test modes. The electrical performance of the feedback system is monitored by the Sigma II computer by a data acquisition channel for each power module and six channels for each position detector and analogue processor.

A capability for positioning the quartz discharge tube inside the compression coil in the plane perpendicular to that of the torus was installed on the sector during the feedback installation. This positioning feature in the vertical plane is used to locate the toroidal axis of the discharge tube on the magnetic equilibrium axis.

Simple auxiliary ℓ = 0 windings have also been installed in the sector to assist in trimming the ℓ = 1,0 plasma equilibrium. Single-turn windings installed in groove and land regions are connected in series opposition in each ℓ = 1,0 wavelength to provide an auxiliary force on the plasma column in the plane (horizontal) of the torus. Similar windings located midway between land and groove regions are capable of producing a force in the plane (vertical) perpendicular to that of the torus. These windings are energized by two small capacitor

banks with independent triggering systems.

2. *Delay and Risetime of the Feedback System.* The delay plus risetime, τ, of the feedback system has been measured to be 1.4 μs, to 90% of full output current. This is for a transformer turns ratio of 9:7 (27-μH module load) and standard operating conditions: 9-V filament voltage and 32.5-kV plate voltage. The delay time to 10% current output was measured to be 0.5 μs and the 90% risetime, 0.9 μs. Bench-measured component delays are: cable, 100 ns; detector, 30 ns; intermediate amplifier (IA), 70 ns; and power module, 280 ns. In computing γτ it is more reasonable to use a time somewhat shorter than the time to 90% of full output since the current has appreciable values before that time. Using the time for $(1-1/e) = 0.63$ of full output as an effective time we find $\tau_{eff} = 1$ μs.

The measurement consisted of using a light emitting diode (LED) to illuminate the feedback position detector and monitoring simultaneously the current in the LED and the current in an ℓ = 2 coil through equal-length cables. In Fig. I-23 are shown the oscilloscope traces of the LED current, and the output current. The noise on the LED current trace is pick-up from the feedback power modules. The measurement was repeated with the cables reversed to check propagation time effects and gave the same result.

3. *Results with Closed-Loop Feedback Stabilization.* The installation and electrical checkout of the feedback system on the derated sector were completed in the first part of December. Initial feedback experiments, without optimization of the parameters of the feedback system, are reported here.

Initial experiments with the feedback system applied to the derated sector show successful closed-loop feedback stabilization of the m = 1 instability in the vertical plane perpendicular to the plane of the torus, Figs. I-24 and I-25. The plasma trajectories (heavy lines) of Figs. I-24 and I-25 were taken with the 20-channel luminosity apparatus, which has a ± 2-cm field of view about the toroidal minor axis in the vertical plane. In these experiments a programmed ℓ ≈ 0 field pulse of 6-μs duration was initially applied to aid in setting the initial equilibrium in the horizontal plane. Although the ℓ = 0 field pulse was spatially phased to produce an
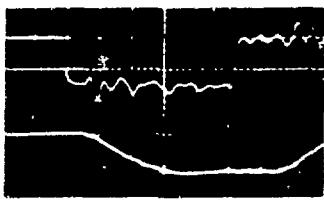
Fig. I-23.

Oscilloscope traces showing the feedback delay-rise-time: Upper trace, light emitting diode input to feedback position detector; Lower trace, feedback output current into $\ell = 2$ feedback coil; Time scale, 0.5 μs/division.

$f_{1,0}$ force in the horizontal plane, there was sufficient coupling to the vertical plane to set off the m = 1 instability in that plane as is observed in the trajectories without feedback in Figs. I-24 and I-25. Without feedback, the m = 1 instability drives the plasma column downward in the vertical plane. With closed-loop feedback applied, the m = 1 instability is controlled in the vertical plane, as shown by the trajectories in both Figs. I-24 and I-25. Figure I-25 also shows the feedback field applied by the closed loop to correct the m = 1

PLASMA VERTICAL POSITION
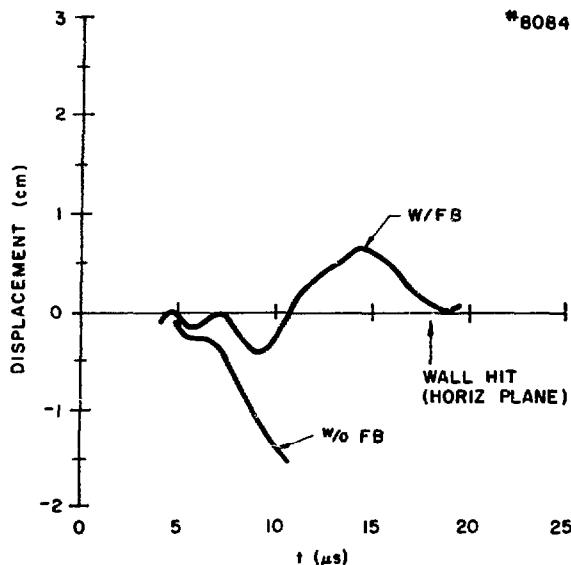
Fig. I-24.

Plasma column trajectories in vertical plane without and with feedback showing closed-loop feedback control of the m = 1 instability in the vertical plane.
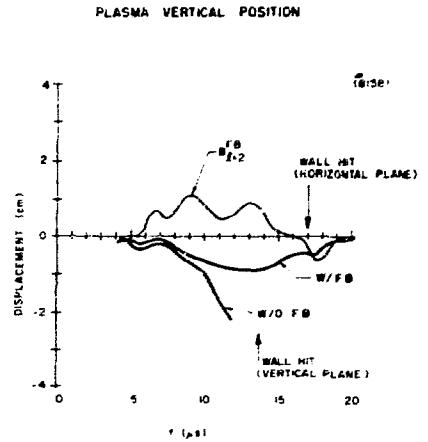
Fig. I-25.

Plasma-position and feedback output current showing closed-loop feedback control of m = 1 instability in the vertical plane.

motion. These plasma experiments with the feedback system show successful closed-loop feedback stabilization of the m = 1 instability in the vertical plane.

However, the m = 1 motion in the horizontal plane of the torus appears to be dominated by loss of equilibrium and is not yet controllable by feedback. Each of the streak photographs of Fig. I-26 shows simultaneous plasma trajectories in land and groove regions in the horizontal plane of the torus without and with auxiliary fields and feedback. Upward in the streak photographs is outward away from the major axis of the torus. In each streak photograph of Fig. I-26 the plasma motion is characterized by the following: (a) initial δ_1 helical oscillations which damp out; (b) a stably confined period of
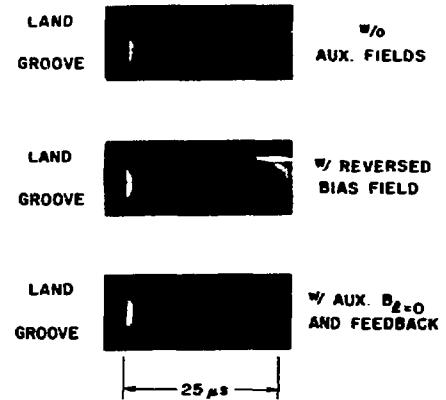
Fig. I-26.

Streak photographs showing plasma motion in toroidal (horizontal) plane: Upper streak in each photograph is taken in a land region and lower streak in a groove region.

19

equilibrium; (c) the helical plasma distortion δ_1, which is directly proportional to the separation of the plasma trajectories in land and groove regions; (d) a fatter plasma column in the groove region relative to the land indicating the bumpy plasma distortion δ_0; and (e) an outward $m = 1$ motion terminating the plasma confinement. These streak photographs show that the application of auxiliary fields prolongs the onset of the outward $m = 1$ motion.

During the initial stable period, the application of either a programmed $\ell = 0$ or $\ell = 2$ field drives the plasma column inward in the toroidal plane to the discharge tube wall. However, once the onset of the outward motion occurs, a force comparable to an appreciable fraction of the $F_{1,0}$ equilibrium force is required to overcome it. The magnitude of the force causing the outward $m = 1$ motion indicates a loss of equilibrium in the toroidal plane, rather than just the $m = 1$ instability. Hence the inability of the feedback system, which can apply at most $0.2F_R$ to control the outward motion. Possible causes of loss of equilibrium include: (a) decrease of the plasma beta with time because of relatively large δ_1 and the possible contact of the plasma density toe with the wall; (b) axial redistribution of the plasma pressure and corresponding changes in the bumpy plasma distortion δ_0. For example, the "sloshing" time between groove and land regions is $\sim 5\ \mu s$, which is larger than the toroidal drift time to the wall; (c) the achievement of only a dynamic equilibrium rather than a time-independent one; and (d) effects of diffuse-plasma equilibrium as opposed to sharp-boundary equilibrium.

4. *Plasma Trajectory Analysis.* The plasma trajectories of the simultaneous land and groove streak photographs have been digitized. Using these data, the trajectory of the centroid of the plasma column is determined by averaging point by point the land and groove position; i.e.,

$$X_C(t) = [X_L(t) + X_G(t)]^{1/2}, \qquad (22)$$

where $X_C(t)$, $X_L(t)$, and $X_G(t)$ are the positions of the plasma centroid, and of the plasma column in the land, and groove regions at time t. This assumes helical symmetry of the plasma column and does not include variations in the helical distortion which accompany a displacement of the plasma column.

There are two major sources of "noise" in the data. The first is introduced by the digitization process itself. The second is a result of the δ_1 oscillation of the column (cf. Section C-1 above) which are evident at early times in the discharge. These are $180°$ out of phase in the land and groove regions and would, in principle, be cancelled out by the averaging process. The δ_1 oscillations, however, are more pronounced in the land regions (owing perhaps to the mass difference between lands and grooves) and therefore survive the averaging process. This introduces spurious apparent motion of the centroid at the characteristic frequency of the δ_1 oscillation.

An interesting manipulation of the data is the determination of the body force, $F(t)$, required to produce the observed trajectory of the centroid of the plasma column. Since this involves taking the second derivative of the data, both the noise from digitizing and the spurious motion at the δ_1 oscillation frequency pose a serious problem. The frequency of both of these noise sources being much higher than that of the gross column motion causes them to dominate the time derivatives of the position. Figure I-27 shows the trajectories of the land, groove, and centroid of the plasma column together with the relative amplitudes of their Fourier components. The white "noise" in the land (from ~ 0.5 to 2.5 MHz) reflects the larger digitization error owing to the fainter streak photographs of this less luminous region. The strong component at ~ 0.34 MHz in the land corresponds to the δ_1 oscillation. In the groove region, there is a relatively smaller contribution near 0.34 MHz, but the spectrum is dominated by the peak at ~ 0.15 MHz which represents the gross motion of the groove region. The contributions of the frequency components carry over to the trajectory of the column centroid in the expected manner with the spectrum being dominated by the peak at ~ 0.12 MHz, but with the troublesome δ_1 oscillation surviving giving a peak at ~ 0.33 MHz. The δ_1 oscillation component and the "white noise" must be removed to get meaningful second derivatives of the trajectory.

A straightforward method of smoothing the data and facilitating the differentiation is the fitting of the data to a polynomial. The solid line in
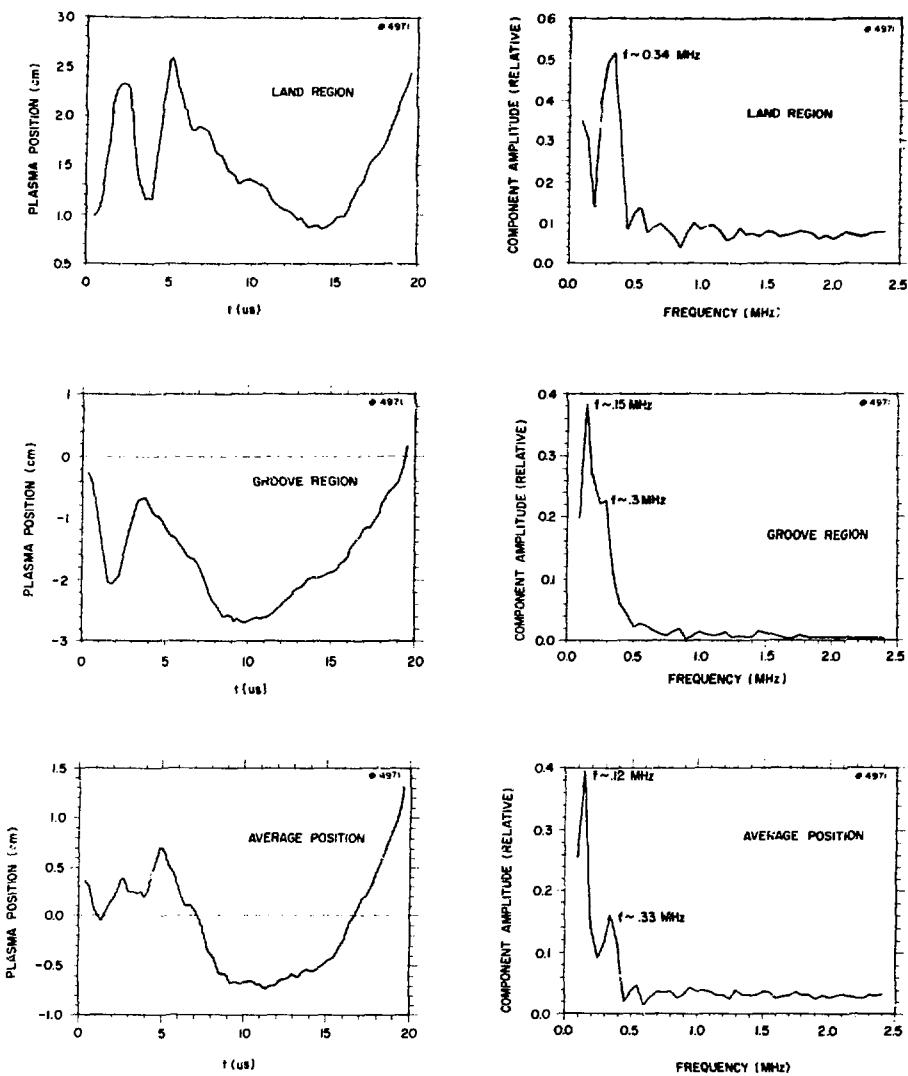
Fig. I-27

Plasma column trajectories in the horizontal plane of land (upper right) and groove (center right) regions and average or centroid position (lower right) with the relative amplitudes of their Fourier components on the left.

Fig. I-28 shows the rms deviation (cm) as a function of the degree of the fitted polynomial. The dashed line in Fig. I-28 shows the relative amplitude of the δ_1 oscillation as a function of the degree of the fitted polynomial. The cross-hatched area represents an estimate of the range for which the δ_1 oscillation is smoothed out and yet the rms deviation is small enough that the curve is representative of the actual data.

The net force F_{NET} acting on the plasma col-

umn required to produce a typical observed trajectory is shown in Fig. I-29. This net force includes the destabilizing force F_γ which is a function of the displacement of the centroid ξ and the $m = 1$ growth rate γ ($\gamma \approx 0.3$ MHz) and is given by

$$F_\gamma \propto \gamma^2 \xi . \qquad (23)$$

The force F_X producing the loss of equilibrium in the derated sector experiments is
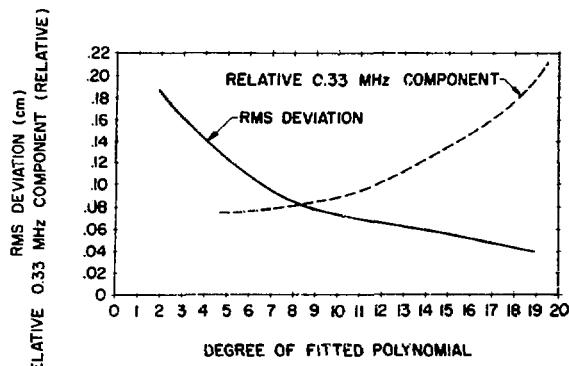
$$F_X = F_{NET} - F_Y \quad . \tag{24}$$

Figure I-30 shows the time dependence of F_X obtained
by correcting the net force for the position-depen-
dent F_Y. The beta variations required to produce
F_X (by creating an imbalance between F_R and $F_{1,0}$)
are shown in Fig. I-31. There is no supportive evi-
dence for such large excursions of the plasma beta.
For any net force on the column, there exists some
position for which the destabilizing force will pro-
vide a new equilibrium. For successful feedback
stabilization, it is required that the plasma col-
umn be located near the equilibrium position at a

time when it has reasonably small momentum. Fur-
thermore, the feedback system must be preprogrammed
through an E-set command, orientation of the posi-
tion detectors, or some other means requiring a
priori information as to the location of the equi-
librium position. The equilibrium position as a
function of time is shown in Fig. I-32. Both the
rapid variations as well as the magnitude of the
excursions suggest that stabilization would be at
best difficult.

This analysis of the observed plasma trajecto-
ries, which yields the net force acting on the plas-
ma column, indicates that only a dynamic equilibrium
is being achieved. Furthermore, it suggests the
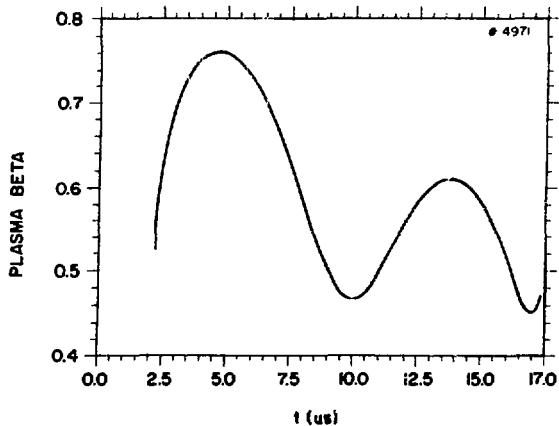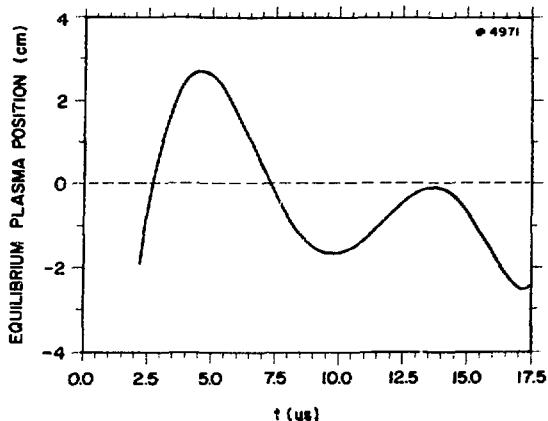
Fig. I-32.

Plasma toroidal equilibrium position as a function of time for a typical plasma column trajectory (Fig. I-27).

application of a programmed auxiliary field to compensate the non-equilibrium force and to ease the *column into its equilibrium position.* The analysis also indicates that the primary cause of the equilibrium loss is not a variation in the plasma beta because of the magnitude of the change that would be required. Variation of the bumpy plasma distortion δ_0 owing to sloshing between land and groove regions remains a likely cause of the equilibrium problem.

   5. *Near-Term Experiments.* Present experiments studying the equilibrium loss in detail include: electron temperature measurements as function of time; measurements of the equilibrium plasma distortions, δ_0 and δ_1, in time; simultaneous plasma beta measurements in land and groove regions; measurements of absolute density profiles in groove regions; detailed magnetic field probing; and observations of possible toroidal plasma structure. A helical discharge tube with a helix radius of 1.4 cm will be installed in the present sector coil to increase the clearance between the plasma helix and the coil wall, to eliminate the δ_1 helical oscillations, and to reduce the plasma "hunting" for the equilibrium position.

   The utilization of larger helical plasma distortions, $\delta_1 \sim 3$, are planned in combination with δ_0 and δ_2 plasma distortions to achieve high-beta toroidal equilibrium. The larger δ_1 has important advantages in the stabilization of the $m = 1$ insta-

bility. In feedback stabilization, the larger δ_1 reduces the growth rate of the $m = 1$ instability and thereby relaxes both the delay-risetime requirement and the magnitude of the feedback field. The required feedback field is further reduced since it also depends inversely on δ_1. In wall stabilization of the $m = 1$ mode, the requirement on the a/b ratio of plasma to wall radii is reduced as δ_1 increases. Sector experiments with $\delta_1 \sim 3$ are planned for the near future. It is also planned to add an $\ell = 2$ equilibrium field and to considerably reduce the $\ell = 0$ field and the corresponding δ_0 plasma distortion.

   The utilization of large helical plasma distortions δ_1 requires the use of a helically shaped discharge tube in order to maintain an appropriate region between the plasma column and the tube wall.

   A mechanical device for shaping a cylindrical quartz tube into a helical, toroidal tube has been designed, fabricated, and assembled. The device incorporates the original tube forming development at the Max-Planck Institute for Plasma Physics in Garching, and is also designed to have sufficient flexibility to form quartz tubes with diameters in the range of 5 to 20 cm into major toroidal radii in the range of 3 m to infinity with helical radii up to 7 cm. A perspective drawing of the device is shown in Fig. I-33, and a photograph of the assembled machine is shown in Fig. I-34.

F.   FEEDBACK DEVELOPMENT AND TECHNOLOGY

   An evaluation and study of the major problems in the feedback power modules, which centered around reliability and performance, resulted in a substantial modification of the modules. The modification and testing of the power modules consumed an appreciable effort during the year. Research has continued on feedback position detectors and has resulted in an improved detector and a simplified mounting and alignment arrangement. A new segmented position detector with an innovative discriminating circuit has been developed and tested. Investigations of both $\ell = 0$ and $\ell = 2$ feedback coil configurations have been carried out and coils fabricated for the feedback experiments. A new feedback control processor is being designed and developed which will perform a Fourier analysis of the signals from the plasma position detectors, give the toroidal

23
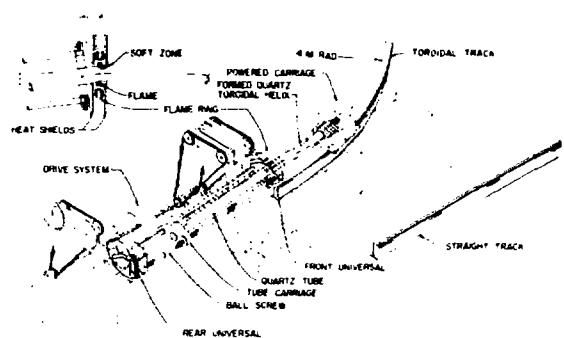
QUARTZ TUBE FORMING MACHINE

Fig. I-33.

Perspective drawing of the device for forming a helical, toroidal quartz tube.

mode structure of the plasma column, and apply the appropriate driver voltages to the various feedback power modules. Analysis has been carried out on the influence of the delay of the feedback system on the feedback force and on the effect of plasma column displacement on the magnitude of the effective feedback force.

   1. Modifications to the Feedback Power Modules. After much deliberation, a decision was made to modify the feedback power amplifier modules to improve their reliability and performance. The original module suffered mainly from overstressed components, a sometimes unstable output tube drive circuit, and excessive risetime and delay. By adding two ML 6544 pulse modulator tubes connected as plate followers to drive the 8618 output tube

Fig. I-34.

Photograph of the quartz forming machine.

grids, most of the module deficiencies were corrected. Voltage stress on transistors and driver vacuum tubes was reduced, trouble-plagued Krytron bias trigger tubes were removed, and oscillations caused by the negative grid impedance of the 8618 tube were eliminated. Drive interstage transformer saturation time increased by a factor of more than three to greater than 40 μs, module delay was reduced from 0.6 to 0.3 μs, output current risetime decreased 10-20%, falltime decreased 30% and output current increased 15-30%. Non-linear zinc oxide varistors were employed to absorb the inductive load energy. A new module output transformer with a selectable turns-ratio of 9:7, 9:9, and 9:12 was fabricated to use with the recently developed four-turn coils for $\ell = 2$ feedback field control of plasma position.

   The process of modifying 30 modules began in June and was completed in September. Many short cuts were taken to reduce the time required for this operation. However, due to many wiring errors it was not until October 20 that 26 operating modules were installed on Scyllac. Several changes were necessary in the Scyllac feedback control system: six 15-kV, 100-ma, vacuum tube voltage regulators were constructed, 5-kV bias supplies were changed to provide more current, and the 115-VAC supply system for the modules were reworked to handle the increased module load.

   After a week of operating 26 modules on Scyllac, it became apparent that further changes in the modules were necessary to correct arcing problems among too closely spaced components. Of the failures occurring in the modified modules in operation on Scyllac, all were located among the added circuitry. None occurred in the previously failure-prone components of the driven transistor and vacuum stages. In two defective modules removed from the system, one had a short-circuited fan, the other a loose vacuum tube plate connector. It would appear that module component reliability is vastly improved. The dominant problem remaining is 8618 output tube arcing due to anode surface heating (arcing due to grid circuit instabilities was eliminated).

   A new source of concern is the recent replacement of five 8618 tubes due to 20-30% loss of cathode emission, a drop too rapid to be explained by normal cathode decarburization, even at elevated

temperatures. Of the init'ally selected 8618 tubes for the 30 operating modules, the maximum plate current at 9 filament volts ranged from 700 to 1000 amperes and at 9.5 volts from 900 to 1200 amperes. In the process of selecting the tubes, fourteen out of seventy were rejected because their maximum plate current was less than 900 amperes at 9.5 filament volts. Most of the rejects had accumulated many 9-volt filament hours from earlier Scyllac and Scylla IV operations.

Modification and construction of fifty-five additional modules for full torus operation are in progress. An attempt is under way to design a new 6544 buffer plate circuit to extend feedback operating time to greater than 100 μs as well as increase the 8618 grid drive power.

2. *Feedback Position Detectors.* A new position detector has been developed and is being used in the feedback experiment. The principle of operation is the same as that of the previous position detector, namely a silicon photodiode produced two signals, a difference (Δ) and sum (Σ) whose ratio Δ/Σ is proportional to the displacement of the centroid of the plasma light imaged upon it. The light sensing element (Quantrad Corp. FPS-100-3 22) is a piece of silicon PIN semiconductor 3 mm wide by 72 mm long. Electrically it behaves as a diode which is operated with a reverse voltage bias and which conducts current in response to light falling on the cathode surface. There are two connections to the cathode at each end, and the way the current divides and flows out the two leads depends on the resistance seen. This resistance consists of the intrinsic resistance of the silicon material and external circuit resistance. The bulk resistivity of the silicon is quite uniform and amounts to about 400 from cathode to cathode. The position detector is mounted in a precise way directly on the Scyllac compression coil so that its location with respect to the viewing slits is quite well defined.

The position-detector amplifier is capable of producing a rather large signal. Saturation of the difference signals occurs at 4 volts output. The risetime of the detector is due to the capacitance and resistance of the PIN diode, since the amplifiers have much faster risetimes. This risetime is calculated to be on the order of 2.3 x 60

pf x 200 Ω = 28 ns using the capacitance and resistance of half the detector. The response of the position detector is linear over a range of plasma column displacements of $\pm$ 3.5 cm. The sensitivity of the detector in terms of the ratio of the difference-to-sum signal (Δ/Σ) i 2.1 per centimeter of plasma column displacement.

A feedback position detector was mounted to look into the same vertical slot viewing a groove region as the 20-channel luminosity apparatus. A comparison of the position information from the feedback position detector and the luminosity is shown in Fig. I-35. The position detector signal is the module input intermediate amplifier output signal scaled empirically to best fit the luminosity data. The velocity gain is set to zero and the position gain is 1.5 where the maximum is 5. The empirically determined position sensitivity is 5 volts/cm.

As shown in Fig. I-36 there is not perfect agreement between position detector and luminosity and the absolute error can be as much as 5 mm. The source of this error is probably that the position detector responds to the centroid of the light intensity whereas the luminosity apparatus gives the fitted position of the peak light intensity. A model of the position detector behavior is given by
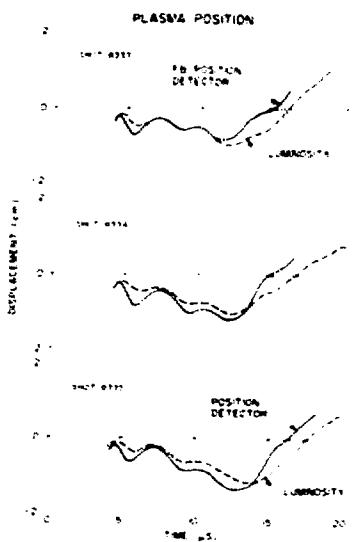
Fig. I-35.

Comparison of the plasma column position in the vertical plane from a feedback position detector and the 20-channel luminosity apparatus.
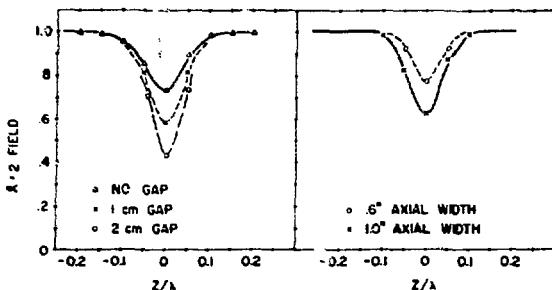
Fig. I-36.

Axial magnetic field perturbations from flux leakage through gaps at ends of $\ell = 2$ coils (left figure) and at diagnostic slots (right figure) as a function of z.

$$\xi_{pd} = \xi/(1+b) + \xi_b \, b/(1+b) \, , \qquad (25)$$

where ξ is the real plasma position, ξ_b the position of the background light, and the background light intensity is b relative to the total light. The sensitivity of the position detector is reduced by $1/(1+b)$ by background light. The measured position detector sensitivity of 5 volts/cm compared with the calculated sensitivity of 10 volts/cm implies that the total background light is about equal to the plasma light. Taking into account that the field of view of the position detector is 6 cm and the apparent plasma width is 1 cm, the average background light intensity is about 17% of the peak plasma intensity, which is not unreasonable.

Whether the performance of this type of detector is adequate for feedback is questionable. Using the criteria given below by Bartsch that ξ_0 must be less than $\xi_{max}/4.4$ (for $\gamma\tau = 0.375$) where ξ_0 is the amplitude of the unstable displacement when first detected and ξ_{max} is the displacement where the unstable force equals the maximum feedback force, we find for a maximum feedback $\ell = 2$ field of 70 G that ξ_0 should be less than about 3 mm. The present detector does not satisfy this criterion. The new 8-segment position detector, which will be used in the near future, should however.

3. Feedback $\ell = 2$ Coils. The $\ell = 2$ feedback coils were wound on plexiglass coil forms which were shaped to the toroidal configuration of the quartz discharge tube. The coil forms were grooved to hold the wire in the proper position at a mean diameter

of 11.4 cm. Each $\ell = 2$ coil is a single $\ell = 1.0$ equilibrium wavelength long, 62.8 cm, less 1.0 cm for viewing between coils at groove regions through slits in the main compression coil. Figure I-22 is a photograph of an $\ell = 2$ coil. The coils have an installed inductance of 18 μH including 1.2-m leads when connected with both coils of a particular force direction in series (one feedback power module per wavelength per force direction). The two force directions correspond to the orientation of the position detectors, plus/minus 45° with respect to the plane of the torus.

The nominal maximum coil current is 1000 A with a four-turn sinusoidal coil configuration to yield an effective four times multiplication of the coil current. The field in a straight prototype coil has been measured with a calibrated pick-up coil and agrees with the field from a two-dimensional calculation. The calculated field inside the $\ell = 2$ coil is given by $B = \nabla\phi$, where

$$\emptyset = -\mu_0 \frac{N I_0}{2 r_c} \left(1 - \left(\frac{r_c}{r_w}\right)^4\right) \frac{r^2}{2 r_c} \sin(2\theta - hz \pm \pi/2),$$
$$(26)$$

and N = number of turns; I_0 = current into coil leads; r_c = coil radius; r_w = wall radius; and z = 0 at a land region. The undulating shape of the inner surface of the Scyllac coil has a minimum radial distance from the $\ell = 2$ coil of ~ 2.5 cm. The factor

$$\left[1 - \left(\frac{r_c}{r_w}\right)^4\right]$$

is in the range 0.77 to 0.98 depending on the local wall radius. At a current of 1000 A, the factor $\mu_0 N I_0/2 r_c$, which is the amplitude of the transverse field components at the i.d. of the coil, has a value of 440 G. At the plasma radius, r = 1 cm, the field has a magnitude of 80 G.

The magnetic field perturbations due to joints between coils and rerouting of wires for viewing windows have been measured on straight versions of the $\ell = 2$ coils. Typical data shown in Fig. I-36 give the $\ell = 2$ field perturbations. The normal coil joint gaps and the position detector windows, which are the most numerous variety, are ~ 1.0 cm wide.

Additional windings have been installed over

the $\ell = 2$ coils to provide capacitor-driven $\ell = 0$ fields for adjusting the initial equilibrium. These coils are constructed with opposing, single-turn coils connected in series and located one-half wavelength apart. Two sets of $\ell = 0$ coils are provided; one for producing a force in the plane of the torus and the other in a plane perpendicular to that of the torus.

4. *Feedback Delay ($\gamma\tau$) vs Feedback Force.* The influence of time delay on the feedback force required to stabilize the $m = 1$ plasma instability in Scyllac has been investigated. The equation of motion of the column for linear velocity and position feedback with time delay is given by[3]

$$\frac{d^2\xi}{dt^2} = \gamma^2\xi - F\left(\alpha + \beta\frac{d}{dt}\right)\xi(t-\tau) \quad , \qquad (27)$$

where ξ = column displacement; γ = exponentiation rate in absence of feedback; $F\alpha\xi$ = position feedback force per unit length divided by the column mass per unit length; $F\beta\, d\xi/dt$ = velocity feedback force per unit length divided by the column mass per unit length; and τ = feedback delay.

The stability of the system described by Eq. (27) has been investigated with a Nyquist stability analysis to determine the allowed range of system parameters. For purposes of numerical computation, the feedback expression has been normalized as follows: $A = F\alpha/\gamma^2$ is normalized position gain; and $B = F\beta/\gamma$ is normalized velocity gain. The lowest region of stability, for several values of $\gamma\tau$, is shown in Fig. I-37 in terms of the normalized position and velocity parameters.

The hand calculations of G. Miller[3] can be seen as limiting cases on two sides of the triangular stability region of Fig. I-37: (1) The obvious requirement that A, $F\alpha/\gamma^2$, be greater than one; and (2) B, $F\beta/\gamma$, be greater than $A\gamma\tau$. In addition, the feedback analysis has provided upper bounds on the feedback force components for stability.

A direct numerical integration of the force equation has been utilized to study the motion and forces for the feedback system. Values of A, B, and $\gamma\tau$ within the stable regions have been inserted into the force expression along with the initial conditions:

$$\xi(t = 0) = \xi_0 \qquad (28)$$

BOUNDARY OF STABLE REGION

$$\frac{d^2\xi}{d(\gamma t)^2} = \xi - (A + B\frac{d}{d(\gamma t)})\xi(t-\tau)$$
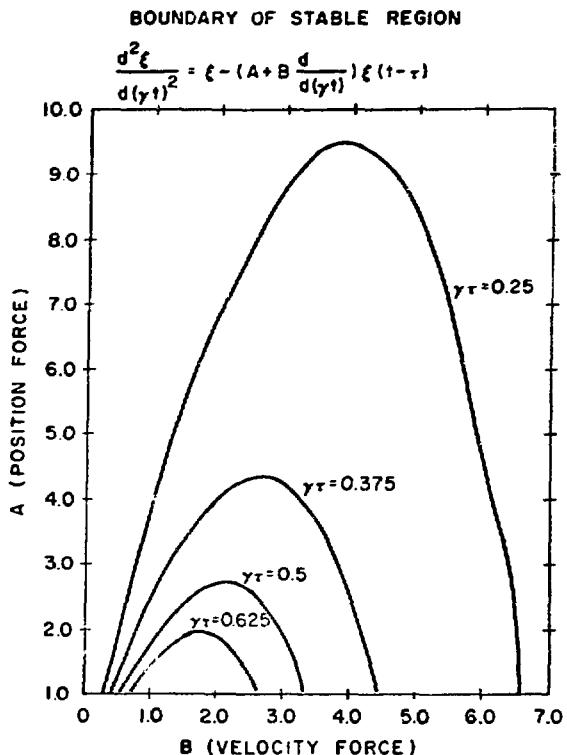
Fig. I-37.

Position and velocity feedback-stability regions for various values of $\gamma\tau$.

$$\frac{d\xi}{dt}\bigg|_{t=0} = \gamma\xi_0 \quad .$$

The resulting computer-generated trajectories are observed for (approximately) critical damping. The normalized force during the motion is observed for the maximum value. Two unstable cases were tracked for $\gamma\tau = 0.375$ as a check on the Nyquist analysis. A choice for position and velocity feedback, which provides approximately critical damping for $\gamma\tau = 0.375$ and $\gamma\tau = 0.5$, is $A = 1.5$, $B = 1.5$. The maximum forces during the motion, for the assumed initial conditions, are

$\gamma\tau$	F_{max}
0.375	$\sim 4.4\ \rho\pi a^2\gamma^2\xi_0$
0.5	$\sim 5.0\ \rho\pi a^2\gamma^2\xi_0$

where $\rho\pi a^2\gamma^2\xi$ is the static force required to hold a stationary column at $\xi = \xi_0$. If the maximum

static displacement that the feedback system can handle is ξ_{max}, then the maximum value of the displacement at detection is given by

$\gamma\tau$	$\xi_{0(max)}$
0.375	$\xi_{max}/4.4$
0.5	$\xi_{max}/5.0$

The interesting portion of the stability region for linear position and velocity feedback is localized by the requirement of returning to near zero position as rapidly as possible without significant overshoot, and with minimum force. The maximum force that can be exerted by the feedback system places constraints on the sensitivity of the position detector. The present $\ell = 2$ feedback system, which is capable of handling a static displacement of ~ 1.5 cm, must be able to discriminate an exponentially growing motion of ~ 0.3 cm.

5. Feedback Force Reduction for Displaced Plasma Column. An analysis has been made of the forces on a displaced plasma column for an $\ell = 0, 1, 2$ system to determine the influence of column displacement on the magnitude of the effective feedback force. Column displacement causes a mixing of the field components, which in the case of $\ell = 0,1$ equilibrium fields leads to the standard $m = 1$ long wavelength instability. Neglecting the influence of walls and column stiffness, the following forces act on the column in a system with $\ell = 0,1$ equilibrium: (a) Grad B forces acting radially outward balanced by the $\ell = 0,1$ equilibrium fields,

$$\frac{-\beta}{u_0} \pi h a^2 \; B_{\ell = 0} \; B_{\ell = 1} \; \frac{3-2\beta}{(1-\beta)\,(2-\beta)} \quad ; \qquad (29)$$

(b) $m = 1$ instability force,

$$hx_0 \frac{\beta}{u_0} \frac{\pi h a^2}{2(2-\beta)} \left\{ B_{\ell=1}^2 \left(\frac{4-3\beta}{1-\beta}\right) + \frac{B_{\ell=0}^2}{2} \left(\frac{3-2\beta}{1-\beta}\right) \right\} , \qquad (30)$$

balanced by an applied, programmed $\ell = 2$ field with force,

$$\frac{-\beta}{u_0} \pi h a^2 \left(\frac{2}{2-\beta}\right) B_{\ell=1} \; B_{\ell=2} \quad ; \qquad (31)$$

(c) A destabilizing force, proportional to displacement, due to the application of $\ell = 2$ fields,

$$hx_0 \; \frac{\beta\pi h a^2}{u_0 2(2-\beta)} \left\{ 4 \; B_{\ell=2}^2 + \left(\frac{4-3\beta}{1-\beta}\right) \; B_{\ell=0} \; B_{\ell=2} \right\} . \qquad (32)$$

The additional, destabilizing force, due to the application of $\ell = 2$ feedback fields can be thought of as either an enhancement of the $m = 1$, long wavelength instability growth rate, or as a reduction of the strength of the applied feedback force. For typical parameters of the "derated" sector and feedback fields as determined from the analysis described above, the reduction of the applied feedback force is $\sim 25\%$.

Both $\ell = 0$ and $\ell = 1$ feedback have been examined for the influence of column displacement. The force reduction in these cases is much less, on the order of 7%, for typical parameters. This is primarily due to the transverse uniformity of the $\ell = 0$ and $\ell = 1$ fields near the axis.

REFERENCES

1. W. R. Ellis, F. C. Jahoda, R. Kristal, W. E. Quinn, G. A. Sawyer, and R. E. Siemon, "Plasma Equilibrium and Stability in the Scyllac Toroidal Sector Experiments," Nuclear Fusion 14, 841 (1974).

2. E. L. Cantrell, W. R. Ellis, H. W. Harris, F. C. Jahoda, R. Kristal, M. D. Machalek, J. R. McConnell, W. E. Quinn, F. L. Ribe, G. A. Sawyer, F. T. Seibel, and R. E. Siemon, "Plasma Experiments in the Scyllac Toroidal Theta Pinch," Proceedings Fifth IAEA Conf. on Plasma Phys. and Controlled Nuclear Fusion, Tokyo, Japan, Nov. 1974, Paper CN-33/E1-2.

3. F. L. Ribe, compiler, "LASL Controlled Thermonuclear Research Program, January–December 1974," Los Alamos Scientific Laboratory report LA-6044-PR, August 1975.

4. J. P. Freidberg, "Vlasov-Fluid Model for Studying Gross Stability of High-Beta Plasmas," Phys. Fluids 15, 1102 (1972).

5. E. L. Cantrell, W. R. Ellis, B. L. Freeman, K. B. Freese, R. F. Gribble, W. D. Gutscher, F. C. Jahoda, K. J. Johnson, R. Kristal, K. J. Kutac, J. R. McConnell, G. Miller, W. E. Quinn, R. E. Siemon, "Scyllac 'Derated' Feedback Sector Experiments," Proc. Seventh European Conf. on Controlled Fusion and Plasma Physics, Lausanne, Switzerland, Sept. 1-5, 1975.

6. E. L. Cantrell, W. R. Ellis, B. L. Freeman, R. F. Gribble, W. D. Gutscher, K. J. Johnson, K. F. Kutac, G. Miller, W. E. Quinn, "Scyllac Feedback Stabilization Experiments," Prof. Third

Third Topical Conf. on Pulsed, High Beta Plasmas, Culham, England, Sept. 9-12, 1975.

7. E. Fünfer, M. Kaufman, J. Neuhauser, G. Schramm, "Recent High-β Stellarator Experiments at Garching," Proc. Seventh European Conf. on Controlled Fusion and Plasma Physics, Lausanne, Switzerland, Sept. 1-5, 1975.

8. M. Kaufman, L. Minko, J. Neuhauser, H. Röhr, "Investigations of the m = 2 Mode on High-Beta-Stellarator Isar TI-B," Proc. Third Topical Conf. on Pulsed High-Beta Plasmas, Culham, England, Sept. 9-12, 1975.

9. B. M. Marder, private communication.

10. G. Miller, "A Dynamic Model of Gross Plasma Motion in Scyllac," Proc. Third Topical Conf. on Pulsed High-Beta Plasmas," Culham, England, Sept. 9-12, 1975.

11. G. Miller, "Motion of a Plasma Column in a Perturbing Magnetic Field," Phys. Fluids $\underline{18}$, 1704, (1975).

12. Leaf Turner, "Finite-Larmor-Radius Stabilization in a Sharp-Boundary Vlasov-Fluid Screw-Pinch," Los Alamos Scientific Laboratory, to be published.

13. M. J. Katz, compiler, "LASL Controlled Thermonuclear Research Program, January-December, 1973," Los Alamos Scientific Laboratory Report LA-5656-PR, July 1974.

II. STAGED THETA PINCH

K. Thomas, W. Borkenhagen, C. Buchenauer, D. Call, J. Downing,
C. Hammer, A. Jacobson, R. Linford, M. McKinstry, D. Platts,
A. Rawcliffe, G. Sherwood

A. INTRODUCTION

Previous theta pinches have performed initial implosion heating of the ions and subsequent adiabatic compression with a single capacitor bank power supply. Projected theta-pinch feasibility experiments and fusion reactors, however, will require separation of the two functions to achieve greater implosion heating and less adiabatic compression. The Staged Theta Pinch program is designed to study the technological and physics problems associated with separating the two functions.

The principal experiment in the program is the 4.5-m-long linear Staged Theta Pinch (STP). The experiment uses a low-energy, high-voltage capacitor bank (PFN I) to produce the plasma, and a lower voltage, higher energy capacitor bank to provide a variable amount of adiabatic compression. A second low-energy, high-voltage capacitor bank (PFN II) is available to shape the implosion magnetic field and to assist in containing the plasma before it contacts the wall of the discharge chamber. This experiment is capable of producing high-temperature plasmas with a much larger ratio of plasma radius to discharge tube radius than is possible in conventional theta pinches. Studies have begun on the properties of the plasma formed and on the effect of magnetic field amplitude and time history on plasma formation. Plasmas have been produced with a ratio of plasma radius to discharge tube radius of 0.5-0.6. The results are complicated by the production of secondary plasma at the discharge tube wall when rapid magnetic field changes occur after the initial implosion. If the ratio of plasma radius to coil radius can be made large enough, the effect of plasma stabilization by image currents in the coil walls will be observable.

After studies of plasma behavior in a straight discharge chamber are complete, the main coil and discharge chamber will be converted to a helical geometry to study the effect of helical magnetic fields on plasma stability.

The other experiment in the program is the 0.9-m Resonant Heating Experiment (RHX). During 1975, it was operated as a 0.9-m-long version of the STP implosion circuit. It was used to study component problems and to conduct preionization studies.

Both experiments were constructed originally to operate in the "free expansion" mode of magnetic field programming. In this mode, the magnetic field is raised during the initial implosion and then reduced while the plasma is reexpanding against the external magnetic field. The magnetic field is then raised again before the plasma contacts the discharge tube walls. If this method of plasma heating works, it will lead to larger values of plasma temperature and radius than a step-function or monotonic magnetic field waveform.

Preliminary studies, using both analytical and computer models, indicate that it may be possible to use the time-varying inductance of the electric circuit, due to the imploding plasma, in conjunction with a simple electric circuit to generate hot plasmas with a larger ratio of plasma radius to main coil radius than will be possible with the present STP design. These concepts are presented in detail in the 1974 Annual Report (LA-6044-PR) and will be investigated in RHX.

B. 4.5-m STAGED THETA PINCH

1. *Description.* The layout of the STP experiment in the old Scylla IV experimental area is shown in Fig. II-1. The staging bank, which is the Scylla IV main bank, is located on a platform above the high-voltage implosion circuit. The start switches for the staging bank have been moved down to the collector plate in order to isolate the load cables from the high-voltage circuit. This necessitated the replacement of the start switch in the Scylla IV capacitor gaps with a shorting column. The crowbar system was left intact. The high-voltage gaps are connected directly into the collector plates to minimize source inductance. The 22-cm-i.d. main coil is fed from two sides to increase the magnetic field risetimes. Because the components are the same on both sides of the machine, the two sides of the experiment operate at different
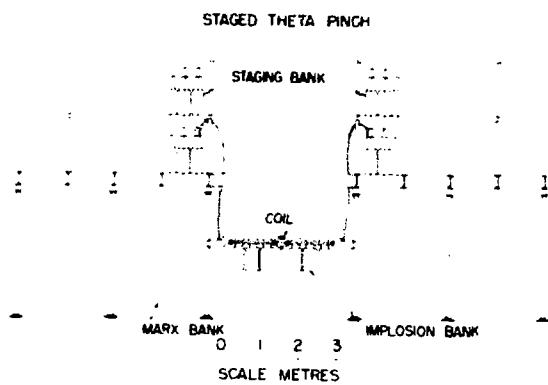
STAGED THETA PINCH

Fig. II-1.

Layout of the Staged Theta Pinch experiment.

voltage polarities.

Figure II-2 shows a circuit diagram for the experiment showing only one feed to the main coil. Also shown is the predicted magnetic field waveform when the experiment is operated in the "free expansion" mode. Table II-I presents the electrical parameters of the various capacitor banks when they are operated alone with no plasma in the discharge tube.

2. Construction, Checkout, and Operation.
Construction of the Staged Theta Pinch was completed August 15, 1975. Construction had progressed enough by February 1975 to allow full-time electrical checkout to begin at that time. During checkout of PFN I the main collector plate insulation was blown. It was found that the insulation had been damaged by the bolts that held the collector plates together. These bolts were slightly longer than they should have been. It was decided to replace all of the collector plate insulation. Replacing the insulation delayed the construction and checkout about three to four weeks. Electrical checkout and taking of physics data alternated until the end of September 1975 at which time checkout of the entire system was completed. Physics experiments have been run with the system being operated at the voltages shown below.

PI ≈ 67 kV

PFN I ≈ 65 kV

PFN II ≈ 85 kV

Staging ≈ 21 kV

Crowbar for Staging Bank ≈ 68 kV
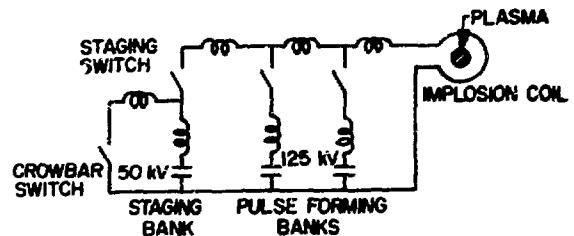
DOUBLE IMPLOSION

STP

Fig. II-2.

Top - Circuit diagram of Staged Theta Pinch.
Bottom - Predicted magnetic field waveform for
"free expansion" case.

At these voltages the machine is very reliable, allowing as many as 20 full-system plasma discharges in one day. Operating range of PFN I, PFN II, and Staging banks is limited by the Staging gap now installed on the experiment. An improved model should be available early in 1976 that will allow the operating range to be very close to design.

3. Engineering.

a. New Staging Gap. The main engineering effort related to the Staged Theta Pinch has been to develop a Staging rail gap which will allow the experiment to operate at design voltage and energy. The design settled on has a larger volume to handle the required energy, and the electrical connections are enclosed in an insulating material to eliminate corona problems. The gap is shown in Fig. II-3. Two methods of fabrication are being pursued. One is a cast version out of fiberglass and epoxy and the other a molded version out of polypropylene.

b. Trigger System Improvements. In order to improve the performance of the high-voltage trigger systems several changes were made. A new submaster gap was designed and installed which used a PFN gap instead of a Scyllac gap as the start switch. Also,

31

TABLE II-I

	PFN I	PFN II	STAGING
Capacitance	6.6 μF	12.6 μF	675.2 μF
Voltage	125 kV	125 kV	45 kV
Energy	52 kJ	98 kJ	684 kJ
Risetime (τ/4)	0.26 μs	0.35 μs	3.7 μs
Peak Magnetic Field	5 kG	5 kG	14 kG

the number of submasters in the staging trigger system was doubled. New $CuSO_4$ bias resistors were designed to eliminate the mechanical and electrical problems with the old design. New methods of triggering master gaps by shorting a cable instead of using the old series-parallel step-up transformer were tested in RHX.

C. 0.9-m RESONANT HEATING EXPERIMENT

The Resonant Heating Experiment began operating with plasma in February 1975. The experiment was operated for the rest of the year with circuit parameters identical to a 0.9-m version of the STP. PFN I and II were operated at voltages up to 100 kV. The experimental program consisted primarily of support work for the STP. New high-voltage trigger system components were designed and tested. An auxiliary preionization capacitor bank was added to the experiment to investigate the effects of increasing the preionization level just prior to the main plasma discharge.

D. EXPERIMENTAL PROGRAM

The Staged Theta-Pinch experiment was operated with plasma the last three months of 1975. During
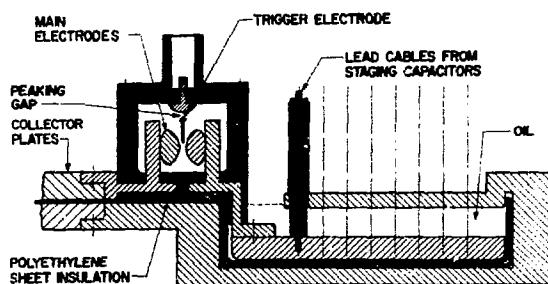
Fig. II-3.

New Staging rail spark gap.

this time approximately 200 plasma discharges were generated with various combinations of capacitor banks. The experiment was operated with both the "free expansion" magnetic field waveform shown in Fig. II-2 and with the closest approximation to a step-function waveform that is possible with the present circuit parameters. The latter is generated by firing PFN II first, using the Staging bank as a power crowbar and then using PFN I to smooth the profile as much as possible. The plasma results presented below are from the STP experiment. Plasma results from RHX were consistent with those from the STP.

1. *Diagnostics*. Plasma diagnostics include magnetic field probes, both internal and external, an arrangement which measures the total flux inside the main coil by monitoring the voltage on the collector plates, and two types of interferometers. A holographic interferometer using a Q-switched ruby laser at 694.3 nm measures the plasma density profile at two times during a plasma discharge. A diagram of the interferometer is shown in Fig. II-4. Holographic interferograms are produced on two separate photographic plates by combining the "scene" beams from the two lasers and keeping the reference beams separate. The other interferometer, a Mach-Zehnder arrangement (Fig. II-5), uses a C-W He Ne laser at 632.9 nm. It measures the plasma density at one radius as a function of time. It is used primarily to establish the absolute plasma density at one point on the holographic interferograms but also is used to measure the preionization level and the amount of plasma left outside the main plasma column after the initial implosion.

2. *Plasma Results*. Although many different magnetic field waveforms were generated in the STP experiment, the results presented here are for a particular case. This case was picked because it illustrates the general features of the plasma results to date. The results presented are from plasma discharges when PFN I was fired first, then the Staging bank is used to prevent the magnetic field from reversing. The initial D_2 fill was 10 mTorr, PFN I voltage was 65 kV and Staging bank voltage was 21 kV. Preionization levels at the time of the main discharge were ∽0%. Because the experiment was operated at approximately half the design voltage, the plasma implosion and reexpansion

TWO EXPOSURE
HOLOGRAPHIC
INTERFEROMETER
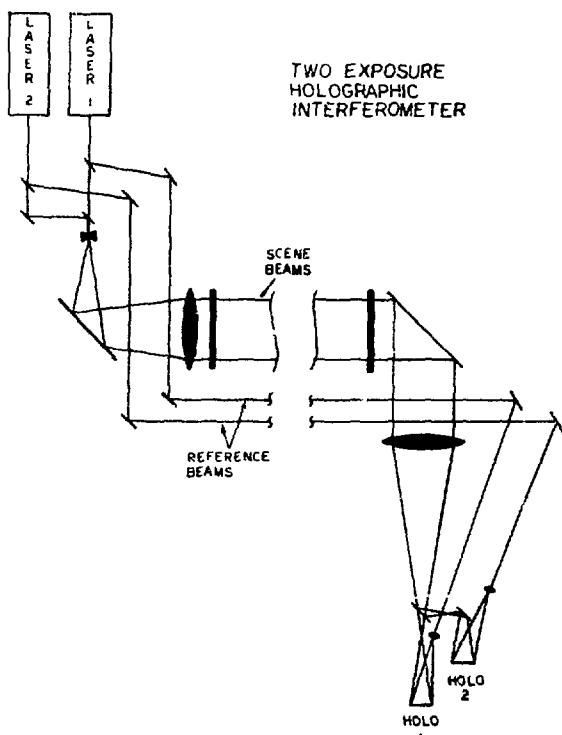
Fig. II-4.

Layout of the holographic interferometer.

MACH-ZEHNDER
He-Ne LASER
INTERFEROMETER

Fig. II-5.

Layout of Mach-Zehnder interferometer.

was only half as rapid as it would be at full voltage. Therefore the larger plasma temperature and radius, which would be expected if the implosion and magnetic field time history were in resonance, does not occur. In fact, plasma heating is less effective for a step-function waveform.

Figure II-6 shows holographic interferograms taken at four times during plasma discharges for the conditions listed above. Also shown is the magnetic field waveform for this case. The arrows indicate the times the interferograms were taken. Figure II-7 shows the reduced data from the interferograms. The earliest time (0.40 μs) shows the plasma column halfway through the initial implosion. A low-density plasma extends all the way to the discharge tube wall. The next time (0.65 μs) shows the column at the time of maximum compression. At 1.15 μs the main column is reexpanding and plasma is observed near the discharge tube wall. This plasma represents additional plasma which comes off the discharge tube wall during the second magnetic field rise. The

last graph shows the plasma column at the peak of the compression magnetic field. The main column has a radius of 5.0-5.5 cm. The shoulder on the profile is the secondary plasma which is near the wall at 1.15 μs. At later times, as the magnetic field decreases, this shoulder becomes more diffuse, indicating that it is low β (β = ratio of plasma pressure to external magnetic field pressure) plasma which moves outward with the magnetic flux as the field decreases. At these later times the main plasma column remains well defined.

E. DISCUSSION

The experiments which have been conducted in the STP have yielded the following results.

1. Plasmas have been generated with a ratio of plasma radius to discharge tube radius of 0.50-0.55. The theoretical prediction for a step-function waveform is 0.63. As was mentioned previously, the experimental case is less effective than a step-function. In addition, the experimental case includes a small amount of adiabatic compression. Therefore, the experiment agrees well with the

33

0.40 μsec   0.65 μsec

1.15 μsec   3.20 μsec
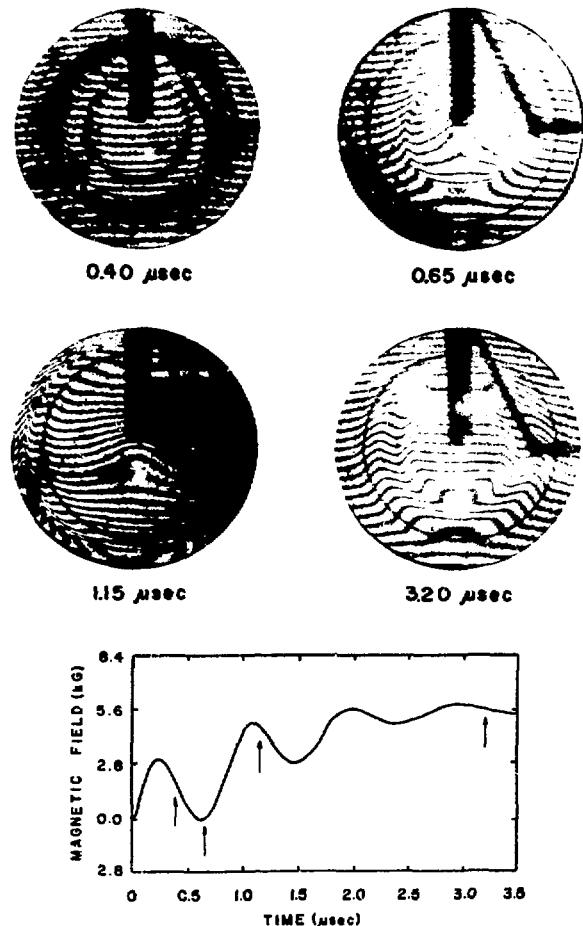
Fig. II-6.

Holographic interferograms taken at four times during plasma discharges with the magnetic field waveform shown.

theoretical predictions. The plasmas generated have a $\beta \approx 1$ on axis. This yields the following values for plasma temperature.

$T_e \cdot T_i \approx 300$ eV @ 10 mTorr initial fill
$T_e + T_i \approx 600$ eV @ 5 mTorr initial fill.

2. A low-density plasma extends from the plasma column to the discharge tube wall after the initial implosion. This probably results from ionization of either neutrals left behind by the magnetic piston or of D_2 adsorbed on the discharge tube wall.

3. Additional plasma is generated at the discharge tube wall whenever a rapid magnetic field rise occurs after the initial rise. For the case shown in Section D, additional plasma is generated
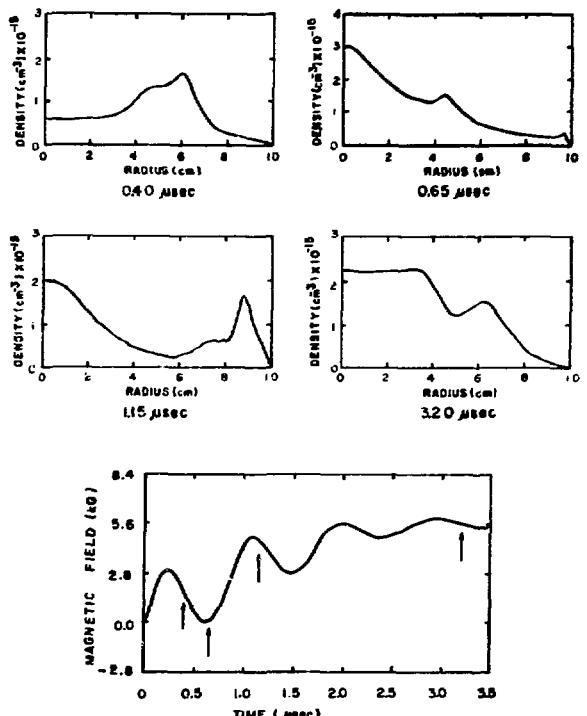
Fig. II-7.

Plasma density vs radius at four times during plasma discharges with the magnetic field waveform shown.

only during the second rise. For other cases, when large modulations of the magnetic field occur at later times, an even larger amount of plasma is generated. The most plausible explanation for this secondary plasma generation is that when the magnetic field decreases, plasma outside the main column is pulled into the wall by magnetic flux leaving the discharge tube. If a rapid field rise follows, this causes a large current at the wall which generates additional plasma. If this is the case the problem might be reduced by increasing the initial preionization level. This could be accomplished with a secondary preionization bank such as the one in use on the Resonant Heating Experiment.

F.   FUTURE PLANS

Future plans for the STP experiment are:

1. Voltages on all capacitor banks will be raised in order to get into the physics regime for which the experiment was designed. This is the

"free expansion" regime described in Section A. It will be necessary to install the new Staging rail gaps in order to operate at the voltages required.

2. A parameter study will be conducted to determine the effect of magnetic field risetime, pre-ionization level, and initial gas fill level on the sweep-up of plasma during the initial implosion.

3. Studies on ways to reduce secondary plasma effects will be conducted.

4. After the above are completed, an $\ell = 1$ helical compression coil and discharge tube will be installed to study the effect of helical magnetic fields on plasma behavior.

III. IMPLOSION HEATING EXPERIMENT (IHX)

I. Henins, T. Jarboe, J. Marshall, and A. Sherwood

A. INTRODUCTION

The Implosion Heating Experiment, IHX, is a 40-cm-diameter, 1-m-long, high-voltage linear theta pinch designed to study the implosion phase of conventional theta-pinch heating. Implosion heating has been successfully employed on theta pinches for many years, but the future development of theta pinches will require a better understanding of the process. For example, with enhanced implosion heating, less adiabatic compression would be required to reach a given temperature, thus allowing the production of theta pinches with fat plasma columns. The importance of the implosion heating process is, of course, not limited to theta pinches alone. As a plasma-heating mechanism the process has application in many other devices as well.

The implosion coil of IHX is fed at four places by low-impedance pulse-forming networks (PFNs) designed to produce a flat-topped current pulse. The PFN capacitors are fast Marx-charged to voltages up to 125 kV, so a total emf of 500 kV is available. The equivalent circuit of one of these PFNs and its associated Marx bank is shown in Fig. III-1. The PFNs are connected to the coil feed slots through multichannel field distortion rail spark gaps. In operation the PFNs are pulse-charged from the Marx generators, and the rail gaps are triggered near the time of maximum charging current. The effective impedance of the four PFNs is approximately equal to that of the imploding plasma, thus coupling the plasma dynamics strongly into the external circuit. The circuit was designed with the help of computer modeling. The model assumed for the plasma is that the particles are enclosed within a thin inward-moving current sheath which originates at the wall and which reflects ions by an elastic bounce process, so that the deuterons move radially inward ahead of the sheath at twice its speed.

The preionization system is shown in Fig. III-1. It presently consists of a pulse-charged 5.6-μF bank, discharged through a single switch and connected in parallel by four cables to each of the four coil feed slots. As will be discussed below, this is an improved version of our original system.

During 1975 the operation of IHX has been
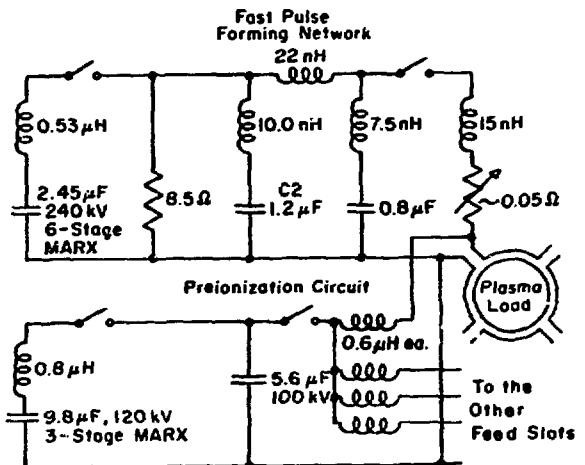
Fig. III-1.
The electrical circuit for the IHX.

pushed up to the full design value of 125 kV on the PFNs. The driving magnetic field and the azimuthal electric field E_θ actually obtained at full design voltage have turned out to be about 0.7 T and 1.4 kV/cm, respectively. These values are 30% lower than had been anticipated from the original circuit designs. The discrepancy has been found to lie mostly in a surprisingly large resistance of the rail gaps which had not been expected.

Technical upgrading of the experiment's high-voltage systems has been done on a more or less continual basis over the lifetime of the experiment. The most notable improvements made this year were to the preionization system and to the optical trigger system. The optically triggered high-voltage trigger generators were revised to be battery powered. This change eliminated a prefire problem due to noise coupling through the power supplies. The preionization system was doubled in size and converted to a different spark gap configuration. These changes produced better preionization and more reliable operation of the bank.

Practically every diagnostic technique being employed on the IHX has been upgraded. Our method for measuring the magnetic flux inside the implosion coil was improved. The internal magnetic probes

have also been improved, mostly by making them smaller, but they are still questionable during the fast implosion phase of the discharge. A second technique has been developed for measuring the magnetic field, namely detecting the Faraday rotation of a polarized 10.6-μ laser beam. This measurement is very difficult and so far has been done at only a single tube radius. The results indicate errors in the probe measurements of the magnetic field, probably due to partial shielding of the probes by the surrounding plasma. The Faraday rotation technique is being refined in preparation for use over a larger range of tube radii. Finally, an extensive series of modifications were made on the fractional fringe interferometer used for measuring the plasma area density. The modifications were required to eliminate various difficulties which had previously prevented trustworthy density measurements of the implosion. Having developed a single beam interferometer that produced satisfactory measurements, the essential features of its design were then incorporated into a four-beam interferometric system which provides measurements at four radii simultaneously for each implosion.

The results of extensive sets of measurements using the above mentioned diagnostics yield a consistent picture of the implosion. The dynamics are found to agree well with models based on particles being perfectly reflected from the inward moving piston (i.e., the "bounce model"). Most of the imploding plasma is pushed out ahead of the current sheath. Neutrons are observed beginning when the imploding particles start to reach the axis, but the neutron measurements are still very preliminary. After passing through the axis the plasma is observed to move outward again pushing the magnetic sheath ahead of it.

B. MODIFICATIONS TO THE EXPERIMENT

The experimental apparatus has continually evolved as technical problems have been identified and corrected. During the past year the most notable changes have been to the preionization system, the PFN line insulation, and to the trigger systems.

1. The Preionization System.

Our original preionization bank consisted of four 0.7 μF, 125 kV capacitors, each with a separate Scyllac-type output switch. Two 6-m-long RG-17 cables connected each capacitor to one of the

four feed slots of the implosion coil. The inductance of these cables provided isolation for the PI bank when the main implosion voltage is applied to the coil, i.e., when the PFN rail gaps are fired. The preionization bank capacitors were pulse-charged in about 5 μs from a three stage 4.9-μF Marx bank to about 100 kV at which time the PI bank switches were triggered. The resulting preionization current waveform is complicated because of the close coupling between the PI bank and its Marx bank, but the higher frequency component of this waveform is about 170 kHz. This preionization bank configuration, having four separate output switches connected effectively in series, was found to have a serious disadvantage. A misfire or jitter in the firing of any one of the four switches results in a high-voltage transient across the respective feed slot of the coil. This transient would often break down or preionize the rail gap switches of the corresponding PFN, causing a premature switch closure when the PFN itself was charged. To remedy this the four Scyllac gaps were removed from the preionization bank and were replaced by a single rail gap switch. This switch connects all four capacitors to all eight feed slot cables, resulting in a completely parallel configuration.

An extensive series of density and magnetic field measurements were made of the preionization discharge with the altered preionization bank. These measurements will be discussed in more detail later, but they showed for typical conditions a preionization particle inventory of only 20% of the filling inventory and very little preionization near the center of the discharge tube. To improve the preionization level we doubled the number of capacitors in the PI bank, doubled the number of cables between the PI bank and the implosion coil, and added another Marx bank for pulse charging this larger bank. The preionization current waveform remained the same, but the magnitude of the current about doubled. With this modification the total preionization level, integrated over the volume, is about 40% and the preionized plasma distribution is much more spatially uniform than it had been before.

The single 40-cm-long multichannel rail gap switch used with the new preionization bank was developed for use as one of two parallel output switch for a PFN. In its PI bank application the switch is

stressed much more severely than had been originally intended; for the preionization system contains about the same energy but twice the charge as one of the PFN circuits, and the PI current is allowed to ring for a much longer time than the PFN current. In the PI application the switch tends to be damaged if it self-breaks in a single channel. Usually the knife-edge trigger electrode gets bent out of shape, and metal vapor may be deposited on the walls leading to further prefires. Also, the polycarbonate cover plates were not able to survive this sort of a fault and had to be replaced with a thicker (5-cm) cover plate made of cloth base phenolic. The fiberglass-epoxy switch housing, however, seems to be able to take the stress with no problems. Normally the switch can be operated in this application for many hundred shots before it needs attention.

2. *Optical Trigger System.*

As originally designed, the optically triggered high-voltage trigger generators for the various spark gap switches were provided high-voltage charging current through isolating resistors from a common supply. It was found that these units were occasionally prefired by noise generated by other previously triggered spark gaps. The problem was solved by changing the power supplies to separate DC-to-DC high-voltage converters powered by rechargeable sealed lead-acid battery packs, hence completely isolating the trigger generators from one another, and by additional electromagnetic shielding of each trigger unit.

3. *Marx Bank Trigger System.*

We have experienced some problems in obtaining good electrical performance of the IHX that were caused by jitter in the erection times of the eight Marx banks used to pulse-charge the PFNs. Jitter times of 200-500 ns were observed under some conditions. When this happens the voltages on the four PFNs are unequal at the implosion time, leading to complicated and undesirable circuit behavior. These jitter times were substantially reduced by altering the Marx bank trigger system to operate at higher voltage and by adjusting the value of the series trigger resistors in the Marx banks. The trigger voltage was raised by replacing the original 40-kV master trigger switch with one of a new design that operates at 60 kV. The higher trigger voltage required the replacement of the original eight

RG/123 trigger cables with new ones using type RG/217 cable. The value of the series trigger resistors was adjusted to give a (statistical) maximum of the number of switches showing an observable arc from the trigger pulse in the absence of charge voltage across the switches. These alterations have not entirely solved the jitter problem at low Marx bank charging voltages, but the system operates satisfactorily at the higher voltages (i.e., voltages corresponding to 100 kV or more on each of the PFNs).

4. *PFN Line Insulation.*

After its initial construction each PFN was voltage-tested to around 130 kV. The system was then run at PFN voltages in the approximate range of 75-95 kV for many months during system shakedown, diagnostic development, and for the acquisition of an initial "complete" set of data. Many failures in the insulation between the parallel plate lines of the PFNs were experienced when we tried to raise the voltage back up towards the 125-kV design value. Finally two changes were made in the line insulation techniques which allowed the experiment to be run at the full design voltage.

The parallel plate line insulation originally consisted of four sheets of 0.8-mm-thick polyethylene with additional 6.4-mm-thick spacers above the capacitor headers. These spacers were previously found to be required to reduce the electric field along the high-voltage gasket used to connect the capacitors into the parallel plate liners. The presence of two different insulation thicknesses, however, turned out to be a mistake because it gives rise to parallel components of the electric field near the thickness discontinuity. These parallel electric fields caused discharge streamers to propagate under the edges of the spacers. The electric field concentration at the tips of these streamers led to the insulation failures under the spacers, that is, through a thick place in the line insulation. Therefore, at a slight sacrifice to the line inductance (~ 3 nH), we installed uniform *insulation of a greater thickness (7.2 mm), which* solved the problem.

The second change concerns the grease applied to the high-voltage gasket and to the polyethylene sheets in the region above it. For ease of application this Dow Corning Silicone Vacuum grease had been thinned slightly with a silicone oil. Under

pressure, with time the oils would extrude from the grease leaving behind a dry, waxy residue. Sometimes this residue was unable to perform the original function of the grease, namely to prevent voltage tracking across the surfaces of the polyethylene, and a failure would result. The reliability of this insulation technique has been improved by using the silicone grease without thinning, although there still is some extrusion of the less viscous components of the grease.

C. THE DATA REDUCTION SYSTEM

All of the data from the IHX are obtained as Polaroid photographs of oscillograms. We have constructed an optical system that, together with the Hewlett-Packard Model 9830 programmable calculator equipped with the Model 9864A digitizer platen and Model 9862A X-Y plotter, allows us to digitize, reduce, and display these data in a convenient form.

The digitizer platen has a resolution of 0.25 mm which is too coarse for direct tracing of the photographs. In other digitizing devices we have seen, the photograph is usually enlarged by opaque projection onto the digitizer. However, for good visibility a very bright light source must be used to illuminate the photograph, and there is a problem with overheating the photograph. In our system we have taken the approach to project a virtual reduced (1:5) image of the platen onto the photograph, thus increasing the effective digitizer resolution to 0.05 mm.

The optical system is shown in Fig. III-2. A small light source is mounted on the digitizer cursor directly above its cross hairs. Three plane mirrors are mounted above the platen, so that they lie on the three intersecting faces of a cube. These mirrors reflect the light into a lens that forms an image of the light onto a flat, ground-glass screen. The photograph is separately illuminated and is held at eye level in a holder so its plane is exactly perpendicular to the ground glass. A 50-50 beam splitter placed exactly on the diagonal plane is used to superimpose the virtual image of the screen onto the photograph. As the photograph is viewed, the light spot can be moved along the features to be digitized, and the coordinates entered into the calculator for storage on magnetic tape and data reduction. A magnifying lens can be placed between the viewer and the photograph, if
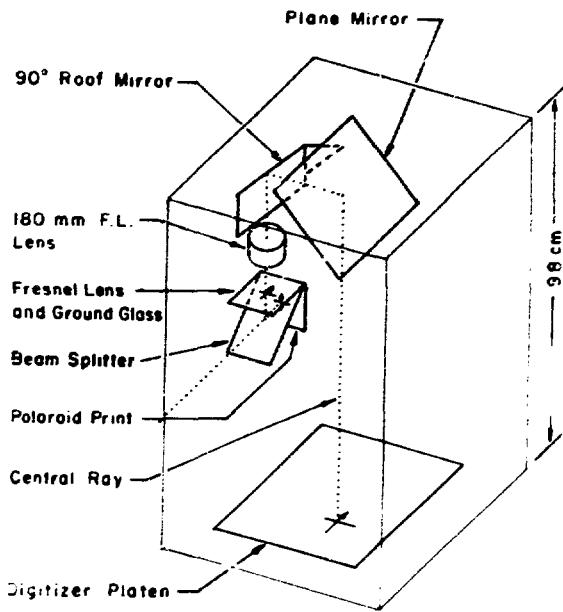
Fig. III-2.

Optical system for the digitizer used in data reduction for the IHX.

desired.

The desk calculator used is powerful enough to accomplish moderately sophisticated processing of data, and the ease of programming and editing the calculator provides great flexibility. The data can also be stored on magnetic tape cassettes for later use. We also have purchased the hardware, and a line is installed for connecting our calculator as a remote terminal to the CTR PDP-10 computer as soon as the software is developed. This will further increase the capability of this data reduction system.

D. DIAGNOSTIC DEVELOPMENT

The diagnostics in use include magnetic probes, fractional fringe interferometry, flux measurements including excluded flux, and voltage and current measurements. Substantial improvements have been made to most of these diagnostics during the year, and two new diagnostics (neutron measurements and Faraday rotation) are being developed. In addition, a holographic interferometric system, to be used for axial viewing and with a circular field of view of about 13-cm radius, was developed for the IHX by CTR-8. This system has not yet been used, however, mostly because our fractional fringe interferometer

has shown that plasma beyond the ends of the implosion coil would introduce significant errors in the measurement.

1. *Magnetic Flux Measurement.*

As is explained in the last annual report, the standard theta-pinch techniques for flux measurements are not applicable to the IHX because of the large total emf in this experiment. The first magnetic flux measurements on IHX were made using a resistive wire loop which linked the total flux within the implosion coil. There were problems with this measurement, however, associated with the RC behavior of the loop-coil system and the effects of the voltage not being applied exactly symmetrically to the four coil feed slots.

A new method of measuring the total flux has been tried and seems to work much better. A thick copper wire is put around the glass vacuum vessel about 30 cm from the end of the implosion coil outside of the coil. Since the wire is a good conductor and forms a shorted turn, the flux going out through the glass between the wire and coil is equal to the flux going through the coil. Because the region near the end of the coil is reasonably clear of field distorting materials, the flux is presumed to come out symmetrically around the coil. Thus the total flux can be deduced by measuring a fraction of the flux coming out between the copper wire and the coil. This is done by running two small parallel wires between the coil and copper wire. The fraction of the total flux which these small wires link can be deduced from geometric considerations.

One check on the symmetry with which the flux comes out between the coil and the thick wire is to compare the fraction of flux actually linked during a vacuum shot to that deduced from geometry. This was done, and the two methods agree to within measurement errors.

2. *Magnetic Probes.*

Investigation of the reliability of the magnetic field measurements obtained in IHX using internal probes has continued. Internal probes are the most convenient way to measure the magnetic profiles during the implosion, and they appear to give an approximately correct qualitative picture of the motion of the magnetic piston. The probes used so far consist of small coils enclosed in fused quartz or ceramic envelopes. There are, however,

several indications that in the presence of plasma the probes are unable to respond fast enough for accurate measurements of the magnetic sheath structure. One such indication is that during the first current pulse, when the main implosion and reexpansion occur, the value of the magnetic flux obtained by integrating the probe signals over the tube area is about 20% below the value measured directly, and the former exhibits a phase lag compared to the latter. (During the following slower oscillations of the driving current, however, the flux calculated from the probes agrees well with the measured values.) Another indication is that if signals from probes of different sizes (ranging from 2 mm to 1 cm o.d.) positioned at the same radius are compared, the onset time of the magnetic signal is the same for all probes, but the smaller the probe the faster the signal rises (corresponding to a narrower sheath structure). On the other hand, magnetic probes positioned at the larger radii agree well with the driving magnetic field after the implosion has passed by. Radial magnetic field gradients behind the sheath are not observed.

Measurement of the magnetic field by an alternate method, namely, detecting Faraday rotation, has been started. This measurement is discussed in the next section. In general the Faraday rotation measurement, when combined with the interferometric measurement of the plasma density, shows a faster rising magnetic field (thinner sheath) than the probes. Also, the probes show a large amount of field-plasma mixing during the reexpansion phase that is not shown by the Faraday rotation measurement.

3. *Faraday Rotation Measurement.*

Faraday rotation is a rotation of the direction of polarization of a plane-polarized electromagnetic wave as it propagates parallel to a magnetic field. The rotation is proportional to the magnetic field, so its determination can be a measurement of that field. If the laser frequency is much larger than any characteristic frequency of the nonrelativistic plasma, the amount of rotation, as derived in many texts,[1,2] is given by the following:

$$\Delta\theta = 2.63 \times 10^{13} \; \lambda^2 n_e \ell B_{rad} \quad .$$

The wavelength of the light is λ, the path length is ℓ, and the density is n_e. Here $\lambda^2 n_e \ell$ is dimensionless, B is in Tesla, and $\Delta\theta$ is in radians.

Faraday rotation has been measured on several plasma devices.[3-6] However, it has not yet become a standard plasma diagnostic. The difficulties with the measurement are that the amount of rotation is small, and that refraction introduces errors because it causes the power to move across the non-uniform detector. The standard method for correcting first-order refraction is to image the apparent position of the source of refraction on the detector.[3] This position is the midplane of the plasma for a linear theta pinch such as IHX. Figure III-3 shows the experimental arrangement used to make the measurement described here. It is a double-pass system with the center of curvature of the spherical mirror at the midplane of the plasma. The beam is reflected to approximately retrace itself through the plasma. This method has the advantage that the beam exits the plasma region with the same position and direction, independent of first-order refraction.

In the measurements reported here, errors due to higher order refractive effects are minimized by using the proper initial half-shade angle for the polarizer such that $\Delta P/P$ is maximized. ΔP is the change in power at the detector due to Faraday rotation and P is the total power on the detector. Maximizing $\Delta P/P$ minimizes errors due to refraction since signals caused by refraction are proportional to P. This proper initial half-shade angle is found by approximating the power from the polarizer as $P = P_0 (\sin^2\theta + f)$, where f is the extinction ratio. The half-shade angle θ is $\pi/2$ minus the angle the plane of polarization makes with the axis of the polarizer. This equation is found experimentally to be very accurate for the small values of θ used here. If this equation is used for small amounts of rotation, $\Delta P/P$ is maximum when $\theta_0 = \pm \sin^{-1}\sqrt{f}$, where θ_0 is the initial value of θ with no Faraday rotation. Since IHX is fairly repeatable from shot to shot, measuring the same amount of rotation with both values of θ_0 insures that the measured change in P is due entirely to Faraday rotation.

In order to deduce the magnetic field from the amount of rotation, it is necessary to measure $n_e \ell$. This is done at the same time and at the same
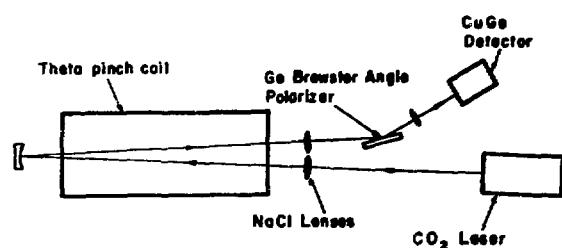
Fig. III-3.

Schematic diagram of experimental arrangement for the Faraday rotation measurements.

radius with a fractional-fringe Mach-Zehnder interferometer which uses the 633 nm line of a He-Ne laser.[7] In making the Faraday rotation measurement, it was found that refractive effects would cause signals on the order of those made by rotation unless care was taken to insure that the beam stayed on a surface of constant radius while traversing the coil. With careful alignment, errors due to refractive effects seem to be small compared to the signals due to rotation. The value of f for the Ge Brewster plate was found to be 1/1600, thus measurements of Faraday rotation were made with $\theta_0 = \pm .025$ radian, which gives a maximum of $\Delta P/P$. Figure IV-4 shows the average value of the magnetic field measured at these half-shade angles. The error bars are the RMS deviation due to shot-to-shot variation. There seems to be a systematic difference between the +0.025 radian and -0.025 radian data. These differences are probably due to refraction. The
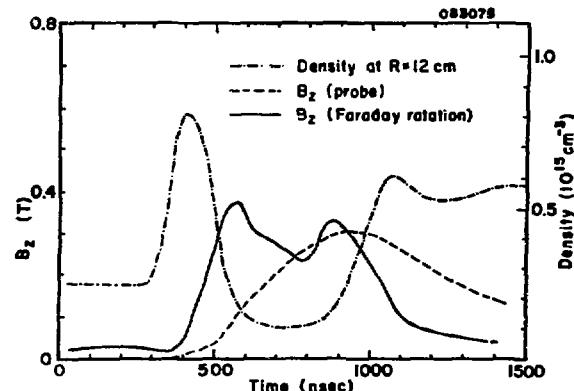
Fig. III-4.

The magnetic field as measured by Faraday rotation and by an internal probe. The density at the same radial position, 12 cm, is also shown.

41

light is focused on the detector to give maximum sensitivity, and a movement in the position of the focal spot will cause a negative ΔP. Since $\Delta\theta$ is positive this error would make the apparent value of B larger for negative θ_0 and smaller for positive θ_0, and thus give the observed differences. This possibility seems likely since the differences are largest where the density gradients are largest (see Fig. III-4). Fortunately, errors due to refractive effects can be compensated for by averaging the value of the field measured at these two values of θ_0. Figure III-4 shows this average and the magnetic field measured by a probe.[7] In contrast with the probe, the Faraday rotation shows that the magnetic field rises as the density drops and later the field drops as the density rises. It appears that the probe immersed in the plasma has a response which is too slow to follow the changes in the magnetic field. Because of this slow response, the probes show a large value of field when the plasma density is high. Thus the probes show a large amount of field plasma mixing or diffusion,[7] which is not shown by the Faraday rotation measurement. Furthermore, this slow response can make the field appear low where the density is low. Thus, the previously observed large magnetic field gradients seen where there is low density,[8] as well as the observed rapid diffusion of magnetic field, can be explained as a consequence of slowly responding probes.

Although it appears from these preliminary data that the response of the probes is slow, more data taken at more radii are needed to substantiate these observations.

4. Interferometric Density Measurements.

Time-resolved measurements of the electron area density are made in IHX using the red light from a HeNe laser (6328 Å) arranged in approximately a Mach-Zehnder interferometer configuration. The interferometer was initially set up in a single beam configuration (i.e., one scene beam going through the plasma), and several modifications were then required to overcome difficulties caused by electrical noise, plasma light, frequency response of the detector, etc. After the single-beam interferometer was made reliable, it was expanded into a multiple-beam system (described below) in order to obtain more data per implosion.

In the single-beam configuration, the scene beam traverses the plasma once along a line parallel to, and at various distances from, the discharge tube axis and is then combined with a reference beam passing outside the coil. The interference pattern is focused onto a detector, and a discriminator fires the experiment when the detector output is within some preset window. Initially the normal room vibrations were relied upon to slowly shift the relative phase of the interferometer. An auxiliary measurement gives the voltage difference of the output of the detector between extrema, and this is used to deduce the phase shift introduced by the plasma from the observed signal during a shot.

Several improvements to this system were required to obtain reliable data during a plasma implosion. The major modifications were the following: a) Electrical noise problems were eliminated by moving the detector into the low-noise environment of the screen room. b) The solid state detector was replaced by a photomultiplier because the Meret detector was found to have insufficient frequency response. c) A mechanical phase modulator was placed in the reference beam to provide a uniform rate of background fringe shift. This system is superior to relying on room vibrations to provide the slow phase shift. d) Copper tubes were installed parallel to the discharge tube axis to shield the scene beam from plasma outside the ends of the coil. In use these tubes extend from each end of the discharge vessel to 5 cm inside the 1-meter-long compression coil. Thus the scene beam passes through a copper tube until it is within the coil region, then passes through 90 cm of plasma before entering the other copper tube. Up to fourteen pairs of these tubes have been installed, allowing measurements at radial increments of 1 cm at the outer radii and 2 cm near the axis. The tubes not in use at a given time are withdrawn to well outside the coil region. A series of measurements were made on the effect of using these copper tubes. Generally speaking the use of the copper tubes has no effect on the area density measured for the imploding plasma in front of the sheath. However, in the measurement of the plasma density behind the sheath the contribution from the plasma beyond the ends of the coil is at least an order of magnitude greater than the contribution of the plasma within the coil
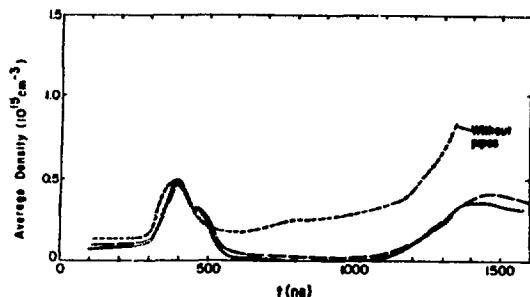
Fig. III-5.

Plasma density measurements in IHX at a radial posi-tion of 16 cm showing the effect of the copper pipes. The unmarked curves are measurements for two shots where copper pipes are used.

region. See Fig. III-5. Various tests were made of such matters as the effect of the presence of a nearby tube on the measurement through a given tube, none of which showed any measureable effect. Never-theless, one worries about the boundary region at the end of these tubes. We regard the measurements of area density made in this manner to provide an upper limit to the true density.

With these modifications the interferometer data became consistent with the other diagnostics, and a four-beam interferometer system was designed and installed. This multibeam system incorporates all the features developed with the single-beam sys-tem, and some additional features necessitated by the added complexity of several beams. For example, a four-channel discriminator is used to fire the ex-periment at a time when the phases of the four fringe patterns are simultaneously within adjustable win-dows. Each channel (or interferometer fringe pat-tern) has its own window. During the initial con-sideration of the design of the interferometer and discriminator the question arose as to how long one would have to wait, using four beams, for a coinci-dence to fire the machine (with windows narrow enough to accomplish their function). Fortunately, it is observed that the phases of the beams with respect to one another stay fairly constant for several minutes, except for a small amplitude rela-tive phase change having a frequency of about 100 Hz. The phase amplitude of this 100 Hz modulation is much less than a radian for adjacent beams but is

near a radian for beams on opposite sides of the discharge tube. These small vibrations do not seem to compromise the measurement, and we can easily operate with discriminator windows that are open 15% of the time. To adjust the relative phases of the four beams with respect to each other, small air-filled gas cells (2 mm long) are placed in three of the beams. By varying the pressure in these cells all four beams can be brought into any desired rela-tion. These cells are used to compensate for the very slow relative phase drifts.

5. *Neutron Measurements.*

Two types of neutron measuring diagnostics are being employed on IHX. A silver activation counter measures the total number of neutrons pro-duced, and scintillation counters are used to mea-sure the time history of the neutron pulse as well as the total number. The measurements taken so far are very preliminary, and questions of calibration, etc., remain to be resolved. Measurements to deter-mine the spatial region of neutron production have also been started, but no conclusions have yet been reached. For typical conditions the silver acti-vation counter measures $\sim 1 \times 10^6$ neutrons/shot, whereas the scintillation counter shows about 5×10^5 neutrons/shot and a neutron pulse duration of ≈ 225 ns. The beginning of the neutron pulse corre-lates with the first arrival of bounce particles on axis, but the peak of the neutron pulse occurs ≈ 30 ns before the peak of the density on axis.

E. EXPERIMENTAL RESULTS

1. *Preionization.*

Diagnostics of the preionization process have been done with the same instrumentation as is used for the main implosion. Studies of the preion-ization discharge were made for both the old preion-ization bank which was half the capacitance and twice the inductance shown in Fig. III-1, and for the present bank with the parameters shown there. With the old bank the initial breakdown occurred at the time of the second zero crossing of the PI cur-rent and at a radius of 14 to 16 cm. Figure III-6 shows typical density profiles 40 μs after the start of the PI current. Implosions are initiated at this time, for the PI current has died away and the preionization conditions are fairly steady. As can be seen from Fig. III-6, the electron density varied
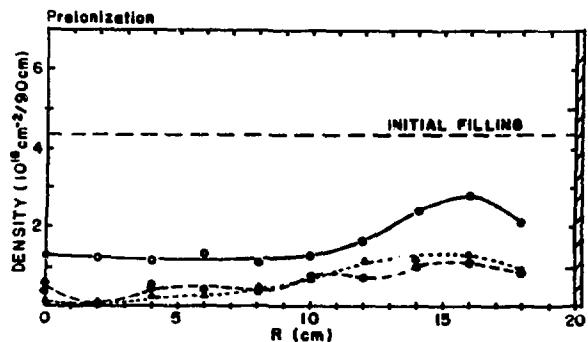
Preionization

Fig. III-6.

Preionization density profiles for the old and new preionization banks. The solid curve is for the new bank, and the two dashed curves are for the old bank.

in space from about 1.4×10^{14} cm^{-3} at the outer radii to about 2×10^{13} cm^{-3} near the axis. Integrated over the volume of the discharge tube the preionization level is about 20% of fill density. At the 40-μs time a magnetic field of $6\text{-}8 \times 10^{-3}$ T, parallel to the implosion field, is trapped in the preionization plasma.

With the new preionization bank the initial breakdown occurs at the first zero crossing of the current, and the preionization process is more violent than before. A peak ionization level, integrated over the volume, of about 75% is reached, but this level has decreased to about 40% at the time of implosion. It is believed that the decrease is due mainly to end losses during the waiting period for the preionization dynamics to calm down.

As in the previous case, the preionization density is larger toward the outer radii, typically 2.5×10^{14} cm^{-3} at the outside and 1.3×10^{14} cm^{-3} at the inside. See Fig. III-6. The trapped magnetic fields of $8\text{-}10 \times 10^{-3}$ T are slightly larger in this case, and they vary a little in the radial direction.

2. Implosion.

The main features of the implosion are about the same for the two preionization cases. As has been mentioned above, in IHX the plasma dynamics are strongly coupled into the driving circuit. So far most of the implosion conditions studied have been selected on the basis that the driving current remains essentially constant during the

time of the implosion. Figure III-7 shows the driving field in such a case. Here the voltage on the PFNs was about 90 kV and the driving field was about 0.5 T. Also shown in Fig. III-7 are magnetic field time histories at various radii as measured by the probes. As has been mentioned, these measurements are somewhat suspect, especially at the inner radii. At the end of the steady period when the driving field begins to fall, an arc always occurs at or near the wall, preventing much of the flux from leaving the pyrex discharge tube. This crowbar arc has not been studied in detail. However, its gross features are observed to vary from run to run, apparently depending upon such things as discharge tube cleanliness.

A typical set of density measurements during the implosion at various radii is shown in Fig. III-8. As can be seen, a density peak forms near the wall and moves inward. As it moves inward it develops distinct fast and slow peaks. The slower peak moves at the velocity of the magnetic sheath, in this case 2×10^7 cm/s. For this data the faster peak moves at 3×10^7 cm/s, and its leading edge has a velocity of about 3.5×10^7 cm/s. When the imploding magnetic sheath has reached a radius of 8-12 cm, an outward moving density component appears. The reexpanding plasma typically moves out to some radius between 12 cm and 18 cm, depending upon the conditions, where it is observed to stop. The magnetic field measurements by the Faraday rotation technique indicate that this reexpanding plasma pushes the magnetic field back towards the wall where it is compressed against the crowbar arc.
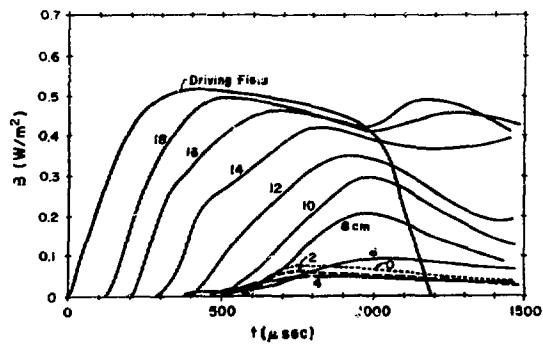
IHX Magnetic Field in Plasma as Measured by Probe

Fig. III-7.

Magnetic field profiles as measured by internal probes in IHX.

44
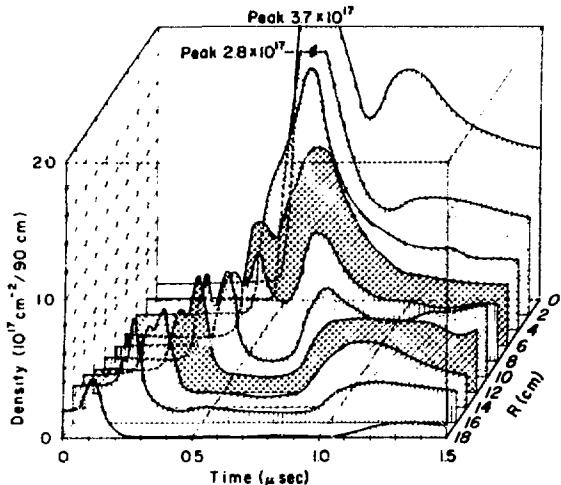
Fig. III-8.

Plasma area density during the implosion at various radial positions. Density is given as the total number per cm² in the 90-cm-long plasma column.

Fig. III-9.

Plasma area density and magnetic field profiles at various times.

This compressed field is believed to be responsible for the stopping of the plasma before it hits the wall. The total particle inventory increases monotonically, typically from about 40% to about 75% of the initial fill, during the implosion. This is believed to be a result of ionization of background neutrals. After the imploding particles have reached the axis, however, the total particle inventory remains nearly constant. Only a few percent decrease occurs out to the end of the observation period (1.5 μs after the start of the implosion).

The density data for the case shown in Fig. III-8 are plotted as a function of radius in Fig. III-9 together with the corresponding magnetic field profile (as measured by the probes). That is, for each time both the density and the magnetic field profiles are plotted. It is seen that at early times there is some plasma-magnetic field intermixing, but after about 200 ns the plasma particles are pushed ahead of the magnetic piston. The magnetic sheath moves inward with a velocity of about 2×10^7 cm/s for about 400 ns. The current sheath stops between 600 and 800 ns at a radius of about 10 cm. The plasma density peaks on axis at about 600 ns, after which the plasma reexpands towards the wall. The magnetic field profile for 1.0 μs is not believed to be accurate, as discussed above.

REFERENCES

1. F. C. Jahoda and G. A. Sawyer, Methods of Experimental Physics, (Academic Press, New York and London, 1971), Vol. 9, part B, Chap. 11, pp. 27-31.

2. M. A. Heald and C. B. Warton, Plasma Diagnostics with Microwaves, (John Wiley and Sons, Inc., New York, London, Sydney, 1965) p. 373.

3. I. S. Falconer and S. A. Ramsden, J. Appl. Phys. 39, 3449 (1968).

4. R. F. Gribble, E. M. Little, R. L. Morse, and W. E. Quinn, Phys. Fluids 11, 1221 (1968).

5. Arwin A. Dougal, John P. Craig, and Robert F. Gribble, Phys. Rev. Lett. 13, 156 (1964).

6. R. Turner and T. D. Poehler, Phys. Fluids 13, 1072 (1970).

7. I. Henins, J. E. Hammel, T. R. Jarboe, J. Marshall, and A. R. Sherwood, "Implosion Measurements in a High Voltage, Large Diameter, Medium Density Theta Pinch," presented at the Third Topical Conference on Pulsed High Beta Plasmas at Culham Laboratory, Abingdon, Oxfordshire, UK, Sept. 9-12, 1975, and for publication in Plasma Physics.

8. K. F. McKenna, R. Kristal, and E. L. Zimmerman, Phys. Fluids 18, 1371 (1975).

IV. SCYLLA IV-P THETA PINCH

A. G. Bailey, G. I. Chandler, C. A. Ekdahl, Jr., J. W. Lillberg, M. D. Machalek, F. T. Seibel

A. INTRODUCTION

Scylla IV-P is a flexible, linear theta pinch designed to investigate high-density linear concepts, end-stoppering, alternate heating methods, and plasma injection techniques relevant to a pure fusion reactor and/or a fusion-fission hybrid system. The Scylla IV-P device was proposed and approved in FY-1974. It is a conventional linear theta pinch with a 5-m length that is energized by a 60-kV, 2-MJ capacitor bank of the Scyllac type. The design, procurement, fabrication, and construction of Scylla IV-P began in early FY-1975 and was completed in the first half of FY-1976. The electrical testing and checkout of the device was completed in December 1975. Scylla IV-P had its first, full-bank plasma discharge on January 8, 1976.

Linear theta pinches have demonstrated stable plasma confinement and intense heating throughout the history of their exploration. In the mid-1960's, the Scylla IV-1 experiment routinely produced ion heating which approached thermonuclear ignition temperatures in a straight theta-pinch geometry. In the linear systems the limiting factor on confinement is the loss of plasma from the ends of the theta pinch and not MHD stability or radial diffusion. However, the particle losses through the ends at conventional densities (a few times 10^{16} cm^{-3}) would require a theta pinch of several kilometers length to achieve economical fusion power production.

The linear theta pinch becomes an attractive candidate for a fusion reactor provided the particle end loss can be reduced by an order of magnitude, which would reduce the required length to approximately 500 m. The application of uranium or thorium blankets surrounding the plasma for the purpose of breeding fissionable materials would require device lengths of about 500 m without end-stoppering. These considerations place the present emphasis in Scylla IV-P on studying methods for stoppering the ends and reducing the plasma end loss.

The planned near-term experiments on Scylla IV-P include the following: (1) initial experiments to measure plasma parameters and establish a reference basis for future experiments; (2) experiments to study end effects, such as particle loss rates and associated phenomena including "area waves," the variation of the plasma beta as a function of time and axial position, end-shorting effects, plasma "wobble," and axial electron thermal conduction; (3) a series of end-stoppering experiments using material end plugs; (4) electromagnetic end-stoppering experiments with multiple mirror fields, with cusp fields at the ends, and possibly moving mirrors will be studied to enhance particle confinement; (5) a study of plasma injection from a coaxial gun; (6) the application of the linear theta pinch to high-plasma densities (1-5 x 10^{17} cm^{-3}) will be investigated. This includes high-density plasma formation and heating, particle and thermal-conduction end loss, and other end effects in the high-density regime; (7) the sustained theta pinch may be investigated. In this system, a constant dc magnetic field is generated by an outer coil and an inner pulsed coil is energized to bring the dc field to zero in the plasma region to allow the initial plasma production; and (8) possible investigations of alternative heating methods such as with lasers and e-beams.

B. EXPERIMENTAL ARRANGEMENT

The Scylla IV-P device has been constructed in the "Pit" room, which has a floor area of 256 square meters and a ceiling height of 8 m. Figure IV-1 shows an elevation plan view of the device. The capacitor-spark gap units of the energy storage system are arranged in clusters on a three-level platform structure rather than in conventional racks. This arrangement provides more convenient access to the bank. The collector plates and 5-m compression coil are situated on the middle or experimental-platform level. A photograph of the device is shown in Fig. IV-2. Another feature of the device is a computer control system. The parameters of the device are given in Table IV-I.

Compression Coil and Discharge Tube. The single-turn compression coil, which has a 5-m length and a 11.2-cm diameter, is divided into six sections per meter. Each meter is fed by a parallel-plate transmission line or collector plate system which is connected to the spark-gap-capacitor
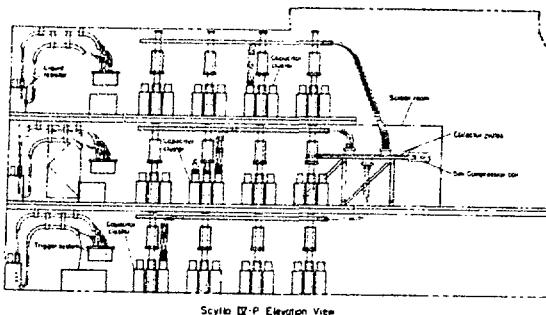
Fig. IV-1.
Elevation plan view of the Scyllac IV-P device.

Fig. IV-2.

Photograph of the "front-end" of the Scylla IV-P device showing the 5-m compression coil and its current feeds.

units by coaxial cables. The quartz discharge tube has an 8.8-cm inside diameter which increases to a 20-cm diameter just beyond the ends of the compression coil. This arrangement minimizes plasma-wall interactions at the ends and provides additional access for plasma diagnostics.

Collector Plate Systems. Each of the five collector plate (parallel plate transmission lines) assemblies is 1 m wide and 3 m long and consists of a pair of 5-cm-thick aluminum plates with Mylar insulation sandwiched between them. Cable cartridges, which adapt the coaxial cables from the bank to the collector plates, are located in a close-packed configuration on both the top and bottom surfaces of the collector plates.

Primary Capacitor Bank. The primary bank consists of 600, 1.85-μF, 60-kV capacitors with an energy storage of 2 MJ. Each capacitor is connected into the collector plate by its spark gap switch through 6 RG-17/14 coaxial cables. The bank has a voltage operating range of 40 to 60 kV and produces a magnetic field of 1.1 kG/kV with a risetime of 3.3 μs. The initial azimuthal electric field is 0.7 kV/cm just inside the discharge tube wall with a bank voltage of 55 kV. A Scyllac-type crowbar system extends the magnetic field in time with an L/R decay of ~ 200 μs. Figure IV-3 shows the waveform of the applied magnetic field which has an initial peak-to-peak modulation of approximately 20%. The system has an energy and voltage transfer efficiency of 0.6 into the 11.2-cm-diameter coil.

Preionization (PI) Bank. The preionization capacitor bank consists of two 0.7-μF, 75-kV capacitors per meter whose spark gap switches are con-

nected into the rear of the collector plate with 12 RG-17/14 coaxial cables. The PI bank oscillates at 400 kHz and produces an initial peak field of 3 kG.

Vacuum Systems. The discharge tube is pumped at each end of the compression coil by independent systems which use turbo-molecular pumps. An arrangement is used to provide a static fill of deuterium gas.

Computer Control System. The Scylla IV-P device is completely controlled by a computer system. The computer hardware consists of a Prime 300 with 32k, 16-bit words, a 3-million-word disk, a Tektronix display terminal, a Versatic printer-plotter, and a CAMAC system to interface to the Scylla IV-P device. Noise buffering relay units are used between I/O registers and the machine to minimize electromagnetic transients into the computer system. Figure IV-4 is a schematic diagram of the Scylla IV-P computer control system. The computer control program functions as a sequence in that the system issues various output signals in a prescribed order and at prescribed times. This program is "list driven" with the ordering and timing of all outputs and tests determined from lists stored on disk files. This allows the device operation to be modified by merely editing the lists.

TABLE IV-1

SCYLLA IV-P MACHINE PARAMETERS

SYSTEM:

Risetime of Current ($\tau/4$)	3.3 μs
Maximum Current	0.47 MA/kV
Magnetic Field	1.1 kG/kV
Inductance	20.7 nH/m
Coil Inductance	12.4 nH/m
Source Inductance	8.3 nH/m
Transfer Efficiency	0.60

COIL:

Length of Coil	5 meters
Number of Collector Plates	5
Number of Coils per Collector Plate	6
I. D. of Coil (Smooth Bore)	11.2 cm
O. D. of Quartz Discharge Tube	9.5 $\pm$ 0.3 cm
I. D. of Quartz Discharge Tube	8.8 $\pm$ 0.3 cm

MAIN BANK:

Number of Capacitors (1.85 μF @ 60 kV)	600
Capacitance	1100 μF
Energy Storage (@ 60 kV)	2.0 MJ
Load Cable Length (RG-17/14) (3600 each)	10.2 m
Trigger Cable Length (RG-17DS) (600 each)	10.7 m
Total Charge Cable Length (12,000 ft)	3.6 km

CROWBAR TRIGGER BANK:

Number of Capacitors (0.75 μF @ 75 kV)	60
Capacitance	45 μF
Energy Storage (@ 70 kV)	111 kJ
Operating Voltage	70 kV

PRE-IONIZATION BANK:

Energy Storage (@ 52 kV)	5 kJ
Capacitance (total)	3.75 μF
Number of Capacitors (0.75 μF @ 75 kV)	5
Operating Voltage	50 kV
Ringing Frequency	$\sim$ 400 kHz

C. CONSTRUCTION

During the construction of Scylla IV-P, funding, parts and components, and labor went through extremes of availability and non-availability. Highlights of these events included the following. (1) Impoundment of funds late in FY'74 by the President slowed the project for many weeks. An allocation of $170k from DCTR in March rescued the project, but the damage to the schedule had already been done and all timetables for Scylla IV-P had to be moved back several months; (2) The contract fabricator for spark-gap parts for Scylla IV-P was months late in delivery of necessary components and, even with constant prodding from LASL, was quite lax in fulfilling their delivery schedules. To compound difficulties, some of the components delivered to LASL were defective and caused delays while repairs and replacements were made. Specifically, as one example, the outer cans for capacitor spark gaps had defective welds which leaked oil and replacement of these cans alone cost half a month's delay. Several other, smaller, difficulties also appeared;
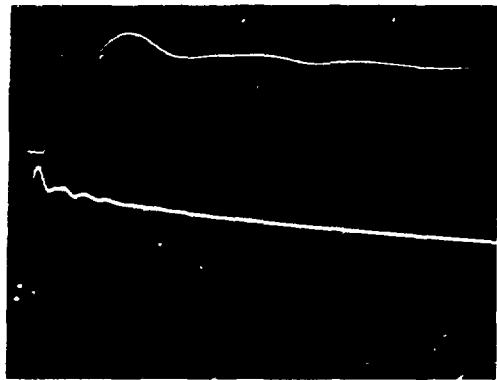
Fig. IV-3.

Oscillograms of the magnetic field waveforms in the Scylla IV-P device. Upper trace: 2 μs/device, Lower trace: 10 μs/division.

Fig. IV-4.

Schematic diagram of the Scyllac IV-P computer control system.

(3) Labor was a problem that at times slowed, and even halted, progress on Scylla IV-P. Due to the rather wild fluctuations in available funds, long-term scheduling of outside skilled labor was difficult. When funds and time were available, labor was not always available. Then, too, the quality of some of the labor was less than expected and work on certain phases of construction went slowly. Additionally, Scylla IV-P experienced the results of three separate labor strikes at LASL which occurred during peak Scylla IV-P work scheduling. None of the strikes was related to any grievances on Scylla IV-P but were from difficulties at other sites at LASL; (4) Continuity of engineering for Scylla IV-P was also adversely affected by the oscillations in funding. Some items which should have been purchased and installed at early stages of construction were delayed, resulting in overall increases in costs. In some cases additional costs and delays were incurred because retro-fitted items had to be re-engineered and re-designed. An example of this retro-fit was the air pressurization and flushing system for spark gaps. Instead of being installed early in the schedule, lack of funds forced installation of the air system almost as the last part of the capacitor bank. Pipes had then to be run over, under, around, and through cables, cable trays, lighting fixtures, etc. Other situations of a similar nature could also have been avoided with steady funding.

In spite of these difficulties the project has

done well and a fully operational, computer controlled, 2-MJ, 5-meter theta pinch has been put on-line in about eighteen months.

The first quarter of CY'75 began very slowly owing to a lack of funds which resulted from the Presidential holdback. Then activity increased as more parts arrived and spark-gap assembly went into full operation. The first collector plate was assembled and installed. The screened room was erected and most of the power supply room set up. By the end of March, activity had reached a high level.

The second quarter of CY'75 continued the activity level of March. Electricians now began installing load cables from capacitors to collector plates. All five collector plates were assembled and installed by the end of this period, as were capacitor/spark-gap units. The assembled and pre-tested computer control system was moved into the screened room and the task of interconnecting the control system, power supply room, and capacitor bank continued through the end of the quarter.

The third quarter of CY'75 saw the last 20-25% of load cables installed, the trigger cables installed and miscellaneous wiring done. Numerous small jobs to complete the entire system were done during this period. The big job of design, fabrication, and installation of the air system was completed. By the end of the third quarter the first rudimentary phases of system check-out were begun.

49

D. ELECTRICAL TEST AND CHECK-OUT

During the fourth quarter of CY'75, the control system was brought to a fully operational status, and electrical check-out of the device under full computer control was completed. This accomplishment included the following tasks.

Development of control software for automatic sequencing of the charge - discharge cycle was completed. This cycle includes charging trigger system capacitors and pre-ionization, crowbar, and primary capacitor banks in the proper order; triggering the bank switches; and purging the air spark gap switches. Various safety features are built into the software (e.g., it is not possible to charge and fire the primary bank unless the crowbar banks are charged), and in addition, the system continuously monitors the interlocks, gas pressures, bank voltages, and charge rates. If any of these fall outside of prescribed limits, the charge cycle is aborted. The control system has a great amount of flexibility, making it possible to perform easily functional tests of various sub-systems (e. g., charging and firing the trigger systems, charging a specific bank, etc.).

Diagnostics to determine electrical performance were installed and calibrated. These included voltage dividers for computer monitoring of capacitor bank voltages and charge rates, dividers for monitoring the trigger system pulse-charge waveforms, and magnetic flux loops for monitoring the magnetic field in the compression coil.

The electrical check-out was accomplished in several stages. The power supplies and capacitor banks were first tested by charging to maximum operating voltages. The number of high-voltage faults developed in this phase of testing was far fewer than had been anticipated. The trigger systems were then tested with no voltage on the main banks. The pre-ionization bank was discharged into the load coil, completing check-out of the preionization system. The crowbar banks were then charged and fired to test the crowbar trigger system, and to measure the bank ringing frequency, providing the selection of the optimum triggering delays for the crowbar and primary banks. All trigger systems were tested in conjunction with firing all energy storage banks, with the exception of the primary bank. At each step of this check-out procedure minor faults were

discovered and corrected, but no more than might be expected in a high-voltage system with this complexity. The first discharge of the primary bank into the load-coil was successful in that all electrical systems operated properly, but resulted in the catastrophic failure of three collector plate cartridges owing to faulty load cables. Following their replacement, several successful shots were obtained with all main energy storage banks firing before disassembling the load coil to install the quartz discharge tube.

While tube installation was proceeding, one meter of the load coil was used in a test facility for measurement of the magnetic fields in order to assess the perturbations introduced by the diagnostic slots. In keeping with the observed quarter-cycle risetime of $3.3\,\mu s$, the coil was excited with a frequency of 80 kHz. The axial fields induced were probed with a 200-turn search coil as a function of axial position at different radii, and as a function of angular displacement near the coil wall to measure the effect of the coil feed-slot.

The deviations from the normal theta-pinch field, on axis, and at a position 4.9 cm off axis are shown in Fig. IV-5. It is observed that the maximum perturbation (see spikes, Fig. IV-5) introduced by the slots is less than three percent at $r = 4.9$ cm. The inner radius of the quartz discharge tube is ~ 4.4 cm, therefore the maximum field perturbation seen by the plasma is less than 3%. The field perturbation at $r = 4.9$ cm as a function of θ in the plane of the diagnostic slots is shown in Fig. IV-6, along with a cross section of the load coil in the same plane indicating the material machined away to form the 0.7-cm-wide slots. To assess the effect of the feed slot the field was probed as a function of θ midway between diagnostic slots again at a radius of 4.9 cm. The perturbation near the feed slot was measured to be $\sim 0.5\%$.
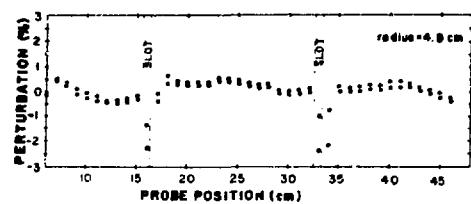
Fig. IV-5.

Axial magnetic field perturbation from flux leakage
through diagnostic slots as a function of Z. The
∿ 1-cm-wide slot locations are indicated by the
dashed lines. Upper: perturbation at a radius of
4.9 cm. Lower: perturbation on axis. Note change
in ordinate scale.

COIL CROSS-SECTION

DEVIATION OF AXIAL FIELD
FROM MEAN VALUE
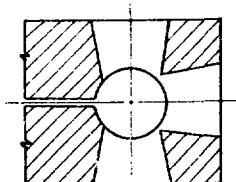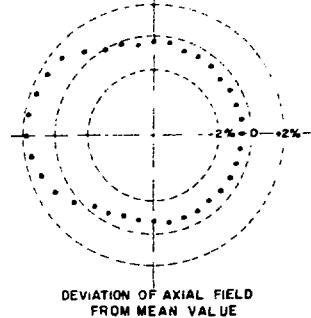
Fig. IV-6.

Axial magnetic field perturbation from flux leakage
through diagnostic slots in the plane of slots as a
function of θ. These data were obtained at r =
4.9 cm. Also shown is a cross section of coil in
this plane indicating material removed to form the
∿ 1 cm wide slots.

V. SCYLLA I-C

K. F. McKenna, W. T. Armstrong, K. B. Freese, E. L. Zimmerman, T. M. York

A. INTRODUCTION

The Scylla I-C linear theta pinch was constructed in order to provide a versatile research instrument to supplement the larger, less flexible theta-pinch programs. Small-scale research studies and the experimental investigation of advanced concepts are carried out on Scylla I-C in order to provide basic physics information and diagnostics development for the present and future main theta-pinch efforts.

The Scylla I-C theta pinch is presently being used in conjunction with a CO_2 cold cathode laser to study the interaction of axially directed long wavelength laser light (10-6 μm) with the dense ($n_e \sim 10^{17}$ cm^{-3}) theta-pinch plasma column.[1] During the past year a major experimental effort was carried out in order to develop a cold cathode CO_2 laser system capable of generating the output energy and laser pulse waveform required for the laser-plasma interaction experiment. The CO_2 laser beam has been directed into the Scylla I-C theta-pinch plasma and initial experiments on the laser-plasma interaction have been conducted.

An investigation of plasma end loss from the Scylla I-C plasma column has recently been completed. The end-loss process was examined with both an end-on interferometer and a specially designed piezoelectric pressure transducer.

B. PLASMA END-LOSS STUDIES IN SCYLLA I-C

1. Introduction. The properties and stability characteristics of linear theta-pinch plasmas have received considerable investigation.[2,4] It has been established that stable, high-energy plasmas of fusion interest can be produced in these devices. However, plasma flow from the open ends of the device has presented a fundamental limitation on the plasma containment time. The detailed processes involved in the transient axial plasma flow have not been clearly identified either experimentally[2-4] or theoretically.[5] In the present work the plasma source properties and end loss, in the collision dominated Scylla I-C theta-pinch plasma, have been experimentally studied. The end-loss process was examined with an end-on interferometer, which responds to the electron density integrated over the

entire length of the plasma column, and with a small diameter pressure sensor, which responds to local conditions at points within the plasma near the coil ends. In addition, diamagnetic loop-probe measurements made at various axial positions, and side-on luminosity measurements have been carried out.

2. Experimental Arrangement. Scylla I-C has a maximum capacitor energy storage of 175 kJ at 60-kV main bank voltage. Fifty-four 1.8-μF capacitors feed the 100-cm-long, 10.5-cm-diameter single-turn compression coil. Main bank operation at 40 kV generates a vacuum E_θ of 0.26 kV/cm at the inner wall of the 3.6-cm-i.d. quartz discharge tube and a peak crowbarred compression field of 33 kG is obtained 2.0 μs after discharge initiation. The end-loss experiments were carried out at 40-kV main bank voltage and with a theta-pinch fill pressure of 100-mTorr deuterium.

Gas preionization was accomplished with an axial Z pinch. The Z-pinch discharge current was supplied by a 0.7-μF capacitor charged to 60 kV. By tailoring the circuit parameters, a single non-reversing 18-kA peak current pulse of 4-μs duration was generated. The density of the preionized plasma was measured by means of a 30-ns pulsed holographic ruby laser interferometer arranged in a single-pass end-on configuration. Spatial integration of the reduced density profiles $n_e(r)$ indicated approximately 50% ionization of the initial fill gas.

3. Properties of the Theta-Pinch Plasma.

a. Plasma Luminosity Measurements. Side-on streak photographs of the main discharge plasma were taken at the coil midplane with an Imacon camera. Figure V-1 shows typical streak pictures taken at different camera-sweep rates. The initial radial shock, associated with the plasma implosion, and the subsequent radial plasma oscillations can be clearly identified. The quiescent plasma column is highly stable and reproducible for a period of approximately 9-10 μs. The compressed plasma breaks up into filaments (m = 2) after this time, probably as a result of classical Rayleigh-Taylor flute-like instabilities characteristic of high-density theta-pinch operation.[6]

b. Plasma Density Measurements. The spatial and temporal evolution of the main discharge

52
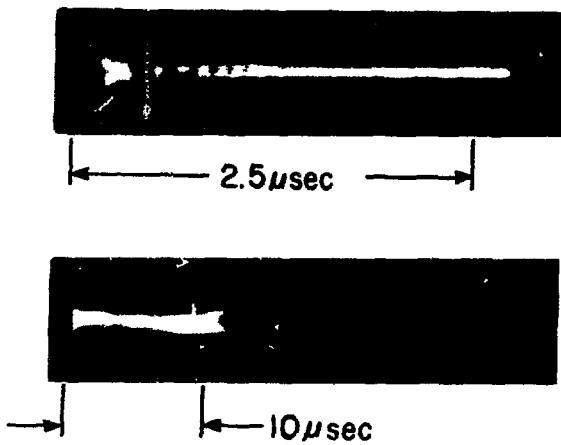
Fig. V-1.

Streak photographs of plasma discharge at 100-mTorr D_2 fill pressure.

Fig. V-2.

Typical end-on interferogram and corresponding electron density profile.

plasma density distribution was determined using a 30-ns pulsed holographic ruby laser interferometer. The interferometer was used in an end-on configuration. Figure V-2 presents a typical interferogram and corresponding density profile obtained at the time of maximum compression. A column length of 100 cm was assumed in density data reduction. From examination of the interferograms, the plasma column formation phase, $t < 1.0$ μs was found to be dominated by high m-number (m > 6) flutes. At later times, $t > 1.5$ μs, the flutes disappear and a well-confined high-density plasma column is observed for several microseconds. The beginning of the plasma column break up and filamentation (m = 2) is evidenced at $t \gtrsim 8.5$ μs.

Electron density profiles $n_e(r)$ reduced from the end-on interferograms are shown in Fig. V-3. The density profiles exhibit a long tail at times $t \gtrsim 3$ μs, which may be a result of plasma flow from the ends of the column. An average peak density on axis, n_A, of approximately 1.1×10^{17} cm^{-3} is obtained at maximum compression. The on-axis density decays to a value of about 0.3×10^{17} cm^{-3} just prior to the column filamentation; a slight increase in on-axis density between 5 and 6 μs results from the low-frequency oscillation of the main compression field. A 1/e plasma radius of 0.55–0.6 cm is indicated from the density profiles.

c. *Plasma Excluded Flux Measurements.* The effective radius, r_{eff}, at which magnetic flux is

excluded from the compressed plasma was determined from diamagnetic loop-probe measurements. Four loop-probe systems were arranged along the axis of the discharge tube. With $z = 0$ defining one end of the 100-cm-long theta-pinch coil, the diamagnetic loop-probes were located at $z = 0$, 14, 28, and 50 cm.

The axial time evolution of the effective plasma radius is shown in Fig. V-4. The lines connecting the data points are introduced only as a visual aid since an insufficient number of data stations are available to define precisely the axial distribution of the excluded flux radius. However, the phenomenology of the time and axially dependent excluded flux radius can be identified. At early times, $t \lesssim 3$ μs, the axial distribution of r_{eff} is as might be expected; i.e., an r_{eff} minimum at $z = 0$ cm and a rise to a maximum value at $z = 50$ cm. The noteworthy feature of Fig. V-4 is the gradual decay in r_{eff} at $z \sim 14$ cm. The $r_{eff}(z)$ profiles at $t \gtrsim 4$ μs appear to imply the formation of a magnetic nozzle well within the theta-pinch coil. In this case, the pressure, temperature, and density of the axially flowing plasma would be at a minimum in the nozzle throat region, producing a decrease in β and a corresponding decrease in excluded flux radius, as observed, assuming that field fringing at the coil end does not significantly distort the loop-probe measurement. The increase in r_{eff} at $z = 0$ could indicate the deceleration and interaction of the plasma with the discharge tube wall as the plasma
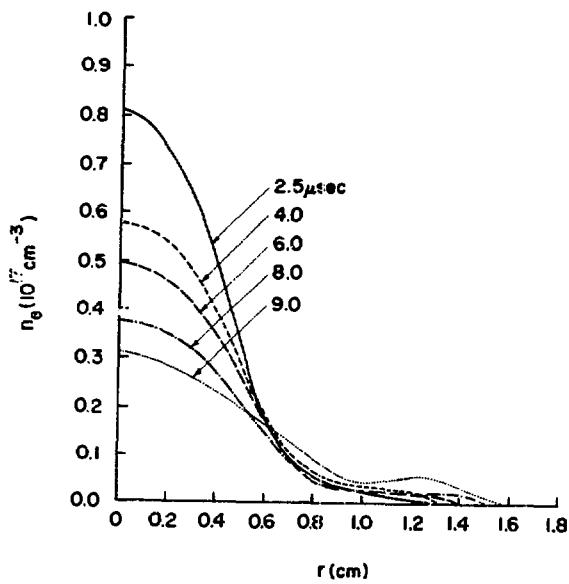
Fig. V-3.

Time evolution of plasma column electron density profiles.

Fig. V-4.

Axial and time evolution of the plasma excluded flux radius.

expands in the diverging magnetic fields near the ends of the theta-pinch coil.

 d. Temperature and β of the Compressed Plasma. The excluded flux data, when appropriately combined with the measured plasma density distribution, yields the plasma β^1 (ratio of plasma pressure to magnetic field pressure). In the high-density plasma column the thermal equilibration time between electrons and ions is small so that $(T_e + T_i) \approx 2T_e$.

 Figure V-5 presents the time history of the plasma density, the plasma component temperatures, and the plasma β_A determined from the loop-probe data obtained at $z = 50$ cm and the end-on interferograms. Although there is significant scatter in the $T_e = T_i$ and β_A data points, a reasonable estimate of average values can be made. The plasma component temperatures are on the order of 45 eV between 1.5 and 6.5 μs. For $t \gtrsim 6.5$ μs a nearly linear (in time) decrease in the temperature is observed. A similiar phenomenon can be identified on the β_A data, where $\beta_A \sim 0.44$ for $1.5 \lesssim 5$ μs, β_A also decreased linearly in time.

 The abrupt decrease in $T_e = T_i$ at $t \sim 6.5$ μs could result from the arrival, at the plasma mid-

plane, of rarefaction waves which can propagate inward from the ends of the plasma column. The speed at which the rarefaction wave travels into the plasma column will be on the order of the plasma acoustic velocity C_0. Thus the time required for the wave to arrive at the plasma midplane ($z = 50$ cm) is about $\ell/2C_0 \approx 5.9$ μs, which is on the order of the observed time of the abrupt decrease $T_e = T_i$.

 4. Plasma End-Loss Time Determined from Interferometry. The total number of electrons N_e contained within the compressed plasma column, at a given time, is determined from the end-on interferograms. Figure V-6 presents the time history of the total electron inventory. At early times, $t < 3$ μs, the total number of particles slightly exceeds that expected for the 100-mTorr filling pressure. A similar effect was reported for the linear Scyllac experiment.[4] The difference may result from the introduction, into the plasma, of gas initially absorbed on the discharge tube walls. Assuming an exponential particle inventory decay rate, expressed as $N_e(t) = N_0 \exp(-t/\tau)$ where τ is defined as the particle end-loss time, a least-squares fit of the data of Fig. V-6 yields $\tau = 14.4$ μs.

 The results of previous end-loss experiments [2-4] have demonstrated that the end-loss time scales as $\ell/T_i^{1/2}$, where ℓ is the coil length and T_i is the ion temperature. Comparing the end-loss times of these experiments with that of the present experiment, an end-loss time of ~ 17 μs is predicted from the $\ell/T_i^{1/2}$ scaling law. The Scylla I-C experiment,
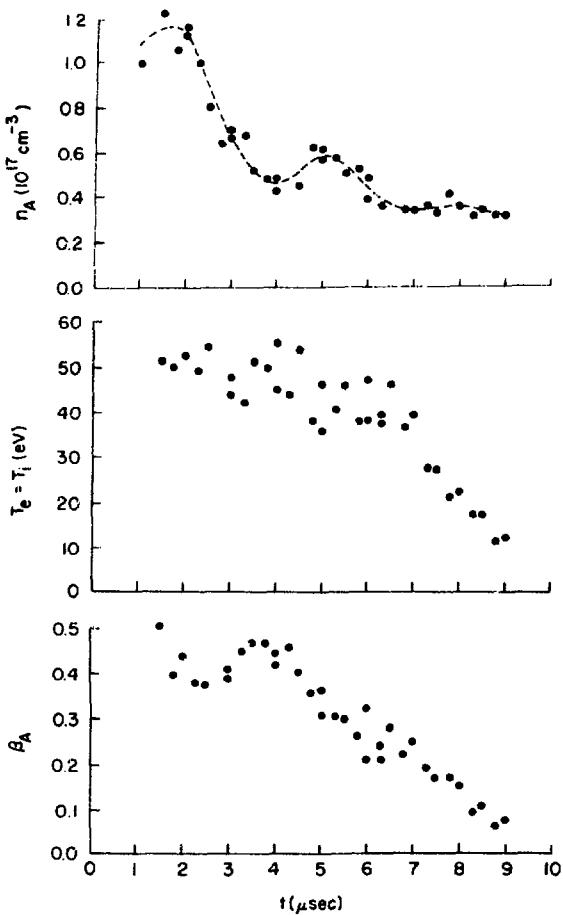
Fig. V-5.

Time history of the plasma density on axis, the plasma component temperature and the plasma beta on axis.

with $\tau \sim 14$ µs, does not scale directly with the earlier results. In Scyllac I-C, where the ion-ion mean free path $\lambda_{ii} \approx 0.1$ cm is much less than the dimensions of the column, the plasma is collision dominated whereas in the earlier experiments[2-4] collisionless plasmas were produced.

In a collision-dominated plasma column the flow from the ends into the vacuum region should be describable by classical MHD concepts. Taylor and Wesson[7] have treated the case of steady choked flow through a magnetic nozzle in the presence of internal magnetic fields. The expression they derived for the particle loss rate is

$$\dot{N}_s = 2n_0 A_0 C_0 \, f(\beta,\gamma), \tag{1}$$
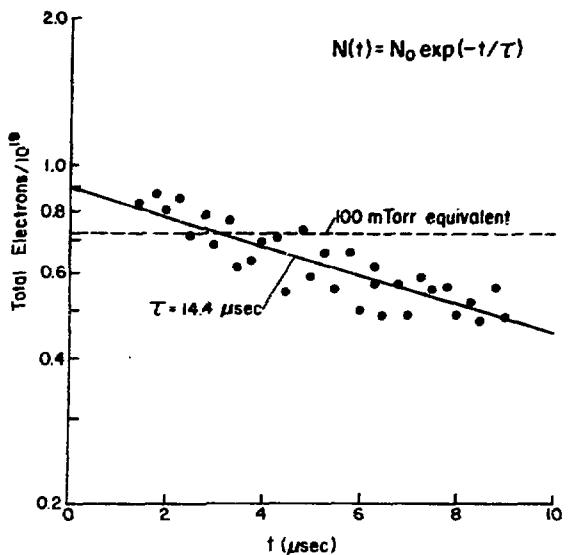
Fig. V-6.

Time history of the total plasma column electron inventory.

where n_0 is the particle number density in the column, A_0 is the column area, C_0 is the acoustic velocity and $f(\beta,\gamma)$ is an algebraic function of the plasma β and the ratio of specific heats. $f(\beta,\gamma) \approx 0.8$ for the parameters of the Scylla I-C plasma so that Eq. (1) can be approximated as $\dot{N}_s \approx 1.6 n_0 A_0 C_0$.

Wesson[8] has treated the case of unsteady collisional flow from the ends of a theta-pinch plasma column where internal magnetic fields were included in the analysis. In Wesson's model a rarefaction wave propagates in from the ends of the plasma column, converting the random thermal energy of the particles into axially directed kinetic energy. The particle flow rate predicted from the transient rarefaction wave model, $\dot{N}_u$, is given by

$$\dot{N}_u = 2n_0 A_0 C_0 \, g(\beta,\gamma), \tag{2}$$

where $g(\beta,\gamma) \approx 0.3$ for $0 \leq \beta \leq 0.8$ and $\gamma = 5/3$. Thus, in the present experiment $\dot{N}_u$ can be approximated as $\dot{N}_u \approx 0.6 n_0 A_0 C_0$.

It should be noted that there exists a fundamental gas dynamic difference in the two models discussed above. The ends of the plasma column are exposed to a relative vacuum region ($P_{background} \ll P_{plasma}$). Accordingly, neglecting MHD effects, any constriction in the plasma column-cross sectional

area will result in the production of a sonic throat since the critical pressure ratio ($P_{plasma}/P_{back-ground}$) required for sonic conditions at the constriction is greatly exceeded. Thus a rarefaction wave, which travels at sonic speed, generated anywhere in the nozzle exit region cannot propagate past the throat and into the source plasma. Conversely, in the rarefaction wave model a sonic throat does not exist anywhere within the plasma column so that the rarefaction wave can traverse the entire plasma.

In collisionless plasma experiments[2-4] where the ion-ion mean free path exceeds the dimensions of the plasma column, the plasma particle loss would be expected to be an effusive process rather than a diffusive process encountered in collision-dominated plasmas. In the collisionless case the effective particle loss rate can be approximated as,

$$\dot{N}_c = -2A_E[1/4 \; n_i \bar{C}] , \qquad (3)$$

where $\bar{C} = (8kT_i/\pi m_i)^{1/2}$ is the mean speed of the ions and A_E is the effective area of the plasma column end orifice. Experimentally,[2] A_E is found to be on the order of A_0. Thus, Eq. (3) can be approximated as $\dot{N}_c \approx 0.4n_0A_0C_0$. Comparing the approximated forms of Eqs. (1), (2), and (3), the particle end-loss rate from a collision-dominated plasma would be expected to exceed that from a collisionless plasma based on the simple models presented above. This prediction agrees qualitatively with the Scylla I-C end-loss results.

5. *Plasma Loss Rate Determined from Local Pressure Measurements.* In order to sense local plasma momentum flux, diagnostics must be placed in direct contact with the plasma. Specially designed,[9] piezoelectric pressure probes, which are optimum for this measurement, have been successfully employed in the investigation of pulsed plasma discharges.[10,11] In the Scylla I-C experiment a small-diameter pressure sensor was used to determine the plasma momentum flux at locations within the plasma near the coils ends.

a. *Piezoelectric Pressure Probe.* A schematic of the pressure probe is shown in Fig. V-7a. The probe is protected from the plasma by a cylindrical quartz outer jacket and a 0.25-mm-thick quartz disk attached by epoxy to the probe front end. The
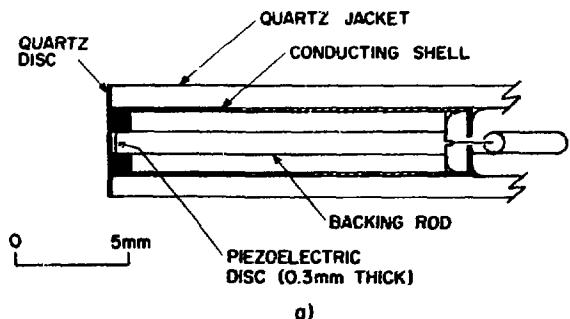
a)
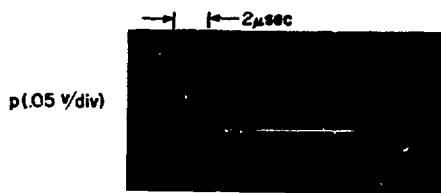
b)

Fig. V-7.

Schematic of the piezoelectric pressure probe (a), and response of pressure probe to a reflected shock wave in the end wall of a shock tube, (b).

probe was calibrated by using the constant pressure generated by a reflected shock wave in a simple shock tube. Figure V-7b shows the response of the probe system to the reflected shock. In these tests the probe system included a 15-m length of coaxial cable and a high-frequency "noise" filter with RC = 150 ns. The evident drop in the theoretically constant pressure signal between 6 and 12 μs is not real pressure, and can be related to an extraneous effect due to the mounting which held the pressure probe in the shock tube. A probe risetime of ~ 1 μs and calibration factor of $V/\Delta p = 0.016$ volt/(std) atm. was obtained from the shock tube data.

The probe was mounted through a plate at the end of the theta-pinch discharge tube. Data were recorded with the probe placed at interior axial locations z = -2.5, 5.1, 7.6, 10.2, 12.7, 15.2, and 20.3 cm relative to the coil end (z = 0), and at radial positions, R = 0, 2, 4, 6, 8, and 10 mm from the discharge tube axis. Reference data at each axial position were recorded on vacuum shots. During initial experiments, it was found that strong extraneous signals were being induced by magnetic field

impact-loading of the pressure transducer conducting shell. This effect was alleviated by placing a 2.5-cm-long, 8-mm-o.d., 6-mm-i.d. stainless steel collar around the transducer. The collar was friction-fitted over the probe quartz jacket and left the forward edge of the probe unobstructed. Pressure data recorded at z = 2.5 cm with and without the collar showed no identifiable effect of the collar on the true pressure data history.

b. *Plasma Pressure Measurements.* Figure V-8a presents a typical pressure probe data record obtained at R = 0 cm and z = 20.3 cm. The corresponding vacuum shot record is shown in Fig. V-8b. The plasma gas-kinetic pressure is determined by sub-traction of the vacuum signal from the pressure signal obtained with plasma. Radial profiles of pressure are presented in Fig. V-9 for z = 0, 7.6, and 15.2 cm. At z = 15.2 cm the pressure profiles are similar to the density profiles in Fig. V-3. The pressure profiles at z = 15.2 cm are approximately Gaussian and decay in magnitude with time, showing a behavior consistent with axial loss of particles from the plasma column. The profiles diminish in magnitude and becomes less Gaussian in shape as the coil end is approached. At z = 0 the profiles are nearly uniform across the radius for times greater than 4.0 µs. Such behavior is indicative of flowing plasma which has expanded in the diverging magnetic fields near the ends of the theta-pinch coil.

c. *Plasma Loss Orifice.* As previously discussed, the axial evolution of the effective plasma radius (Fig. V-4), obtained from the diamagnetic loop-probe data, indicated the formation of a mini-mum plasma area or throat region within the theta-pinch coil (z > 0). This phenomenon is also ob-served from examination of the pressure data. Fig-ure V-10 presents the 1/e plasma radius, r_p, obtained from the measured pressure profiles, as a function of axial position and time. For t ≲ 6 µs a minimum plasma radius of about 0.5 cm can be identified at z = 7-10 cm, again well within the theta-pinch coil. At axial position z > 10 cm, r_p approaches the 1/e plasma radius indicated from the end-on interfero-grams, 0.55-0.6 cm. For z < 7 cm, rapid radial ex-pansion of the plasma is evident. For t > 6 µs the r_p minimum advances further into the coil and a correspondingly greater radial expansion is observed.

Defining the minimum plasma area, observed from

a) **PLASMA**
p(0.1 V/div)
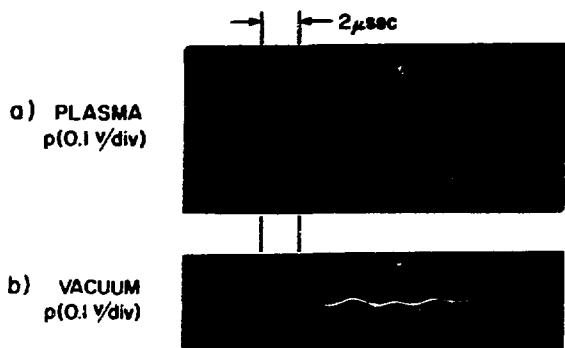
b) **VACUUM**
p(0.1 V/div)

Fig. V-8.

Pressure probe response in plasma (a), and vacuum (b), discharges. Probe positioned at z = 20.3 cm, R = 0 cm.

the pressure data, as the effective particle loss orifice, the magnitude of this orifice can be com-pared with that indicated from theory. In the ab-sence of radial electric fields within the plasma sheath the minimum orifice radius is expected to be on the order of an ion gyroradius, r_i. Taking t ~ 3 µs as a representative time during the loss pro-cess when r_p ~ 0.5 cm, then with T_i ~ 45 eV and B ~ 25 kG, r_i ~ 0.06 cm. Collisionless plasma the-ories predict orifice sizes on the order of the ion sheath thickness, $r_{is} = c/\omega_{pi} = r_i/\sqrt{\beta}$ where ω_{pi} is the ion plasma frequency. With β = 0.44, $r_{is} \approx 0.1$ cm.
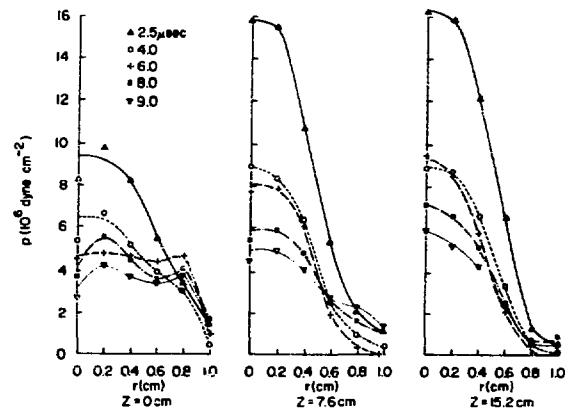
Fig. V-9.

Radial pressure profiles at z = 0, 7.6, and 15.2 cm.

57
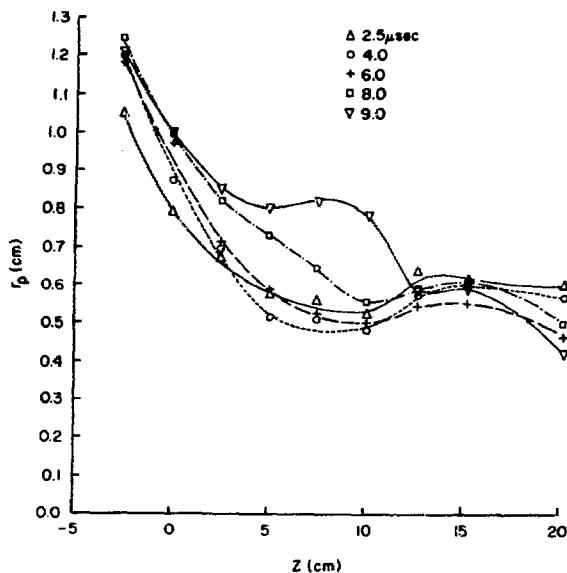
Fig. V-10.

Axial and temporal variation of the 1/e plasma radius obtained from pressure profiles.

The steady collisional plasma flow theory of Taylor and Wesson,[7] predicts that the minimum plasma radius, r_{min}, is related to the plasma column radius at mid-coil, r_0, through the expression

$$r_{min} = r_0(1-\beta)^{1/4} , \qquad (4)$$

where β is evaluated at the coil mid-plane. For the present experiment, at $t = 3$ μs, $r_0 \sim 0.6$ cm, and $\beta \sim 0.44$, then $r_{min} = 0.52$ cm.

For unsteady collisional flow of plasma, treated by Wesson,[8] the relationship for the minimum radius is given by

$$r_{min} = r_0 \left(\frac{1-\beta}{\gamma} \right)^{1/6} , \qquad (5)$$

in the approximation of high β; this relationship is presented to demonstrate a functional form different from the steady case. With $\beta = 0.44$, in the Scylla I-C experiment, $r_{min} = 0.50$ for $r_0 = 0.6$ cm, and $\gamma = 5/3$.

To summarize, the effective loss orifice radius of 0.5 cm determined from the pressure data is in excellent agreement with predictions from collisional MHD theories, but in poor agreement with collisionless theories.

d. *Rate of Plasma Loss.* The rate at

which particles are lost from one end of the plasma column can be expressed as $J = nAv$ where n, v are number density and flow velocity averaged over the plasma column cross-sectional area, A. The loss rate involves the interaction between the density, temperature, and velocity of the plasma as it varies with time at a given location. Pressure, as it involves a combination of these variables, can be used in conjunction with other diagnostics to indicate the magnitude of plasma loss rate.

The quantity which is sensed by the pressure probe is the momentum flux from the plasma particles impinging upon the probe surface area. The measured pressure p, which contains a component due to the random kinetic motion and a component due to directed particle motion, can be expressed as

$$p = nk(T_e + T_i) + nmv^2 , \qquad (6)$$

where n is local number density, T is local particle temperature, m is ion mass, and v is directed plasma velocity. The second term in the above equation assumes a Newtonian interaction of flowing particles with the probe; the particles do not interact with each other when colliding with the probe surface, but lose their normal momentum component. In the present case where the ion mean-free-path is of the same order of magnitude as the probe sensing diameter (1 mm), little upstream influence can be expected and the above formulation provides an adequate description of the plasma-probe interaction.

In order to determine the component pressures that comprise the total measured pressure, the pressure probe data taken at $z = 15.2$ cm is combined with the diamagnetic loop-probe data obtained at $z = 14$ cm. It is assumed that strong axial gradients do not exist over this short, 1.2-cm, plasma length. Taking the plasma density profiles, determined from the interferograms, to be approximately equal to the density profiles at $z = 14$ cm, the plasma β is evaluated.

While local values of n(r) could lead to local values for flow velocity, v(r), from the pressure data, it is more reasonable to deal with radial average values of n and p in order to determine average values of velocity, $\bar{v}$. Since the density and pressure profiles are approximately Gaussian,

$$\int_{r=0}^{\infty} n(r) \ 2\pi r dr = \int n_A e^{-(r/a_c)^2} \ 2\pi r dr = n_A \ \pi a_c^2 \quad (7)$$

$$\int_{r=0}^{\infty} p(r) \ 2\pi r dr = \int p_A e^{-(r/a_c)^2} \ 2\pi r dr = p_A \ \pi a_c^2 \ , \quad (8)$$

where n_A and p_A are the measured density and total pressure on axis. Accordingly, the plasma column is treated as having a uniform density n_A and pressure p_A over a radius a_c (determined from the pressure data). The average flow velocity is then evaluated from, $p_A - p_{sA} = n_A \ m \ \overline{v}^2$. From this formulation, average flow velocities, $\overline{v}$, slightly less than the ion thermal velocity, v_i, are indicated for $t < 6.0$ μs; at $t = 3.0$ μs; $\overline{v} = 7.7 \times 10^6$ cm/s and $v_i = 8.5 \times 10^6$ cm/s. For times greater than 6 μs, $\overline{v}$ becomes somewhat larger than v_i. It should be noted that this calculation is approximate since n_A has been assumed constant in z between the coil mid-plane and z = 14 cm.

From the calculated values of $\overline{v}$, the total loss rate of particles from both ends of the plasma column can be expressed as

$$\dot{N}(t) = 2J = 2n_A \ (\pi a_c^2) \ \overline{v} \ . \quad (9)$$

For comparison, the variation of particle loss rate predicted from the steady collisional theory of Taylor and Wesson,[7] Eq. (1), and the unsteady collisional theory of Wesson,[8] Eq. (2), are evaluated for the time-dependent parameters of the present experiment. Figure V-11 presents the loss rates determined from the reduction of the end-on interferograms, the pressure probe data, and the steady and unsteady collision dominated flow theories. The two analytical models predict similar functional behavior for loss rates ($\dot{N}_s$, $\dot{N}_u$) with time, but there are substantially different loss magnitudes in each case. The loss rate determined from the interferograms is based on axial and radial averages of density with an assumed functional form for the particle inventory decay rate and so does not respond to the fine structure of the loss process. The loss rates obtained from the pressure data tend to follow the high values of the steady theoretical model and also display more detail of the loss process than can be obtained from the interferograms.
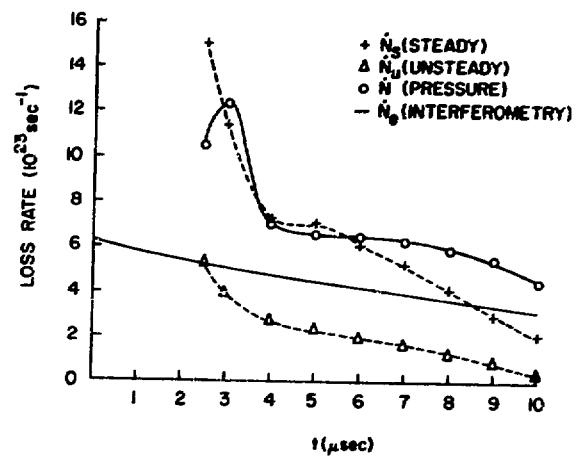
Fig. V-11.

Comparison of experimentally determined plasma loss rates and loss rates predicted from analytical models.

C. CO_2 LASER SYSTEM

1. Introduction. The CO_2 cold cathode laser used in the Scylla I-C experiment was constructed by the L-1 Group of the Laser Research and Technology Division. A modification of the A-3 amplifier[12] of the LASL CO_2 laser system was chosen as the source for the ~ 150-J requirement of the laser-plasma interaction experiment.

2. CO_2 Laser Operating Characteristics. The modification of the A-3 amplifier from a hot cathode to a cold cathode configuration resulted in a significant alteration of the amplifier's operating characteristics. In the Scyllac I-C experiment the A-3 amplifier is actually used as a gain switched oscillator. For the hot cathode design, optimum electrical excitation, "pumping," of the laser gas molecules is achieved at a pumping chamber electric field stress, S, of 3-4 kV/cm-atm. Operating the Scyllac I-C cold cathode laser system within this range of S resulted in gas breakdown and arc formation problems within the laser pumping chamber. Although design changes[13] in the pumping chamber anode configuration and electrical circuitry reduced somewhat the frequency of chamber breakdowns, the laser output pulse energy remained irreproducible, varying as much as 50% between shots.

As a result of the CO_2 laser gas breakdown problems discussed above, operation within the 3-4 kV/cm-atm electrical stress limit was abandoned and

59

an investigation of the laser characteristics over a wide range of stress (essentially applied pumping chamber voltage and fill pressure) was carried out. Figure V-12 presents the results of this investigation where the total laser energy output is plotted against the pumping chamber electrical stress S, for two different laser gas mixes; 3:1/4: 1:: H_e: N_2: CO_2 and 3 : 1: 1:: H_e: N_2; CO_2. Each data point represents the average value of energy obtained over several laser discharges and the error bars give the $\pm$ standard deviation. An applied pumping chamber voltage of approximately 63 kV was found to be optimum over the entire range of pumping chamber fill pressure, 700 to 1600 Torr absolute; operation at lower values of applied voltage resulted in a decrease in recorded output energy, higher applied voltages produced only a minimum increase in energy while stressing the electrical limitations of the laser system components. The curves of Fig. V-13 represent the data collected at the optimum 63-kV pumping chamber voltage. It can be seen that the maximum laser output energy is obtained with S > 4 kV/cm-atm for both gas mixes. Reproducible laser output pulses are obtained without pumping chamber breakdown when the laser system is operated at the stress level corresponding to the maximum in recorded output energy.

3. *Small Signal Gain Measurements*. An additional measurement of the CO_2 laser system performance was obtained from the results of an experiment which measured the laser system small signal gain. Small signal gain was measured on the laser optical axis for the R(16) transition of the 10μ CO_2 band, using a CW probe laser in conjunction with a Hg-Cd-Te photovoltaic detector. The CW signal was mechanically chopped and the detector dc signal level, I_o, was compared with the signal amplitude at peak gain, I_A, to yield the system gain.

The small signal gain parameter, g_0, is given by

$$g_0 = \frac{1}{L} \, \ln \frac{I_A}{I_0} \quad , \tag{10}$$

where L is the active length of the CO_2 laser discharge device.

For the 3:1/4:1::H_e:N_2:CO_2 laser gas mix at S = 4.3 kV/cm-atm (optimum condition), $g_0 = 0.041 \pm$ .002 cm^{-1} for an active length of 100 cm. This value
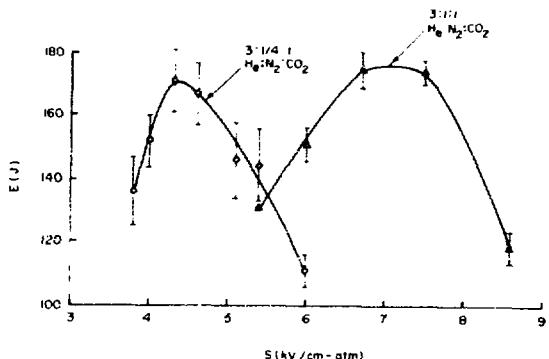
Fig. V-12.

Variation of CO_2 laser output energy with pumping chamber electrical stress level.

compares favorably with the small signal gain measurements taken on the A-3 amplifier of the L-DO single-beam laser system. In that system the measured small signal gain on R(16) of the 10μ band was 0.040 ± 0.002.

Using the measured value of small signal gain and the known CO_2 laser voltage and current characteristics, the output waveform and energy of the gain switched laser pulse can be estimated from computer simulations. The results of this analysis indicate that the laser system, when operated at the optimum conditions, performs as would be expected and that the results obtained when the system is used as an unstable resonator oscillator are in reasonable agreement with the computer calculations.

4. *Characteristics of the CO_2 Laser Output Pulse*. For the 3:1/4:1::H_e:N_2:CO_2 laser gas mix, used for initial laser-plasma interaction experiments, the laser output pulse contains a total energy of about 175 J at optimum operating conditions.
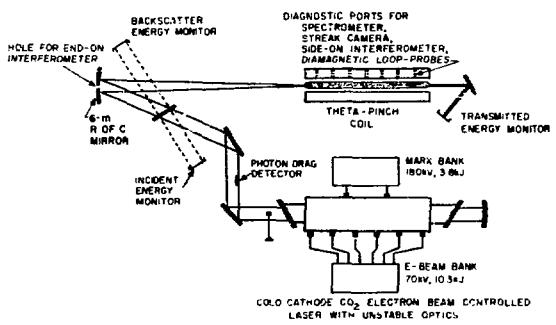
Fig. V-13.

Schematic of the laser-plasma interaction experiment.

Approximately 50% of this energy is contained within the initial $\sim$ 60-ns FWHM spike and the remaining energy resides within an $\sim$ 1-μs-long tail.

The spectral distribution of the CO_2 laser light was measured by focusing a small portion of the laser beam onto the entrance slit of a 0.5-m Ebert monochrometer and scanning, shot to shot, over the appropriate wavelengths. The intensity of the light appearing at the monochrometer exit slit was monitored by a fast (10^9-Hz) photovoltaic (S.A.T.) detector. This setup will be used for the detection of stimulated Brillouin and Raman backscatter from the laser irradiated Scylla I-C plasma. The results of the spectral analyses of the CO_2 laser light indicated that the laser was lasing on the P-20 and P-18 transitions, with $\sim$ 70% of the energy resulting from the P-20 transition and $\sim$ 30% from P-18.

D. LASER-PLASMA INTERACTION EXPERIMENTS

1. Experimental Arrangement. A schematic of the CO_2 laser and theta-pinch experimental arrangement is shown in Fig. V-13. The 8-cm-diameter CO_2 laser beam, generated with unstable optics, is focused near the input end of the theta-pinch plasma column by a spherical reflecting mirror with a 6-m radius of curvature. The focal spot size was measured in air by observing the laser burn patterns recorded on type 107 Polaroid film. In order to avoid air breakdown by the focused beam, several fine-mesh copper screens were introduced into the 8-cm-diameter beam path. The screens attenuated a sufficient fraction of the laser beam energy to allow a determination of the focal spot size and mirror focal length. The measured minimum focal spot diameter was $\sim$ 2 mm at a distance of 3.2 m from the 6-m radius of curvature mirror. In the laser-plasma interaction experiments the focusing mirror was positioned 3.1 m from the end of the theta-pinch coil so that the laser beam was focused at a point 10 cm within the theta-pinch coil. At optimum CO_2 laser operating conditions, the focused laser beam power density is $\sim 4.3 \times 10^{10}$ W/cm^2, which exceeds the theoretical thresholds for both Raman and Brillouin backscatter instabilities.

Because of the early CO_2 laser operational problems discussed above, only limited experiments on the laser-plasma interaction have been carried out. These initial experiments were conducted at relatively low laser output energy levels, approximately 70 J.

As noted earlier, the CO_2 laser beam was focused to a 2-mm-diameter spot at an axial position 10 cm within the theta-pinch coil. The characteristics of the laser beam energy distribution, after axially traversing the plasma column, were recorded on Polaroid film targets placed $\sim$ 2 m from the exit end of the theta-pinch coil. Experiments were conducted for an initial theta-pinch fill pressure of 100 mTorr. Laser burn patterns were taken at various times during the main and preionization plasma discharges. The shape of the burn pattern without plasma was recorded with the theta pinch under vacuum conditions.

With no plasma, an approximately circular burn pattern of about 7-cm diameter was observed on the film target. The pattern obtained by firing the CO_2 laser $\sim$ 10 μs after the preionization discharge (prior to the main bank discharge) was also circular with a diameter of $\sim$ 5.5 cm. At this time, the preionization plasma has a broad density maximum on axis with a density maximum at the discharge tube wall. It thus appears that the laser beam travels within the light pipe formed by the preionization plasma density profile, as would be expected. When the laser is fired during the plasma implosion phase an intense burn pattern of $\sim$ 3 cm is recorded on the film target, indicating that the incident laser radiation is channeled and focused in the strong density gradients formed by the imploding plasma. The compressed plasma column generated in Scylla I-C has a density maximum on axis (Fig. V-3). Accordingly, the incident laser beam will be refracted out of the column if a laser induced density minimum is not produced. When the laser beam is fired into the plasma column, no burn pattern is observed on the film target, indicating that the beam is refracted out of the column. For the measured plasma column density profiles at 100-mTorr fill pressure, theory predicts that one-half of the laser beam energy will be refracted out of the column at axial distances on the order of 50 cm. It should be noted that the laser absorption length at 100-mTorr fill pressure is $\gg$ 100 cm, thus if the beam was not refracted out of the plasma a laser burn pattern should be observed. In summary, initial experiments on the laser-plasma interaction indicate that the

classical laws of beam refraction govern the inter-
action process. Self-channeling of the beam in the
plasma column has not, as yet, been observed.

REFERENCES

1. K. F. McKenna, E. L. Zimmerman, and K. B. Freese,
   "Laser-Plasma Interaction in the Scyllac I-C
   Theta Pinch," Third Topical Conference on Pulsed
   High-Beta Plasmas, Culham, England, Sept. 9-12,
   1975.

2. E. M. Little, W. E. Quinn, and G. A. Sawyer,
   "Plasma End Losses and Heating in the Low Pres-
   sure Regime of a Theta Pinch," Phys. Fluids, 8,
   1168 (1965).

3. R. F. Gribble, W. E. Quinn, and R. E. Siemon,
   "Plasma Experiments With a Three-Meter θ Pinch,"
   Phys. Fluids, 14, 2042 (1971).

4. K. S. Thomas, H. W. Harris, F. C. Jahoda, G. A.
   Sawyer, and R. E. Siemon, "Plasma Experiments
   on the Linear Scyllac Theta Pinch," Phys. Flu-
   ids, 17, 1314 (1975).

5. J. P. Freidberg and H. Weitzner, "Endloss From
   A Linear θ-Pinch," Nucl. Fusion, 15, 217 (1975).

6. H. A. B. Bodin, T. S. Green, G. B. F. Niblett,
   N. J. Peacock, J. M. P. Quinn, and J. A.
   Reynolds, "The Influence of Trapped Field on
   the Characteristics of a Magnetically Compressed
   Plasma (Thetatron)," Nucl. Fusion 2, 521 (1961).

7. J. B. Taylor and J. A. Wesson, "End Losses from
   a Theta Pinch," Nucl. Fusion 5, 159 (1965).

8. J. A. Wesson, "Plasma Flow in a Theta-Pinch,"
   in Plasma Physics and Controlled Nuclear Fusion
   Research (Proc. 2nd Int. Conf. Culham, 1965) 1,
   223 IAEA, Vienna (1966).

9. T. M. York, K. F. McKenna, and C. J. Mickels,
   "Dynamic Pressure Transducer System for Pulsed
   Plasma Flow Diagnosis," Rev. Sci. Instr. 44,
   588 (1973).

10. T. M. York and E. K. Stover, "Transient Flow
    and Heating in a Pinched Plasma Column," Phys.
    Fluids, 18, 127 (1974).

11. K. F. McKenna and T. M. York, "Transient Flow
    and Expansion of a Pinch Discharge Plasma in
    Self-Induced Magnetic Fields," Plasma Physics
    17, 1 (1975).

12. R. E. Stapleton, K. B. Riepe, E. L. Jolly, Jr.,
    J. Weinbrecht, J. J. Hayden, E. O. Ferdinand,
    and T. A. Carrol, "Electron-Beam Controlled
    Lasers; Discussion from the Engineering View-
    point, Part I. Design of the 1-kJ and 10-kJ
    CO_2 Lasers, "Fifth Symposium on Engineering
    Problems of Fusion Research, Princeton Univer-
    sity, November 5-9, 1973.

13. K. F. McKenna, E. L. Zimmerman, W. T. Armstrong,
    S. E. Linzey, and K. B. Freese, Los Alamos
    Scientific Laboratory internal document, 1975.

VI. TOROIDAL REVERSED-FIELD PINCH

D. A. Baker, L. C. Burkhardt, J. N. Di Marco, A. Haberstich,
R. B. Howell, N. J. Karr, S. Ortolani, A. E. Schofield

A. SUMMARY

The containment of a plasma in a toroidal axisymmetric magnetic bottle is one of the promising approaches to the realization of a fusion reactor for energy production. Such systems fall into the following general categories (1) tokamaks, (2) belt pinches, (3) screw pinches, and (4) reversed-field pinches.

The reversed-field pinch differs basically from the other approaches in that it is designed to operate above the Kruskal-Shafranov limit and owes its predicted MHD stability to wall and shear stabilization of special plasma-field profiles. The grossly unstable modes are excluded by locating the bounding conductor so that these modes would require larger radial eigenfunctions than the minor radius of the device. The localized unstable modes are eliminated by using a strongly sheared magnetic field. These configurations are not restricted to small aspect ratios and can have equilibria in which MHD theory predicts stability for total beta values of up to ~ 40%.

The reversed-field pinch approach offers possible ways of raising the total beta, raising temperatures through fast compression and large ohmic heating, lowering the impurity content, reducing (and possibly make insignificant) the enhanced diffusion due to trapped-particle banana orbits, and associated instabilities.

Present critical objectives for the Los Alamos reversed-field Z-pinch program are to optimize the operating parameters and determine the scaling laws which govern heating, diffusion, and lifetime of the pinch.

The past year was spent obtaining temperature, diffusion rates, programming, and confinement time data on ZT-1. The ZT-1 device has a toroidal ceramic discharge tube (major diameter = 76 cm, minor diameter = 10 cm) and is energized from a capacitor bank making use of a magnetic core to induce the fast rising toroidal current. Reversed-field programming is accomplished by switching another capacitor bank onto the toroidal field coils at the desired time.

The following information has been obtained which will be needed to make the scaling comparisons with later larger bore experiments:

(1) The parametric dependence of ion temperature on gas filling pressure, toroidal current, current risetime, stabilizing magnetic field, and reversed-field programming.

(2) Thomson scattering measurements of electron temperature at various times and radial positions in the discharge.

(3) Measurements of field penetration and flux loss for various programming modes.

(4) Spectroscopic measurements of average electron temperatures and impurities.

(5) Energy balance and impurity levels.

The results of these investigations are summarized in the subsequent sub-sections.

The confinement time is limited by resistive effects in the plasma that cause a departure from initially favorable configurations with time. To study the effect of the scaling of confinement time and heating with minor diameter, ZT-1 has been modified to allow a larger bore tube (15 cm diam) and faster reversed-field risetimes. If favorable scaling results are obtained from this experiment (ZT-S), it is anticipated that the next generation experiment ZT-P will be constructed. This experiment will be energized by a capacitor network, which will allow a range of current risetimes and long sustained fields.

B. ION TEMPERATURE MEASUREMENTS

Ion temperatures in the ZT-1 diffuse toroidal pinch have been determined from impurity spectral line Doppler broadening measurements facilitated by the use of analog-to-digital convertors and an on-line computer. The experimental setup is shown in Fig. VI-1.

The variation of ion temperature with system parameters of gas filling pressure, toroidal current, current risetime, stabilizing toroidal magnetic field, and magnetic field reversal has been
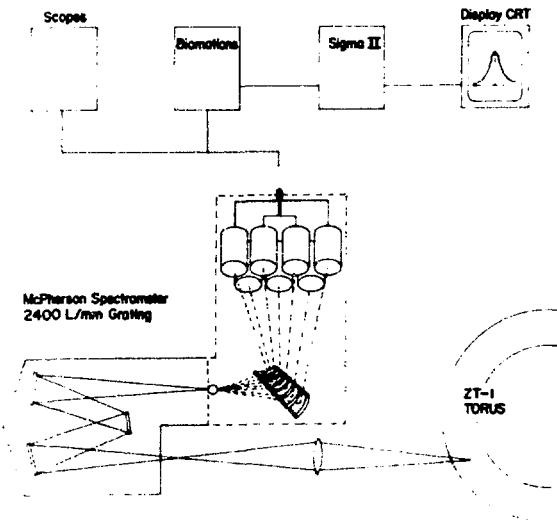
Fig. VI-1.

Block diagram of the polychromator, analog-to-digital converter, and on-line computer system used in the Doppler broadening measurements of plasma ion temperature.

Fig. VI-2.

Ion temperature vs toroidal plasma current for a gas filling pressure of 2.1 pascals (80% deuterium, 20% helium) $0 - B_{\phi o} = 0.06$ T, $\square - B_{\phi o} = 0.1$ T, $\Delta - B_{\phi o} = 0.15$ T. The top curve is a plot of $T_i + T_e$ for $B_{\phi o} = 0.6$ T obtained from magnetic field probe data using pressure balance and from density measurements obtained with a laser densitometer.

determined for operation in the five derate modes used with ZT-1. Results of the change of T_i with the more sensitive parameters--toroidal current, current risetime, and stabilizing magnetic field-- are shown in Figs. VI-2, VI-3, and VI-4. The values of T_i shown in these figures are a time average over the interval from ~ 2.5 μs, at the completion of the implosion, to ~ 5 μs. This upper time limit was selected since the measurements were not all made under optimum stability conditions, and in some discharges evidences of instability were observed at ~ 6 to ~ 7 μs.

The results in Fig. VI-2 show a linear rise of T_i with the toroidal current, I_ϕ, over the range from 30 to ~ 120 kA. However, extrapolation to the earlier fuse mode results at ~ 200 kA indicates a nonlinear, more rapid rise in the interval between ~ 100 to ~ 200 kA. T_i is found to decrease, as expected, with increasing toroidal stabilizing magnetic field as shown in the family of curves in Fig. VI-2. The upper trace (dashed line) in Fig. VI-2 shows results for $T_e + T_i$ obtained from pressure balance calculations using magnetic field probe measurements.

Figure VI-3 shows the variation of T_i with the

initial rate of rise of toroidal current for constant toroidal current and stabilizing toroidal magnetic field. It is apparent that both the magnitude and rate of rise of the toroidal current are important in obtaining higher T_i values.
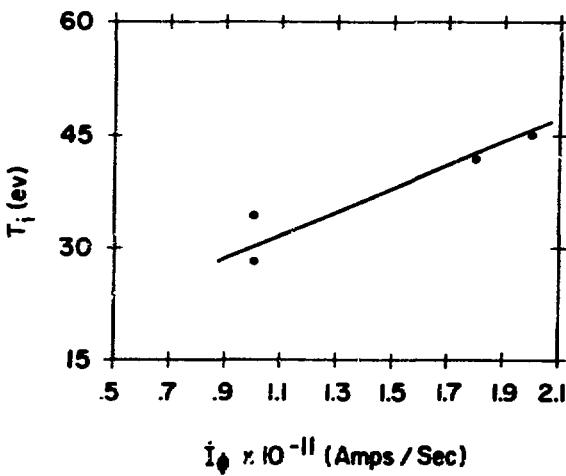
Fig. VI-3.

Ion temperatures vs initial rate of rise of toroidal current for $p_o = 2.1$ pa, $B_{\phi o} = 0.15$ T, and $I_\phi = 75$ kA.

Figure VI-4 shows the rise in T_i with increasing values of the initial rate of rise of current for constant values of the "compression" parameter θ_0 (where $\theta_0 = B_{poloidal}(r_{wall}, t)/B_{toroidal}(t=0)$). T_i rises linearly with $\dot{I}_\phi$ at constant θ_0. Extrapolation to the higher values of $\dot{I}_\phi$ obtained in the earlier fuse mode experiments ($\dot{I}_\phi \sim 2 \times 10^{12}$ A/s) indicates a linear rise over the whole range of $\dot{I}_\phi$ from $\sim 3 \times 10^{10}$ to 2×10^{12} A/s for constant θ_0.

Experimental tests of several possible sources of error in the T_i measurements have been made including instrumental error, normal Stark effect, anomalous Stark effect, and dependence of the apparent ion temperature on the mass and ionization state of the impurity ion used in the Doppler broadening measurements. These corrections have been made in the results shown in Figs. VI-2, VI-3, and VI-4.

C. ELECTRON TEMPERATURE MEASUREMENTS

1. Local Temperature from Thomson Scattering.
The electron temperature in ZT-1 has previously been measured by means of Thomson scattering at a fixed radial position of 1 cm.[1] The diagnostic has now been modified to measure the electron temperature as function of radius.

The scattered laser light is collected by a set of two 100-mm FL lenses with an 8.5-mm-diam
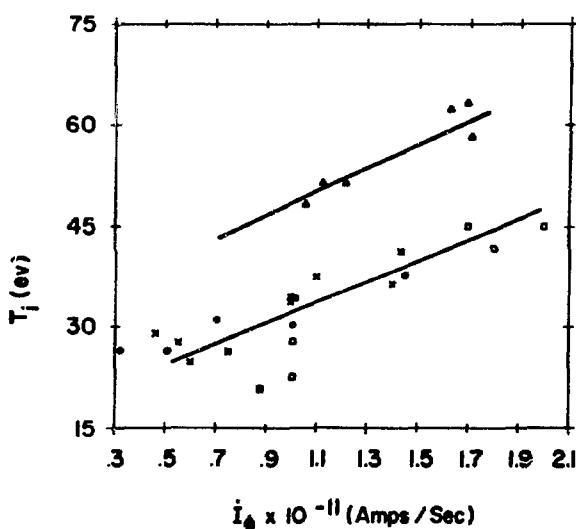
Fig. VI-4.

Ion temperature vs initial rate of current rise for constant values of the "pinch ratio" parameter $\theta_0 = B_{p(wall)}/B_{\phi 0}$, $\Delta - \theta_0 = 4.0$, $X - \theta_0 = 3.2$, $o - \theta = 2.6$, $\square - \theta_0 = 2.0$.

aperture mounted on a movable platform. The plasma scattering volume is approximately 1.5 mm in diameter and 5 mm long. The light is transmitted to a 7-channel polychromator by means of a 2.5-m-long flexible light guide. The exit of the light guide, 22 mm high and 0.36 mm wide, acts as entrance slit to the polychromator. A straight entrance slit would normally result in a curved image at the exit slit. To counteract this effect, the entrance slit is curved with a radius of 120 mm. The instrumental scattering is nearly independent of radius over the range of 1 to 4 cm. It is equivalent in magnitude to Rayleigh scattering by 6650 Pa of nitrogen.

Electron temperatures have been measured in the derated mode 4 of operation at radii of 1, 2, and 3 cm with unmatched risetimes of the poloidal and toroidal magnetic fields, and at radii of 2, 3, and 4 cm with matched risetimes. The filling gas was 80% D_2 + 20% He and the filling pressure was 5.3 Pa with unmatched risetimes and 4.3 Pa with matched conditions. The 694.3-nm wavelength of the scattered spectrum was centered on channel 3 of the polychromator, with a channel separation of 1.76 nm. Due to alignment problems, 10 to 15% of the instrumental light was also present in the adjacent channels 2 and 4. The fact that the amplitude of this unwanted signal varied from shot to shot made it necessary to determine the electron temperature mainly on the basis of channels 1, 5, and 6.

The results of the Thomson scattering measurement are shown in Fig. VI-5. Because of the alignment difficulty, the error bars are rather large. The unmatched mode results can be compared with the earlier measurement at 1-cm radius,[1] which indicated a rapid temperature increase from less than 5 eV to more than 20 eV at 3 μs. Such an increase is seen at 2-cm radius but does not occur at 1 cm during the first 4 μs of the discharge. The discharge parameters in the earlier measurement were somewhat different. The filling pressure was 20 mTorr and the initial rate of rise of the poloidal field was faster by a factor of 2.

The arrows on top of the figure indicate the observed time of onset of an MHD instability. Note that the instability follows the increase in temperature within 1 μs or so. This effect can be observed also in the earlier data. It will be essential in the future to determine how the two
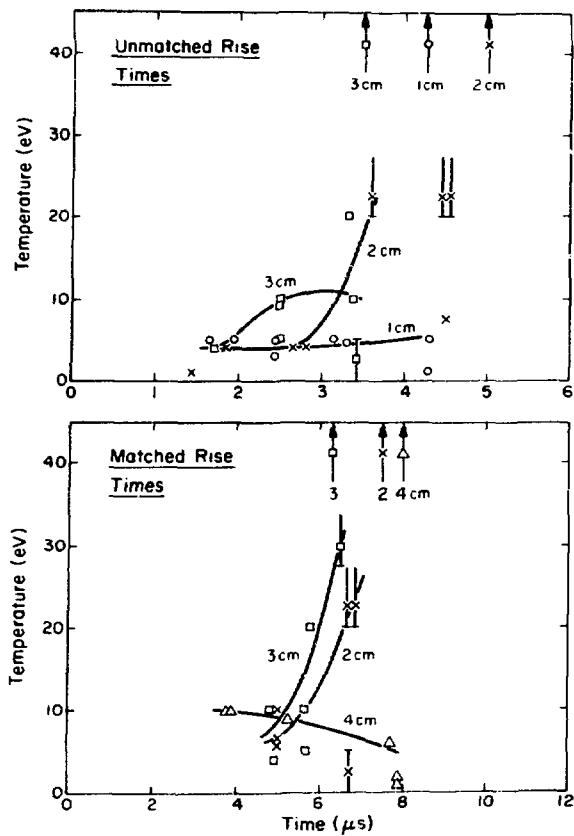
Fig. VI-5.

Measured electron temperatures as functions of time and radius with unmatched and matched discharge conditions. The arrows indicate the observed time of onset of an instability.

events are related. It is worth mentioning also that many of the measurements exhibit a rather large signal in channel 7, making it sometimes impossible to fit a simple maxwellian to the data. The presence of a hot component in the electron distribution function would help explain the observed discrepancy between electron and ion temperatures.

2. *Average Temperature from Impurity Line Intensities.* A spatial average of the electron temperature has been determined from the line intensity ratios of CIV 465.8 nm to CIII 464.7 nm, making use of Eq. 13-6 of Ref. 2. For the electron densities in ZT-1, the upper level of the CIV line is assumed to be in local thermodynamic equilibrium with respect to the CV ions, but the population of the upper level of CIII lies below the Boltzmann level.

In the modes of operation used for the

parameter studies, the average electron temperature $<T_e>$ obtained has been found to be relatively insensitive to the preionization voltage and to the 80% D_2 + 20% He filling pressure. For example, with a toroidal current I_ϕ of 75 kA, and a toroidal bias magnetic field $B_{\phi 0}$ of 0.15 T, $<T_e>$ was obtained for two different filling pressures. At 2.27 Pa, $<T_e>$ was 11.2 eV at 4 μs into the discharge, whereas at 4 Pa, $<T_e>$ was 10.5 eV at 4 μs.

For the conditions I_ϕ = 105 kA, $B_{\phi 0}$ = 0.19 T, and a filling pressure of 4 Pa, $<T_e>$ was 10.4 without preionization. At 4 kV preionization voltage $<T_e>$ was 9.2 eV. The lower temperature at 4 kV may be due to an increase in impurity level from 0.1% without preionization to 1% with preionization.

3. *Average Temperature from Time-Dependent Ionization States.* Estimates of the electron temperature of the pinched plasma have also been made from observations of the time dependence of ionization states of impurity ions. CII, CIII, and CIV lines were detected during the main discharge. With added oxygen impurities, only OII and OIII were detected in spite of a search for several OIV lines. The absence of OIV places an upper bound on $<T_e>$. The experimental discharge conditions during the measurements with oxygen impurities were I_ϕ = 100 kA, $B_{\phi 0}$ = 0.14 T, initial 80% D_2 + 20% He filling pressure of 4 Pa, and average electron density of 8.6 x 10²¹ m⁻³. The obtained electron temperatures varied between 6 and 10 eV.

D. ENERGY BALANCE MEASUREMENTS

Energy balance for the ZT-1 pinch is determined by comparing the energy input obtained from current and voltage measurements with the energy content obtained from magnetic field probe measurements. The difference between the energy input and content represents an energy loss presumed to be due to radiation loss and kinetic energy transport to the walls. However, the plasma energy is determined from pressure balance assuming, as a constant of integration, zero pressure at the minimum of the pressure-versus-radius plot--usually at or near the tube wall. Since the minimum may not be zero, the plasma energy is undetermined within an additive term. Therefore, the energy balance plot presents a lower limit for the plasma energy and an upper limit for the energy loss.

Figure VI-6 shows a typical energy balance plot. The energy loss rate in this figure from ~ 2 μs at the completion of the implosion stage to ~ 7 μs is approximately 75 joules per meter length of the plasma column per microsecond. It is important in the understanding of the energy containment capabilities of the stabilized pinch device to determine the cause of this loss.

E. IMPURITY RADIATION LOSSES

1. Theoretical Model. The energy loss by impurity line radiation has been studied using simple models.[3] In the limit of the corona model the radiated power loss due to the resonance line of an ion is given by[4]

$$P_J = n_e n_{imp} \frac{n_J}{n_{imp}} \frac{5.44 \times 10^{-16} f_J}{T^{1/2}}$$

$$\exp\left(\frac{-1.16 \times 10^4 E_J}{T}\right) erg \ cm^{-3} \ sec^{-1}.$$

ENERGY INPUT vs ENERGY CONTENT ZT-I SHOT #10115

—○— ENERGY INPUT = $\int I_z V_z \, dt + \int I_\theta V_\theta \, dt$

—X— PLASMA + MAGNETIC ENERGY CONTENT

—●— MAGNETIC ENERGY CONTENT
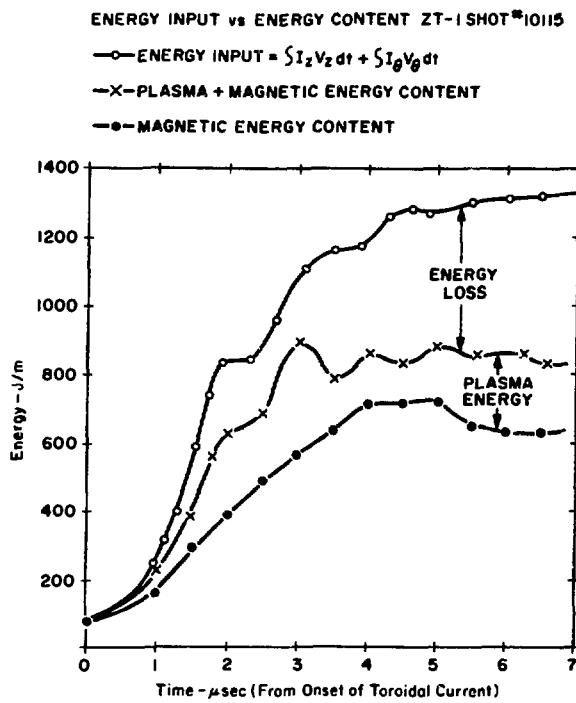
Fig. VI-6.

Energy balance vs time for ZT-1 shot #10115. Energy input is determined from current and voltage measurements at the torus feedpoints. Magnetic energy and plasma energy are determined from magnetic field probe measurements.

In the equation, n_e is the electron density (cm^{-3}), n_{imp} is the impurity density (cm^{-3}), n_J/n_{imp} is the fractional abundance of a particle ion, f_J and $E_J(eV)$ are the oscillator strength and the excitation potential of the resonance line and T is the electron temperature (K). The sum over the different ions present gives the total radiation.

Using this radiation formula, the power lost with a steady state corona model was computed versus electron temperature for impurities of carbon, nitrogen, and oxygen. From this the fraction of the plasma energy radiated per unit time was found. To further assess the importance of impurity radiation, the power radiated was compared with classical ohmic heating. Even in this crude estimate, impurity radiation was found to be capable of severely limiting the electron temperature at impurity concentrations of 1%, electron densities of 10^{16} cm^{-3}, and current densities typical of ZT-1.

The set of equations describing the rate of change of population in the various ionization levels was solved. When the power radiated as a function of time was found, it was usually much larger than the corresponding steady state value.

2. Application to ZT-1 Results. Spectral analysis of the radiation from ZT-1 shows that the impurities present are mostly carbon and oxygen. The quantity of these impurities was determined roughly by observing the change in the amplitude of a spectral line of the impurity with addition of known amounts to the discharge. Extrapolation to zero added impurity gives ~ 0.5% 0 and ~ 0.5% C with an estimated accuracy of a factor of 2. The amount of impurity increases with the amplitude of the preionization current and the diameter of the compressed pinch.

Figure VI-7(a) shows the computed radiated power loss for ZT-1 with an assumed 1% oxygen impurity and the discharge conditions of shot 10115 for which the energy balance calculation was made above. The radiation loss was calculated using the corona model discussed above. However, the losses have been increased by a factor ~ 5 in Fig. VI-7(a) with the use of a value of 1 instead of 0.2 for the Gaunt factor following the revisions described in Newsletter, Atomic Data for CTR, July 1975. An additional factor of ~ 2 should be inserted to include radiation from other lines in addition to the
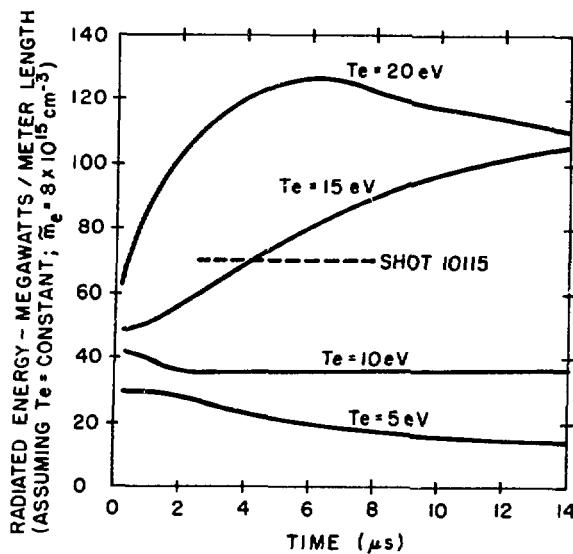
Fig. VI-7(a).

*Theoretical radiation loss ratio calculated for se-
lected electron temperatures and an electron densi-
ty of 8×10^{15} cm^{-3}. The experimental mean energy
loss rate for shot 10115 (see Fig. VI-5) is shown
as a dashed line.*

resonance lines used in the computer calculation
(private communication, H. R. Griem). This addi-
tional factor of 2 has not been included in the
results shown here.

The dashed line in Fig. VI-7(a) shows the mean
rate of energy loss for shot 10115 of $\sim$ 70 J/μs per
meter length described in the previous section.
Preliminary measurements of the electron tempera-
ture radial distribution for 10115 and discharges
under similar operating conditions give T_e from $\sim$ 10
to 20 eV during the time interval the energy losses
were measured. The predicted radiation loss rates
are comparable with the measured loss rate and could
well be a major factor in causing the power loss.

Because of the uncertainties in the ionization
and excitation cross sections of the several ioniza-
tion states of the impurities, the theoretical pre-
dictions of the radiation losses have only order of
magnitude accuracy. Experimental measurements of
the radiation loss will be necessary to determine
how important this effect is in the pinch behavior.

Reduction in the radiation losses can be at-
tained by decreasing the impurity content in the
discharge and by raising the electron temperature
above the radiation barrier. As shown in Fig.

VI-7(b), raising the electron temperature $\geq$ 100 eV
causes penetration of the "radiation barrier" and
rapid reduction of the radiation loss from the C and
O impurities.

Figure VI-8 shows the results of computer cal-
culations of the time-dependent electron temperature
as a function of selected fixed values of electron
density and current density for a fractional oxygen
impurity density of 0.01 after 10 μs. The computer
program (written by Sergio Ortolani) uses the simple
model of Ohmic heating of the electron with classical
(Spitzer) resistivity and cooling by radiation. The
radiation loss is increased by a factor of $\sim$ 5 above
the values given by McWhirter with the use of the
more recent experimental factors mentioned above.
The latest operation of ZT-1 in the derated modes
employs $j \leq 3000$ A/cm^2 and compressed electron den-
sities of $\sim$ 4 $\times$ 10^{15} to 8 $\times$ 10^{15} cm^{-3}. The theoret-
ical curves in Fig. VI-8 predict low T_e($<$ 20 eV) for
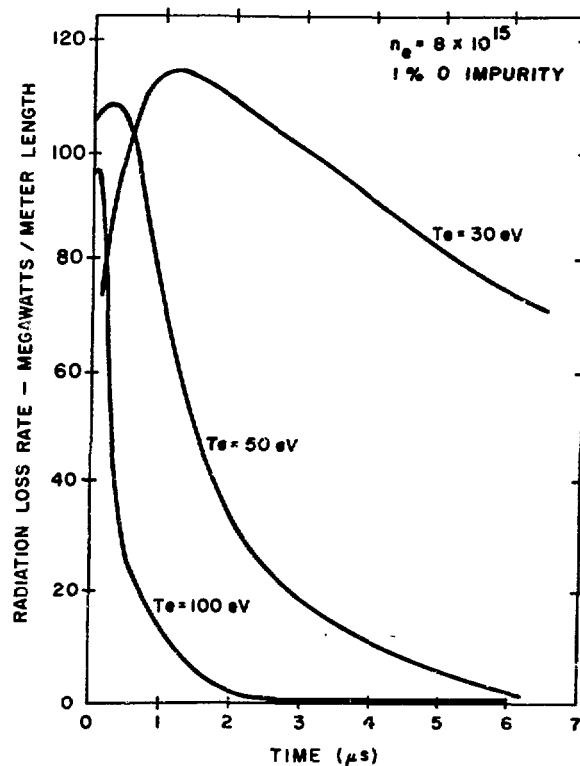
Fig. VI-7(b).

*Theoretical rates of radiation loss at higher elec-
tron temperatures. The first part of the "radia-
tion barrier" from low-Z impurities such as C and O
is penetrated for $T_e \sim$ 100 eV.*
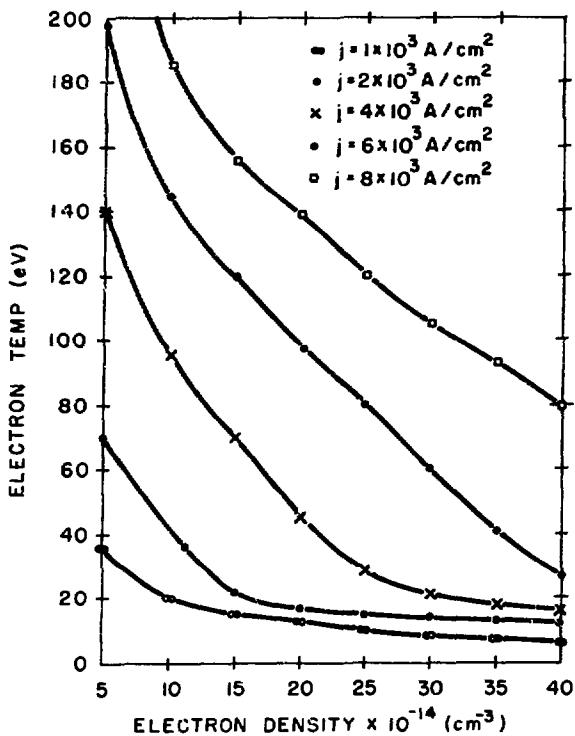
Fig. VI-8.

Theoretical time-dependent electron temperature vs plasma electron density for the simple model of ohmic heating (Spitzer resistivity) competing with radiation energy loss from an assumed 0.01 fractional oxygen impurity. Plots show predicted values of T_e after 10 μs heating at the indicated current densities.

Fig. VI-9(a).

Theoretical electron temperature at 2 μs for a constant current density of 4000 A/cm^2 as a function of electron density and impurity content.

these values of j and n_e. Lower n_e and higher j will give much higher T_e in this simple model as shown in Fig. VI-8. The latest experiments on ZT-1 were concentrated on stability control and the higher particle density and lower current densities facilitate these studies. The effect of higher current densities and lower particle densities on T_e are to be explored in future ZT-S and ZT-P experiments.

Figures VI-9(a) and VI-9(b) are plots of the theoretical values of T_e obtained after 2 μs and 10 μs with j = 4000 A/cm^2 and 0, 0.001, 0.002, 0.005, 0.01 fractional oxygen impurity over a range of particle densities from 1 x 10^{15} to 8 x 10^{15} cm^{-3}. These time points are in the range of interest in setting up the stabilized Z pinch. The importance of current density, particle density, and impurity radiation loss in determining T_e in the Ohmic heating model is apparent.

F. FORMATION AND STABILITY OF REVERSED-FIELD PROFILES

1. *Introduction.* This section will present the programming results of ZT-1 with the matched mode of operation and compare them with some of the previous results with the unmatched mode. Detailed results with the unmatched mode are described in a previous paper.[5]

In the "matched mode" of operation the initial toroidal field and the peak poloidal field have approximately the same amplitude, and both the poloidal and the reversing toroidal fields have approximately the same rate of change. The unmatched mode is obtained with the initial toroidal field less than the peak poloidal field, and the rate of change of the poloidal field larger than that of the toroidal field. An example of the field programming is given in Fig. VI-10.

The motivations to operate the experiment in the matched mode are as follows:

a) If the rate of change of two field components is approximately the same, a much more efficient penetration of the reversed B_z is expected as compared to the case where the B_z is slower and field programming is effective only in the very

69
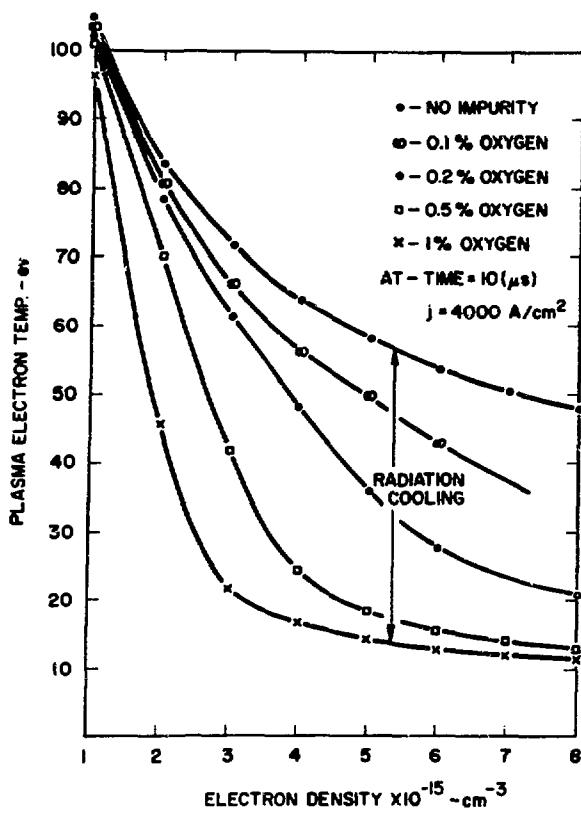
Fig. VI-9(b).

Theoretical electron temperature at 10 µs.

outer region of the discharge. The necessity to balance the two rates was recognized previously.[5]

b) Experimental evidence from ETA-BETA[6] (where the two fields have ~ 1-µs risetime) shows the following important features: formation of thin current sheets, very hollow pressure profiles, good control over the initial plasma-wall interaction, and small diffusion during the setting up phase. Diffusion during the setting up phase is a systematic problem of ZT-1 in the previous "unmatched mode" of operation. These differences in the behavior of the two experiments motivated the attempt to operate in the matched mode of programming on ZT-1.

To accomplish this match with ZT-1 requires the I_z bank to be operated at as low a voltage as possible and the toroidal field-reversing bank at its maximum design voltage. The maximum rate of change of the toroidal magnetic field is ~ 2 x 10^5 T/s (with plasma and 40 kV on the coil). At the lowest voltage at which the I_z bank will fire reliably, a

rate of change of I_z of ~ 2 x 10^{10} A/s is obtained. This is equivalent to a rate of change of the poloidal field at the wall of the discharge tube of ~ 10^5 T/s. Experimental conditions are then (see Fig. VI-10): starting with a bias field of about 0.2 T the toroidal current rises to ~ 60 kA and the toroidal field reverses to ~ - 0.1 T in ~ 3 µs.

2. *Toroidal and Poloidal Field Diffusion.* A comparison between the matched and unmatched modes of operation can be obtained through the radial dependence of the toroidal and poloidal magnetic fields. From these data the following is calculated: (1) the toroidal and poloidal current densities, (2) the plasma pressure, (3) the pitch of the magnetic field on axis, and (4) the total and trapped toroidal flux in the pinch. Here, trapped flux is taken to mean the integral from the axis to the radius at which the toroidal field is zero. In Figs. VI-11 and VI-12 the toroidal and poloidal magnetic fields and pressures are plotted vs radius for a few specified times for the unmatched and matched modes, respectively. In the unmatched mode relevant
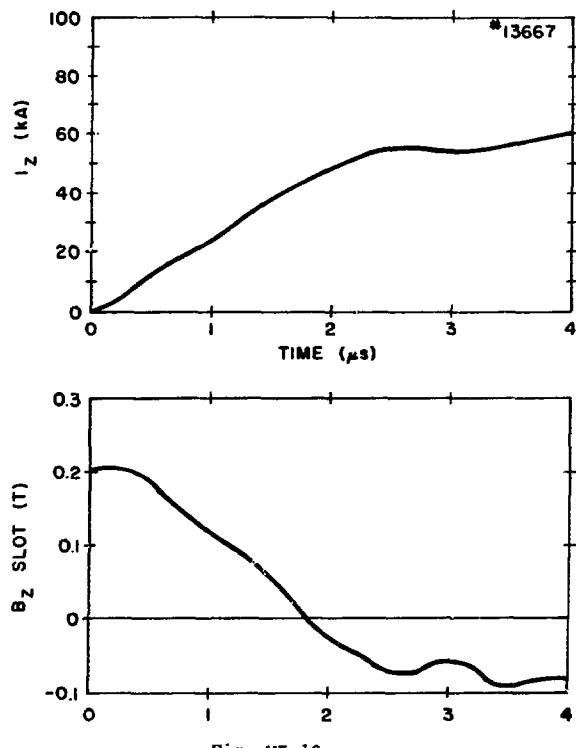
Fig. VI-10.

Time programming of the toroidal current and field in the matched mode.
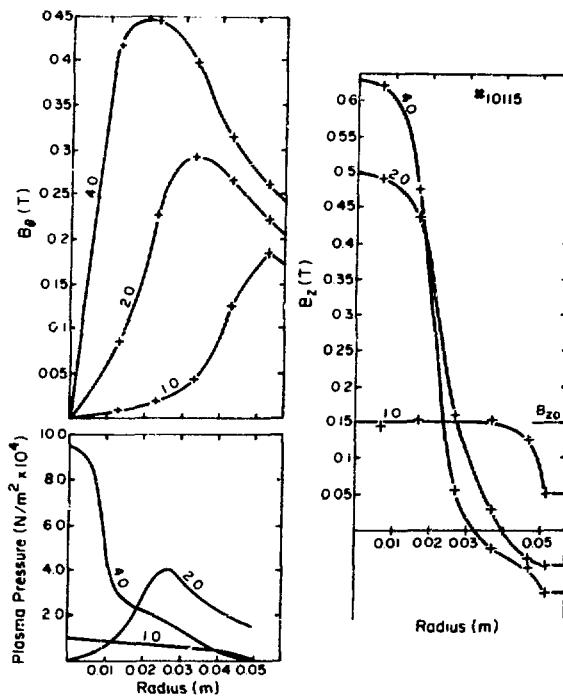
Fig. VI-11.

Poloidal (B_θ) and Toroidal (B_z) magnetic fields and equilibrium plasma pressure profiles at various times (μs) for the unmatched mode of operation.

Fig. VI-12.

Poloidal (B_θ) and Toroidal (B_z) magnetic fields and equilibrium plasma pressure profiles at various times (μs) for the matched mode of operation.

field diffusion takes place during the setting up phase, the Z-current density diffuses early to the axis, and the pressure profile tends to peak on axis. On the other hand, in the matched mode of operation, thinner j_z and j_θ current sheets, which localize approximately at the same radial position, are obtained together with very hollow pressure profiles. The Z-current density peaks well off axis. An attempt was made to clearly distinguish between diffusion and plasma motion. First, the radii at which the j_z and j_θ current densities peak (r_{jz} and $r_{j\theta}$) and the radius which contains 50% of the total plasma pressure (r_p) were considered and their motion in time followed. Figures VI-13 and VI-14 show the dynamics of these three radii for two discharges: #10103 (unmatched mode); #13668 (matched mode). It is seen that, in the unmatched mode, the Z-current density very quickly peaks on axis, slipping across the plasma and the other current component; whereas, in the matched mode, the three radii show approximately the same dynamics (note the different time units in the different diagrams).
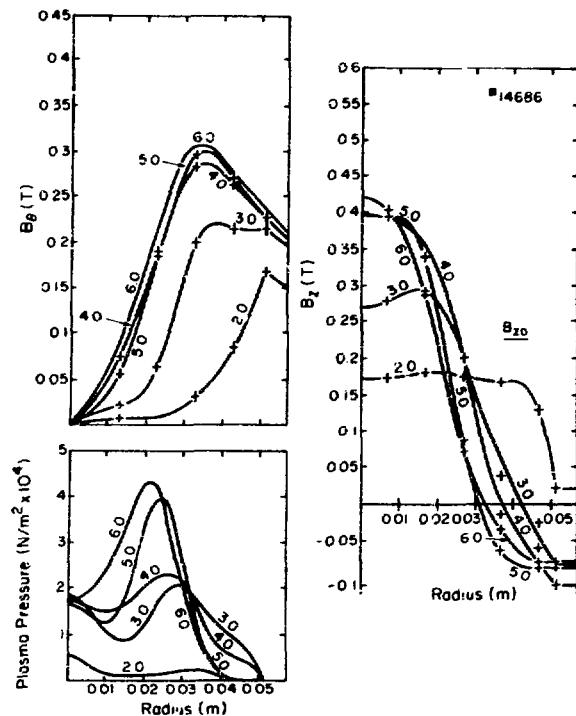
Additional evidence for a reduced diffusion rate with the matched mode is obtained from the magnetic field pitch on axis vs time. Figure VI-15 shows a comparison between matched and unmatched modes by plotting 1/P vs time. A smaller value for 1/P indicates a reduction in the toroidal current density at the axis. Referring back to the pressure shown in Figs. VI-11 and VI-12, it can be seen that for both cases a pinch is formed well away from the wall. However, in the matched mode the pressure is peaked at approximately one-half the radius. This information, as well as the reduced rate of change of the pitch with time, indicates that the lower values of 1/P are obtained through a reduced diffusion and are not due to just the difference in initial conditions, i.e., a higher initial bias field.

3. Toroidal Flux Loss. When considering the loss of toroidal flux it is convenient to consider three time intervals. The first, or the initial phase, occurs between the start of the toroidal current and the time when the toroidal field at the

71
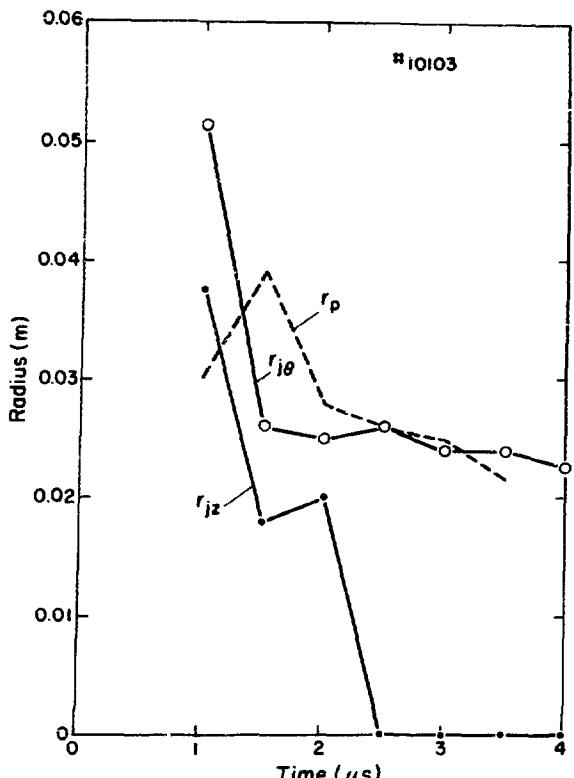
Fig. VI-13.

Dynamics of the toroidal (r_{Jz}) and poloidal ($r_{J\theta}$) current sheets and of the plasma (r_p) for the unmatched mode: r_{Jz} and $r_{J\theta}$ are the radii at which the current densities peak; r_p is the radius containing 50% of the total plasma pressure.

Fig. VI-14.

Dynamics of the toroidal (r_{Jz}) and poloidal ($r_{J\theta}$) current sheets and of the plasma (r_p) for the matched mode: r_{Jz} and $r_{J\theta}$ are the radii at which the current densities peak; r_p is the radius containing 50% of the total plasma pressure.

wall of the ceramic falls to zero, $(B_z(r_w) = 0)$. The second, or the intermediate phase, now starts. It ends when the crowbar is applied to the toroidal field. This phase can be considered to be the start of the trapped-flux phase. The toroidal flux is now "trapped" in the plasma and loss only can take place due to plasma resistance. The third, or the confinement phase, starts when the crowbar is applied and continues until the pinch goes unstable.

During the initial phase the toroidal flux loss with the unmatched mode could be controlled by delaying the application of the voltage that caused the toroidal field to reverse. Figure VI-16 shows the flux loss of 0.2 mWb ($\sim$ 15%) that occurs with early application of the reversing voltage. On the other hand, Fig. VI-17 shows the flux is maintained or even increased by delaying the application of the reversing voltage. The toroidal flux for two shots

with the matched mode is shown in Fig. VI-18 (a and b). In this mode delaying the reversal does not affect the large flux loss of $\sim$ 0.6 mWb during the initial phase.

During the intermediate phase trapped flux is always lost when in the unmatched mode of operation. However, in the matched mode there are some shots where the flux loss is less during this phase.

During the third phase the rapid loss of trapped flux seen in the unmatched mode slows down or even has a positive slope at the time the crowbar is applied to the coil. With the matched mode no additional effect is noted on those shots that preserved the trapped flux during the second phase while the other shots behaved as the unmatched mode.
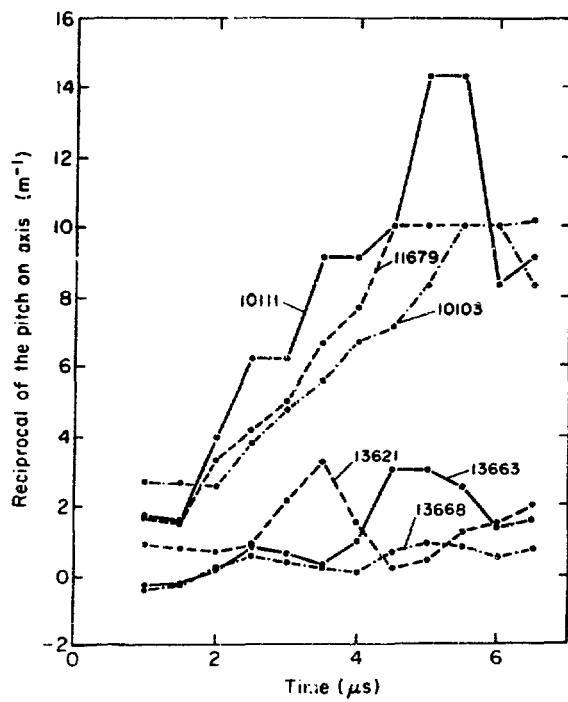
Fig. VI-15.

Reciprocal of the pitch on axis as a function of time: 10103, 10111, 11679 (unmatched mode); 13621, 13663, 13668 (matched mode).

One of the diagnostics used to attempt to understand the flux loss was a measurement of the Poynting vector. One of the important questions was whether the loss of flux could be reduced by maintaining the total Poynting vector always inwards. In the unmatched mode $E_z > E_\theta$, therefore, a slight delay in applying the reversal, to allow for the build up of some B_θ, virtually assures that the total Poynting vector is always inwards. As shown in Fig. VI-17 a delay does indeed eliminate the initial flux loss. The loss during the intermediate phase could then be caused by flux annihilation between the interior "trapped" field and the reversed field due to resistive diffusion. However, it remains to be answered why there is a reduction in the positive flux loss rate at the time the external crowbar is applied to the toroidal circuit. Moreover, the data in Fig. VI-16, obtained without a delay in the application of the reversal voltage, shows a reversal of the total Poynting vector for only the first ~ 0.2 μs (see Fig. VI-19), while
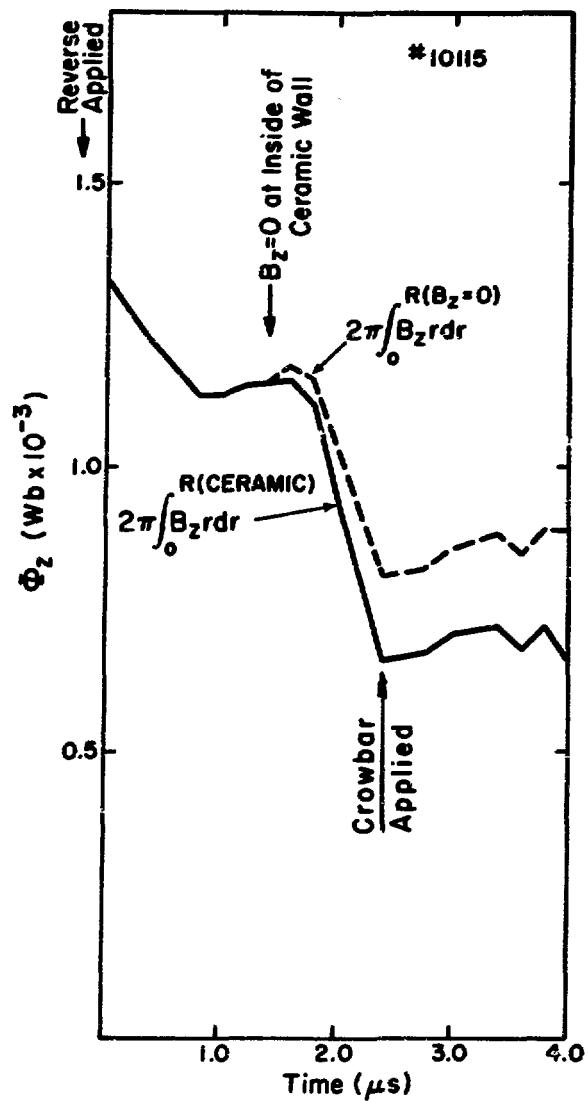
Fig. VI-16.

Toroidal flux as a function of time: the solid line is for the flux integrated out to the ceramic wall (0.0515 m); the dashed line is for the flux integrated out to the point where B_z reverses. The sharp inflection at 2.2 μs occurs when the crowbar is applied.

during the initial phase the flux is lost over a time interval of ~ 1 μs.

With the matched mode a substantial reversal in the Poynting vector is observed in the initial phase as shown in Fig. VI-20. There is also a large loss of the toroidal flux. The application of the reversal voltage to the B_z circuit can substantially

73
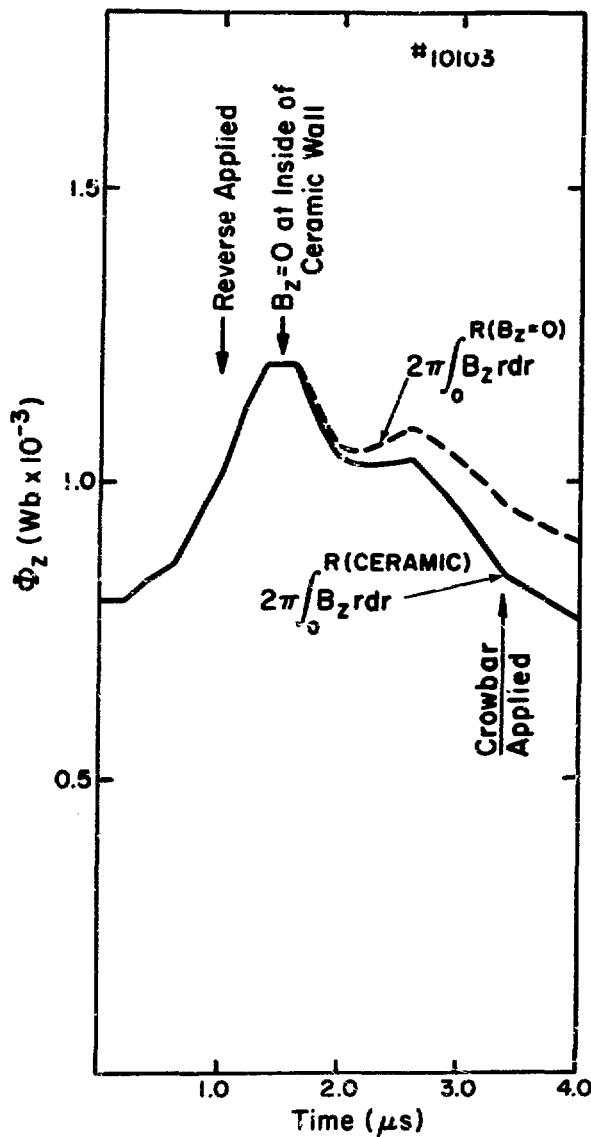
Fig. VI-17.

Toroidal flux as a function of time: the solid line is for the flux integrated out to the ceramic wall (0.0515 m); the dashed line is for the flux integrated out to the point where B_z reverses.

Fig. VI-18(a).

Toroidal flux as a function of time for two shots in the matched mode: the flux is that within the metal wall (0.057 m) until the B_z reverses, then it is the flux integrated out to the point where B_z reverses (trapped flux). The #1 indicates where the reverse is applied, #2 where B_z $(r_w = 0)$, and #3 where the crowbar is applied.

reverse the total Poynting vector and even reverse the energy flow of the B_θ circuit. This coupling must arise from the plasma dynamics.

During the intermediate phase the Poynting vector is always inward, and in some cases the trapped flux is maintained in the pinch. There is some indication that with these shots the total current density is higher, increasing the local heating

rate. If a higher electron temperature resulted, an improved trapping of toroidal field would occur.

So far, no direct correlation between reversal of the Poynting vector and the loss of the trapped flux has been observed.

4. MHD Stability. Magnetic field profiles measured under matched discharge conditions have been analyzed for MHD stability, following the method used in earlier reports.[7] The results indicate much fewer unstable m = 1 modes during the formation of the discharges than under unmatched conditions. At later times, instabilities develop at the edge of the plasma column, that is in the region of steepest negative pressure gradient. The radial position of these instabilities regions changes only slightly in time, and the value of the pitch on axis remains large for at least 6 μs (Fig. VI-15).

Calculated growth times are compared in Fig. VI-21(a) against those of an unmatched discharge with delayed reversal. The improved stability during the setting up phase is confirmed, but the two
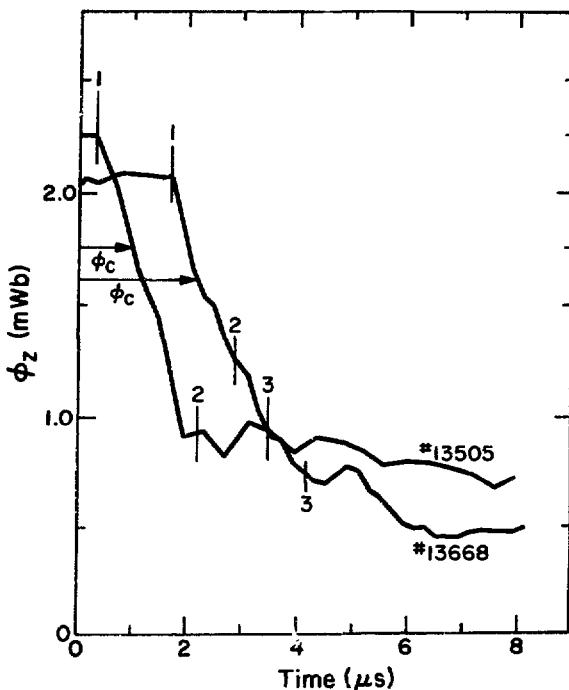
Fig. VI-18(b).

Toroidal flux as a function of time for two shots in the matched mode: the flux is that within the metal wall (0.057 m) until the B_z reverses, then it is the flux integrated out to the point where B_z reverses (trapped flux).

Fig. VI-19.

Radial components of the Poynting vector as a function of time: positive corresponds to energy flowing in; negative to energy flowing out.

growth times are seen to become comparable after about 4 μs. The poloidal betas for the two cases are plotted in Fig. VI-21(b). Following the implosion, the matched condition results in a poloidal beta of 0.3 in contrast with the value of 0.5 of the unmatched condition. At 3 to 4 μs, the poloidal beta of the matched discharge begins to rise and eventually reaches the same value as that of the unmatched case.

Figure VI-22 shows a plot of the predicted growth time as function of pressure gradient in the unstable region for an unmatched case with delayed reversal and for three matched cases. The rapid decrease in the growth time is seen to coincide with a steepening of the pressure profile in all four cases. Also shown in the figure, for comparison, are pressure gradients obtained from theoretical reversed-field pinch profiles with poloidal betas varying between 0.19 and 0.58.[8] The figure suggests that, under the present mode of operation, the maximum pressure gradient in the experiment should be

kept below 1.5 to 2 MPa/m for stability.

5. *Post-Implosion Simulation.* The reason for the steepening of the pressure gradient has been investigated by means of our one-dimensional time-dependent MHD code. This code solves the equations of conservation of particles, momentum, and energy for the ions and electrons in cylindrical coordinates.[9] Full ionization and charge neutrality are assumed. The transport coefficients are the electrical resistivity tensor, the ion and electron heat conductivities transverse to the magnetic field and there is an exchange of energy by collisions between the ions and electrons.

The essence of these calculations was to simulate the changes taking place in the magnetic field profiles during the post-implosion period from a time when the stability analysis predicts relatively good MHD stability to a later time when the field profiles are predicted to be clearly unstable. The goal was to see whether the changes in the magnetic
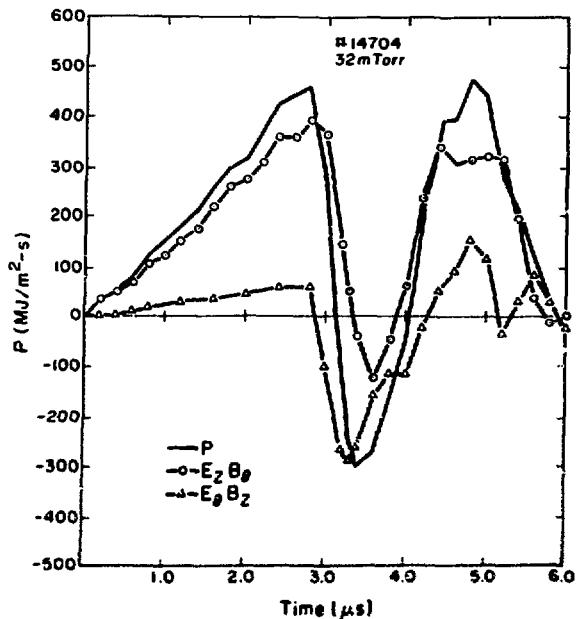
Fig. VI-20.

Radial components of the Poynting vector as a function of time: positive corresponds to energy flowing in; negative to energy flowing out.

Fig. VI-21.

Comparison of (a) calculated m = 1 growth times and (b) poloidal betas as functions of time for a matched pinch (solid line) and an unmatched reversed-field pinch (dashed line).

fields, and therefore in the pressure profiles, could be explained in terms of elementary MHD processes such as field diffusion and plasma motion.

The main unknowns in the calculation are the actual values of the transport coefficients, which are sometimes chosen to be much larger than classical, and the energy losses, such as impurity radiation, for example. Another unknown at this time is whether part of the ohmic heating energy associated with field diffusion goes to ion rather than electron heating. In spite of these shortcomings, valuable information can be obtained from the MHD code. Given the freedom to choose the values of the local resistivity and magnitude of the energy loss, one asks whether the fluid model can explain the behavior of the magnetic field profiles. If so, one can then compare the calculated temperatures and density with the measurements and then relate the assumed values of the transport coefficients with the local plasma parameters.

The present results have been obtained by assuming classical ion heat transport and ion-electron equipartition time. The parallel and transverse resistivities were determined by trial and error and

the electron heat conductivity was enhanced over the classical value in the same proportion as the transverse resistivity. There were no additional heat losses by radiation. If heat losses by impurity radiation should turn out to be important in the experiment, they can be accounted for by a corresponding reduction of the ion and electron heat transports to the wall.

The resistivities predicted by the time dependent computations are shown schematically in Fig. VI-23. Within the range of validity of the hydromagnetic model, the values shown are probably correct within a factor of two. The plasma resistivities are seen to be much lower near the axis than in the lower density outer region of the pinches.
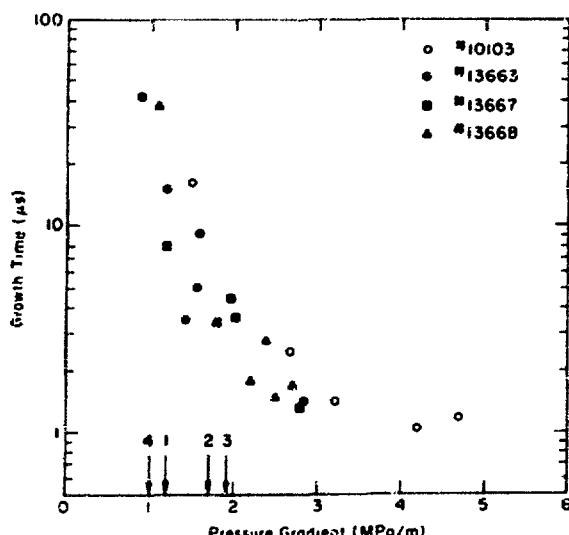
Fig. VI-22.

Plot of calculated m = 1 growth times as functions of the plasma pressure gradient in the unstable region of an unmatched pinch with delayed reversal (open circles) and of three matched pinches (solid circles, squares, and triangles). The arrows show the maximum pressure gradients of four theoretical reversed-field-pinch configurations.

The parallel resistivity is somewhat higher and the perpendicular component lower in the matched mode than in the unmatched case during this post-implosion period.

The shapes of the resistivity profiles suggest that the higher values of resistivities might be due to some sort of microinstability dependent on the electron drift velocity. The lower hybrid drift mode has recently been proposed as a possible candidate,[10] and a preliminary calculation of the transverse resistivity profile during the post implosion phase of an unmatched discharge shows a radial dependence similar to that of Fig. VI-23, although the resistivities are higher by a factor of approximately 10.[11] These are early calculations based on an estimate of the maximum level of turbulence to be expected from this mode, and more detailed calculations will follow.

An alternate explanation for the high rate of field diffusion is that the computed resistivities might be classical and that the electron temperature is very low in the outer region of the pinch. The electron temperatures that would be required to
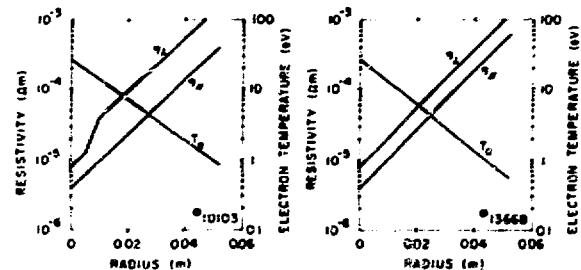
Fig. VI-23.

Parallel and perpendicular resistivities $\eta_\parallel$ and $\eta_\perp$ used in the simulations of (a) an unmatched reversed-field pinch and (b) a matched pinch. T_e is the electron temperature derived from classical parallel resistivity. The shaded areas indicate the range of electron temperatures measured by Thomson scattering.

interpret the parallel resistivity as classical Spitzer[12] resistivities are shown in the same figures. The shaded areas in the figures represent the ranges of electron temperatures observed with Thomson scattering during the 3-to 5-μs interval. The conclusion is that the accuracy of the electron temperature measurement is not sufficient at present to conclude whether the predicted resistivity is classical or anomalous. Note that the plotted temperatures do not include any high-Z correction. In the event that a few percent of oxygen and carbon impurities might be concentrated in the low-density region of the pinches, the classical temperatures in this region could be higher by a factor of order 2.

G. ASSEMBLY OF THE ZT-S EXPERIMENT

ZT-1 has been modified to the ZT-S configuration. A comparison of dimensions follows:

	ZT-1	ZT-S
Aspect Ratio	6.67	4.85
Major Radius	38 cm	40.44 cm
Ceramic Inside Radius	5.15 cm	7.71 cm
Metal Wall Inside Radius	5.7	8.33

A new preionization system and B_z system have been installed. The preionization system was modified to allow rapid changes in both capacitance and polarity. The capacitance can easily be changed from 15 μF to 150 μF at a maximum charge voltage of ~ 15 kV. The polarity to the machine is reversable without changing the charge polarity. The system consists of 150 μF that is charged positively

77

regardless of the polarity or magnitude of the capacitance actually discharged into the PI system. A pre-preionization circuit is used as on ZT-1. Namely a 2 μF capacitor is charged to ~ 1/4 PI voltage and discharged into the PI circuit a few microseconds prior to the main PI discharge. The PI current can be crowbarred or allowed to ring out.

The B_z magnetic field is supplied to ZT-S by way of forty-eight 5-turn coils around the minor circumference of the torus, Fig. VI-24. The coils are fed in parallel with a vacuum field inductance of 0.27 μH, and carry both the forward and reverse I_θ. The forward B_z system consists of capacitor bank C_1, a series inductance L_1 that is used with C_1 to determine the period of the system, and the B_z windings L_2. Fields of well over 0.5 T with a τ/4 of ~ 100 μs are obtained. The reverse B_z circuit consists of a capacitor bank C_2 that feeds the shaping capacitor C_s in parallel with the B_z windings, L_2, and the crowbar switch. A varistor assembly, VR, is used in parallel with L_2 to limit the peak voltage across L_2 and C_s. This voltage can be quite different with and without plasma in the torus and some means of protection for the insulation on L_2 is necessary when a plasma is not present. If one takes into account the plasma implosion, the B_z field can be reversed from + 0.5 T to - 0.2 T in ~ 10^{-6} s.

H. TRANSFER-PEAKING CAPACITOR PROTOTYPE CIRCUIT

The peaking capacitor study is intended to determine whether a pulse-charged back-biased, low-inductance capacitor system can effectively replace the inductive storage explosive-fuse method of achieving high dI/dt's and large currents with constant current characteristics suitable for driving Z pinches. Ultimately the test of this energy source will come when it is connected to a plasma pinch load. This present work is confined to data resulting from switching the circuit into a metallic load of nominally 8 nH, and covers two phases of testing. The first phase is summarized by the data in Fig. VI-25 in which the Marx stored energy capability is one-third that of phase two.

Fig. VI-25.

Two separate shots, #2035 and #2047, in which the load current is transferred at slightly different times. As seen on the input voltage, the peaking capacitor is charged to a reverse 50-kV peak, which is defined as t = 0. Note the load current is not crowbarred as in Fig. VI-27, and falls off quickly.

C₁ 2880μf 10kV
C₂ 22.2μf 60kV
C_s 0.4μf 50kV
L₁ 1.6μH
L₂ 0.27μH
VR₁ V=75201
(1ea of 8)

ZT-S, B_z SYSTEM

Fig. VI-24.

ZT-S, B_z System.

78

Fig. VI-26.

The transfer-peaking capacitor circuit's load side photographed during its present configuration.

Fig. VI-27

Waveshape of the high-current output of the trans-fer-peaking capacitor circuit having the high dI/dt's, high currents, and flat-topped constant current characteristic required to drive Z pinches.

The second phase of experimentation is based on the higher energy configuration of the device, the load side of which is shown in Fig. VI-26. In addition to the higher energy (due to triple the number of Marx modules), crowbars have been added, resulting in a close approximation of the desired waveshape as seen in Fig. VI-27. The current has an initial rise of about 3×10^{12} A/s, has an amplitude of 185 kA, and being crowbarred, has an L/R decay time of ~ 40 μs as extrapolated from Fig. VI-27.

A plasma (linear Z pinch) load will replace the present metallic load when the improved triggering will allow more reproducible operation. With this linear pinch load the first question to be answered is whether this transfer capacitor method has low enough residual $\vec{E}$ field after pinch formation to prevent a secondary breakdown at the walls of the discharge tube.

REFERENCES

1. D. A. Baker, L. C. Burkhardt, J. N. Di Marco, P. R. Forman, A. Haberstich, R. B. Howell, H. J. Karr, J. A. Phillips, and A. E. Schofield, "Plasma Parameters and Stability of the ZT-1 Pinch Experiment," Proc. V Intern. Conf. Plasma Phys. and Controlled Nuclear Fusion Research, Tokyo, 1974 (Intern. Atomic Energy Agency, Vienna, 1975), Vol. III, pp. 36-45.

2. H. R. Griem, Plasma Spectroscopy (Mc-Graw-Hill, New York, 1964).

3. S. Costa and S. Ortolani, University of Padua report to be published.

4. R. W. P. McWhirter, Plasma Diagnostic Techniques, Academic Press Inc., p. 243 (1965).

5. J. N. Di Marco, "Formation of Reversed Magnetic Field Profiles with a Toroidal Diffuse Pinch (ZT-1)," to be published.

6. A. Buffa, et al., Fifth Conf. on Plasma Phys. and Controlled Nuclear Fusion Research, Tokyo, Japan, 1974, IAEA CN-33/E9-3.

7. A. Haberstich, "Ideal MHD Stability of the ZT-1 Toroidal Pinch Experiment," to be published.

8. J. P. Goedbloed and P. H. Sakanaka, Phys. Fluids 17, 908-918 (1974), P. H. Sakanaka and J. P. Goedbloed, Phys. Fluids 17, 919-927 (1974), D. A. Baker and J. N. Di Marco, Compilers, "The LASL Reversed-Field Pinch Program Plan," Los Alamos Scientific Laboratory report LA-6177-MS (December 1975).

9. A. Haberstich, "Numerical Calculations of the Theta, Z, and Screw Pinches," Los Alamos Scientific Laboratory report LA-4782-MS (December 1971).

10. R. C. Davidson and N. T. Gladd, "Anomalous Transport Properties Associated with the Lower-Hybrid-Drift Instability," Phys. Fluids 18, 1327-1335 (1975).

11. R. C. Davidson, R. A. Gerwin, N. T. Gladd, and R. B. Howell, Proc. of Third Topical Conf. on Pulsed High Beta Plasmas, Culham, 1975, paper A2.6.

12. L. Spitzer, Jr., Physics of Fully Ionized Gases, 2nd Ed., (Interscience Publishers, New York, 1962), pp 136-143.
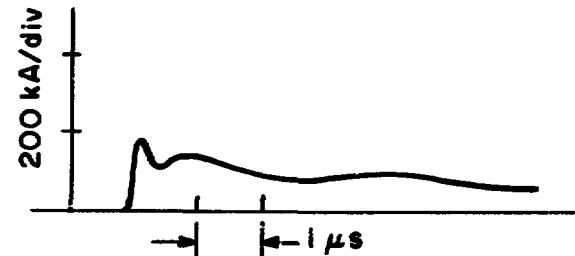
VII. THEORY

J. P. Freidberg, D. Barnes, J. U. Brackbill, R. C. Davidson, D. Forslund,
S. P. Gary, R. A. Gerwin, N. T. Gladd, D. Hewett, H. R. Lewis, L. Mann,
M. Menzel, W. Pracht, W. Riesenfeld, L. Turner, D. Winske

A. SUMMARY

This section summarizes some of the main accomplishments of the LASL theory group over the past year as well as identifying the most important theoretical problems currently facing the LASL program. As might be expected, the spectrum of problems considered covers a wide range, from low-frequency MHD and transport phenomena to high-frequency microinstability theory. Much of the effort is applied to the θ-pinch program.

The most important problem in the area of MHD is the calculation of diffuse toroidal Scyllac equilibria. Although equilibria, calculated on the basis of a surface current model have been known for several years, the three-dimensional nature of toroidal helical systems makes the extension to diffuse profiles difficult. Several analytic expansions are currently being investigated by R. Dagazian, J. Freidberg, and B. Marder. The equilibrium problem is also being studied by solving for the time evolution of the plasma away from some appropriate initial condition. This requires the use of a full nonlinear-3D time dependent MHD code. J. Brackbill and D. Barnes have developed perhaps the most accurate and sophisticated version of such a code and preliminary Scyllac equilibrium results are presented in the main text.

Another very important problem facing the Scyllac program is the finite Larmor radius stabilization of $m \geq 2$ modes. A recent calculation by L. Turner shows that the original Finite Larmor Radius (FLR) estimate given by J. Freidberg was pessimistic by a factor of four. If this factor is borne out in real experiment, it would significantly alleviate the problem of higher m modes in future large Scyllac devices. The calculations by L. Turner and J. Freidberg were based on surface current models. A novel approach to estimated $m \geq 2$ FLR criteria for diffuse Scyllac configurations has been proposed and implemented by J. Freidberg and D. Hewett. In their procedure, the techniques of particle simulation codes are adapted to study linear stability problems. A general approach to the study of finite

ion Larmor radius effects in plasmas is being investigated by R. Lewis and L. Turner. Considerable analytical and numerical progress has been made in the past year.

Because of the importance of implosion heating a great deal of effort has been expended in this area. C. Nielson and A. Sgro have developed the first 1-D hybrid code which includes both $B_\theta(r)$ and $B_z(r)$ and which is capable of following plasma motion for macroscopic times. The ions are treated with a full Vlasov description by particle simulation techniques. The electrons are treated as a massless fluid with a tensor electrical conductivity. In addition the code contains impurity radiation and ionization. The code has been applied to four experiments: Scylla IB, ZT-1, Staged θ Pinch and IHX. Remarkably, best agreement is obtained between numerical results and real experiments when a quasi-empirical formula for resistivity, which is identical for each different experiment is used. Either pure classical, or theoretically derived values of resistivity give noticeably poorer agreement. Results are presented for STP and IHX.

The most important problem in microinstability theory is the nonlinear evolution of the lower hybrid drift instability. Studies made by R. Davidson, J. Freidberg, R. Gerwin, and T. Gladd indicate that this may be the dominant instability in θ pinches (and perhaps Z pinches as well) during the implosion and post-implosion phases. This instability is driven by the density gradient. In order to study the nonlinear evolution, plasma simulation codes including density gradients, finite β effects and the capability of following many hybrid gyro times are required. C. Nielson has developed the first and perhaps only working 2-D (in space, 3-D velocity) simulation code based on the nonradiative Darwin model. Using this code D. Hewett and D. Winske have simulated the lower hybrid drift instability in a regime corresponding to the implosion. Results of this simulation are discussed.

B. MAGNETOHYDRODYNAMIC THEORY AND COMPUTATIONS

We have been using two- and three-dimensional codes for time-dependent MHD flow to study equilibrium and stability properties of high-beta confinement geometries. Among the problems which have been addressed are the injection of a plasma from a large diameter theta pinch into a small diameter holding field to test wall stabilization, the mass end loss from a straight theta pinch, the rotation induced instability in a straight theta pinch, the internal kink mode in high-beta plasmas, and the post-implosion dynamics of the Scyllac plasma. Development on the axisymmetric equilibrium and stability code has allowed application to curvilinear boundaries.

1. Two-and Three-Dimensional Magnetohydrodynamics Computations. The wall stabilization calculations used a two-dimensional code in which the computational domain is divided into a vacuum and a plasma region. With this division, it is easier to apply arbitrarily varying boundary conditions. The results indicate that axial pressure gradients are not sufficiently large to drive strong axial flow, and that forces due to magnetic field curvature result in axial mass redistribution on a time scale significantly longer than the Alfven transit time. It was also noteworthy that the time required for injection is much longer than the confinement time for the plasma in the open-ended experiment. This is discussed in more detail below.

The study of the mass end loss from a straight theta pinch also used a two-dimensional code. The calculations were for parameters corresponding to several experiments at Los Alamos from which good data had been obtained. The computational model included the full MHD equations without thermal conduction. The boundary conditions were that the pinch was terminated at each end by a completely absorbing plate at which the plasma pressure was zero. The variation of the mass loss as the plasma beta was varied was determined from a sequence of calculations. The results could be summarized by a simple exponential decay equation in which the normalized decay time scales linearly with the length of the pinch. The decay time, which was normalized by dividing the computed decay time by the thermal transit time, was in numerical agreement with the

experimental results. An important qualitative result was that the end loss is a transient process. That is, mass end loss is associated with the propagation of a rarefaction wave into the plasma from the open end. The effect of mirrors and other end-stoppering schemes are the subjects of continuing studies.

Rotation induced instabilities in straight theta pinches have been studied using a code for three-dimensional MHD flow. Preliminary results have been obtained which are in full agreement with the results of linear stability theory. The studies are continuing to determine the scaling of the saturation amplitude to longer systems.

The internal kink mode instability is the subject of a continuing study using the three-dimensional code. The object of these studies is to gain an understanding of the fundamental nature of this instability and its nonlinear behavior. The studies also provide useful benchmark calculations which allow direct comparison of the computational results with linear stability theory and the results of nonlinear computations obtained with other methods.

Finally, considerable progress has been made on the computation of the post-implosion dynamics of the Scyllac plasma. The progress has come about through the development of a very fast vacuum field solution algorithm for three-dimensional geometries. This development makes it possible to perform calculations in which the computational domain is divided into vacuum and plasma regions so that a wide range of geometries can be easily and quickly modeled. A computation of the dynamics of one helical period of the plasma for the full-torus experiment has been carried well beyond one microsecond. The results of the computation clearly show the plasma responding to the helical fields, and axial pressure equilibration occurring through flow in the toroidal direction. The preliminary results indicate the diagnostics already in the code will give a clear picture of the response of the plasma to the perturbing fields, and that it will be easy to determine the conditions under which toroidal force balance is established. In addition, the cost of each calculation is reasonable enough that a moderately large number of numerical experiments can be performed.

2. *Axisymmetric Toroidal Equilibrium and Stability Code.* The equilibria section of the global stability code has been plagued with an inaccuracy that made the results questionable near the outer boundary for all torus cross sections except the belt pinch which has a rectangular cross section. The two-dimensional spline interpolator used in the code requires the solution of the equilibrium equation governing the poloidal flux function Ψ be known in a rectangular region. This required us to extrapolate the solution for a semicircular cross section out to the rectangle in which the semicircle is inscribed. This gave smooth results for Ψ near the boundary but gave rise to large errors for the derivative of Ψ (B-field) near the boundary.

In the past, this difficulty has been circumvented by running the problem oversize and using an interior flux surface as the boundary for the stability analysis and calculation of accurate B-field values.

A finite element code developed for high-explosive work at Los Alamos[1] was adapted[2] for use in our equilibrium calculation. This method has been tested on a straight cylinder for which we have analytic solutions and gives accurate solutions and their derivatives over the entire region. It also may be much faster than our previous over-relaxation method. We are now incorporating this finite element method into the equilibrium section of our stability code.

The stability of the reversed-field pinch configuration to localized modes for various plasma pressure profiles was studied using the Mercier Q criterion.[3] The pressure profiles studied are shown in Fig. VII-1 along with the associated poloidal and toroidal magnetic fields. Figure VII-1a shows a flat profile as both large and small aspect ratios; Figure VII-1b shows the peaked and dipped profile at large aspect ratios. The result for the flat top pressure profile is shown in Fig. VII-2. It is interesting to note that for cases having poloidal beta below a critical value, there is an optimum aspect ratio which maximizes the Mercier Q value indicative of an enhanced stability margin. The set of curves for the peaked profile and dipped profile look similar, with the peaked profile being generally less stable and the dipped profile more stable. The dipped profile has curves which are

unstable at large aspect ratio and cross over and become stable at smaller aspect ratios.

A series of curves was also run for a tokamak-like profile having negligible poloidal plasma current and a peaked pressure profile. (See Fig. VII-3). This study shows that the commonly used $q > 1$ criterion is quite an accurate predictor of localized instability in a low-beta tokamak device. The only regions where q predicts stability where the Mercier criterion gives instability is at small aspect ratio and relatively high total beta (above $\sim 10\%$).
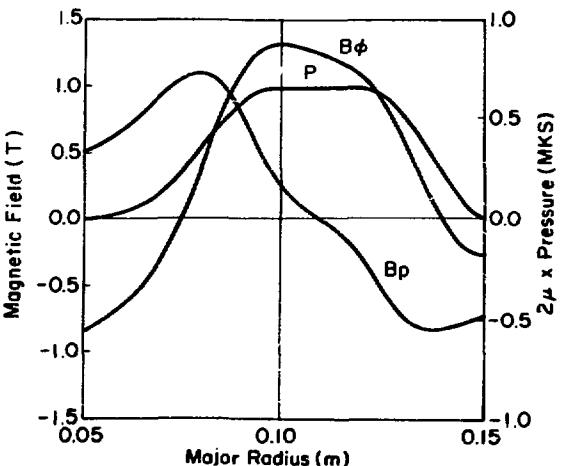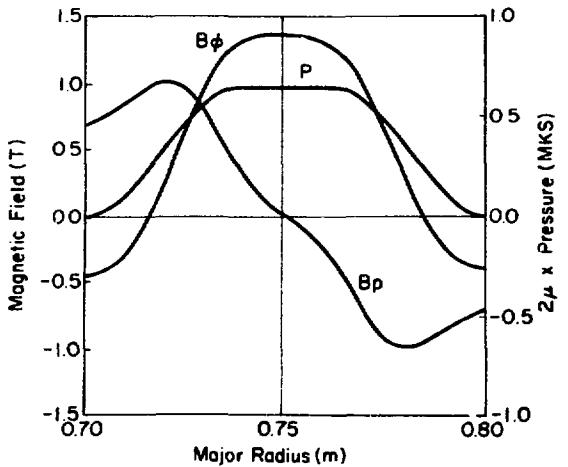
Fig. VII-1a.

Flat pressure profile and toroidal and poloidal magnetic fields for a large aspect ratio and a small aspect ratio.
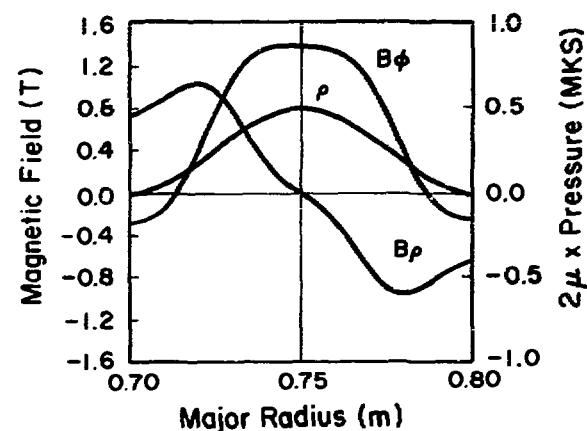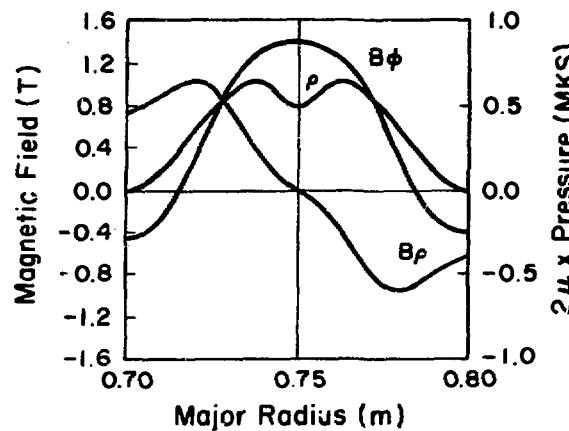
Fig. VII-1b.
Peaked pressure profile
and dipped pressure profile
at large aspect ratio.

Fig. VII-3.
Tokamak profile with toroidal
and poloidal magnetic fields.

Fig. VII-2.
Localized instability as a function of
aspect ratio for various poloidal betas.

C. FLUID KINETIC MODELS

These models have been applied to Finite Larmor radius stabilization of pinches and implosion modeling in Z and theta pinches. A new technique in this area has been developed for the numerical evaluation of orbit integrals.

1. Finite Larmor Radius Stabilization. Stabilization of MHD instabilities by means of finite-ion-gyroradius effects for modes whose azimuthal mode

number is two or greater is of considerable importance in the conceptual design of fusion reactors based on theta-pinch devices such as Scyllac.[4] In order to achieve stabilization of the m=2 mode (where m is the azimuthal mode number), it is necessary that the ratio of the average ion gyroradius (as defined in Eq. [11] below) to the plasma radius be larger than a critical value. However, other considerations, such as possible wall stabilization of the m=1 mode, require that the ratio of plasma radius to wall radius be as large as possible. Clearly, for fixed wall radius and ion temperature, increasing the plasma radius to satisfy the wall stabilization condition for the m=1 mode will tend to make the m=2 stabilization condition not satisfied. It is important to determine the critical ratio of ion gyroradius to plasma radius in order to ensure that the m=1 and the m=2 stabilization conditions can be satisfied simultaneously for proposed devices.

Freidberg[5] proposed a model for studying FLR effects in high-beta pinches, the Vlasov-fluid model, which is appropriate for low-frequency phenomena. He applied the model in an approximate way to determine the influence of finite ion temperature on the m=1 and m=2 MHD modes of instability of sharp-boundary screw-pinch equilibria for the case in which the ratio of the azimuthal magnetic field to the longitudinal magnetic field is small (nearly θ-pinch equilibria). For a range of parameters relevant to experimental devices such as Scyllac, Freidberg found that the m=2 MHD mode is effectively stabilized when the ratio of ion gyroradius to plasma radius is greater than a critical value, and that there is negligible effect of finite ion temperature on the m=1 mode. However, some recent experiments in Garching[6] and Los Alamos[7] suggest that this value of the critical ratio is too large by about a factor of 2.

We are using two approaches, one computational and the other analytical, to obtain a more precise understanding of the implications of the Vlasov-fluid model regarding the stability of sharp-boundary screw-pinch equilibria. The computational approach is based on a numerical method that has been developed for studying the linearized behavior of systems in which one or more components are collisionless.[8,9,10] The numerical results that we

present here are for long wavelength m=1 and m=2 modes of a sharp-boundary screw pinch in which the magnetic field configuration is nearly that of a θ pinch. For the particular wavelength that was used, we find little effect on the m=1 mode due to finite ion temperature, whereas the m=2 mode is stabilized for sufficiently large temperature, in qualitative agreement with the results of Freidberg.[5] However, the critical value of the ratio of ion gyroradius to plasma radius above which the m=2 mode is stabilized is lower than predicted by Freidberg by a factor of about 2.5. The analytical approach,[1] some results of which we report here, is valid for long wavelength modes of arbitrary azimuthal mode number when the ion temperature is sufficiently small. The analysis requires a certain physically reasonable approximation for the region within about an ion gyroradius of the boundary. However, the eigenvalue problem for an unstable mode is solved, in contrast to Freidberg's treatment in which an approximate "trial-function" method is used instead. A result of the present analysis is that the influence of finite ion temperature on the m=1 and m=2 modes is in qualitative agreement with that found by Freidberg. However, in rather good agreement with the numerical results, the critical value of the ratio of ion gyroradius to plasma radius for the m=2 mode is lower than found by Freidberg by exactly a factor of 2. The numerical and analytical work on this problem is continuing.

In the following sections of this preliminary report, we present brief accounts of the Vlasov-fluid model, the numerical method for evaluating the Vlasov-fluid model, the mathematical description of the sharp-boundary screw pinch, the analytical treatment of the sharp-boundary screw pinch, and the numerical and analytical results for the particular problem that we have studied numerically.

a. Vlasov-Fluid Model and Numerical Method.

In the Vlasov-fluid model, as proposed by Freidberg,[5] the ions are treated as collisionless, the electrons are treated as a massless fluid, charge neutrality is assumed, and displacement current is neglected. The governing equations of the model are

$$\vec{E} + \frac{1}{c} \vec{u}_e \times \vec{B} = 0 \quad , \tag{1}$$

$$\nabla \times \vec{E} = -\frac{1}{c} \frac{\partial \vec{B}}{\partial t} \quad , \tag{2}$$

$$\frac{\partial f}{\partial t} + \vec{v} \cdot \nabla f + \frac{Q}{M} \left(\vec{E} + \frac{1}{c} \vec{v} \times \vec{B} \right) \cdot \nabla_v f = 0 \quad , \tag{3}$$

and

$$(\nabla \times \vec{B}) \times \vec{B} = 4\pi Q \int d^3\vec{v} \left(\vec{E} + \frac{1}{c} \vec{v} \times \vec{B} \right) f \quad , \tag{4}$$

where $\vec{u}_e$ is the perpendicular electron velocity, f is the ion distribution function, and Q and M are the ionic charge and mass, respectively.

The eigenfrequency spectrum of this model for small perturbations of an equilibrium can be approximated by the roots of a determinantal equation of the form[10]

$$\det \left[(L - \omega) - \sum_{n=0}^{N} q^{(n)}(\omega) c^{(n)+} \right] = 0 \quad , \tag{5}$$

where ω is an eigenfrequency, L is a hermitian square matrix, $q^{(n)}(\omega)$ and $c^{(n)}$ are column matrices, and $+$ denotes hermitian conjugate. The summation of (N+1) rank-one matrices in Eq. (5) is associated with an expansion of $\vec{\xi} = \vec{B}^{(0)} \times \vec{A}^{(1)}/B^{(0)2}$ in eigenfunctions $\vec{\xi}_n$ of an MHD-like operator $\vec{F}$:

$$\vec{F}(\vec{\xi}) = \frac{1}{4\pi} \left[(\vec{\nabla} \times \vec{B}^{(0)}) \times \vec{B}^{(1)} + (\vec{\nabla} \times \vec{B}^{(1)}) \times \vec{B}^{(0)} \right]$$

$$+ \vec{\nabla}(\vec{\xi} \cdot \nabla p^{(0)}) \quad , \tag{6}$$

$$\vec{F}(\vec{\xi}_n) = \lambda_n \rho^{(0)} \vec{\xi}_n \quad , \tag{7}$$

where superscripts 0 and 1 denote equilibrium and perturbation quantities, respectively, $p^{(0)}$ is the equilibrium ion pressure, $\rho^{(0)}$ is the equilibrium ion density, and $\vec{B}^{(1)} = \vec{\nabla} \times (\vec{\xi} \times \vec{B}^{(0)}) = \vec{\nabla} \times \vec{A}^{(1)}$. The matrices in Eq. (5) are representations of physical quantities in a truncated space of eigenfunctions of the unperturbed Liouville operator

$$\mathcal{L}(\vec{r}, \vec{v}) = \vec{v} \cdot \vec{\nabla} + \frac{Q}{M} \left[\vec{E}^{(0)}(\vec{r}) + \frac{1}{c} \vec{v} \times \vec{B}^{(0)}(\vec{r}) \right] \cdot \vec{\nabla}_{\vec{v}} \quad . \tag{8}$$

L is the matrix representation of $(1/i)\mathcal{L}$ in this space of eigenfunctions of $\mathcal{L}$. Because $(L-\omega)$ is diagonal, and therefore easily invertible, it is very

useful for numerical and analytical purposes to replace Eq. (5) by an equivalent form,

$$[\det (L-\omega)] \det D = 0 \quad , \tag{9}$$

where D is an (N+1) x (N+1) matrix:

$$D_{jk} = \delta_{jk} - c^{(j)+} (L-\omega)^{-1} q^{(k)}(\omega) \quad . \tag{10}$$

Equation (9) is a polynomial equation in ω, all of whose roots may be found simultaneously with the aid of a global Newton's method.[12,13]

   b. *Sharp-boundary Screw Pinch.* The sharp-boundary screw-pinch equilibria that we consider are characterized by constant plasma density and pressure, and by a uniform axial magnetic field B_z, within an infinitely long cylindrical volume of radius r_0. The equilibrium ion distribution function is taken to be a function only of the total energy. Exterior to the cylinder there is a vacuum region bounded by an infinitely conducting cylindrical shell of radius R. Between the plasma cylinder and the conducting shell, there is a B_z field and/or an azimuthal field B_θ.

The boundary at radius r_0 requires special attention with regard to boundary conditions and the derivation of Eq. (5). One boundary condition is continuity of the normal component of $\vec{B}$ at the perturbed plasma-vacuum interface. In ideal MHD the other boundary condition at r_0 would be derived by integrating the pressure balance equation corresponding to Eq. (4). However, this is not possible in the Vlasov-fluid model because of the kinetic treatment of the ions. The reason for this is as follows. In the Vlasov-fluid model, the electrons are tied to the magnetic field lines and the ions are confined electrostatically by space-charge fields. With the sharp-boundary approximation, the confining electric field has a delta-function character at the boundary, corresponding to the assumption that the sheath thickness, of the order of the ion Debye length, is much smaller than any other length of interest. The details of the plasma density and electric field in the sheath region as functions of position and time are not known a priori. Because of this fact, the term in Eq. (4) involving the electric field and the discontinuous density

85

cannot be integrated across the boundary until after the system of Eqs. (1)~(4) has been solved. Therefore, Eq. (4) is not helpful in deriving a useful exact boundary condition. The appropriate condition, derived from the assumed specular reflection of the ions by the confining electric field, is that the normal component of the electric current vanish at the boundary.

During the evolution of a sharp-boundary screw pinch, the boundary moves and deforms, thereby affecting the motion of the collisionless ions. We take these boundary motions into account by introducing a time-dependent transformation of the phase to a set of variables in terms of which the time-dependent perturbed boundary appears like a rigid cylinder at rest. Writing the collisionless Boltzmann equation and the $(\vec{V} \times \vec{B}) \times \vec{B}$ equation in terms of the new variables, we then consider perturbations about a state which is the equilibrium modified to include the specular reflection of the ions from the perturbed boundary. Formally, in terms of the new variables, the equations for the linearized problem are the same as those that would describe perturbations of a system with a hypothetical, rigid cylindrical boundary, except that a boundary term must be added to the collisionless Boltzmann equation.

In general, the degree of the polynomial equation for the eigenfrequencies, Eq. (9), is (d_L+N+1), where d_L is the number of Liouville eigenfunctions used to represent the phase space; d_L is also the dimension of the matrices in Eq. (5). However, it can be shown analytically that if the elements of D, Eq. (10), are evaluated exactly with a complete set of Liouville eigenfunctions for a sharp-boundary screw pinch, then the degree of the polynomial is reduced to (d_L+1). That is, as the boundary of a diffuse screw pinch is steepened until it is infinitely sharp, N eigenfrequencies move to infinity and are lost. When the elements of D are evaluated approximately with a finite set of Liouville eigenfunctions, there are N unphysical eigenfrequencies whose moduli are very large if sufficiently many Liouville eigenfunctions are used. This result is helpful in determining whether an adequate number of Liouville eigenfunctions have been used.

For a sharp-boundary screw pinch, we can solve Eq. (7) analytically for the eigenfunctions and

eigenvalues $\vec{\xi}$ and λ_n. The smallest eigenvalue vanishes: $\lambda_0 = 0$. The associated eigenfunction, $\vec{\xi}_0$, corresponds to a perturbed magnetic field whose source currents all flow on the surface of the pinch. $\vec{\xi}_0$ is the same as the incompressible ideal MHD eigenfunction.

c. Analytical treatment. The analytical results that we use for predicting the growth rate of an unstable mode of a sharp-boundary screw pinch are based on an expansion in which the quantities kr_0 and ω/ω_c are assumed to be small compared to unity, where k is the wavenumber in the longitudinal direction, r_0 is the equilibrium plasma radius, ω is the eigenfrequency, and ω_c is the equilibrium cyclotron frequency within the pinch. By using this expansion, and by making some physically plausible assumptions about the ordering of quantities at distances from the boundary less than approximately an ion gyroradius, it is possible to use Eq. (4) to derive a pressure balance condition that is correct to leading order in the small quantities. This condition connects the interior plasma region, in which the ions do not strike the boundary, to the vacuum region; the two regions are separated by a boundary region whose thickness is of the order of an ion gyroradius. A consequence of this long wavelength, low-frequency approximation is that the eigenfrequency of an unstable mode of azimuthal mode number m satisfies the equation

$$\left(\frac{\omega}{\omega_c}\right)^2 - \frac{1}{2} m \, (m-1) \left(\frac{r_L}{r_0}\right)^2 \left(\frac{\omega}{\omega_c}\right) + \left(\frac{\gamma_0}{\omega_c}\right)^2 = 0, \quad (11)$$

where γ_0 is the growth rate for azimuthal mode number m predicted by incompressible ideal MHD, and r_L is an average ion gyroradius defined by

$$r_L^2 = \frac{2KT}{M\omega_c^2} \quad , \tag{12}$$

where T is the ion temperature and K is Boltzmann's constant.

The solutions of Eq. (11) have the following properties:

a) $|\omega| = \gamma_0$ for all values of m.

b) $\lim_{r_L/r_0} \omega = \pm i\gamma_0$ for all values of m. That is, the unstable eigenfrequencies equal those

predicted by incompressible ideal MHD when the ions are cold.

c) $\omega = \pm i\gamma_0$ for $m=1$, independently of r_L/r_0. That is, the unstable eigenfrequencies equal those predicted by incompressible ideal MHD for all values of r_L/r_0 if $m=1$.

d) For $m \geq 2$, if the condition

$$\left(\frac{r_L}{r_0}\right) > \left(\frac{r_L}{r_0}\right)_{crit} = \frac{4}{m(m-1)} \left(\frac{r_0}{r_L}\right)\left(\frac{\gamma_0}{\omega_c}\right)$$

$$= \frac{4}{m(m-1)} \frac{r_0\gamma_0}{(2KT/m)^{1/2}} \tag{13}$$

is satisfied, then $\text{Im } \omega = 0$, which means that the mode is stable. These properties, a) through d), are leading-order predictions of the long wavelength, low-frequency analytical treatment of Turner[1]. Properties a) through c) are also results of Freidberg's analysis.[5] However, for $m=2$, the critical value of r_L/r_0 found by Freidberg is twice as large as $(r_L/r_0)_{crit}$ defined by Eq. (13).

In the next section, we compare the solution of Eq. (11) to computational results obtained with our numerical method for a particular case, and show rather good agreement between the analytical and computational results.

d. A Particular Case. The results described here are for a sharp-boundary screw-pinch equilibrium that is obtainable from a θ-pinch by adding a small azimuthal magnetic field B_θ. At the plasma boundary, the external magnetic fields are $B_z^{(external)} = 2.0 \, B_z^{(internal)}$ and $B_\theta^{(external)} = 0.2 \, B_z^{(internal)}$, and the ratio $R/r_0 =$ (conducting wall radius/plasma radius) is 1000. Perturbations are proportional to $\exp[i(m\theta+kz)]$, where $kr_0 = -.05$ and $m=1$ or 2. The equilibrium ion distribution function is Maxwellian; expressed in terms of $\tilde{\varepsilon} = 2\varepsilon/(Mr_0^2\omega_c^2)$, where ε is the total energy of an ion, the equilibrium distribution function is proportional to $\exp[-\tilde{\varepsilon}(r_0/r_L)^2]$. The equilibrium is unstable to the $m=1$ and $m=2$ modes in incompressible ideal MHD.

Our computations for this equilibrium, as well as for some other unstable equilibria, indicate that the eigenfrequency spectrum for a sharp-boundary screw pinch with the Vlasov-fluid model consists of

a continuum on the real axis plus one discrete complex conjugate pair of frequencies. Thus, there appears to be, at most, one unstable mode. With this near θ-pinch, the growth rate is insensitive to (N+1), the number of eigenfunctions of $\vec{F}$ that are chosen; $\vec{\xi}_0$ is a very good approximation to $\vec{\xi}$. More eigenfunctions may be needed when the equilibrium is not near a θ-pinch equilibrium. Also, with this near θ-pinch example, quite good estimates of the growth rate are obtained with rather small numbers of Liouville eigenfunctions (<100) when r_L/r_0 is either much smaller than $(r_L/r_0)_{crit}$ or much larger than $(r_L/r_0)_{crit}$. For values of $r_L/r_0 \lesssim (r_L/r_0)_{crit}$, the growth rate converges more slowly with increasing numbers of Liouville eigenfunctions.

In Figs. VII-4-7 we present a direct comparison of computational and analytical results for this case. The quantities graphed are γ/γ_0 and $|\omega|/\gamma_0$ for $m=1$ and $m=2$, where $\gamma = \text{Im } \omega$ is the growth rate, and γ_0 is the growth rate predicted by incompressible ideal MHD. The solid lines represent the analytical results and the points are results of the numerical method. The error bars are determined from an examination of the approach to convergence as the number of eigenfunctions is increased. Where no error bar is shown, the uncertainty is too small to be indicated on the graph. The agreement between the analytical and computational results is quite good. The largest discrepancy is that the value of $(r_L/r_0)_{crit}$ indicated by the computations is even smaller than that given by Eq. (19). From the standpoint of controlled fusion, as was indicated in the introductory section of this paper, it is desirable that $(r_L/r_0)_{crit}$ be as small as possible.

2. Implosion Simulations. Computational results obtained with the one-dimensional hybrid simulation code described previously[14] have been compared in detail with the ZT-1 experiment, and the code has been modified to allow the calculation of high-voltage θ pinches.

a. ZT-1 Results. Using the semi-empirical resistivity algorithm

$$\eta = \frac{m_e\nu}{ne^2} \quad \nu_\parallel = \max\left\{\nu_{c\parallel}, c_\parallel\omega_{pi}[1-\exp(-V_{d\parallel}/f_\parallel V_s)]\right\}$$

$$\nu_\perp = \max\left\{\nu_{c\perp}, c_\perp\omega_{pi}[1-\exp(-V_{d\perp}/f_\perp V_s)]\right\} \quad ,$$

Fig. VII-4.

γ/γ_o vs r_L/r_o for $m=1$.
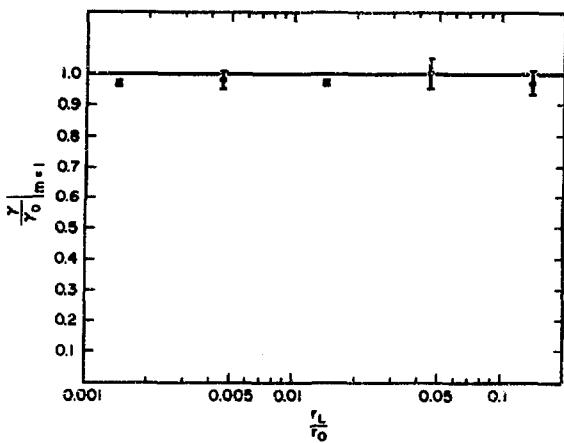
Fig. VII-6.

$|\omega|/\gamma_o$ vs r_L/r_o for $m=1$.

where $\nu_{c\parallel}$, $\nu_{c\perp}$ are the "classical" resistivities[15] parallel and perpendicular to the magnetic field, $V_{d\parallel}$, $V_{d\perp}$ are the drift velocities similarly projected, $V_s = (\gamma k T_e/m_i)^{\frac{1}{2}}$, and $c_{\parallel} = c_{\perp} = 1.0$, $f_{\parallel} = f_{\perp} = 3.0$, we have been able to obtain agreement, the degree of which is illustrated in Fig. VII-8, with most of the ZT-1 experiments simulated. Further illustrations and a detailed discussion of our calculations may be found in Ref. 16.

From this work we have concluded:

1) The semi-empirical resistivity described above modeled satisfactorily both the older field-programming mode and newer field-programming mode (in which the rise times of both fields are equal and of which Fig. VII-8 is an example) of ZT-1,
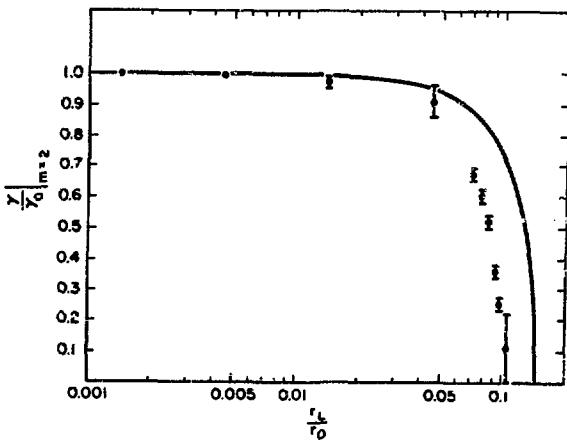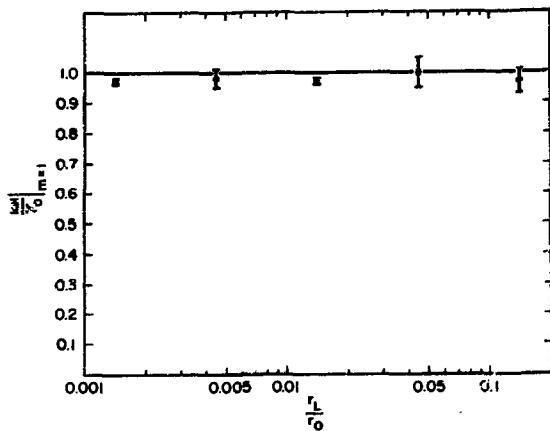
as well as the University of Padua Screw-Pinch experiment. The only exceptions were for ZT-1 experiments with very high fill density (100 mT) or high initial temperature (6 eV) in which case a higher perpendicular resistivity was required. We stress that all results were obtained with the same choice of $c_{\parallel}$ ($=c_{\perp}$), $f_{\parallel}$ ($=f_{\perp}$), independent of position, time, and experiment, so that only two degrees of freedom were available to match the numerous data points.

2) T_e computed at 1 cm from the axis agrees well with the measured value,

3) T_i computed is much less than T_i measured. This implies either an error in the code or the

Fig. VII-5.

γ/γ_o vs r_L/r_o for $m=2$.
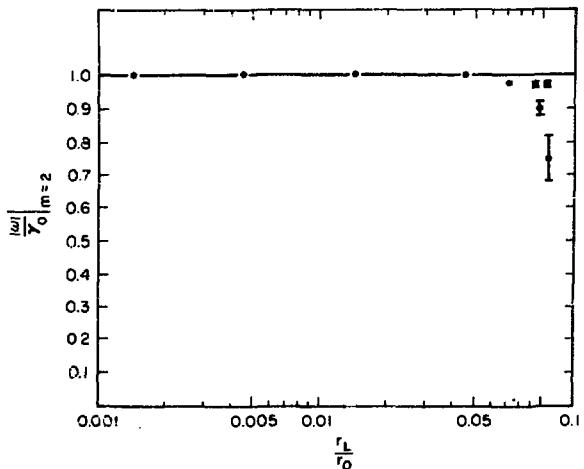
Fig. VII-7.

$|\omega|/\gamma_o$ vs r_L/r_o for $m=2$.
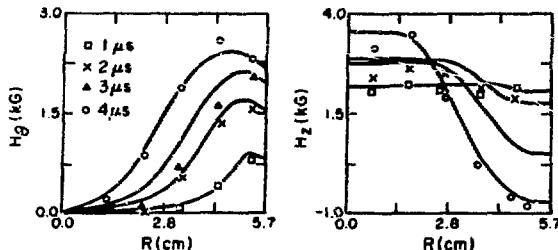
Fig. VII-8.

Comparison of ZT-1 experiment. The curves are computed fields and the symbols are the measured fields at the appropriate position and time.

Fig. VII-9.

Comparison of IHX. The curves are the computed values and the x's are the measured values.

need to include turbulent heating when computing an experiment with a high bias field. Our θ-pinch calculations will show the latter to be correct.

    b. *High-Voltage θ Pinches*. Three modifications were required to compute high-voltage θ pinches:

    1) The accuracy of the differencing of the ion equations of motion was increased to second order.

    2) The electron energy equation, as presented previously, was numerically unstable when computing the high-voltage θ pinches (but not when computing ZT-1). We proceeded as follows: The equation used in the ZT-1 calculations was

$$\left(\frac{\partial}{\partial t} + v \cdot grad\right) p_e = -\gamma p_e \, div \, v + (\gamma-1)\dot{\phi}$$

$$\dot{\phi} = \text{electron heat source}$$

$$= \eta J^2 - \xi r + div(k_\perp grad \, T_e) - \dot{\epsilon}_{rad} .$$

Here r is the ionization rate (to be discussed later) and ξ is the energy lost per ionization. To stabilize the equation we eliminated div v by using the continuity equation $\left(\frac{\partial}{\partial t} + v \cdot grad\right) n_e = -n_e \, div \, v + r$ to get $p\left(\frac{\partial}{\partial t} + v \cdot grad\right) \ell n \, (pn^{-\gamma}) = -\gamma p \frac{r}{n_e} + (\gamma-1)\dot{\phi}$. When we solved for s = $\ell n(pn^{-\gamma})$, numerical stability was achieved.

    3) The preionization used for the high-voltage θ pinches leaves a significant fraction of the gas un-ionized. The ionization and subsequent sweeping up of this gas must be included in the calculation. To do this we define the ionization rate r = $c(T_e)n_e n_n$, where c is a function of T_e only (= $\langle \sigma v \rangle$ over a Maxwellian electron distribution) and n_n is the neutral particle number density, and then define the ionization probability per time step

for a neutral simulation atom as $\rho = \frac{r\Delta t}{n_n} = c(T)n_e\Delta T$. Once the particle is ionized it is automatically swept up by the imploding field. We use the ionization rates given by Lotz.[17] However, at the densities involved in the Los Alamos θ pinches, two-step ionization processes may also be important. We are currently looking into this and into the possibility that charge exchange might be a significant effect.

    Calculation of IHX and STP were performed with these three modifications included. In both cases, the initial preionization was ~ 60%. For both experiments, the resistivity chosen was identically the one stated above. Figure VII-9 illustrates the agreement obtained between the calculated and experimental magnetic fields and densities for one IHX experiment, while Fig. VII-10 illustrates the agreement obtained in the density profiles for a 5-mT and a 10-mT STP experiment.

    An unexpected physical effect noticed in these calculations is illustrated in Fig. VII-11, which displays V_r-r and V_θ-r phase spaces at various times. Due to the final resistivity, the particles acquire a large θ velocity as well as a large r

89

10mT FILL

EXPERIMENT | THEORY

5mT FILL
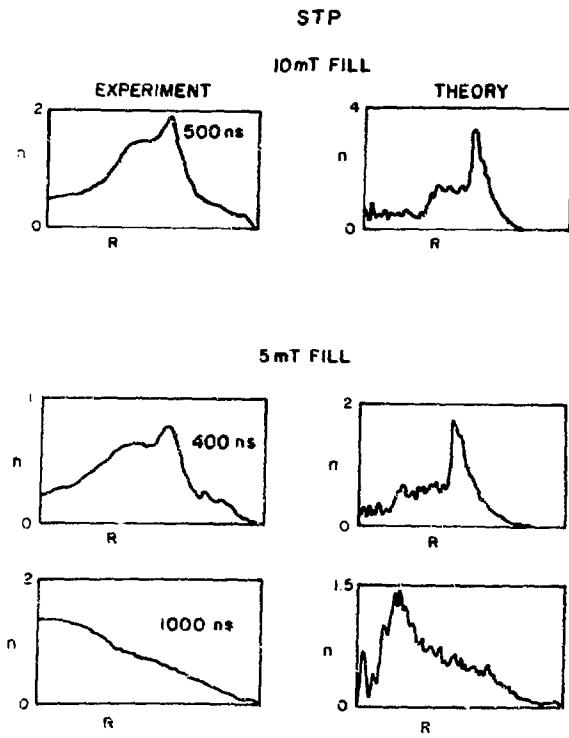
Fig. VII-10.

Comparison of 5-mT and 10-mT STP.

velocity. As a result, the imploding particles turn
around (450 ns) and begin to hit the magnetic piston
(600 ns) well before the time predicted by the per-
fect conduction-bounce model.

The Scylla 1B experiment, which has a 15% pre-
ionization, was also calculated. Fig. VII-12 com-
pares the observed density profile at 385 ns with
that calculated at 400 ns with 100% P.I., 15% P.I.,
and 15% P.I. with ionization rate doubled to mock
up the effects of two-step ionization). We note
that the main consequences of lowering the P.I. is
that, a) the front of the reflected ion beam has
advanced closer to the center, b) the density peak
at 5 cm has been decreased, and c) the gas which
is no longer in the peak has been left behind (due
to ionization) and causes the decline in density
from ~ 5 to 8 cm to be much more gradual. All
three effects cause the computations to agree
better with experiment.

T_i was found, from pressure balance, on Scylla
1B to be ~ 500 eV, while the code predicts 600-700
eV. The implication is that for the low bias field

θ pinches the code calculates the correct T_i since
in this case the ion energy is achieved principally
by bouncing off of the piston, while for the highly
biased ZT-1, the computed T_i is too low because
anomalous ion heating is dominant.

3. Numerical Evaluation of Orbit Integrals.
Orbit integrals occur frequently in various types
of linear Vlasov stability analyses in cylindri-
cally symmetric plasmas. In particular they occur
in the linearized eigenmode analysis of systems
which exhibit azimuthal symmetry and for which
axial (z) motion of particles is irrelevant. The
techniques described here are presently being ap-
plied to the nonlocal stability analysis of the
lower hybrid drift (LHD) instability and to the
finite Larmor radius (FLR) stabilization of the
$m = 2$ instability of a diffuse $\beta = 1$ MHD
equilibrium.

These orbit integrals are of the form

$$I = \int_0^R dr\, r\, n(r) \int_0^\infty dv \int_0^{2\pi} d\phi$$

$$F(r,v,\phi)\, \hat{s}\,(r,v,\phi) \tag{14}$$

$$\hat{s}\,(r,v,\phi) = \int_{-\infty}^0 d\tau\, e^{i\chi(\tau)}\, f\,[r'\,(\tau),$$

$$v'\,(\tau),\, \phi'\,(\tau)]\,, \tag{15}$$

$$\chi(\tau) = (\omega_r + i\omega_i)\,\tau + m\theta'\,(\tau)\,. \tag{16}$$

where the primed coordinates are parameters of in-
dividual particle trajectories at previous time τ
such that

$$\left.\begin{array}{l} r'\,(\tau) \to r \\[4pt] \theta'\,(\tau) \to 0 \\[4pt] v'\,(\tau) \to v = |\vec{v}| \\[4pt] \phi'\,(\tau) \to \phi = \tan^{-1} \dfrac{v_r}{v_\theta} \end{array}\right\} \text{ as } \tau \to 0.$$

Implied by the integration over time (τ) in
Eq. (15) is the integration over all past time along
the trajectory of the particle which has position r
and velocity $\underline{v} = |v|\,(\cos\phi\,\hat{e}_r + \sin\phi\,\hat{e}_\theta)$ when τ
equals zero. The particle trajectory backwards in
time is determined by these final trajectory para-
meters and the equilibrium electric and magnetic
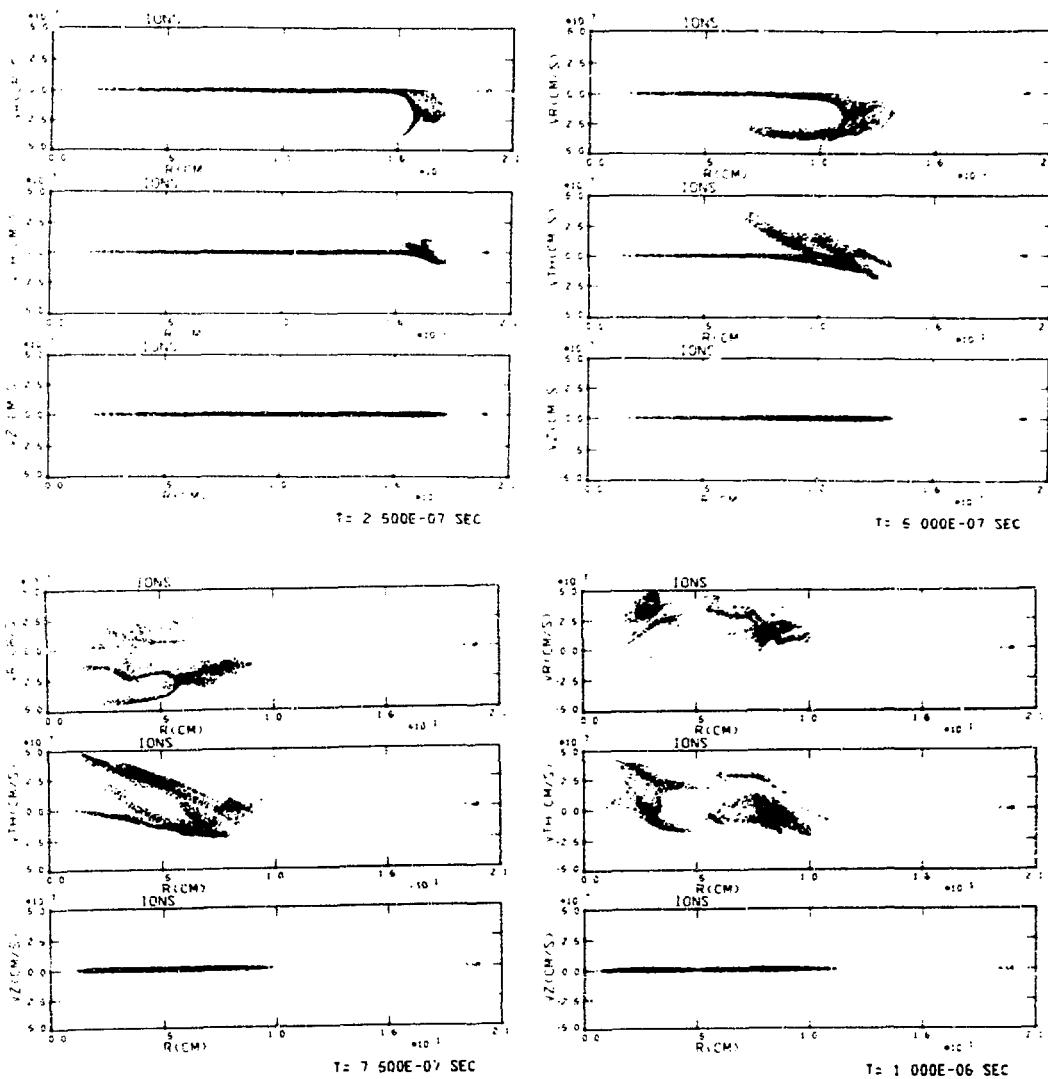
Fig. VII-11.

V_r-r and V_θ-r phase space of
the calculation represented
in Fig. VII-8.

fields. Since this is a linear analysis, the fields are unaffected by particle motion and are constant in time--greatly simplifying the required numerical evaluation.

Considering the dimensionality of the integration required by Eqs. (14) and (15), it is obvious that the numerical effort required may become excessive if not prohibitive unless methods are found which limit the effort spent on the infinite integrations. The infinite integration over velocity magnitude v is always aided by the kinetic

requirement of vanishing particle number as $v \to \infty$; but, unless $\omega_i \gg 1$, there is no a priori reason that the integrand in Eq. (15) should become small quickly as $\tau \to -\infty$.

The computation necessary to accurately evaluate Eqs. (14) and (15) can in fact be reduced considerably by a transformation of the infinite interval over τ to a finite interval. This transformation is made possible by the fact that with azimuthal symmetry in the equilibrium fields each particle trajectory is periodic in time. Such
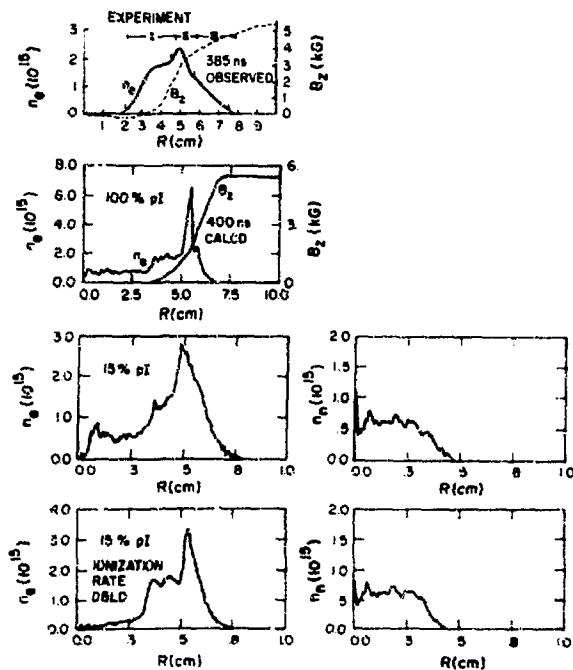
Fig. VII-12

*Comparison of experiment
and theory for Scylla 1B.*

periodicity can be understood by noting that, with
θ - symmetry in the fields, each particle has a
constant angular momentum $P_\theta [= mv_\theta r + \frac{e}{c} A_\theta(r)]$
and a constant total energy $E [= \frac{m}{2} (v_r^2 + v_\theta^2) + e\phi(r)]$. From these considerations, it is easy
to deduce that v_θ and v_r^2 along a particle trajec-
tory are simple functions of radius; and, since
there is no dissipation, each particle oscillates
in radius between the turning points determined
by final conditions at $\tau = 0$. This means there is
a time T_1 such that

$$r^\circ (r,\dot\phi,v,\tau - T_1) = r^\circ (r,\phi,v,\tau)$$

$$\theta^\circ (r,\phi,v,\tau - T_1) = \theta^\circ (r,\phi,v,\tau) + \Delta\theta$$

$$\phi^\circ (r,\phi,v,\tau - T_1) = \phi^\circ (r,\phi,v,\tau) \tag{17}$$

$$v^\circ (r,\phi,v,\tau - T_1) = v^\circ (v,\phi,v,\tau) ,$$

where T_1 and $\Delta\theta$ are themselves functions of the
particle position at $\tau = 0$.

Making use of this symmetry in time, Eq. (15)
can be written

$$\hat{s} = \int_{-\infty}^{0} d\tau \, e^{i\cdot\tau} f = \int_{-T_1}^{0} d\tau \, e^{i\cdot\tau} f + \int_{-2T_1}^{-T_1} d\tau \, e^{i\cdot\tau} f$$

$$+ \int_{-3T_1}^{-2T_1} d\tau \, e^{i\cdot\tau} f + \ldots\ldots$$

$$= \left[1 + e^{i\cdot(-T_1)} + e^{i2\cdot(-T_1)} + \ldots\ldots\right] \tag{18}$$

$$\int_{-T_1}^{0} d\tau \, e^{i\cdot(\tau)} f[r^\circ(\tau), \phi^\circ(\tau), v^\circ(\tau)]$$

$$= \frac{1}{1 - e^{i\cdot(-T_1)}} \int_{-T_1}^{0} d\tau \, e^{i\cdot(\tau)} f[r^\circ(\tau), \phi^\circ(\tau), v^\circ(\tau)].$$

Equation (14) can now be replaced with this new
representation Eq.(18) which has the advantage of
requiring numerical evaluation of the integral over
a finite interval of time.

A consequence of using Eq. (18) as opposed to
Eq. (14) is that now the period T_1 and azimuthal
shift $\Delta\theta = \theta^\circ(-T_1)$ must be determined for each par-
ticle. Whereas using Eq. (14) involves integration
backwards in time until s remains sufficiently con-
stant, utilization of Eq. (18) requires integration
backwards in time to fixed limit which remains un-
determined until the variable of integration τ be-
comes less than that limit.

Detection of this limit is accomplished by
noting that the quantity $(r - r^\circ)$ will change sign
twice as τ goes from 0 to $-T_1$. Such a condition
can easily be tested for as each particle is
stepped backwards in time using a standard second-
order particle pusher. In addition, the integrand
is accumulated at each time step so that when the
second sign change of $[r - r^\circ(\tau)]$ is detected, an
interpolation procedure is used to provide not only
T_1 and $\Delta\theta$ but a value for the integral as well.
(The quantity $[v_r - v_r^\circ(\tau)]$ also changes sign the
second time when $\tau = -T_1$. This quantity is used
in those instances for which $r = r^\circ(\tau = 0)$ is near
an extremum in order to improve the numerical ac-
curacy of the interpolation procedures.)

The remaining integrals in Eq. (14) have been
approached in a variety of ways. The approach based

on stochastic or Monte Carlo methods has been abandoned because of the unacceptable large variance which occurs in the integral value I. Investigations are presently underway to determine the feasibility of selecting an upper limit for the velocity magnitude integration and computing all integrals in Eq. (14) by Gauss-Legendre quadrature.

We can now make application to the LHD instability. For certain rigid rotor equilibria, namely,

$$f_{jo} = \frac{n_j m_j}{2\pi T_j} F\left(\frac{H_j - \omega_j P_j}{T_j}, v_z\right),$$

where

$$P_{\theta j} = r\left[m_j v_\theta + \frac{e_j}{c} A_\theta(r)\right]$$

$$H_j = \frac{m_j}{2}(v_r^2 + v_\theta^2) + e_j \phi(r).$$

in conjunction with the assumption of charge neutrality, it is possible to write the dispersion relation for electrostatic oscillations as

$$\det\left|\frac{1}{\epsilon}\delta_{m,n} + \chi_{n,n}^e + \chi_{n,n}^i\right| = 0.$$

where the susceptibility $\chi_{n,n}^j$ is given by

$$\chi_{n,n}^j = -\frac{4\pi e_j^2}{m_j k_n^2}\left\{\int^{R_c} r\,dr\, \phi_n^* \phi_n \int d^3v \frac{1}{V_\perp}\frac{\partial f_{jo}}{\partial V_\perp}\right.$$

$$+ i(\omega - \omega_{*j})\int^{R_c} r\,dr \int d^3v \frac{1}{V_\perp}\frac{\partial f_{jo}}{\partial V_\perp}$$

$$\left.\int_{-\infty}^{0} d\tau\, \phi_n(r)\phi_n(r')e^{-i\omega\tau + il(\theta'-\theta)}\right\}. \quad (19)$$

and the electrostatic potential $\phi(r,t)$ has been assumed to have the form

$$\phi(r,t) = \phi(r)e^{-i\omega t + il\theta}.$$

with

$$\bar{\phi}(r) = \sum_n \phi_n \phi_n(r).$$

with $\phi_n(r)$ suitable radial eigenfunctions. In Eq. (19) $V_\perp \cos\phi = v_x + \omega_{*j}y$ and $V_\perp \sin\phi = v_y - \omega_{*j}x$ define polar velocity coordinates.

In dealing with the lower hybrid drift instability the motion of the plasma particles parallel to the magnetic field is irrelevant and the exact orbits of the particles perpendicular to the magnetic field may be written down. It is shown in Ref. 18 that the orbit integrals involved in Eq. (19) may be obtained in closed form in certain cases. These cases have been of great value in that they provide needed analytic results necessary for proof-testing the code.

It should be noted that it is only for the special case of a constant axial magnetic field and a linearly increasing radial electric field that the orbits may be written explicitly and attendant orbit integrals be obtained in closed form. While this case is of substantial theoretical interest in bridging the gap between local stability theory and a completely nonlocal theory, it is desirable to be able to deal with the more general field configurations within the scope of the numerical procedure.

c. Application to FLR Stabilization in the Vlasov Fluid Model. Equations of the form illustrated in Eq. (14) arise in the Vlasov fluid model when one considers the complex frequency spectrum of a small perturbation of an ideal MHD equilibrium.[1] In the fully nonlinear problem, the functional forms of $F(r,v,\omega)$ and $f(r',v',\omega')$ in Eqs. (14) and (15) are unknown functions of the perturbation. For purposes here, the ideal MHD eigenfunctions are substituted into the function forms F and f; and the resulting forms are used as trial functions in Eqs. (14) and (15). The resulting equation has the character of a dispersion relation which includes integrals over ion orbits in the unperturbed fields of the diffuse rigid rotor equilibrium.

Fig. VII-13 shows some typical ion orbits; and Fig. VII-14 shows some preliminary results obtained

Fig. VII-13.
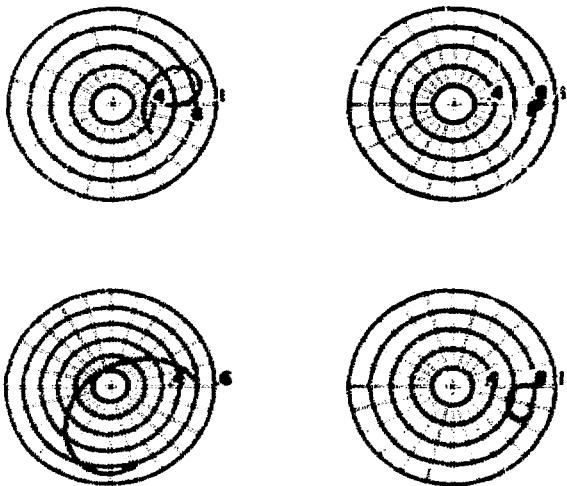
Typical ion orbits.

for the stabilization of the ideal MHD $m = 2$ instability. The results indicate stabilization of the $m = 2$ mode for $\beta = .0$ when the ratio of ion Larmor radius to plasma radius is roughly midway between the sharp boundary results of J. Freidberg[2] and L. Turner.[3]

D. MICROINSTABILITIES

This section describes results obtained on electrostatic microinstabilities, such as the LHD

Fig. VII-14.

FLR stabilization of $m = 2$ instability as the Larmor radius increases.

instability, as they apply to Z pinches and θ pinches. There is also a description of electromagnetic instabilities such as whistlers and how they heat the ions. Finally, we give some results of computer simulation leading to flute instabilities associated with the LHD instability.

1. *Electrostatic Microinstabilities.* During the first quarter, a survey of electrostatic microinstabilities was completed with the conclusion that the Lower-Hybrid Drift (LHD) instability may be involved in the diffusion of post-implosion profiles in the ZT-1 experiment. An estimate of the diffusion time associated with this instability indicates that increases in density, magnetic field, and minor radius would all be beneficial.

Although this anomalous transport may presently be masked by classical diffusion associated with low electron temperatures (possibly due to derated operation and impurity radiation), there is, as yet, no compelling reason to disregard its effect upon eventual achievement of higher electron temperatures. The LHD instability is a strong candidate because of its low threshold ($v_{drift} \sim v_{thermal\ ion}$) and its high growth rate ($\gamma \sim \sqrt{\omega_{ce}\omega_{ci}}$).

The important investigations that continue on this instability are the elucidation of finite-beta effects and computer simulation of the nonlinear saturation level of this mode under post-implosion conditions.

During the second quarter, Freidberg's Vlasov-fluid model for studying the perturbational stability of hot pinches was extended to include electron temperature and electron heat conduction. This is an important extension because the simpler model neglects terms of order T_e/T_i. (Prior to derated operation, the Scyllac full torus had $T_e/T_i \approx 0.5$.) The Vlasov-fluid code of H. R. Lewis could, in principle, handle this extended model without fundamental modifications, i.e., the expansion in Liouville eigenfunctions is still a viable method.

During the third quarter, FLR effects on the $m = 1$ mode were re-examined. Results obtained earlier by Gerwin for a diffuse, high-beta, near-theta pinch showed that the $m = 1$ growth rate was identical to that predicted by ideal MHD. These results rested upon certain assumptions made when solving the ion orbit equations. During the third quarter, said assumptions were verified analytically
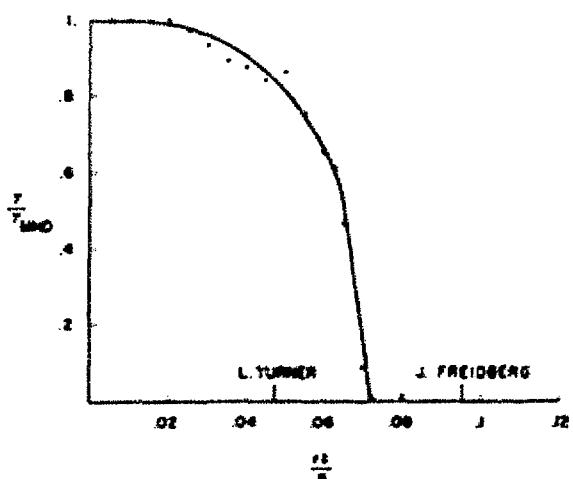
by studying the orbit equations in third order in the small parameter, Larmor radius over radial scale length. Thus, the m = 1 results now rest upon a firmer foundation.

2. *Electromagnetic Microinstabilities.* Also during the third quarter, the properties of a resonant-ion-driven whistler instability were elucidated, and its influence on anomalous resistivity and ion heating were estimated in terms of the non-linear level of fluctuation energy. This electromagnetic instability is relevant to high-beta screw pinches (such as ZT-1) because of its low threshold $(v_{drift} : v_{thermal\ ion})$, high growth rate $(\cdot \cdot _{ci})$ and short wavelength $(\cdot : \text{ion gyro-radius})$. The latter property implies that such an instability might be immune to the effects of magnetic shear and other profile inhomogeneities. A quasi-linear analysis shows that it preferentially heats the ions, in qualitative agreement with the unexpectedly hot ions found in the ZT-1 experiment. Conservative estimates of parallel electric fields near the magnetic axis (10 volts/cm) yield a non-linear fluctuation level that furnishes an ion heating time, $T_i/(dT_i/dt)$, on the order of 1 .sec, well within the pinch lifetime of ZT-1.

Important ongoing work is the computer simulation of this instability, in particular, its saturation level. Further needed work involves uncovering the effects on this mode of magnetic shear and profile inhomogeneities.

3. *Numerical simulation of microinstabilities.* Plasma simulation studies of the microinstabilities that are thought to play an important part in the anomalous effects found in imploding pinches have continued throughout the year using the particle code DARWIN.[1] The major innovation of this work has been the successful initialization of the simulations with strongly inhomogeneous, self-consistent Vlasov equilibria that model the sheath region of an imploding θ-pinch.[2] Strong flute instabilities were observed and subsequently identified with the lower-hybrid-drift instability.[3] The heating rates and anomalous resistivity were found to be in good agreement with quasilinear theory.[4] An example of what was observed is illustrated in Fig. VII-15. Contour plots of the magnetic field B_z at four different times are shown. Initially the magnetic field is strongly inhomogeneous in x (which
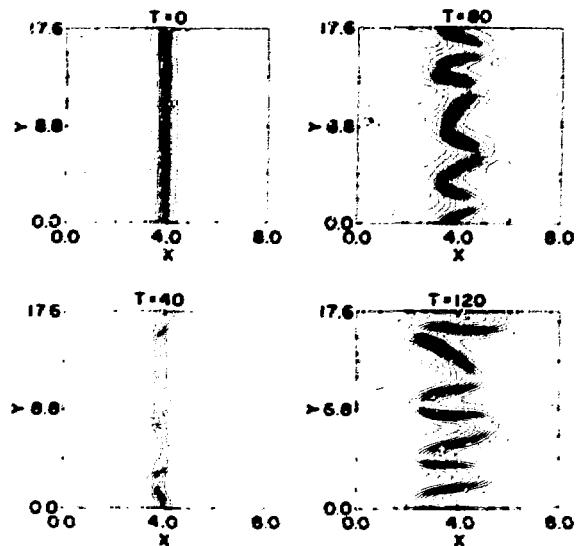
Fig. VII-15.

Contour plots of the axial magnetic field at several times showing the development of a flute instability, which has been identified as the lower-hybrid-drift instability. (See Ref. 3 for details.)

corresponds to the radial direction) and uniform in y (the θ direction). At later times a strong flute instability develops, and significantly broadens the radial profiles. The instability shows no tendency to coalesce to longer wavelengths, much like the flutes observed in actual θ-pinch experiments.[5]

A more recent effort has been aimed at understanding the properties of the newly discovered current-driven electromagnetic modes.[6] In particular, the heating rates of the electrons and ions as well as the nonlinear saturation level of the turbulence and their relation to simple theoretical predictions are of direct interest for comparing the relative contribution to the anomalous effects observed in ZT-1 of this instability to others (such as the lower-hybrid-drift instability). Preliminary results suggest that the nonlinear effects observed in the simulation are somewhat less pronounced than theory indicates.

E. EXAMINATION OF ALTERNATIVE CONCEPTS

During the year we have examined three other magnetic confinement schemes. This was done partially as an adjunct to the work of a task force set up within the division office to seek alternatives to Scyllac.

1. Dense Plasma Focus. In conjunction with
the survey undertaken by the task force an assess-
ment of the dense plasma focus (DPF) was initiated
during the fourth quarter. The worldwide interest
in this device stems from its impressive neutron
yield ($\sim 10^{12}$ D - D neutrons from less than 0.5 MJ
stored energy) and the observed scaling of this
yield as bank-energy-squared over more than an order
of magnitude in bank energy.

Two DPF configurations have been examined in
detail, and some important experimental results
have been successfully explained by our scaling laws.
In treating the scaling-up to break-even, the low
transfer efficiency of stored energy to pinch ener-
gy, c, has been explicitly included. (Here, break-
even just means that the DT fusion energy produced
is equal to the initial energy stored.)

A rough estimate as to what is needed to reach
break-even conditions can be obtained from the fol-
lowing simple considerations. Suppose the fusion
energy produced, E_f, is some fraction f of the bank
energy, E_{bnk}. Then

$$E_f = f \, E_{bnk}. \tag{20}$$

But the energy in the pinch, E_{pch}, is related to the
bank energy by the transfer efficiency, c.

$$E_{pch} = c \, E_{bnk} \tag{21}$$

where c is basically a geometrical factor for pulsed
pinch devices. Furthermore, since

$$E_{pch} = 3nT \times volume. \tag{22}$$

and

$$E_f = \frac{Q_{DT}}{4} \, n^2 \, \langle \sigma v \rangle_{DT} \times Volume \times \tau, \tag{23}$$

where $Q_{DT} = 2.8 \times 10^{-5}$ ergs is the energy released
per reaction, we immediately find from Eq. (20) a
condition on the Lawson number vs T namely

$$n\tau = \frac{f}{c} \, \frac{3T}{Q_{DT} \langle \sigma v \rangle_{DT}/4} \,. \tag{24}$$

The latest values of $\langle \sigma v \rangle_{DT}$ vs T were furnished us
by R. Krakowski. Equation (24) then leads to the
curve plotted in Fig. VII-16. This curve forms the
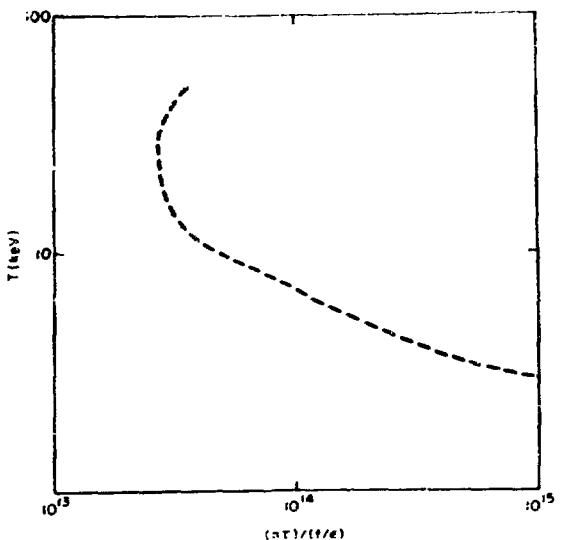
basis of our subsequent estimates. The resulting
$n\tau$-values do not differ much from those obtained by
a more detailed look at the problem which includes
Bremsstrahlung radiation and employs various re-
covery efficiencies. In this initial attempt to
consider break-even relative to DPF machines, we
have limited ourselves just to capacitive storage.

For the Mather configuration, we use the theo-
retical scaling relations which we have derived in
our forthcoming report, to go to full break-even
(f = 1 starting with the base point furnished by
DPF 5 of the Los Alamos DPF series (E_{bnk} = 120 kJ,
V_0 = 50 kV, $n_0 \sim$ 10 torr, T $\sim$ 5 keV, $n\tau \sim 6 \times 10^{12}$
sec/cm³, $c \sim 3\%$; - the temperature, Lawson number,
and transfer efficiency values are justified in our
forthcoming report). To reach full break-even by
increasing the capacitance appears useless for the
Mather configuration. With the help of Fig. VII-16,
we thus find that enormous filling pressures ($\sim$ 1
ktorr) and extreme voltages ($\sim$ 5 MV) are required.
The bank energy proves to be $\sim$ 1 GJ. (Electrode
linear dimensions would require only a factor 3 in-
crease. The temperature has increased likewise by
a factor 3 to $\sim$ 15 keV.)

The Filippov configuration has superior scaling
properties, at least on paper. Scaling with capaci-
tance becomes viable, and obviates the necessity of
going to such huge filling pressures and such extreme

voltages. As a base point, we take the Frascatti 120-kJ machine (E_{bnk} = 120 kJ, V_o = 50 kV, $n_o \sim 2$ torr, $T \sim 5$ keV, $n\tau \sim 1 \times 10^{12}$ sec/cm³, $\epsilon \sim 10\%$, - the temperature, Lawson number, and transfer efficiency values are justified in our report). With the help of Fig. VII-16 and our theoretical scaling laws, we find that break-even can be reached with filling pressures of ~ 50 torr, and sub-megavolt voltages, 750 kV. The temperature has increased by a factor 3 (to ~ 15 keV) and the capacitance by a factor ~ 150. The required bank energy is ~ 3 G Joules. A disadvantage of the Filippov device is that the required electrode radius becomes rather large, 3 meters, whereas the inter-electrode spacing should remain small (of order 5 to 10 cm) for good energy compression.

Since detailed reactor considerations have been avoided here, the above figures can only be regarded as ball-park estimates. In this same vein a factor 2 uncertainty in the required (ratio) increase in Lawson number leads to a factor of ~ 4 uncertainty in the required bank energy. Finally, we have assumed a basically thermonuclear model, and hence that acceleration or beam-target mechanisms do not determine the neutron production. This question remains open, and the answer may be device-dependent, and operation-dependent.

An important message to be broadcast by our DPF assessment is that the entire CTR effort would gain in credibility if a laboratory observation were actually made of a significant fraction of bank energy being returned in fusion neutrons. According to our scaling laws, a 1% return could be realized as follows. Scaling the Mather device at constant capacitance from DPF 5 as a base point, and using Fig. VII-16 with f = 0.01, we find 1% break-even at V_o = 200 kV, E_{bnk} = 2 MJ, and $n_o \sim 40$ torr. The pinch temperature has increased from 5 to 7 keV. The linear electrode dimensions have increased by only 20%. Similarly, for the Filippov configuration, we again take the 120-kJ Frascatti machine as a starting point and then find it possible to reach 1% break-even with V_o = 210 kV, $E_{bnk} \approx 5$ MJ, $n_o \approx 4$ torr. The capacitance has about doubled (from 100 μF), the electrode radius has increased from 15 to 40 cm, and the pinch temperature has tripled to 15 keV. The pinch length has remained constant at ~ 10 cm. These theoretical predictions are fairly consistent with the yields obtained by the extrapolation of worldwide experimental results accrued over many years.

With the above modest changes from present devices (excepting the high-voltage requirement), one might observe a DT-equivalent 1% return for the first time in the laboratory. The primary technical problems to be mastered in such a program are to learn how to run a DPF machine at higher pressures and at voltages exceeding 100 kV. The basic physics problems yet outstanding here are: 1) the observed pinch lifetime (or its radiation pulse-widths), and 2) the mechanisms of neutron production. In our opinion, progress could be forthcoming in all these areas from a moderate-sized program working with a 100-kJ bank.

2. Status Report on the High-Beta "Figure-Eight" Stellarator Configuration. The question of the toroidal MHD equilibrium and stability of a high-pressure, high-beta plasma column has seen a revival of interest in recent months. This development was prompted to a great extent by a conjecture and supporting preliminary calculations made by Shafranov and Mikhailovsky[25,26] for the case of a current-carrying tokamak equilibrium as well as for the case of a "figure-eight" stellarator equilibrium with zero net toroidal current. They found that with increasing plasma pressure the growth rate of flute instabilities does not increase, as one might think at first glance, but actually decreases. The physical origin of this self-stabilization effect is the diamagnetic well set up by the currents in the high-beta plasma.

In view of the stability difficulties of the standard Scyllac equilibrium, in which unstable m = 1 modes dominate plasma behavior, it was tempting to speculate that these difficulties might be overcome in a high-beta stellarator equilibrium of the Shafranov-Mikhailovsky type, which features large helical magnetic field line excursions and large rotational transforms (of order 180 degrees per field periodicity length). In such equilibria the diamagnetic self-stabilization effect is generated by the helical shift of the magnetic axis as well as by the deformation of the cross-sectional shape of the magnetic surfaces. The shift and deformation are lower order quantities (i.e., of

larger magnitude) than assumed in usual perturbation theory.

The geometrical properties of such equilibria were investigated numerically by Kondoh et al..[27] who set themselves the task of minimizing the transverse plasma column excursions in such a system. They found that for high beta values the excursions could be accommodated within a practical conducting coil radius for a large enough number of helical periodicity sections around the torus. Preliminary experimental results on helical magnetic axis systems have been reported for the Asperator-K device[28] and more recently and informally for the Garching High-Beta Stellarator. The latter device sees no unfavorable effects attributable to the large field line excursions.

Unfortunately, the first flush of optimism is tempered by a more critical appraisal of this confinement system. It must be noted that the work of Ref. 27 deals with the equilibrium properties of the system, and not with its stability as has sometimes been erroneously assumed. A relationship between stability and the direction of equilibrium shift of the plasma column is not established for the present truly three-dimensional configuration, in which neither Fourier analysis in the toroidal direction, nor off-axis expansion, nor perturbation theory in line excursion parameters are valid. In fact, the equilibrium analysis of Ref. 27 uses the second of these techniques for lack of a better tool, and the numerical results are accordingly suspect. The stability analysis of Refs. 25 and 26 has been restricted to pressure-driven, long-wavelength flute modes which seem indeed to be stabilized according to the Mercier criterion[29]. Yet serious questions remain with respect to shorter wavelength ballooning modes and localized exchanges due to unfavorable field line curvature. In view of the analytical difficulties in performing the required calculations for diffuse plasma and field profiles, it is likely that credible stability predictions can be made only numerically for some specific equilibrium model, and here also the inherent three-dimensional nature of the problem will make results slow in coming.

Preliminary experimental information, on which we must mainly rely at present, gives some cause for optimism. However, the best attitude to adopt currently is one of caution, especially with respect to

a possible application of this configuration as a Scyllac alternative. The unresolved questions are at least as formidable as those for Scyllac itself, and the theoretical basis for a sound proposal is still lacking. Planned Scyllac experiments with large line excursions (~3) may provide some needed guidance in this unexplored area of plasma confinement physics.

3. Equilibria and MHD Studies for a High Beta Tokamak. In November a committee was formed to study the possibilities of building a modest high-beta tokamak experiment at Los Alamos. At this time interest was revived in a study on high beta tokamaks made in 1974.[13] Our previous calculations on the belt pinch are also closely related to the elongated cross-section tokamak.[11]

The race track shape for the Los Alamos high beta tokamak has been decided on and a subroutine has been developed to solve for the equilibrium in a device with a boundary cross section of any shape. (Previous work has been done on devices with circular or rectangular cross sections.) The code will be used to 1) calculate the equilibria and fields for design and engineering considerations, 2) calculate the q and Mercier Q for localized instabilities, 3) calculate the effect of force-free fields, 4) calculate the energy beta and poloidal beta, and 5) possibly calculate the global stability properties as predicted by a stability method which discretizes δW as a large quadratic form.[12]

REFERENCES:

1. C. A. Anderson, O. C. Zienkiewicz, "Spontaneous Ignition: Finite Element Solutions for Steady and Transient Conditions," J. of Heat Trans. Transactions of ASME, Aug. 1974.

2. Private Communication with C. A. Anderson and W. A. Cook (ADO).

3. C. Mercier, Nucl. Fusion 1, 47 (1960).

4. J. P. Freidberg and F. L. Ribe, Comments on Plasma Physics and Controlled Fusion 1, 163 (1972).

5. J. P. Freidberg, "Vlasov-Fluid Model for Studying Gross Stability of High-β Plasmas", Phys. Fluids 15, 1102 (1972).

6. E. Fünfer, M. Kaufmann, J. Neuhauser, and G. Schramm, "Recent High Beta Stellarator Experiments at Garching," Seventh Fusion Conference, Lausanne, 1975; M. Kaufmann et al., "Investigation of the m = 2 Mode on High Beta

Stellarator ISAR T1 - B," Max Planck Institut
für Plasmaphysik, Garching, West Germany.

7. E. L. Cantrell et al., "Scyllac Feedback Sta-
    bilization Experiments," Third Topical Confer-
    ence on Pulsed High Beta Plasmas, Culham
    Laboratories, England, September 9-12, 1975, to
    be published.

8. H. R. Lewis and J. P. Freidberg, Proceedings of
    the Fifth European Conference on Controlled
    Fusion and Plasma Physics (Grenoble, France,
    August 21-25, 1972), paper 41.

9. H. R. Lewis and L. Turner, "Stability Analysis
    of Sharp-Boundary Vlasov-Fluid Screw-Pinch
    Equilibria," Third Topical Conference on Pulsed
    High Beta Plasmas, Culham Laboratories, England,
    September 9-12, 1975, to be published.

10. B. L. Buzbee, G. H. Golub, and H. R. Lewis,
    Proceedings of the Seventh Conference on Numer-
    ical Simulation of Plasmas held at the Courant
    Institute, New York University, June 2-4, 1975
    (pp. 196-198).

11. L. Turner, Finite-Larmor-Radius Stabilization
    in a Sharp-Boundary Vlasov-Fluid Screw-Pinch,
    to be published.

12. I. O. Kerner, Numerische Mathematik $\underline{8}$, 290
    (1966).

13. O. Aberth, Mathematics of Computation $\underline{27}$, 339
    (1973).

14. W. B. Riesenfeld et al., Los Alamos Scientific
    Laboratory Report LA-6044-PR (1975).

15. L. Spitzer, Jr., "Physics of Fully Ionized
    Gases," 1961 (J. Wiley & Sons, NY).

16. A. G. Sgro & C. W. Nielson, Phys. Fluids, to
    be published in Jan. 1976.

17. W. Lotz, Ap. J. Suppl. $\underline{8}$, 207 (1967).

18. R. C. Davidson, "Vlasov Equilibrium and Non-
    local Stability Properties of an Inhomogeneous
    Plasma Column," to be published.

19. C. W. Nielson and H. R. Lewis, Meth. Comp.
    Phys. $\underline{16}$ (1975).

20. D. W. Hewett, C. W. Nielson, and D. Winske,
    Phys. Fluids $\underline{19}$, in press (1976).

21. D. Winske and D. W. Hewett, Phys. Rev. Lett.
    $\underline{35}$, 937 (1975).

22. R. C. Davidson and N. T. Gladd, Phys. Fluids
    $\underline{18}$, 1327 (1975).

23. K. F. McKenna, R. Kristal, and E. L.
    Zimmerman, Phys. Fluids $\underline{18}$, 1371 (1975).

24. S. P. Garry, R. A. Gerwin, and D. W. Forslund,
    Phys. Fluids $\underline{19}$, in press (1975).

25. V. D. Shafranov and A. B. Mikhailovsky, Sov.
    Phys.-JETP Letters to the Editor $\underline{18}$, 124
    (1973).

26. V. D. Shafranov and A. B. Mikhailovsky, Sov.
    Phys.-JETP $\underline{39}$, 88 (1974).

27. Y. Kondoh, S. Nagao, K. Sugita, and
    H. Watanabe, Journal of the Physical Society
    of Japan $\underline{36}$, 852 (1974).

28. K. Koyama, Y. Suzuki, and S. Nagao, Journal of
    the Physical Society of Japan $\underline{37}$, 209 (1974).

29. C. Mercier, Nuclear Fusion $\underline{1}$, 47 (1960) and
    Nuclear Fusion Supplement $\underline{2}$, 801 (1962).

30. D. A. Baker and L. W. Mann, "Equilibria and
    MHD Studies for a High Beta Tokamak," Bul.
    Amer. Phys. Soc. $\underline{19}$, 642 (1974)

31. D. A. Baker and L. W. Mann, "Belt Pinch Equi-
    libria Studies," Bul. Amer. Phys. Soc. $\underline{18}$,
    1327 (1973).

32. D. A. Baker and L. W. Mann, Proc. Second Topi-
    cal Conf. on Pulsed High Beta Plasmas,
    Garching (1972).

VIII. EXPERIMENTAL PLASMA PHYSICS

H. Dreicer, M. E. Banton,
J. C. Ingraham, F. Wittman, B. L. Wright

A.   SUMMARY (J. C. Ingraham)*

The Experimental Plasma Physics group's main efforts continue to be directed toward the understanding of the mechanisms of electromagnetic energy absorption in a plasma, and the resultant plasma heating and energy transport. At the start of 1975 the accomplishments of the group consisted of detailed measurements of the interaction of a microwave signal in a plasma for the case where the signal frequency is near the electron plasma frequency.[1-5] Measurement of the low-power absorption[1] provided quantitative confirmation of the theoretically predicted linear high frequency resistivity[6] of a fully ionized plasma. At high powers it was found that the absorption rate of the microwave signal could be increased or enhanced above the low-power rate through excitation of parametric instabilities[7,8] by the microwave signal itself. On the other hand, it was found that at intermediate or high powers under conditions where no parametric instabilities were excited, the microwave absorption rate was actually <u>reduced</u> below the low-power rate through nonlinear effects of the oscillating microwave electric field on the Rutherford scattering cross section of electrons with ions.[1] This observed reduction was considerably greater than that predicted by theory.[9] The deposition of energy in the plasma at high powers resulted in body heating of electrons in all cases, but in some of those cases where parametric instabilities were excited, nearly all of the microwave energy was deposited in a small fraction (less than one percent) of electrons in the tail of the electron energy distribution.[2]

During this past year we have extended these studies of high-frequency absorption in two directions:

1) The high-frequency spectrum of plasma waves parametrically excited by the microwave signal at high powers has been measured (H. Dreicer and J. C. Ingraham).[10] The observations show that <u>both</u> the decay[7] and oscillating-two-stream[8] parametric

instabilities are excited. This is the first laboratory observation of excitation of the oscillating-two-stream instability by an electromagnetic pump. Results are being prepared for publication.

2) We are studying the absorption of a small test microwave signal in a plasma made parametrically unstable by a separate high-power driver microwave signal (M. E. Banton, H. Dreicer, J. C. Ingraham, and B. L. Wright).[11] We expect that by separating the absorption measurement task from the task of exciting the instabilities we will be able to learn more about the details of the process that leads to enhanced absorption. Experimental results to date show that a test signal separated in frequency from the driver signal by only 15 MHz out of 2000 MHz, experiences considerably less enhanced absorption than does the driver signal. Furthermore, for the set of conditions studied, the enhanced absorption of the test signal depends on whether the test signal frequency is higher than, or lower than the driver frequency, being much weaker for the former case.

The experiment for studying parametric instability excitation with $T_e \sim T_i$ (J. H. Brownell, H. Dreicer, and J. C. Ingraham) was terminated at the end of September because plasma density fluctuations in the plasma prohibited measurements of enhanced absorption with sufficient accuracy. We plan in the future to repeat these experiments on the Q-machine plasma with independently heated electrons, since there are as yet no definitive studies in the literature of enhanced absorption near the electron plasma frequency in the case where $T_e \sim T_i$.

A short-term experiment was carried out (J. E. Hammell** and J. C. Ingraham) to reproduce the reportedly large neutron bursts ($\sim 10^{14}$) observed by D. Y. Cheng.[12] Attempts to reproduce this result were unsuccessful,[13] and the experiment was terminated after seven months operation. Experimental conditions were varied widely but there was not sufficient time to allow complete evaluation of the Cheng experiment.

B. ELECTROMAGNETIC WAVE ABSORPTION, PLASMA HEATING, AND ENERGY TRANSPORT

We have extended our studies on the mechanisms influencing electromagnetic wave absorption in a plasma, and the associated plasma heating and energy transport. We utilize high-Q microwave resonators (Q ~20 000) combined with miniature high-frequency Langmuir probes to study these effects in a single-ended, fully ionized Q-machine potassium plasma column ($T_e - T_i \approx 2250°K$, $n \approx 1 - 5 \times 10^{10}$ cm^{-1}, diameter ≈ 2.5 cm, length ~200 cm) as shown schematically in Fig. VIII-1. A strong magnetic field (≈ 5 kG) restricts the radial motion of the plasma. The plasma ions drift with a velocity of 10^5 cm/s to the cold plate where they are collected. All ambient plasma electrons are reflected from the cold plate by a negative bias voltage. The microwave excitation experiments are performed on a pulsed (~ 10 μs), repetitive basis, so as to minimize perturbing effects on the plasma column.

In Sec. B.1 we present frequency and wavelength measurements of the high-frequency waves that are parametrically excited by a microwave pump signal in the single mode resonator (Fig. VIII-1). In Sec. B.2 and B.3 we describe, respectively, the technique, and the principal results of a new technique that utilizes the Dual-Mode-Resonator (DMR) shown in Fig. VIII-1, and which makes possible the measurement of the absorption of a weak test signal in a plasma having a controlled level of plasma turbulence. In Sec. B.4 we present some qualitative results showing how heat flow may be studied by using one resonator to heat the plasma, and a second resonator some distance removed to detect the arrival of the heat pulse produced at the first resonator.

1. Spectral Identification of the High-Frequency Parametric-Decay and Oscillating-Two-Stream Waves Excited by a Microwave Pump. A tiny high-frequency probe (P) has been used to measure the high-frequency wave spectra parametrically excited within the Single Mode Resonator (Fig. VIII-1) by a strong microwave pump signal. Similar probes are utilized outside of the resonator to detect waves that escape from the resonator by propagation along the plasma column.

It is important to note that such waves are observed to escape from the resonator only when the microwave pump frequency is less than the plasma
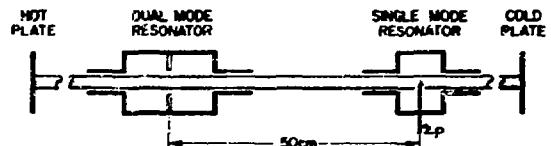
Fig. VIII-1.

Schematic of Q-machine showing single-mode and dual-mode resonators.

frequency, that is, for the overdense case. In the underdense case all plasma waves excited are damped before they can escape from the resonator volume so that they can be observed only by using a probe inside of the resonator. These observations are in good agreement with the dispersion relation for plasma wave propagation in our plasma column, which shows that collisional and Landau damping act strongly on the electron plasma waves in an underdense plasma, whereas the damping is weak on such waves in an overdense plasma (Gould-Trivelpiece waves).

In a plasma without ion drift the electron plasma wave of the parametric decay (PD) instability excited by the microwave pump would appear as a lower sideband frequency to the pump frequency. The separation frequency would correspond to the ion acoustic wave that is excited along with the electron wave. In the case where the ions drift at a velocity v_D, however, the lower sideband to the pump is split into a doublet corresponding to the cases where the parametrically-excited ion wave propagates either parallel, or antiparallel, to the ion drift. The simple picture of this Doppler splitting would suggest that the doublet splitting frequency would be $2 k_{\parallel} v_D/2\pi$, where $k_{\parallel}$ is the component of the propagation vector of the excited waves parallel to the drift. In fact, the predictions of a rather complete computer code,[14] which we have modified to include particle drift and a dc magnetic field, indicate a doublet splitting more on the order of $1.65 k_{\parallel} v_D/2\pi$. This difference arises from the fact that the electrons do not drift with the ions but have a zero drift velocity relative to the laboratory frame. Thus, with an independent measurement of v_D, it becomes possible to measure the wavelength

101

of these waves as well as their frequencies using only a single probe.

The ion drift also has an important effect on the electron wave spectrum excited as a result of the oscillating-two-stream (OTS) instability, which theory predicts should also be present in our experiment. For a plasma without drift the ion disturbance excited in the OTS instability does not oscillate, and therefore the electron wave will have a frequency equal to the pump frequency and thus be extremely difficult to observe. With ion drift, however, the electron wave frequency is shifted away from the pump frequency to both a lower and an upper sideband, thus becoming detectable.

Figure VIII-2 shows typical spectrum analyzer displays of the signal of the probe in the resonator in an underdense plasma for three levels of the ratio of the microwave pump power P, to P_T, the microwave power at the threshold for production of anomalous absorption and hot electrons.[1,2,3,5] It should be noted that since all of our experiments are performed on a pulsed, repetitive basis, great care must be exercised in producing such spectrum analyzer traces so as to eliminate sideband structure on the pump frequency because of the turn-on and turn-off of the pump power.

As this threshold is exceeded three lower frequency sidebands appear relative to the pump frequency at f_0. These features are labeled 1, 2, and 3 for the intermediate-power level shown in the figure.

By comparison with theory (for an infinite homogeneous plasma) we have identified features 1 and 2 as the doublet of the PD instability and feature 3 as the lower sideband of the OTS instability. This identification is based on both wavelength and

frequency measurements of the waves. For features 1 and 2 we have measured the doublet splitting as a function of ω_p/ω, and plotted the resultant $k_{\parallel}\lambda_D$ values for the underdense case for the waves on Fig. VIII-3. Theoretical curves for propagation of the excited PD waves parallel to the dc magnetic field ($\cos\theta = 1.0$) and at a slight angle ($\cos\theta = 0.95$) are shown for comparison. The better agreement for the $\cos\theta = 0.95$ may arise because of finite plasma effects on the waves, since it is likely the excited waves must propagate at some finite angle to the magnetic field in order to satisfy boundary conditions at the plasma edge.

In Fig. VIII-4 the three lower sideband-pump separation frequencies are plotted for the underdense case, versus ω_p^2/ω^2. The theoretically predicted frequencies for $\cos\theta = 1.0$ for the PD instability (D1 and D2) and the OTS instability are also shown. It is seen that the observed PD frequencies are considerably larger than predicted by theory, but as in the case of the wavelengths in Fig. VIII-3, estimates show that propagation of the excited waves at a slight angle to the magnetic field can bring the theory into better agreement with experiment.

In the overdense case where the waves propagate freely out of the resonator along the plasma column, we observe the same three lower sideband features on a probe outside of the resonator, but in addition, a fourth lower sideband feature is seen with a separation from the pump equal to the ion plasma frequency,

$$\omega_p^2/\omega^2 = 0.9$$

P/P_T = 1.1   P/P_T = 1.6   P/P_Y = 3.3

Resonator Probe

1 2 3 f_0

2 MHz/DIV

Fig. VIII-2.

Spectrum analyzer display of signal on probe inside resonator.
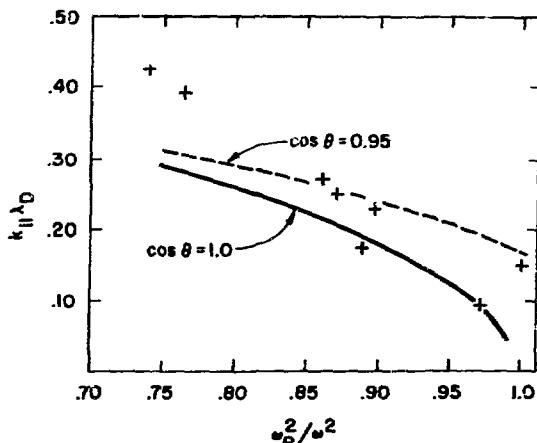
Fig. VIII-3.

Comparison of experimentally measured wavelengths with theoretical predictions for infinite homogeneous plasma.
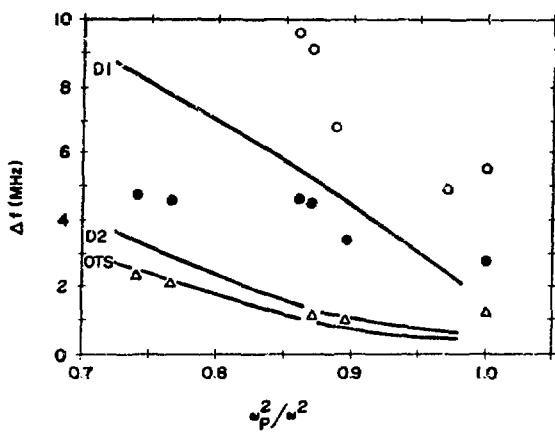
Comparison of experimentally measured sideband pump separation frequencies with theory for infinite homogenous plasma (underdense case).

Comparison of experimentally measured sideband pump separation frequencies with theory for infinite homogeneous plasma (overdense case).

f_{pi}, as shown in Fig. VIII-5. Once again features 1, 2, and 3 are compared with theory for the case where the waves propagate at the angle corresponding to the minimum threshold (for the overdense case this angle is given by $\cos \theta \simeq \omega/\omega_p$). The agreement in frequencies and wavelength is greatly improved if a theoretical angle only a few degrees larger is assumed, once again indicating that the finite geometry of the plasma may be playing a role.

Experimentally it is observed that as the pump power is increased above threshold the sideband separation frequencies increase (for example, compare the separation frequencies in Fig. VIII-3 for P/P_T = 1.6 and 3.0). Since it is always necessary to operate somewhat above threshold, typically P/P_T = 1.5 to 2.0, in order to detect the sidebands, it is quite likely that this effect also plays a role in causing the observed sideband separation frequencies to be larger than theory. Another important experimental effect is the perturbation on the plasma density introduced by the probe in the resonator. The probe lowers the density in the resonator, especially on the downstream side of the probe (relative to the ion drift). Though an approximate correction (about 5 percent) has been applied to the average density in plotting the data of Figs. VIII-3 and VIII-4 (a probe <u>outside</u> the resonator was used in collecting the data of Fig.

VIII-5), it is likely that a further density reduction correction should be applied in plotting the data to account for the strong density reduction in the immediate vicinity of the probe. As can be seen from Figs. VIII-3 and VIII-4 this could also bring the data and theory into better agreement.

The new feature at separation of f_{pi} from the pump, which appears only for the overdense case, shows no Doppler splitting, thus suggesting that the low-frequency mode at f_{pi} propagates nearly perpendicular to the ion drift. Thus, it is possible that the low-frequency mode associated with this new feature is the lower hybrid wave.[15] This feature may also be the mode studied earlier by Chu and Hendel.[16]

These results are the first laboratory observation of the excitation of the OTS instability by an electromagnetic pump. The fact that both the PD and OTS instabilities are simultaneously excited and could therefore interact nonlinearly with each other is of special importance in interpreting our previously published observations of anomalous absorption and hot electron production.[1-3] Also, it is predicted theoretically that the OTS instability can generate very intense localized electric fields ("Spikons"),[17] which in turn are predicted to cause a bump in the tail of the velocity distribution of the hot electrons produced[18] in a parametrically unstable plasma. Our earlier observation[2] of such

a bump in the tail of the electron velocity distribution combined with our current identification of the OTS instability for these cases tends then to confirm the above theoretical predictions.

2. *Principles of Operation of the Dual-Mode Resonator.* In previous studies of anomalous absorption, a simple cylindrical resonator operating in the TM_{010} mode was used to apply microwave fields to the plasma column. The dual-mode resonator now in use (Fig. VIII-1) provides a method for simultaneously applying two such fields at frequencies that differ by a controlled amount. It consists essentially of two cylindrical sections coupled by a circular opening in their common wall. Because of this coupling, the TM_{010} fields in each section--which normally would share the same resonant frequency near 2 000 MHz--combine to form modes of opposite symmetry and slightly different frequency. As illustrated in Fig. VIII-6, both modes provide AC electric fields parallel to the column axis, but the mode with opposing fields in the two sections has a frequency about 20 MHz higher than the mode with aligned fields. The degree of frequency separation between the two modes is governed both by the dimensions of the circular coupling hole and, to a lesser extent, by the plasma column size and density. Computer routines used to calculate resonator fields and frequencies in earlier experiments have been extended to give reliable results for the dual-mode resonator as well.

In the context of the experiment, one of the two resonator modes is operated at a moderately high field strength so as to induce a controllable level of parametric instability in the plasma column. This mode, whether at the upper or lower frequency is called the driver mode. The remaining mode is then simultaneously operated at a strength too low to affect the plasma directly. It is called the test mode and it is used simply to probe the plasma AC resistivity at a frequency close to that of the driver.

The principal techniques of the experiment are identical to those previously reported for simpler resonators. To maintain the excitation of a given mode, a microwave signal produced by that mode is weakly coupled out of the resonator, amplified, and adjusted in phase so that it may be fed back to the resonator as a source of further oscillations at the
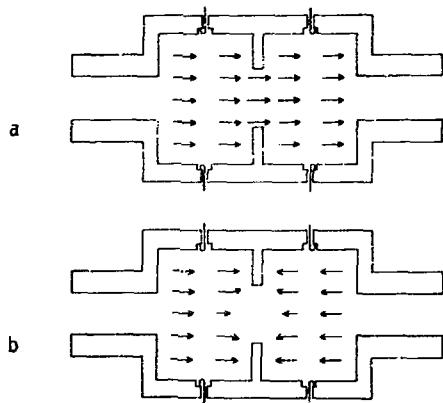
Fig. VIII-6.
(a) *Lower frequency mode;* (b) *Upper frequency mode.*

proper frequency. As in prior work, these self-oscillating feedback circuits also include attenuators for control of power level and fast microwave switches for pulsed operation. The rate of microwave absorption by the plasma is measured by observing the rate of decay of microwave energy stored in the resonator after the excitation pulse is switched off. The resonant Q factors so obtained are typically 17 000 without plasma, 9 000 with classically absorbing plasma, and a range of lower values if absorption is anomalous.

Despite heavy dependence on earlier methods, achieving simultaneous operation of two nearly degenerate modes required further development of the external feedback circuits. In particular, a single microwave pickup probe coupled to the resonator field will generally receive both the strong driver and weak test signals. These two components must then be extracted and isolated in separate feedback systems. The degree of isolation necessary is determined by two considerations:

(1) The test and driver signals used for rate-of-decay measurements of absorption must be free of interference (beats) from the unwanted component.

(2) If a signal leaked through the "wrong" feedback circuit is too strong, it may provide residual excitation that influences the rate of decay of an otherwise switched-off mode.
Because of these constraints, an isolation factor of about 70 Db is needed in the test circuit; about 40 Db in the driver circuit. The required isolation

is achieved in two stages. The first stage takes advantage of the geometric difference between the two modes. Matched pickup probes couple signals out from both sections of the resonator. These signals pass through a network of simple tees that produces their sum at one output and their difference at a second output. Because of the symmetry of the fields in the resonator sections, these sum and difference combinations represent largely the driver or the test mode oscillations. Fine tuning is accomplished by trimming an attenuator and two phase shifters included in the network. The second stage of isolation takes advantage of t. frequency difference of the two modes and involves the use of controllable narrow-band filters. In the present experiment, these filters provide an additional 30 Db of isolation, yet their bandwidth is sufficient to pass all the essential time-dependent signals without distortion.

In the course of early trials with dual-mode operation a number of minor transient effects were observed that were unrelated to the isolation problems discussed above. These effects were successfully analyzed by a theory for the response of driven, damped, coupled, harmonic oscillators. The theory indicates the importance of balancing the resonator sections so that their natural resonant frequencies--without coupling--are well matched. It further shows how transient effects can be eliminated by having the symmetry of each resonator input signal agree with that of the mode to be excited. Both these suggestions have been adopted with good results: (1) the resonator balance has been successfully measured and adjusted; and (2) a sum and difference network (similar to that used at the outputs) has been used to symmetrize the driver and test signals as they are applied to microwave input probes on each section.

3. *Absorption of a Weak Microwave Signal by Controlled Levels of Plasma Turbulence.* By utilizing the Dual Mode Resonator technique described in the previous section we are able to study the absorption of a weak microwave signal caused by controlled levels of plasma turbulence: One of the resonator modes (Test Mode) is operated at a very low level of power and the other mode (Driver Mode) is operated at a high-power level so as to create adjustable levels of plasma turbulence through

excitation of the PD and OTS instabilities already discussed in Sec. B.1. The frequency separation between the test and driver signals ranged between 15 and 20 MHz for the cases described below.

In Fig. VIII-7 we show the measured value at threshold of the ratio of the ac drift speed $v_E = eE_0/m_e\omega$ of the electrons to the thermal speed $v_T = \sqrt{2kT_e/m_e}$ of the electrons as a function of ω_p^2/ω^2. Our test signal is chosen to be at least 13 Db below the minimum threshold. The driver signal ranges from just below to well above the threshold. For the case where the test signal is $\underline{less}$ than the driver frequency and $\omega_p^2/\omega^2 \gtrsim 0.8$ we observe a marked increase in the test absorption, provided the driver power is sufficiently far above threshold as shown in Fig. VIII-8. Both driver and test absorption, ($\sim \Delta \ 1/Q$) are plotted on the figure as a function of driver power, and it is apparent that the test absorption is considerably less than the driver absorption for all driver powers above threshold. At lower densities ($\omega_p^2/\omega^2 \simeq 0.65$) the test and driver absorption appear in some preliminary measurements to be more nearly the same at all driver powers for
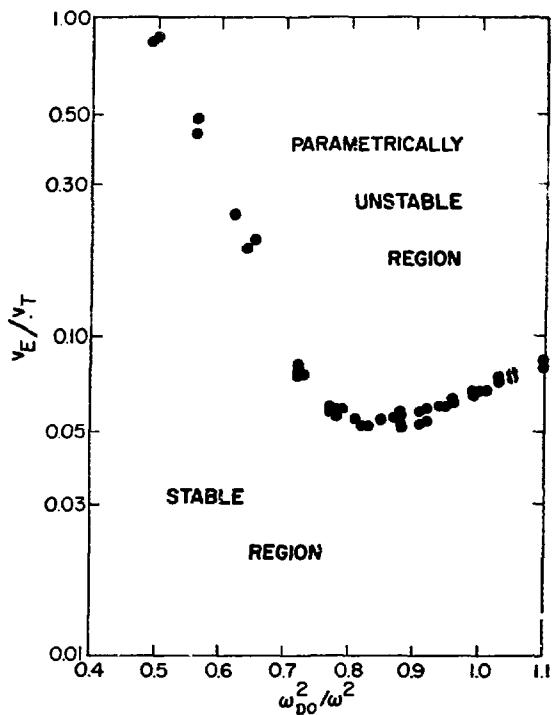
Fig. VIII-7.

Experimental threshold curve for parametric instabilities.

105
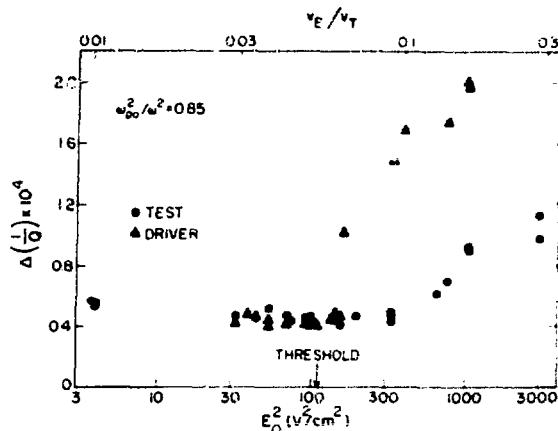
Fig. VIII-8.

Driver and test absorption as a function of driver power. Test frequency less than driver frequency.

Fig. VIII-9.

Driver and test absorption as a function of time. Test frequency greater than driver frequency.

the case where the test frequency is less than the driver power. It may be noteworthy that in the former case ($\omega_p^2/\omega^2 \gtrsim 0.8$), where the driver and test absorptions differ considerably above threshold, the collisional damping of the parametrically excited waves plays an important role, whereas at $\omega_p^2/\omega^2 \approx 0.65$, Landau damping of the excited waves is predominant.

In the case where the two resonator mode roles are reversed, so that the test frequency is higher than the driver frequency, strikingly different results are obtained: at $\omega_p^2/\omega^2 \gtrsim 0.8$ the test mode absorption is less than it was when the test was the lower frequency. As a matter of fact the measured test absorption is actually less with the driver on, than with the driver off, as shown in Fig. VIII-9. In Fig. VIII-9 is plotted the test and driver absorption ($\sim \Delta$ i/Q) as a function of time for the case where the driver power is 7 dB above threshold. As expected, the driver absorption jumps up to a high value after the driver power is turned on at time zero, but the test absorption actually decreases, except for a very early transient period, $t < 1.0$ μs, to be discussed below. Estimates indicate that this decrease of absorption in the test signal can be explained by heating of the electrons by the driver signal, which reduces the electron-ion collision rate, but only if there is sufficiently little enhanced absorption caused by the turbulence, so as not to mask the effect.

In other words, it appears that the turbulence-enhanced absorption on the test signal for this case is small or absent. Subsequent measurements have shown that when the test signal is the upper frequency, it does experience turbulence-enhanced absorption provided the driver power is increased to levels greater than 7 dB above threshold.

For comparison, Fig. VIII-10 shows the driver and test absorption as a function of time under the same conditions as Fig. VIII-9 (driver 7 dB above threshold), but where the test is the lower frequency. It is apparent that the test signal for this case does experience some enhanced absorption because of the turbulence, in agreement with the data of Fig. VIII-8.

Returning to the case of Fig. VIII-9 again, we have found that at early times ($t < 1.0$ μs) during the transient build-up of the instability, the test signal does experience enhanced absorption at a very high rate, even though it may experience little or no enhanced absorption in the steady state. This is shown clearly in Fig. VIII-11 where driver and test power levels are plotted as a function of time on an expanded time scale near the time of instability onset. In this particular case the excitation power to the test mode has been terminated some time before time zero so that what is observed at the test power output port is a sample of the freely decaying test mode energy in the resonator. Thus,
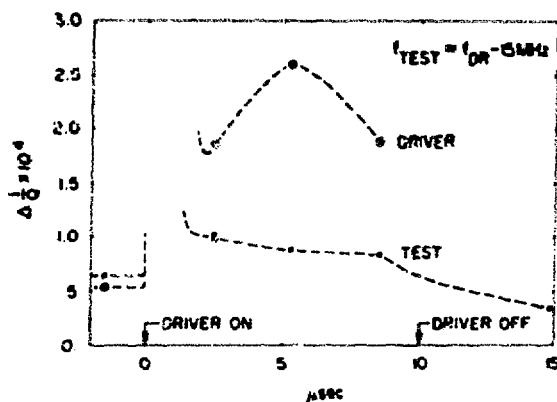
Fig. VIII-10.

*Driver and test absorption as a function of time.
Test frequency less than driver frequency.*

Fig. VIII-11.

Driver and test power as a function of time.

the absorption rate experienced by the test mode is proportional to the magnitude of the logarithmic slope of this test power decay curve. While the test power is decaying the driver signal is rapidly turned on. The driver power increases up to about $t = 0.3$ μs when the instability onset occurs, and decreases somewhat, thereafter, as the instability approaches a steady-state excitation level. The interesting feature to note is the sharp increase in the rate of decay of the test power shortly after instability onset. This increased rate of decay corresponds to a plasma absorption rate that is about 10 times the absorption rate of the test caused by the plasma in the absence of the driver. It corresponds to a value of $\sim 1/Q = 5.6$ 10^{-} and hence, would be too large to be plotted on the scale of Fig. VIII-9. For times greater than about 1 μs the test power absorption has decreased to the levels plotted on Fig. VIII-9.

These results suggest that there is much information to be gained about the mechanisms of turbulent electromagnetic wave absorption by studying the test signal absorption as a function of mode separation frequency and ω_p^2/ω^2. It is possible that the stronger enhanced absorption of the test when it is lower in frequency than the driver is related to the observations in Sec. B.1 that the spectra of parametrically excited plasma waves occur primarily on the low-frequency side of the pump, and as the

pump power is increased the observed spectra spread to greater separations in frequency from the driver (i.e., towards the test frequency if it is lower than the driver), whereas little high-frequency wave spectra is observed on the high-frequency side of the driver (cf Fig. VIII-2). On the other hand, the very strong absorption observed in the test signal, even as the upper frequency, during the early transient buildup of the instability is intriguing, but various possible explanations have not yet been subjected to experimental test.

4. *Electron Heat Flow Parallel to a Magnetic Field.* We have initiated studies of the electron heat flow parallel to a dc magnetic field. As part of the study, heat will be generated locally on a pulsed basis in a plasma, and the propagation of the resultant heat wave away from the heat source studied. Our microwave measurements of the classical low-field plasma absorption yield, as a by-product, a measurement of the electron temperature through the $T_e^{-3/2}$ dependence of the electron-ion collision rate. This temperature measurement technique, which is primarily sensitive to the electrons in the body of the distribution function, complements the probe and energy analyzer techniques, which are primarily sensitive to the electrons in the tail of the distribution function. To demonstrate the principal of the microwave technique the single mode resonator of Fig. VIII-1 is used as a plasma heater, and one

mode of the dual-mode resonator 50 cm distant is used as a sensor of changes of electron temperature. As shown in Fig. VIII-12(a) the heater pulse is applied for about 10 μs. The sensing mode is excited with a constant excitation power beginning prior to the application of the heater pulse. Under these conditions any change of the power level within the sensing resonator is directly related to a change of plasma absorption, which in turn is related to electron temperature. Thus, the increase in the power level of the sensing mode shown in the figure, which begins about 5 μs after the start of the heater pulse, occurs because hot electrons are beginning to reach the sensing resonator after having diffused from the heating resonator. It is interesting to note that the velocity of the heat-wave front thus determined is 10^7 cm/s, which is of the order of the electron thermal speed. In Fig. VIII-12(b) the compressed time scale shows also how this technique can be used to study at later times the decay of the plasma temperature, after the heating has been terminated, and thus to study the effects of boundary conditions on heat transport.

C. EXPLODING-LINER INITIATED HIGH-DENSITY Z PINCH

The High-Density Z-Pinch experiment was performed on a short-term basis (seven months) in an attempt to quickly reproduce the results of D. Y. Cheng[12] on the exploding-liner initiated high-density Z-pinch, in which a very large burst of neutrons ($\sim 10^{14}$) was reportedly produced in two out of a large number of shots. The experimental parameters were varied over a range including those in the original experiments. In none of these cases were neutrons detected,[13] placing an upper limit on neutron production of 10^5 neutrons. Unfortunately, there was not sufficient time to allow a complete evaluation of the Cheng experiment.
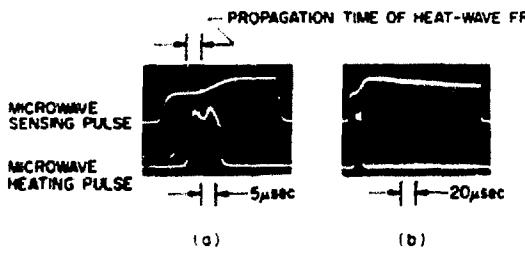
In the experiment a thin-walled metal tube, typically stainless steel and having a 10-cm length, 0.013-cm wall thickness, and 0.75-cm diameter, is exploded by being subjected to a strong current that rises to a few hundred kiloamperes in about 10 μs. This is accomplished using a 1400-μf capacitor bank charged to between 10 and 15 kV. The total system inductance is 300 nH. The tube is initially filled with a few atmospheres of 50 D_2-50 H_2. The diagnostic measurements used in the experiment included current, voltage, integrated neutron detectors, fast neutron detectors, flash x-ray shadowgraphy, a fast framing camera, and high-resolution x-ray inspection of the thin-walled tubing for quality control.

A one-dimensional hydrodynamic code calculation of the compression of a few atmospheres deuterium gas-fill by the exploded stainless steel tube vapor shows that the gas can be compressed to a very high density ($\sim 10^{21}$-10^{22} cm^{-3}) and a temperature of a few eV. This would be sufficient to cause thermal ionization of the gas after which the large current that had been flowing through the stainless steel tube could be transferred to the ionized deuterium. If such a transfer occurred there is sufficient power available to ohmically heat the compressed deuterium plasma in a few 100 ns to temperatures approaching those required to produce the intense neutron bursts reported by Cheng, provided the hot plasma could be confined for at least 1 μs.

As shown in Fig. VIII-13 the voltage across the tube increases as the current in the tube rises. The melting point of the tube (mp on the figure) shows a change of resistance of the tube. Following this the molten tube is compressed somewhat by the pinch effect as can be seen from the flash x-ray shadowgraph taken at the time marked "1" on the current voltage trace. Following this the tube compresses further and begins to vaporize (time "2"), which results in a sudden voltage increase and current decrease. This in turn is followed by a rapid voltage decrease ("voltage break"), because of a low-impedance path being established for the current, and a strongly striated expansion of tube vapor (shadowgraph at time "3").

Variations of tube parameters in the experiment involved primarily tube wall thickness (0.005 cm - 0.025 cm), tube length (5 - 15 cm), tube diameter (0.64 cm to 1.3 cm), gas-fill pressure (0.1 atm. to

— PROPAGATION TIME OF HEAT-WAVE FRONT

MICROWAVE SENSING PULSE

MICROWAVE HEATING PULSE

5μsec   20μsec

(a)   (b)

Fig. VIII-12.

Quantitative measurement of heat flow.

Voltage
4 kV/div

Current
170 kA /div

mp   1   2   3

⊢⊣ 2 μ sec/div

Static

1

2

3
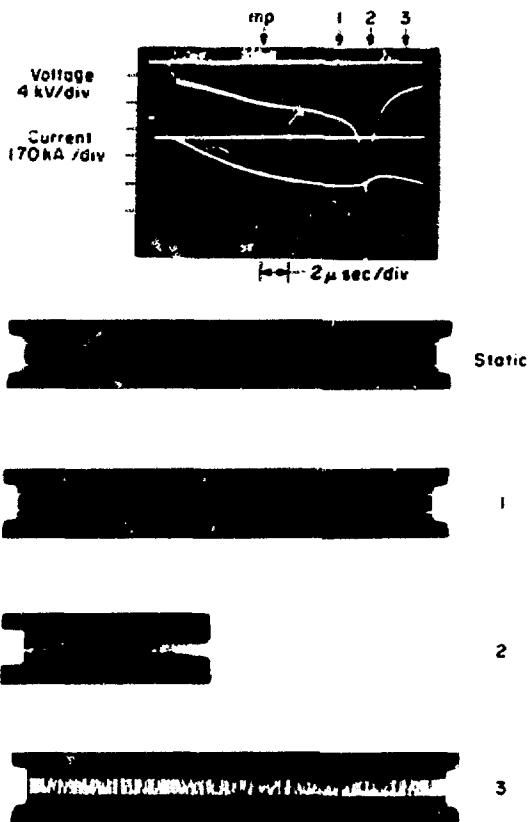
Fig. VIII-13.

Voltage and current of exploded thin-walled tube.
Flash X-ray shadowgraphs of tube at different stages
of vaporization.

8 atm), preparation of tubes (commercially drawn or machined from thicker walled stock), and various schemes to determine the cause of the voltage break (gas type and pressure on outside of tube, dielectric coatings on tube or dielectric filling on inside of tube).

In ninety-four separate shots no neutrons were detected. A summary of other experimental findings is as follows:

a. Commercially Drawn Tubes (Uniform Tubes, Inc.)

- Uniformity of the tube is very good as shown by x-ray inspection before the shot.
- Large voltage spike before voltage break.
- Light produced over a large portion of the tube just before voltage break. First light

occurs 0 to 1/2 μs before break and originates from the hot tube material rather than from a discharge in the gas.

b. Machined Tubes (Cheng's two favorable shots were machined tubes)

- Very non-uniform tubes with frequent deep machine marks in some cases.
- Smaller voltage spike than in case of drawn tubes. No voltage spike at all in some cases.
- Large burst of light at one point along the tube (frequently at the ends). This burst of light comes 1/2 to 1 μs before the voltage break. When burst of light comes from a point not at the ends, its location correlates well with a thin-walled part of the tube, as shown by comparison with x-ray measurements made before the shot.

c. Plastic material (heat-shrinkable tubing) around the tube, which could evaporate easily when the tube becomes hot, was tried as a means of providing high-pressure gas outside the tube as the tube pinched. These attempts failed to hold off the voltage break. A solid insulator within the tube, which would prevent pinching, also failed to prevent early voltage breaking.

d. Both the variation in bank voltage and the variation in D_2 pressure failed to show any significant correlation between these variables, and shot features such as quality of voltage spike or framing camera pictures.

e. Secure clamping of the tubing at the ends to provide good electrical connection was found to be necessary in order to prevent a premature voltage break.

It is quite apparent from the flash x-ray shadowgraphs showing the striated tube breakup that the compression of the gas fill is far from one dimensional as assumed in the simple 1-D Hydro computation. This would suggest that the predictions of the computation would not apply to the experiment. It is also likely, because no neutrons were detected and because of the results of c. and d. above, that the decrease of the voltage after time "2" is not due to current transfer to the compressed deuterium channel but rather to some other low-impedance path, perhaps through the tube vapor itself. Furthermore, this voltage break always occurred before the tube was completely vaporized and

therefore before maximum compression and heating of the deuterium gas fill had occurred.

The largest voltage spikes were achieved with the commercially drawn tubes, which were much more uniform in wall thickness than the machined tubes. This would suggest that the voltage break is initiated by the non-uniformities in the initial tube. However, the striated tube break-up shown on the x-ray shadowgraphs was present in all cases regardless of tube uniformity.

REFERENCES

1. H. Dreicer, D. B. Henderson, and J. C. Ingraham, "Anomalous Microwave Absorption Near the Plasma Frequency," Phys. Rev. Lett. 26, 1616 (1971).

2. H. Dreicer, R. F. Ellis, and J. C. Ingraham, "Hot Electron Production and Anomalous Microwave Absorption Near the Plasma Frequency," Phys. Rev. Lett. 31, 426 (1973).

3. H. Dreicer, R. F. Ellis, and J. C. Ingraham, "Anomalous Microwave Absorption Near the Plasma Frequency," Proceedings of the Fifth European Conference on Cont. Fusion and Plasma Physics, 1, 120 and 2, 242 (Grenoble 1971).

4. J. H. Brownell, H. Dreicer, R. F. Ellis, and J. C. Ingraham, "Influence of Intense AC Electric Fields on the Electron-Ion Collision Rate in a Plasma," Phys. Rev. Lett. 33, 1210 (1974).

5. J. H. Brownell, H. Dreicer, R. F. Ellis, and J. C. Ingraham, "Hot Electron Production, Anomalous Absorption and Effect of Intense Electromagnetic Fields on Inverse Bremsstrahlung Absorption Near the Electron Plasma Frequency," Paper CN-33/H-4-2, Proceedings of the Fifth International Conference on Plasma Physics and Controlled Nuclear Fusion Research, (Tokyo, Japan November 11-15, 1974).

6. J. M. Dawson and C. R. Oberman, "High-Frequency Conductivity and the Emission and Absorption Coefficients of a Fully-Ionized Plasma," Phys. Fluids 5, 517 (1961).

7. D. F. DuBois and M. V. Goldman, "Radiation-Induced Instability of Electron Plasma Oscillations," Phys. Rev. Lett. 14, 544 (1965); V. P. Silin, "Parametric Resonance in a Plasma," Zh. Ehsp. Teor. Fiz. 48, 1679 (1965) [Sov. Phys. JETP 21, 1127 (1965)].

8. K. Nishikawa, "Parametric Excitation of Coupled Waves-II. Parametric Plasmon-Phonon Interaction," J. Phys. Soc. Japan 24, 1152 (1968); P. K. Kaw and J. M. Dawson," Laser-Induced Anomalous Heating of a Plasma," Phys. Fluids 12, 2586 (1969).

9. A. Salat and P. K. Kaw, "Nonlinear High-Frequency Plasma Conductivity," Phys. Fluids 12, 342 (1969); T. P. Wright, "Strong Field High-Frequency Plasma Response," Phys. Fluids 18, 195 (1975).

10. J. C. Ingraham, H. Dreicer, and R. F. Ellis, "Spectral Observation of Electromagnetic Wave Decay Due to the OTS and Decay Parametric Instabilities," Bull. Amer. Phys. Soc. 20, 1361 (1975).

11. M. E. Banton, H. Dreicer, J. C. Ingraham, and B. L. Wright, "Enhanced Weak-Field Resistivity of a Parametrically-Unstable Plasma," Bull. Amer. Phys. Soc. 20, 1383 (1975).

12. D. Y. Cheng, C. W. Hartmann, R. Munger, and T. Fesseuden, "Confinement Time of a Gas-Embedded Z-Pinch," Bull. Amer. Phys. Soc. 19, 937 (1974); D. Y. Cheng, Private communication, 1975.

13. J. E. Hammel and J. C. Ingraham, "Exploding Liner Initiated Dense Z-Pinch," Bull. Amer. Phys. Soc. 20, 1298 (1975).

14. J. P. Freidberg and B. M. Marder, "High-Frequency Electrostatic Plasma Instabilities," Phys. Rev. 4A, 1549 (1971).

15. A. Hasegawa, Bell Telephone Laboratories, private communication.

16. T. K. Chu and H. W. Hendel, "Measurements of Enhanced Absorption of Electromagnetic Waves and Effective Collision Frequency Due to Parametric Decay Instability," Phys. Rev. Lett. 29, 634 (1972).

17. V. E. Zakharov, "Collapse of Langmuir Waves," Zh. Eksp. Teor. Fiz 62, 1745-1759 (May 1972), (JETP 35, 908 [1972]); G. J. Morales, Y. C. Lee, and R. B. White, "Nonlinear Schrödinger-Equation Model of the Oscillating Two-Stream Instability," Phys. Rev. Lett. 32, 457 (1974).

18. B. Bezzerides and D. F. Dubois, "Electron Heating and Landau Damping in Intense Localized Electric Fields," Phys. Rev. Lett. 34, 1381 (1975).

E. L. Kemp, W. D. Gutscher, K. J. Johnson, K. J. Kutac, K. W. Hanks, T. R. Cole,
W. H. Borkenhagen, A. G. Bailey, W. C. Nunnally, J. G. Melton, L. D. Hansborough, K. J. Bickford,
G. P. Boicourt, W. H. Borkenhagen, R. S. Dike, C. F. Hammer, E. M. Honig, R. W. Kewish, Jr.

A. CONCEPTUAL STUDIES

1. *Staged Scyllac.* Several conceptual designs for a Staged Scyllac experiment have been examined. The present Scyllac has the capacitor racks around the outside of the 4-m major-radius toroidal coil. The Staged Scyllac would have the capacitor racks inside a 12-m major-radius toroidal coil. An additional high-voltage, low-inductance capacitor bank would be added to shock heat the plasma before it is compressed and confined with the present 10-MJ, 60-kV capacitor bank. Staged Scyllac is to demonstrate wall stabilization of a collisionless plasma in a toroidal geometry. The basic parameters of the system are listed in Table IX-I.

TABLE I
STAGED SCYLLAC PARAMETERS

Major Radius	R = 12 m
Minor Radius	b = 11 cm
Magnetic Field	B_s = 8 to 10 kG
Risetime	$\tau/4$ = 0.2 to 0.3 μs
L/R Decay Time	L/R = 10 to 50 μs
Staging System Magnetic Field	B_f = 17 to 20 kG
Risetime	$\tau_f/4$ = 4 μs
L/R Decay Time	L/R_r ≈ 100 μs

The Staged Scyllac would be operated in the resonant heating mode, which requires that the implosion field be crowbarred.

Initially, the new experiment was designed using the Staged Theta-Pinch circuit and technology. The circuit for Staged Scyllac, shown in Fig. IX-1, uses two feed slots to a 22-cm-diam coil. The implosion banks on each side are pulse-charged to plus and minus 125 kV. The present Scyllac 60-kV start gaps are replaced with shorting bars and multichannel staging gaps are added to isolate the Scyllac load cables from the initial 125-kV implosion transients. The Scyllac bank is divided in this circuit, half charged positive and the other half charged negative.

In order to use this for Staged Scyllac, the present Staged Theta-Pinch components and systems must be improved to increase their reliability and to reduce their complexity and cost. Several prob-
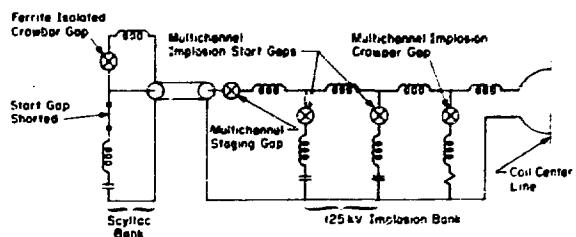
Fig. IX-1.
Staged Scyllac circuit.

lem areas have been observed in the STP experiment which would affect a Staged Scyllac using this circuit concept. The trigger systems must be improved in order to reliably multichannel the various gaps. The second major problem is the linear rail staging gap that isolates the staging bank from the high-voltage implosion bank and then switches 24 kJ and 10 C into the load coil. This gap is difficult to trigger and a reliable gap body of insulating material operating at a maximum voltage of 45 kV has yet to withstand the large shock pressures produced when conducting the large power levels required for this experiment.

A new coaxial spark gap for a Staged Scyllac has been designed and a prototype version was tested. The new gap shown in Fig. IX-2 is much simpler to assemble and install than the present Staged Theta-Pinch PFN gap (6 parts vs 20 parts for the PFN). Another advantage is a lower inductance (10 nH vs 15 nH for the PFN gap). A universal gap was designed around the new gap geometry. The universal gap can be used as an implosion start gap, an implosion crowbar gap, or a staging gap, depending on the transition section that is used.

A major consideration in using the Staged Theta-Pinch circuit for Staged Scyllac is the requirement that the present 3150 start gaps in Scyllac must be removed and replaced with shorting bars. This operation would be time-consuming and expensive.

Other circuit concepts using saturable inductors to isolate the fast and the slow banks have recently been investigated for use in Staged Scyllac. The

CONCENTRIC CROWBAR SPARK GAP
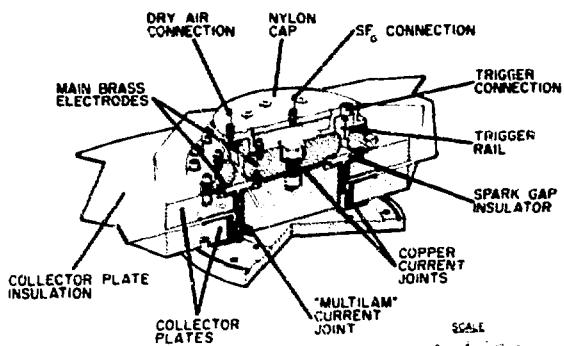
Fig. IX-2.

Coaxial spark gap for Staged Scyllac.

Fig. IX-3.

Staged Scyllac circuit using a saturable reactor.

saturable inductor concept does not require that the Scyllac start gaps be removed.

A Staged Scyllac circuit using a saturable inductor to add the 60-kV staging-bank energy to the implosion-bank energy is shown in Fig. IX-3. Both the implosion bank and the Staging Scyllac bank are triggered simultaneously. The saturable inductor (SR) is initially unsaturated and exhibits an inductance at least ten times the coil inductance. The large inductance of SR is in parallel with the load coil via the staging bank. The current from the high voltage initially opposes the current from the staging bank. When the implosion bank is resistively crowbarred, the implosion-bank current in the saturable inductor current decreases and the crowbar resistance causes the staging-bank current to flow through the saturable inductor. The staging-bank current now saturates the inductor (SR), crowbarring the implosion bank with a parallel inductance approximately one-tenth the coil inductance. The Scyllac bank current now increases rapidly ($\tau/r \approx$ 4 μs) in the coil and is crowbarred at peak current with the Scyllac ferrite-isolated crowbar gaps. With a $\mu_e \approx$ 100, the saturable inductor absorbs 10% of the implosion-bank energy and 10% of the staging energy from the Scyllac bank. However, a staging spark gap for the Scyllac bank is not necessary and the Scyllac start gaps need not be shorted out for this circuit.

2. *Large Staged Scyllac.* Conceptual studies for the Large Staged Scyllac (LSS) were also carried out in 1975. The LSS is a large toroidal theta pinch with a major radius of 30 m and a minor radius of 0.11 m. The parameters of LSS are listed in Table IX-II. The Large Staged Scyllac is the physics prototype for the Scyllac Fusion Test Reactor (SFTR) investigating extended confinement time by wall stabilization.

TABLE II
LARGE STAGED SCYLLAC PARAMETERS

Major Radius	R = 30 m
Implosion Coil Radius	b = 0.11
Compression Coil Radius	r_c = 0.18 m
Implosion Magnetic Field	Bs = 10 kG
Implosion Field Risetime	$\tau/4 \leq$ 0.3 μs
Implosion Field L/R Decay Time	L/R (i) > 50 μs
Compression, Confinement Magnetic Field	Bf = 30 kG
Compression, Confinement Magnetic Field Risetime	$\tau/4$ (f) ~ 50 μs
Compression, Confinement Field L/R Decay Time	L/R (f) · 3 ms

A major technological advantage of the LSS over the Staged Scyllac is the physical separation of the implosion-heating system and the adiabatic compression and confinement system by using separate concentric load coils isolated with magnetic material. The implosion-heating system for LSS uses a radially fed, fractional-turn Marshall coil to resonantly implode and initially confine the plasma. A multi-turn or a single-turn compression coil is concentric with the fractional-turn Marshall coil and is isolated from the high-voltage transients by magnetic material. A cross section of the LSS coil assembly is shown in Fig. IX-4.

A circuit diagram of the implosion-heating system is shown in Fig. IX-5. The basic unit of the implosion-heating system is a 50-cm-long section
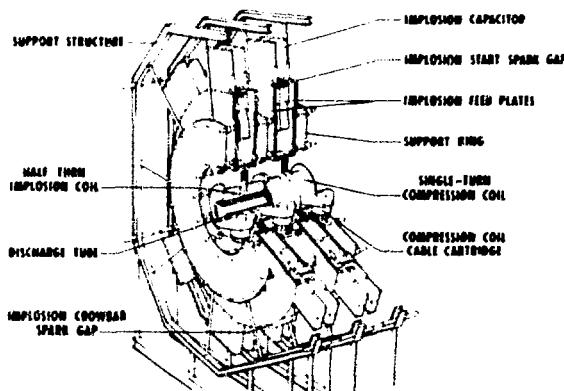
LARGE STAGED SCYLLAC COIL ASSEMBLY

Fig. IX-4.
LSS coil assembly.

Fig. IX-6.
End view of LSS implosion-heating system.

consisting of two 25-cm-long, back-to-back, counter-wound Marshall coils. Each Marshall coil is driven by six parallel pairs of two series, 0.1-μF, 90-kV capacitor modules. One-half of the series capacitors are charged positive, and the other half are charged negative. Figure IX-6 shows an end view of the implosion-heating system. The start and crowbar gaps are linear, multichannel spark gaps. The length of the Marshall coils (25 cm) was chosen as 1/16 of the wavelength for fabrication considerations. The capacitor modules are dc charged to positive and negative 75 kV. The Marshall coil produces the implosion voltage necessary to obtain a 1-keV implosion temperature by the transformer properties of the fractional-turn coil.

Fig. IX-5.
LSS implosion-heating system circuit.

The reliability and operation of a large system of this type can be compared with the present Scyllac. The total number of start switches for LSS is 1130 and the total number of crowbar switches is 565. These numbers can be compared to 3150 start and 3150 crowbar switches in the present Scyllac. The largest dc charging voltage for LSS is 75-kV dc which is equal to the highest dc charge voltage in the Scyllac system. An advantage of the LSS implosion system is the absence of load cables connecting the high-voltage bank to the load.

A significant difference between Scyllac and LSS is the trigger system voltage requirement. The Scyllac trigger system operates at a pulse voltage of 100 kV. A multichannel trigger system for LSS must produce 200 kV pulses with risetimes of less than 20 ns. A similar 200-kV system is now being used on the Staged Theta Pinch, but the system is operating at the voltage limits of present cables and components.

The proposed trigger system for LSS would consist of small, optically coupled Marx banks mounted on each of the multichannel gaps. These small Marx circuits are dc charged to 30 kV and triggered with a 30-kV pulse. In this trigger system the high trigger voltage is only present when the gap is triggered. Prototypes of this small Marx circuit

113

have produced 200-kV trigger pulses with a risetime of less than 20 ns and a triggering jitter of less than 10 ns. An LSS trigger system of this type should be more reliable than the present Scyllac system.

Several designs of a compression system for LSS have been studied. Initially a single-turn coil driven by high-density, 170-μF, 10-kV capacitors and switched with ignitrons was examined. The one-turn coil is necessary to produce the desired 50-μs risetime using 10-kV capacitors. However, the desired L/R compression field decay time of 3 ms is difficult to obtain without using many crowbar ignitrons in parallel. The parameters and the number of components for the 10-kV, single-turn compression system are shown in Table IX-III.

TABLE III

SINGLE-TURN, 10-kV, COMPRESSION SYSTEM FOR LSS

Minor	0.18 m
Maximum Magnetic Field	30 kG
Field Risetime	50 μs
L/R Field Decay Time	$\geq$ 3 ms
10-kV Bank Energy	75 MJ
No. 10-kV, 170-μF Capacitors	8824
No. Size D Start Ignitrons	1103
No. Size D Crowbar Ignitrons	4412

3. *Notch Compression Circuit.* More cost-effective energy systems using inductive energy storage or homopolar generators with solid-state switching must be used as fusion compression and confinement systems become larger. However, certain compression requirements are not necessarily compatible with the containment requirements. Adiabatic compression of a preheated plasma required a relatively fast-risetime magnetic field ($T_r \sim 50$ μs), which in turn requires a low-inductance single-turn compression coil. Alternately, plasma containment requires a long field decay time (L/R $\sim$ 100 ms), which requires a large inductance, multiturn compression coil, and a low crowbar resistance. The desired current profile for a typical compression and confinement system is shown in Fig. IX-7. This waveform is usually produced by a capacitor bank that is crowbarred at $t = t_{cB}$. Capacitors may not be cost effective or practical for very large systems
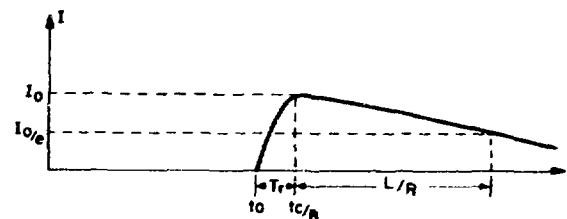
Fig. IX-7.
Desired current profile.

(U > 100 MJ) when the number of components are considered, as well as the usual crowbar times.

An alternate current profile that produces the desired results is shown in Fig. IX-8. The notch circuit that produces this waveform is shown in Fig. IX-9. The appropriate waveforms of the currents and voltage in this circuit are shown in Fig. IX-10. A cost-effective homopolar generator C_H charges several multiturn compression coils L_1 in series to an initial current I_0 in time $\tau_h/4 \simeq 30$ ms. At time $t = t_0$, breakers B_1 are opened and simultaneously the SCRs are triggered. The current I_0 in each coil L_1 is transferred via the transfer capacitors C_t to storage coil L_2 and then transferred back to compression coil L_1 in a time T_N. At time $t = t_0 + T_N/2$, the current in L_1 coil goes to zero. The plasma may be initially heated at this point by an appropriate heating system. This can be accomplished because the current approaches zero rather slowly, 10 to 20 μs for $T_N = 100$ μs. At time $t_0 + T$, the SCRs are allowed to turn off and the switches S_1 are closed to crowbar the compression coils and take any voltage off the opening SCRs.

The notch circuit is the inductive inverse of a capacitive Marx circuit. The field coils are charged in series and discharged in parallel. The breakers B_1 are necessary to initiate the current transfer from L_1 through C_t to L_2. The breakers also isolate L_1 voltages so that they do not add in
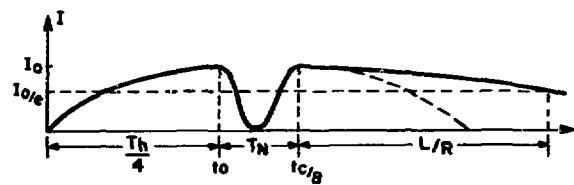
Fig. IX-8.
Notch homopolar current profile.

Fig. IX-9.

Notch circuit.

Fig. IX-11.
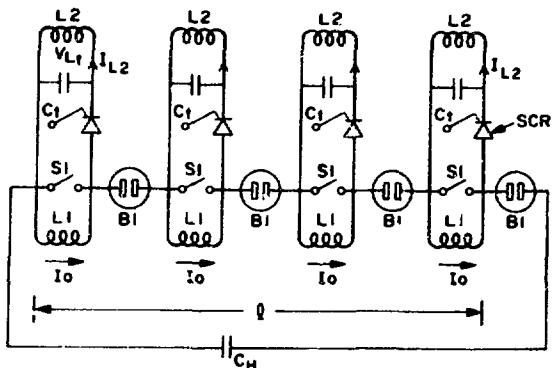
Saturable inductor breaker for notch circuit.

series across the homopolar generator. The homopolar generator is matched to the load by paralleling series groups of L_1 coils.

The maximum value of the voltage V_m across the transfer capacitor C_t is given by

$$V_m = \frac{\mu_0 I_0 N^2 \pi^2 r^2}{\ell T_N n} \quad ,$$

where I_0 is the maximum current in the compression coil, N is the total number of turns per length of coil ℓ, r is the coil radius, T_N is the notch period, and n is the number of series compression coils per length of coil ℓ to be discharged. The current in the compression coil has the form

$$I(L_1) = I_0 \left\{ 1 - \frac{L_1}{L_1 + L_2} \left[1 - \frac{L_2}{L_1} \cos\left(\frac{2\pi}{T_N}\right) t \right] \right\} \quad .$$
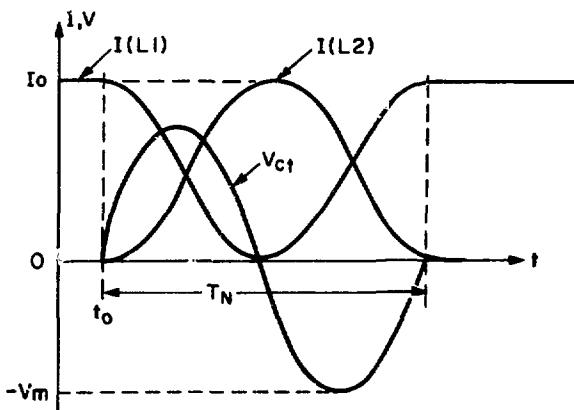
Fig. IX-10.

Notch circuit current and voltage waveforms.

The storage inductance L_2 is chosen slightly larger than L_1 so that the current in L_1 goes to zero at the bottom of the notch.

The notch circuit has several advantages that are applicable to large compression and confinement energy systems. Cost-effective energy storage systems, such as low-voltage homopolar generators, can be used with multiturn compression coils to produce both fast field risetimes for plasma compression and long field decay times for plasma containment.

Energy from a low-voltage source is slowly stored, inductively, in the compression coil instead of a storage inductor. Then this energy is transferred temporarily to a storage coil, identical to the compression coil, and then back to the compression coil. This rearrangement of the standard energy-transfer circuit permits a complete current oscillation to the form $1 - \cos \omega t$ so that reliable solid-state switches can be used as transfer switches. The SCRs in the notch circuit open when $I = 0$ and $dI/dt = 0$, instead of when I is maximum as in other inductive energy-transfer circuits.

The breaker B_1 is a critical component in the notch circuit. It must open in a time less than or equal to $T_N/10$ and must hold off at least the maximum voltage across the transfer capacitor. It may be possible to use a saturable inductance for breaker B_1. Unsaturating an inductance with an external control winding can change the inductance by several orders of magnitude, reducing the series current and affecting transfer to the temporary storage coils. A schematic of such a breaker is shown in Fig. IX-11. The inductor is initially saturated with a dc current prior to charging the compression coils L-1.

When the compression coils are charged, the capacitor of Fig. IX-11 is switched so that the core is driven out of saturation. The inductor control winding current and the breaker inductance versus time are shown in Fig. IX-12. The current in the capacitor and the control winding oscillates, but since the inductance of the control winding increases, the period of oscillation increases. The capacitor is resistively crowbarred at the peak of the second half-cycle current.

The inductance of the breaker winding can be made to increase several thousand times when it is driven out of saturation on the order of 10 μs. This is true for 1.0-mil, tape-wound cores made with 50% Ni, 50% steel tapes.

The saturated inductance breaker has several advantages. It has fast opening times with no moving parts and is electrically controlled. It can be designed to have low-resistance and high-current capability when saturated and no parallel switch is necessary. Finally, temporary or continuous interruption is possible, depending upon the control circuit.

B. COMPONENT DEVELOPMENT

    1. Low-Cost Capacitor-Bank Components. Essentially all future large experiments being considered at Los Alamos will require hundreds of megajoules of capacitive energy storage. For high-efficiency (> 90%) energy transfer, the METS system will also require a transfer capacitor bank which will store about half of the stored energy in the METS system. Low-cost capacitors and crowbar igni-

trons are being developed to meet this requirement.

The standard 10-kV energy storage capacitor stores about 0.08 J/cm^3. A 170-μF, 10-kV capacitor is being developed which stores 0.21 J/cm^3. Since the cost scales inversely with energy density, the cost of the 170-μF capacitor is expected to cost < 4¢/J in 1975 dollars.

The size D ignitron is commonly used to crowbar low-voltage capacitor banks. Published data indicate this size ignitron is limited to about 200 C. It has been found that the coulomb rating can be greatly increased by mounting the ignitron in a coaxial geometry.

The circuit shown in Fig. IX-13 is used to simultaneously test ten or more capacitors and one crowbar ignitron. The capacitors are charged to 10 kV and the series ignitron discharges the capacitors into the load coil, delivering a peak current of 95 kA with a risetime of 250 μs. The crowbar ignitron is automatically fired by the 7703-trigger ignitron at peak current and at a minimum voltage. The reverse voltage on the capacitors never exceeds 20%. The current in the load coil and crowbar ignitron decays with an L/R time constant of 10 to 18 ms, depending on the design of the load coil. The normal repetition rate is one shot per minute.

Seven 170-μF, 10-kV capacitors were operated for over 30 000 discharges at rated voltage with no failures. Several of the units in the test system are approaching 250 000 discharges. Two new higher energy density 225-μF units with a new dielectric
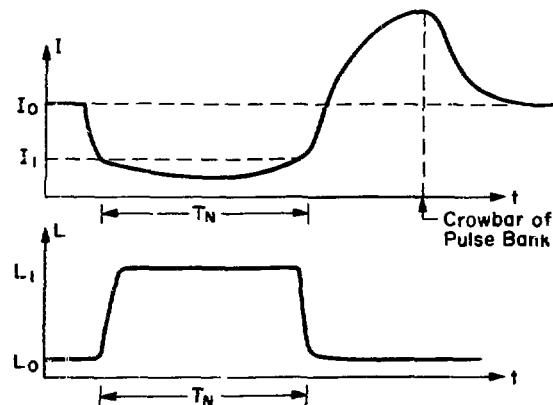
Fig. IX-12.

Saturable inductor breaker waveform.
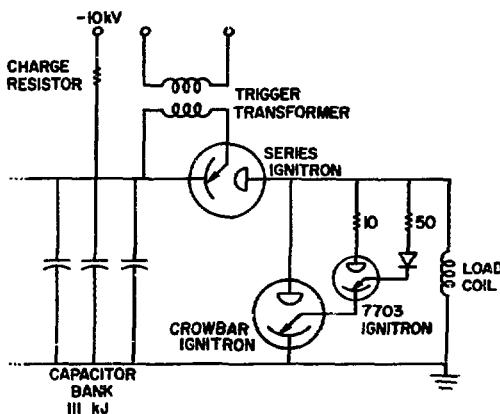
IOkV CAPACITOR AND SIZE D IGNITRON
TEST CONFIGURATION

Fig. IX-13.

10-kV test bank schematic.

have been tested for over 15 000 discharges with no failures. These capacitors afford a 33% increase in energy over the 170-μF units and will be even more economical.

Fourteen crowbar ignitrons were tested at power levels of 400 to 1700 C. One mechanical problem with all incoming ignitrons involved a poor weld connection of the flexible braid to the solid anode stud. This problem was eventually solved by developing a soft-silver-soldering technique to improve this connection. After the connection problem was overcome, one ignitron was run for 13 000 discharges at 95 kA and 1700 C. Lifetime was limited by the formation of a mercury amalgam at the cathode, causing improper ignitor operation. Future testing will investigate the cause of the amalgam and other lifetime limitations.

The most prominent difficulty of the testing system was the fabrication of a load coil capable of withstanding the electromechanical stresses which occur during operation. During the past twelve months, five load-coil designs have been fabricated and tested. Four failed between 400 and 13 000 discharges with the most recent one still operating at 5000 discharges.

It has been determined that the windings of the load coil must be potted with an appropriate epoxy compound in order to withstand the magnetostrictive shock of thousands of repetitive discharges. Extensive development efforts were made to discover a satisfactory epoxy for this application. Shell Epon 828 epoxy resin with 15% Furane D-40 hardener and 30% Thiokol LP3 polysulfide polymerizer, all mixed by weight, was found to be the most satisfactory mixture for this application. The epoxy was mixed using applied heat until the temperature reached 170°F. The applied heat was removed and the mixture was evacuated of all air bubbles. The hot epoxy was poured into a heated mold and allowed to cure for one week at room temperature.

2. 60-kV High-Density Capacitor Development. A development program was started in 1974 to develop a high-energy-density, 60-kV capacitor for use in Scyllac and future machines. The goal of the program is to produce a 60-kV capacitor that is more economical than the standard Scyllac capacitor ($0.15/J) by storing 5 kJ in the same size can

as the present 3-kJ Scyllac capacitor.

Two different types of developmental capacitors were ordered from each of three manufacturers. The first type was made to the 1.85-μF, 60-kV specification, but using 0.9-gm/cm³ paper instead of the usual 1.0-gm/cm³ paper. These capacitors were tested to end-of-life in a ringing discharge (85% reversal) so that the results could be compared to previously obtained test results for the standard Scyllac capacitor. The second type obtained is a 2.85-μF, 60-kV capacitor to be operated at less than 20% reversal. Testing has not been completed on the second type.

Tests were completed on the 0.9-gm/cm³ units and the capacitors were disassembled to determine the cause of failure. Average lifetime for these units was comparable to that for standard Scyllac units. Postmortem analysis revealed that 14 of the 17 units failed for the same reason. Gas pressure produced in the capacitor caused the case to either swell or split, lowering the oil level and allowing internal arcing at the top of the capacitor. Two early failures occurred from other causes and no cause could be found for one failure.

Since the use of lighter weight paper greatly increased the probability of this type of failure, it appears that either increased gas production or increased gas diffusion and accumulation occurred. No definite conclusion has been reached concerning the effects of lower density paper on lifetime. Average lifetime increased for one manufacturer and decreased for another.

Upon completing the preceding tests, the test bay was converted to test the 2.85-μF, 60-kV, high-density capacitors. Crowbar circuits were added and tested, and instrumentation was added and calibrated to detect voltage reversals of greater than 20%.

An additional development program was begun to correct a shortcoming of the Scyllac piggyback crowbar gap. The spark plugs that trigger the crowbar section of the gap erode heavily and need to be replaced after ~2000 shots. It was estimated that the time required to change the spark plugs over the anticipated lifetime of the 18 test capacitors would be at least 800 man-hours.

Two gap modifications were tested to ease the problem of spark plug replacement. First, a

RESULTS OF LIFE TESTS

(1.85-μF, 60-kV Capacitors with 0.9 gm/cm³ Paper)

Supplier	No. of Units	Avg. Life	Earliest Failure	Avg. Life for Standard Paper
Aerovox	6	45 000	24 443	40 000
Maxwell	6	40 000	1 487	(no base)
Sangamo	5	27 000	21 682	62 000

mechanical modification was tried, adding a threaded current joint in the inner current-carrying conductor in the ferrite stack. The two units tested failed after 1500 and 3400 shots due to the joint erosion. Next an electrical modification was tried which consisted of inserting a current-limiting resistor in series with the spark plug. It was found that the spark plug and gap triggered satisfactorily with the resistor in place and that wear was reduced by about 75%. Several commercial resistors were tested until one was found that could withstand the voltage and current. The test capacitors will be fitted with this modification so that some idea of statistical failure of this resistor will be available.

While the above testing was being done, life testing of the high-density capacitors began. However, because of frequent bay shutdowns for modifications, spark plug changes, replacement of blown resistors, etc., only 9000 shots have been accumulated. Six capacitors are presently being tested, four at a time, and they have undergone 1500 to 6500 shots with no failures. This testing will continue.

3. *General Capacitor Development.* During the year a number of projects were directed toward the analysis and solution of certain capacitor problems. Some problem areas are: the design of lower inductance capacitors, the drying of the insulant, the detection of underdrying in the insulant, and the study of castor oil as a capacitor impregnant.

   a. *Low-Inductance Capacitors.* The development of low-inductance capacitors for fast CTR experiments continues to be of interest. It is complicated by the fact that very low inductance usually leads to very high currents and this in turn leads to current connection failures. A project has been initiated to develop a 160-kV, very low inductance capacitor. The unit will use

conventionally wound packs, but will employ spring-loaded connections. The waste volume required to make and insulate the current connections contributes significantly to the inductance of present capacitors. The spring-loaded connections allow a substantial reduction in this waste volume. Windings have been procured from Maxwell Laboratories, and the header and case have been designed and fabricated by LASL. Assembly and preliminary inductance measurements are under way.

   b. *Drying of Capacitor Windings.* Over the past years, LASL has had a substantial number of capacitor failures due to insufficient drying of the Kraft paper in the windings. This problem arose again this year in connection with an order for 650 capacitors. In this case, the manufacturer reduced the low vacuum portion of the drying cycle to one-day duration without adequate checks on the resultant moisture content of the paper.

   Such process changing by the manufacturer makes it desirable to have methods at hand to estimate the moisture content of the paper at various times in the drying procedure. A method used by Lampe in connection with transformer paper has been adapted to make lower bound estimates of the moisture content.[1] The method consists of solving the one dimensional diffusion equation under assumptions which assure that the solution values will be equal to or less than the actual moisture content. In the case at hand, these estimates showed that a minimum of 7.5 days drying would be required to reach a suggested 0.1% moisture content everywhere inside the winding.

   c. *Diagnosis of Underdrying.* CTR capacitor failures due to underdrying are generally difficult to diagnose. One excellent diagnostic clue is the presence of margin arcs in the failed units. The connection between these arcs and underdrying was made several years ago when underdrying was

first shown to be a problem.[2]

Another more sensitive clue has been found. This is margin spotting. It has been possible to connect the presence of margin spotting, both empirically and theoretically, with the presence of free water in the capacitor paper. A paper detailing this analysis was presented at the 6th Symposium on Engineering Problems of Fusion Research.[3]

d. Capacitor Impregnant. For approximately fifteen years, castor oil has been the primary impregnant used in energy storage capacitors for pulse application. It attained this primacy when it was shown to improve the life of capacitors by about a factor of twenty over similar units impregnated with PCBs. At the present time, PCBs are under heavy attack as environmental hazards and it is possible that their use may be prohibited in a few years, even for power factor correction units. This has stimulated interest in new impregnants as replacements. Castor oil is an obvious candidate.

Little effort has been spent on learning what chemical properties of castor oil contribute to its success as an impregnant. Such knowledge would be helpful in two areas: it would provide a guide in finding replacement impregnants, and it would also lead to better processing of the castor oil.

A literature study was made with the objective of explaining some of castor oil's impregnant properties on the basis of its chemistry. The results of the study are presented in Ref. 4. Among the findings were that castor oil can act as its own inhibitor (inhibitors are added to PCBs) and that castor oil can chemically combine with free water to remove small amounts of water from the capacitor dielectric. This fact provides an explanation for the observation that castor-oil capacitors improve with standing before service. The study also suggests ways that these properties can be enhanced through processing of the oil.

4. Cable Development

a. Crowbar Trigger Cable. The Scyllac crowbar trigger cable has continued to exhibit very low reliability. A new trigger cable was designed using semiempirical procedures to improve Scyllac reliability and also to provide a better cable for future machines.[5]

Sample cables have been ordered from three manufacturers. Attention was given to the type of polyethylene the various manufacturers proposed to use in the cable. In the past, specification control in this area was limited to a requirement that the polyethylene conform to military standards. By the end of the year, two manufacturers had delivered samples and testing had begun.

Prior to delivery, standardized tests of the cable presently used in Scyllac were made to establish a basis for comparison with the new design. The present cable was produced by two manufacturers and the tests show a distinct performance difference between them. The tests performed on the new cable design, although incomplete, show that it is at least a factor of two better than the old cable. This comparison is based on the losses experienced in the first 10 000 shots. If a comparison is based on median life, the new cable appears to be better by at least a factor of 500.

b. METS Pulse Lead Cable Connector. The design and layout were completed for a seven-cable header to connect the pulse lead of the superconducting coil to the vacuum interrupter. The coaxial header takes minimal Dewar-lid space by routing the cables vertically. The design allows cables to be replaced individually, if required, and allows the header to be purged with gaseous nitrogen to prevent frost buildup. A schematic of the header is shown in Fig. IX-14. Tests are being run to determine the best method for terminating the coaxial cables in the connector under high-current conditions. The connector has a calculated inductance of about 120 nH.

C. SYSTEM DESIGN AND CONSTRUCTION

1. Scyllac. The conversion of Scyllac to a 120° derated sector was completed on January 2. The energy of the sector was reduced by disconnecting 108 of the 210 capacitors and spark gap switches on each of the five racks. The first plasma shot on the derated sector occurred on February 18. During the year there were 3198 main-bank shots with 2605 of these being plasma shots. The bank was normally operated at 40 kV with a few shots taken at 45 kV and 50 kV.

An $\ell = 0$ coil system was added to the main coil in preparation for feedback experiments. A five-capacitor 60-kV capacitor bank with its associated hardware was installed to drive the $\ell = 0$ coil
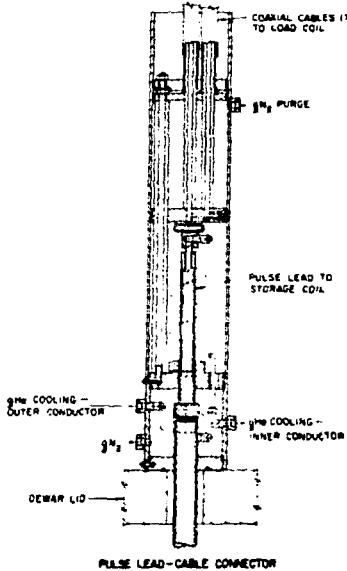
Fig. IX-14.

NETS pulse lead cable connector.

system. Later this capacitor bank was doubled to ten capacitors. An $\ell = 2$ coil system was also added to the main coil. After initial tests with the $\ell = 0$ capacitor bank, the $\ell = 2$ coils were driven by feedback modules.

A feedback system has been added to the derated Scyllac sector. This system consists of 26 power-amplifier modules driving 26 $\ell = 2$ feedback coils through output transformers. The feedback system has operated satisfactorily on more than 100 plasma shots. The total risetime and delay of the system is 1.14 μs. The risetime is 700 ns (10% to 90%) and the delay is 440 ns. Each of the 26 modules is capable of supplying 900 A at 35-kV plate voltage.

The success of the feedback system is due to an extensive redesign of the power-amplifier modules by Gribble, CTR-3. The performance and reliability of the modules were greatly improved by adding a new low-gain amplifier stage between the driver stage and final push-pull output stage. After the design was completed, a considerable effort was required to modify all existing modules. About half of the existing 65 modules have been modified with the remainder presently undergoing modification.

A number of diagnostic instruments and devices were developed to improve the diagnostics of the Scyllac energy system. A set of specially cali-

brated probes were built to simultaneously measure the load-coil magnetic field generated by all five racks. Special instruments were used with the probes to determine the field, and the voltages on the various capacitor banks were adjusted to give a uniform magnetic field throughout the coil. Active integrators were designed and built to assist in pulse current measurements. Their high gain and frequency response have been very beneficial in measuring high-voltage, fast risetime pulses. Special low-inductance resistance voltage devices were designed and built for use in the bank. Their small size and accuracy have proven useful during numerous diagnostics and maintenance measurements.

A number of other modifications were made to the derated sector during the year. All five collector plates were connected solidly together to prevent arcing between adjacent plates. This problem had broken two quartz tubes before it was corrected. The crowbar trigger system was modified to provide greater reliability in preventing a current reversal. The system was split into independent halves with separate backups to provide crowbarring for every known failure mode. The vacuum system was modified to electrically isolate the plasma and eliminate possible resonances with the I_z current. This was accomplished by installing 50-cm links of ceramic tube to the two vertical lines that connect the discharge tube with the vacuum manifold.

The design and assembly of a quartz-forming machine was essentially completed in 1975. The device shown in Fig. IX-15 is designed to take straight 5-, 10- or 20-cm quartz tubes and form helical twists into a final straight or toroidal shape. The quartz-forming machine is completely assembled and is being evaluated. The first tube being formed for the next sector experiment has a major diameter of 8 m, a quartz tube outside diameter of 10 cm, a helix radius of 1.4 cm, and a wavelength of 63.82 cm.

2. Scylla IV-P. The construction of the Scylla IV-P, shown in Fig. IX-16, has been completed. The Scylla IV-P energy system contains 650 1.85-μF, 60-kV capacitors, each with a Scyllac-type start and crowbar spark gap. This bank generates a 70-kG field in an 11-cm-i.d. load coil with a risetime of 3.1 μs and has a crowbar L/R time of 250 μs. The first plasma shot on the system was obtained on

120

QUARTZ TUBE FORMING MACHINE
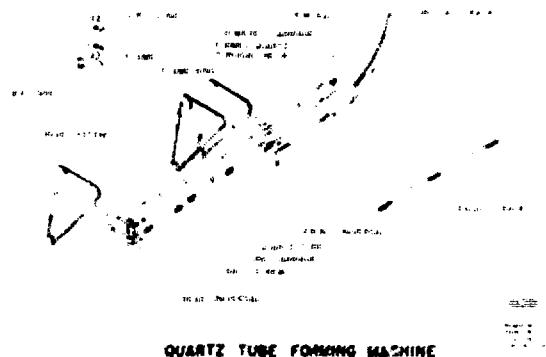
Fig. IX-15.

Quartz-forming machine.

Fig. IX-16

Scylla IV-P.

January 8, 1976.

The capacitor bank is similar to the Scyllac bank with a few modifications to improve the system reliability. The Scylla IV-P spark gaps were installed on O-ring seals on the gap lid to allow a higher level of oil in the gaps. The spark-gap airline fittings were changed from brass to nylon to prevent arcs, and several of the interfaces under the oil were sealed with an impregnant to prevent small air leaks which sometimes cause arcs.

The Scylla IV experiment is completely controlled by a computer. The Prime 300 computer is housed in a double-wall shield room immediately adjacent to the computer. Commands from the computer are sent through a CAMAC interface and through solid-state relays to electromagnetic relays which perform the operation or drive the appropriate device. Signals from the system, such as interlocks, are fed into the control logic by similar route. All commands are introduced into the control system by appropriate computer peripherals. Software has been written to operate the entire system or to operate any part of it independently. This feature was found to be invaluable in the checkout phase. After the usual debugging, the computerized control system for Scylla IV-P is operating very successfully.

5. Plasma Gun-Injection Experiment. A plasma gun-injection experiment was designed to study the feasibility of injecting a hot plasma into a solenoid for further compression and heating. The injection of hot plasma is one possible way of replacing the implosion heating usually found in theta-pinch devices.
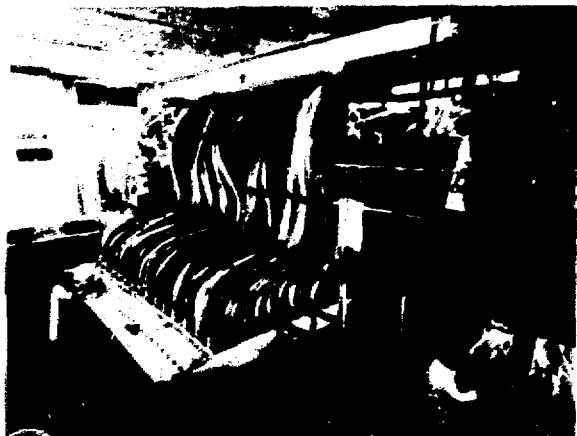
The gun-injection experiment is shown in Fig. IX-17. The gun assembly will be driven by one hundred 1.85-μF, 60-kV capacitors. Each capacitor will have a Scyllac-type spark gap with six output cables which will feed the collector-plate assembly through cable cartridges. The output of the gun will be injected into a 4-m-long solenoid. The solenoid and the gun assembly are in modularized vacuum tanks which can be disassembled as required. The solenoid will be driven by two shelves of the Zeus capacitor bank to produce a peak field of 20 kG with a 2-ms risetime. Procurement of all the components of the plasma-injection experiment is essentially complete and construction of the capacitor bank and the experimental hardware has begun.

D. ENGINEERING ANALYSIS

1. NET-2 Analysis. A number of circuit analyses using the NET-2 code were performed during the
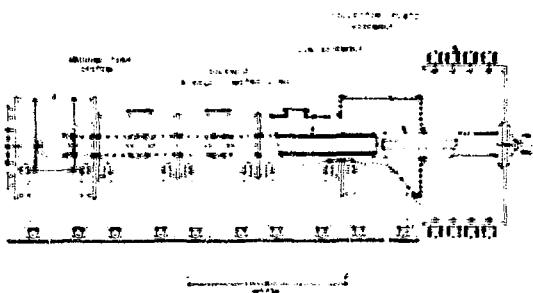
Fig. IX-17.

Plasma gun injection experiment.

121

year. The following three represent the greatest expenditure of time.

a. *Pulse Lengthening Circuit for the LTPHR*. An effort was made to find economical capacitive circuits to drive the Linear Theta-Pinch Hybrid Reactor (LTPHR) compression coils. The aim was to produce long, flat-top pulses. Good results were obtained. The effort was switched to homopolar circuits (see below) when new inputs suggested that a) capacitors would be unsuitable, and b) a flat-topped pulse would not be required.

b. *Homopolar System Studies for the LTPHR*. A study was made of a homopolar system to drive LTPHR compression coils. In the proposed system, current would be built up through a short circuit and then transferred to the load by simultaneously opening the short circuit and closing a circuit to a transfer capacitor and the load coil. The most serious problem in such a system is that the shunt switch must be opened at peak current and must withstand very high voltage. Since the state-of-the-art is not up to these requirements, it was decided to investigate a system where a shunt resistor always remains across the shunt switch.

A primary concern in systems for reactors is the energy lost compared to the energy delivered to the load. Thus, the study was aimed at determining where the losses occur and reducing them by optimal design, as well as determining if the system would operate with a shunt resistor. The NET runs showed that good transfer to the load could be achieved even for values of shunt resistance as low as 5 Ω. Moreover, the energy losses in the shunt resistor did not seriously affect the system efficiency. The system's efficiency was shown to depend primarily on the resistance of the homopolar generator, the connecting leads, the load, and the switches.

c. *Argonne Peristaltic Theta Pinch*. Scientists at the Argonne National Laboratory have been studying a concept for reducing the end losses of a linear theta pinch.[6] The concept, called peristalsis, is based on the production of a rippling magnetic field with the ripples moving against the direction of the particles streaming out the ends.

A question has been raised concerning the ability to produce such in-moving ripples. On the proposed system coils are energized sequentially by individual circuits, but the circuits cannot act independently because of mutual inductance between the coils. The NET-2 program was used to investigate the effects of the mutual inductances.

The initial effort has been limited to modeling the central one-eighth of Argonne's proposed system. This consists of ten coils driven by five individual sources. Intuitively, it should be more difficult to produce the desired ripples in the shortened system because the coupling to the opposite end is greater. So far the study has shown that an in-moving wave can be achieved with no plasma present; however, it is difficult to determine its speed. The problem arises because the mutual inductances cause the central field to rise at a rate which depends on the activation times of the ripple-producing circuits. It has also been established that the concept will not work if the mutual inductances are too large.

2. *Computation of Guide Fields for Plasma Gun Injection*. Gun injection of a theta pinch requires the establishment of a guide field between the plasma gun and the theta pinch. This field must be shaped so that the plasma produced by the gun is led into the theta pinch without striking the walls of the apparatus. The guide field is produced by combined action of the theta-pinch coil and a guide-field coil. Field lines from the guide field link the theta pinch, and this affects the current distribution in the theta-pinch coil. Similarly, the theta-pinch flux affects the current in the guide-field coil. These interactions make the design of the guide-field coil nontrivial.

The guide-field coil can be designed in one of several ways. Two ways which immediately suggest themselves are: a coil made up of individual turns of wire with the field shaped by passing the proper current in each turn or a single-turn coil properly shaped to produce the field. In either case, it is desirable to have a computational method that can be applied to the proposed design to determine the shape and intensity of the field produced, as well as the current distributions that produced it.

A FORTRAN program is being developed to meet this need. At the present time the program is in the advanced debugging stage. That is, it is producing useful material with all bugs apparently removed, but the testing of the program is incomplete. The

program also lacks editorial safeguards against bad input. In its present state, the program automatically computes the field and current distributions only for rectangular theta-pinch and guide-field coils. The addition of other automatic-setup subroutines will allow the computation to be made for nonrectangular coils. Odd-shaped coils could be input directly from data cards. This would require a special input routine. This capability is also expected to be added in the future.

The printed output of the program consists of: a) a list giving the position of the current and flux loops, along with the current in the loops; b) a list giving the coordinates of the points where the B field is computed, B_z, B_r, $\tan^{-1} B_z/B_r$, and the flux inside the radius of the point at this z position; and c) a list giving z position and the values of B_z on the axis at that position.

Since the amount of data is large, several graphical summaries are also output. The magnetic field in the region of interest is shown on an arrow plot with the length of the arrows proportional to the strength of the field. A plot of lines of constant flux is provided as well as a plot of the field on the axis.

REFERENCES

1. W. Lampe, "Beitrag zur Berechnung der notwendigen Trocknungszeit von Grosstransformatoren," Archiv fur Electrotechnik 53 Band, Heft 2, 1969.

2. G. P. Boicourt, "Analysis of Component Failure Problems Using Partially Ordered Sets," Proc. of 4th Symp. on Eng. Problems of Fusion Research, NRL, Washington, DC, April 20-23, 1971. IEEE Trans. on Nuclear Science, Vol. NS-18, No. 4., August 1971.

3. G. P. Boicourt, "The Diagnosis of Underdrying in Paper Castor Oil Capacitors," 6th Symp. on Eng. Problems of Fusion Research, San Diego, California, November 18-21, 1975. To be published by IEEE Trans. on Nuclear Science.

4. G. P. Boicourt, "Some Properties of Castor Oil Affecting its Performance as a Capacitor Impregnant and Their Significance to Future Impregnant Research," ibid.

5. G. P. Boicourt, "Semiempirical Cable Design," Los Alamos Scientific Laboratory Report LA-5691 (1974).

6. R. J. Burke, "Adaptation of a Linear Theta Pinch for a FERF," Int. Conf. on Radiation Test Facilities for CTR Surface Materials Program, Argonne National Laboratory, Argonne, Illinois, July 15-18, 1975, Argonne National Laboratory Report.

X. COMPUTERS

L. W. Mann, R. C. Amsden, K. A. Klare, J. W. Lillberg, F. T. Seibel,
S. T. Bennion, J. C. Newell, F. C. Jahoda, G. I. Chandler, G. A. Sawyer,
C. Nielson

A. INTRODUCTION

The establishment during the past year of the National CTR Computer Network will benefit both theoretical computing and experimental data reduction. Large theoretical problems will be transmitted to the 7600 computer at Livermore. The PDP-10 computer at LASL will provide a local medium computing facility.

In addition to running theoretical problems, the local node will greatly expand data archiving capability and immediate on-line analysis. In addition, it opens possibilities for the automation of two-dimensional data formats which require much more storage than is available on the front-end minicomputers.

There has also been a considerable advance in use of minicomputers on experiments. A completely computerized control system has been successfully developed for Scylla IV-P. Such a system has considerable advantages over a hardwired relay control system, and will be essential on larger next generation devices (Sec. C-1). The Sigma II operating system has been completely revised with numerous improved features for the user (Sec. C-2). A CAMAC Branch Driver has been designed and constructed for the Sigma II (Sec. C-3). On-line analysis programs have been developed for the toroidal Z-pinch, and extensive monitoring of the Scyllac feedback system has been undertaken (Sec. C-4).

B. CTR USER SERVICE CENTER

A National CTR Computer Network is being established by the Division of Controlled Thermonuclear Research (DCTR) of ERDA. It consists of a central computer facility at Livermore linked over high-speed phone lines to medium-scale facilities at Oak Ridge, Princeton, Los Alamos, General Atomics, and Livermore. The central computer is a CDC-7600 with a supporting CDC-6400 for file transport and a DEC PDP-10 with two PDP-11/50's for network functions. Each network node is a User Service Center (USC) consisting of a DEC PDP-10 general purpose computer and a PDP-11/40 for network communications. The LASL center also has an additional PDP-11/40 computer

as part of the link to the local experiment areas.

The network was originally conceived to facilitate theoretical calculations, but, within this past year, experimental data processing needs have received nearly equal priority for use of the local USC. Therefore, DCTR allocated funds to increase the primary and secondary memory capacities of the PDP-10 computers as well as funds for interfacing them to the experiments. This action was taken in lieu of additional and separate computer facilities for expansion of data acquisition capacity for confinement experiments. Thus, the User Service Center has been established at Los Alamos for the following reasons:

1) To serve as a major node in the National CTR Computer Network.

2) To facilitate the acquisition and processing of data from LASL experiments.

3) To provide a medium size general purpose computing facility.

The latter two functions greatly expand upon the original concept for the USC. In particular, it provides for doing those tasks, which because of their small size, required interaction, time constraints or utility, are better suited for the software-rich USC computer. The larger computers in the CTR Computer Center located at LLL can thus be reserved for doing the large numerical calculations. Examples of some of the uses for which the USC may be utilized include:

1) Program creation and modification via interactive text editors.

2) Development of numerical techniques for subsequent inclusion in larger physics programs.

3) Preparation of input data and parameters as well as the post-run analysis of results via interactive graphics terminals.

4) Word processing (i.e., the preparation of research proposals, progress reports, technical papers, memoranda, etc.).

5) Electronic circuit analysis and other similar engineering design programs.

6) Image processing as well as linear signal analysis.

7) Engineering calculations such as electrical circuits, stresses, loading, magnetic field strength, etc.

8) Calculations in support of advance technology and design.

The Los Alamos USC became a reality in 1975. The design and planning functions (e.g., equipment layout, electrical, and mechanical requirements, etc.) were completed in May, and the computer room modification and preparation were completed in September. The computer hardware and software were then installed and accepted with operations commencing in November. The facility at the end of the year had only one disk and 64k of memory and no link to LLL or the experiment areas. Additional equipment has been ordered and another disk and an additional 128k of memory will be added in the first quarter of 1976. The hardware for the link to the experiment areas is also expected by the end of the first quarter with operation commencing at the end of the second quarter. The link to LLL is tentatively scheduled for operations in a preliminary sense in the first quarter of 1976.

The computer currently has three lines of dial-in service available twenty-four hours a day. This will be expanded to eight lines in the first quarter of 1976. Operator service is available 8:00 a.m. to 5:00 p.m. during weekdays. (See Fig. X-1 for a block diagram of the USC and Table X-I for details about the system). Future expansion will include a third disk, 64k additional memory to bring the total to 256k, and more terminal service especially for remote graphics.

The PDP-10 at Los Alamos has been extremely reliable from the start. It is especially free from the curse of most computer systems -- that of losing files.

C. AUTOMATED DATA PROCESSING AND COMPUTER CONTROL

1. *Scylla IV-P Control System.* In a departure from the usual hardwired relay control system used on theta-pinch experiments in the past, a computer-based control system was developed for Scylla IV-P. The system was fully operational for the initial bank check-out at the end of calendar year 1975. It is performing according to its design criteria under both normal and fault conditions, and has successfully survived the electrical transients
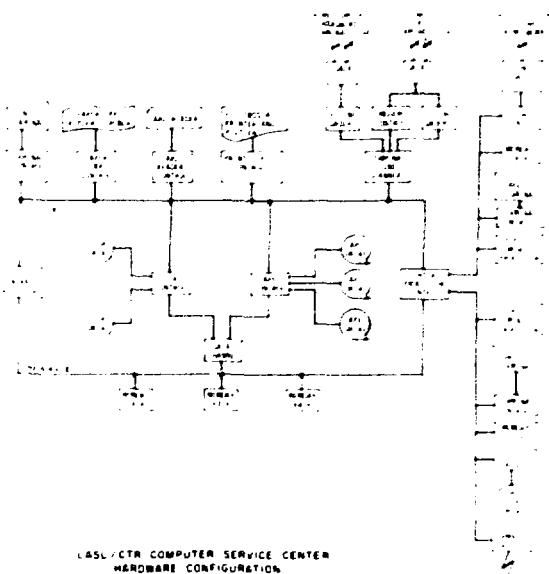
LASL/CTR COMPUTER SERVICE CENTER
HARDWARE CONFIGURATION

Fig. X-1.
LASL/CTR Computer Service Center hardware configuration.

associated with massive bank component failures, e.g., simultaneous rupture of several cable cartridges.

In this system almost all of the logic is contained in the software, so that the sequencing of all electrical or electro-mechanical devices must be performed by the software programs. The only exception is the personnel safety interlock system, which is wired directly into the ac power distribution system and is logically in series with the computer control.

The hardware, a Prime 300 minicomputer with 32k 16-bit words and a three-million-word disk, is interfaced to the experiment with a CAMAC branch driver. The experiment connects to various CAMAC modules (digital input registers, digital output registers, and analog-to-digital converters) through either buffer relays for digital signals or low-pass filters for analog signals. This isolation was deemed necessary to prevent transients from possibly damaging the computer circuitry. The computer, located in a double-shielded screen room, is shown in Fig. X-2.

TABLE X-I

LASL/CTR COMPUTER SERVICE CENTER

PDP-10 Information

Hardware:

No. of Instructions: 378
4 x 15 Index Registers
4 x 16 Accumulators
I/O Bus Bank Width: 13.32 Mbits/sec
Memory Bus Band Width: 144 Mbits/sec
Fixed Point Add   1.5 μsec
Fixed Point Multiply   4.1 μsec
Jump   1.1 μsec
Floating Point Add   3.6 μsec
Double Precision Floating 7.6 μsec
 Add
Virtual Memory Addressing
192K 36 Bit/Work Interleaved Memory,
950-μsec cycle time.
  (~ 20 M 36-bit/words)
2 Disk_, 737.28 Mbits at 6.43 Mbits/sec each
2 7-track tapes, 720 Kbits/sec, 150 ips
1 9-track tape, 288 Kbits/sec, 45 ips
1000 Lpm electrostatic printer/plotter
1000-cpm card reader

Software:

General purpose timesharing and batch
 operating system
Avg. No. Users: 30-80
Languages: MACRO Assembler
            FORTRAN
            ALGOL
            COBOL
            BLISS systems language
            AID algebraic interpreter
            BASIC
Scientific Library
Graphics Library
Utilities Library
Word Processing Library

Fig. X-2.

Prime Computer on Scylla IV-P.

In order to generate the right sequence of outputs from the computer to the experiment, various software features were developed. Each signal in the system was assigned a unique mnemonic interpretable by experienced personnel. A Control Program Language (CPL) was developed that allows an experimenter to write a control program using English language commands e.g., TURN ON PRBKCØ1P, WAIT UNTIL PRBKMØ1V GT 45.0. Here PRBKCØ1P is a digital output signal controlling an ac contactor on Primary Bank Supply #Ø1 and PRBKMØ1V is an analog signal monitoring the output voltage of that supply.

The structure of the control program is shown in Fig. X-3. The core resident software consists of the Real Time Operating System supplied by Prime, Inc. An I/O driver performs all CAMAC functions and tests all digital inputs and analog inputs for

validity as determined by the Status Tables. This program runs to completion every 50 ms. If due to a computer problem this does not occur within a narrow time window, the charge system is brought down in a safe sequence.

A second program called Control Program Interpreter reads instructions written in CPL from a disk file and sets and resets the appropriate entries in the Status Tables with an update every 50 ms. The interpreter handles the interaction between the operator and the system by providing diagnostic messages and accepting set point information from a TTY keyboard.

The system allows the continuous monitoring of all digital and analog inputs, and any signal can be flagged to stop the charge sequence if it goes to an illegal state. In the case of analog signals, this can mean staying within time-dependent limits. That is to say, if a supply charges either too quickly or too slowly, it can be detected and the charge cycle can be aborted. All set points for

STATUS TABLES / DISK FILES

I/O DRIVER / LIMIT TEST / STATUS CHECKS / ANALOG DISPLAY DRIVER

INPUT SIGNALS / OUTPUT SIGNALS / ANALOG SIGNALS / LEGAL INPUTS / ANALOG LIMITS & TRIPS

CONTROL PROGRAM INTERPRETER

CONTROL PROGRAM / ANALOG LIMITS / PROGRAM LOG

CRT MESSAGES
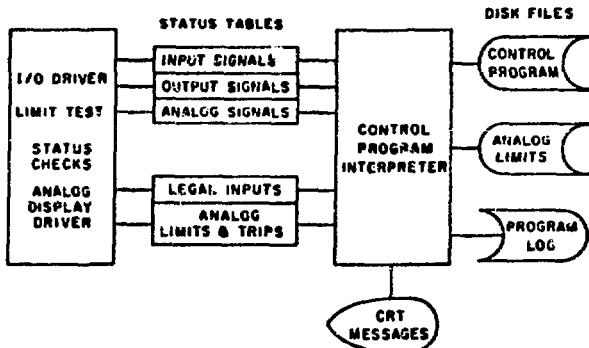
Fig. X-3.

Logical structure on Scylla IV-P Control Program.

monocyclic controlled power supplies are determined under program control. This includes the sequencing of various high-voltage switches involved in switching a supply off. The CPU also has built-in checks to prevent a programmer from inadvertently performing predetermined illegal operations such as charging a supply not connected into a load.

The advantages of computer control are:

1. The system can be designed, built, and tested independently of the experiment.

2. The system is self-documenting. The system cannot run without a program; therefore, the program is always available for inspection. In addition, each step of the control program as executed is written to a disk file for post-mortem analysis if desired.

3. The system is readily reprogrammed for changing circumstances. In fact, multiple programs can be prepared and debugged in advance.

4. The system supplies informative diagnostics about the charge cycle itself. For example, if a power supply goes outside of its dynamically varying legal range, the limit that was exceeded and the value at that time are printed out.

5. The system greatly extends the "eyes and ears" of the operator at a reduced stress level.

Since the required control function is sporadic in nature, the same computer will be used for plasma physics data acquisition and communication with the CTR network local node.

2. *Sigma II Computer System Revision.* An extensive revision of the system software has been completed for both Sigma II computers that significantly enhances their capabilities.

The most significant system change apparent to the user is the replacement of the basic FORTRAN compiler by the ANS FORTRAN compiler. This change permits quicker writing of more powerful programs and allows for interchange of programs with other computers. Among the many new FORTRAN capabilities are logical variables and constants, relational operators, and mixed mode arithmetic.

Another important change is the addition of driver modules for the four TV displays. These drivers make the TVs look like line printers, and along with improved format options, allow both background programs and foreground programs to use the TV displays as output devices just as simply as they would use the keyboard printer.

3. *CAMAC Branch Driver.* Design and construction of a CAMAC Branch Driver, not commercially available for the Sigma II, was successfully carried out. Its primary functions are: 1) to establish the experimental link with the local User Service Center (USC) of the CTR computer network, and 2) to enable interfacing to the new CAMAC compatible A/D transient waveform recorders (Standard Engineering Corp.) that will augment considerably the number of currently available channels (Biomations) at greatly reduced cost/channel during 1976. In addition, it provides a universal interface for front-end devices such as gated integrators, scalers, etc., that have had to be custom interfaced in the past.

4. *Programming.* For the Toroidal Z-Pinch experiments of CTR-2, a complete set of software programs was developed and documented for: 1) data acquisition from Biomation transient waveform recorders, 2) various on-line immediate analyses, and 3) archiving for subsequent further use.

For Scyllac, several new programs were developed for monitoring and displaying the behavior of the feedback modules and position detectors, and continual flexibility was maintained in the various Scyllac programs to serve changing needs of that experiment.

F. C. Jahoda, G. I. Chandler, K. B. Freese, P. R. Forman, R. Kristal, R. E. Siemon

A. INTRODUCTION

The spatially resolved Thomson scattering experiment, incorporating a special design polychrometer capable of extreme stray laser light rejection matched to a SIT target tube under dedicated minicomputer control, has been brought to the point of final checkout and calibration (Section B).

Double exposure holographic interferometry, including background fringes with arbitrarily close time separation between the two pulses, has been achieved. This makes time differential interferograms possible when the ordinary fringe spacing is too dense to be resolved. It also opens a way for near real-time automated electro-optical read-out of visible or infrared interferograms from a single Vidicon frame. Furthermore, it simplifies elimination of spurious phase distortions to which large field-of-view systems are particularly susceptible. The method has been demonstrated both with two lasers and with a single laser design incorporating a second Pockels cell and a calcite prism within the laser cavity. The latter modification can also yield two independent interferograms per plasma discharge when the holographic system is operated in the usual manner (Section C).

The toroidal mode structure framing camera has been redesigned to yield three independently timed exposures during a single discharge and allow forty slits uniformly spaced over a 360° field of view. The key to this improvement, over the earlier version of one frame and eleven slits, is increased light amplification by means of channel plate image intensifier tubes (Section D).

A new type of heterodyne gas-laser interferometer, fast enough for implosion phase studies and capable, in principle, of multiple probing beams without requiring accurate synchronization, has been proved out on CTR-7's 0.9-meter theta pinch. The sensitivity limit is $\int nd\ell = 1.7 \times 10^{16}$ cm^{-2} when operated at 12.5-ns time resolution (Section E).

Simultaneous HF laser interferograms in lands and grooves on Scyllac have not succeeded because of a combination of cylindrical refraction, plasma dynamics, and energy limitations of the laser. A new high-energy amplifier stage for the laser is under

development in order to remedy this situation (Section F).

A new luminosity apparatus incorporating a zoom lens for a variable field-of-view and an improved twenty-channel photomultiplier system has been developed (Section G).

B. DEVELOPMENT OF SPATIALLY RESOLVED THOMSON SCATTERING

The Thomson scattering system being developed (LA-6044-PR, p. 110) will make it possible to determine a spatial temperature profile and a relative density profile from a single laser pulse on a single discharge. Previously, spatial information from Thomson scattering has been obtained by scanning from one discharge to the next. Large inaccuracies, because of shot-to-shot variations, limit the information gained in such a manner, and the procedure is tedious. The new system obtains the entire set of data on a single discharge by means of a computer-controlled digital television camera. We describe here the use of such a detector as it is being developed for Thomson scattering, but other potential and significant applications exist.

The optical system for the spatially resolved measurements is very similar to that in use at the present time on Scyllac (LA-5656-PR, p. 46). The scattered light from different radial locations in the plasma is directed by a lens to different portions of the entrance slit of a polychrometer. After the light is dispersed by the stigmatic instrument, a two-dimensional image is formed in which one direction corresponds to position in the plasma, and wavelength is dispersed along the orthogonal direction. The polychrometer built for this purpose uses two stages of conventional ruled gratings for preliminary stray laser light supression at 1:1 imaging followed by a specially designed concave stigmatic holographic grating from J-Y Optical in the third stage. An image of the entrance slit (40 mm by 1 mm at f/5) is transformed by the holographic grating, without any additional collimating optics, to a spectrum on the television detector (16 mm x 16 mm at f/2). Limitations in

the resolution result from aberrations in the image formed by the holographic grating, but they are acceptable for this application. The measured resolution is 1.5 mm along the 40-mm entrance slit and 120 Å in wavelength. Transmission efficiency from input slit to detector surface is about 10%, and stray light at the laser wavelength is attenuated by 10^{11}.

The detector system is basically a Model 959-D Optical Data Digitizer from EMR Photoelectric. As purchased, it used an RCA 4826 SIT television camera tube. Measurements indicated that a better shutter ratio (transmission-gated-on relative to transmission-gated-off) was required, and greater sensitivity would be desirable, so an ITT channel plate intensifier was combined with the SIT tube. Spatial resolution is more than adequate since aberrations from the holographic grating determine the resolution available. The sensitivity can be varied over a wide range. In the most sensitive regime, individual photoelectrons can be detected in each resolution element (pixel), but the anticipated signal intensity in the present application is 10^2 - 10^4 photoelectrons/pixel. Linearity and dynamic range, while adequate, are limited by the details of the electronics in the Optical Data Digitizer. These have been adjusted so that the full dynamic range of the 8-bit intensity digitizer can be utilized, but the response will have to be calibrated to account for nonlinearities. The intensifier is gated on for 100 ns in synchronization with the laser pulse and has a shutter ratio greater than 10^6.

Computer control is implemented with a mini-computer (Prime 100 with 16k core), which stores the data immediately after a discharge. The amount of data available is limited by the dark current leakage drain in the SIT silicon target (used at room temperature) and the finite computer cycle time for reading individual points. The maximum number of available points from the detector (leakage time/ time per point) is approximately (0.5 s/50 μs) 10 000, but we plan to utilize a much smaller number ($\sim$ 1000).

The system is undergoing final check-out and calibration. It is planned to be operational on Scylla IV-P during early 1976.

C. TIME DIFFERENTIAL DOUBLE EXPOSURE HOLOGRAPHIC INTERFEROMETRY

Fractional fringe holographic interferograms of a plasma have been produced without mechanical motion to produce the background fringe pattern using either two separate ruby lasers for the reference and event exposures or, in a further improvement, a single ruby in a modified cavity. A schematic diagram of the initial apparatus is shown in Fig. XI-1. The polarizations of the lasers are arranged to be orthogonal. The purity of the polarizations and their orthogonality is assured by the Nichol prisms P_1 and P_2. The two laser beams are then carefully combined at beam splitter BS-1. From this beam splitter on, the scene beam for both lasers is identical. The same is true for the reference beam until it reaches the Wollaston prism P_3. Because of the orthogonal polarization, the two laser beams undergo slightly different deflections as indicated by the dots and arrows of Fig. XI-1. This deviation of the reference beam provides the background fringes. In a one-laser system, these are usually introduced by tilting a mirror between exposures.

Because there is no mechanical mirror tilting in this scheme, one is free to fire the two lasers at any time one chooses. In particular, they can be fired with very little time (Δt) between them, which yields interferograms of $\Delta n/\Delta t$ rather than of n, i.e., the total change in n (electron density) referenced to vacuum. This will be valuable on the Scylla 1-C laser heating experiment. In that experiment, the effect of a focused 100-J CO_2 laser upon a cold dense theta pinch is to be investigated.
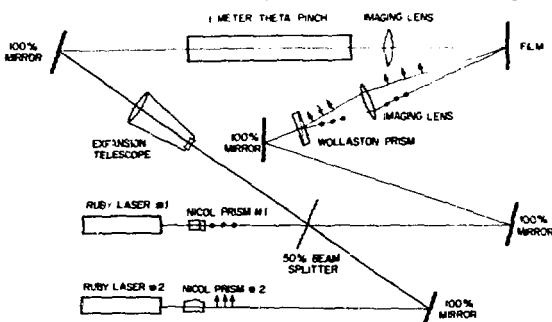
Fig. XI-1.

Schematic diagram of two-laser apparatus for fractional fringe holographic interferograms.

Conventional end-on interferograms of the plasma near the upper end of the pressure range of interest have fringe densities too great to be resolved. With time differential holography, the overall plasma effect will be subtracted out and only the change during a short time recorded. In particular, this time interval could span just the period of laser heating. Such an interferogram (without CO_2 laser heating) is shown in Fig. XI-2. The two exposures were made 300 ns apart at a time when a plasma column of about fifteen fringes total was present. During this time, there was approximately a one-fringe change.

An undesirable feature of this system is the necessity of using a second laser. To overcome this, a new type of ruby laser cavity has been constructed. This is shown in Fig. XI-3. One of the features of holographic lasers is that very little of the ruby rod is actually used. Of the total rod diameter available, only about 1.5 mm somewhere near the center is used. If Pockels Cell #2 and the calcite prism of Fig. XI-3 were removed, the cavity would be a conventional Q-switched ruby cavity with the pinhole for transverse mode selection in an unusual location. The PC #2 and calcite prism are included in an orientation such that the cavity operates in the usual way by energizing PC #1. A second pulse occurs when PC #2 has voltage applied at a later instant. To understand the mechanism, consider light reflecting from the front mirror of polarization orthogonal to that of the conventional mode. This light is then of the extraordinary polarization with respect to the calcite prism, and hence, is deflected upward. It enters Pockels Cell #2 and emerges with its polarization rotated by 90°. Because of this rotation, it proceeds through the cavity as in the conventional mode; however, a part of the ruby that has not been depleted by the first pulse is being used. Because of the displacement, the prism intercepts the beam and sends it to the second back mirror. The result is a laser that has one pinhole and one output mirror, which puts out two independently timed pulses that are colinear and of orthogonal polarization. Test interferograms have been successfully made with this laser.

Such a laser will have several uses:

1. Time differential interferometry will be made simpler.

2. By firing the first beam about 50 μs before the plasma event and the second beam during the event, conventional interferograms are obtained; however, there is no time for room vibrations or air turbulence in the beam paths to distort the data. This elimination of extraneous disturbances could be an important advantage in some situations.

3. Of potentially great significance is the fact that this method opens the way to record a double exposure hologram with background fringes on a single frame (millisecond time scale) of a Vidicon camera (at visible or infrared laser wavelengths). The camera must still have a resolution capability determined by the fine scale fringe structure of the individual exposures, but the automated data readout need occur only once at the lower resolution level required by the product interferogram.

4. If conventional holographic systems are
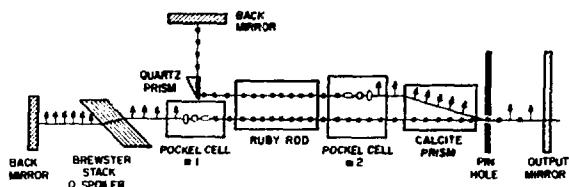
Ruby laser cavity for single-laser time differential holographic interferograms.

sufficient, this type of single ruby laser can be made to yield two conventional holograms at different times in the discharge by simply inserting a Nichol prism with large angular difference for the two polarizations in the reference beam oriented at 45°. Both polarizations would be produced first before the event and then at selected times during the event. A possible further extension of this scheme is to double pulse the voltage on Pockels Cell #1 and thus eliminate the prism and extra rear mirror. Once this is achieved, the addition of a second calcite prism orthogonal to the first, double pulsing the second Pockels cell, and adding a third Pockels cell, will produce four independent pulses, two of each polarization. The beams are physically separated in space at the back mirror; therefore, one would try to take the reference beam out of the back of the laser and the scene beam out the front. Such a laser could produce four independently timed interferograms during a single plasma discharge.

D. TOROIDAL IMAGE INTENSIFIER FRAMING CAMERA

The toroidal mode structure framing camera (LA-6044-PR, p. 25) has been redesigned to incorporate three separate frames per discharge (compared to one previously) and up to forty slit views (compared to eleven previously). The new system is built and installed on the Scyllac derated sector. A schematic of the setup is shown in Fig. XI-4. The system is positioned on the Scyllac major axis and is designed to view the plasma in the groove region of every wavelength (9° intervals). The pyramid mirror device, therefore, contains forty facets, and the axis of the pyramid is adjustable with respect to the Scyllac toroidal plane. A real toroidal image is formed at the output of the catadi-
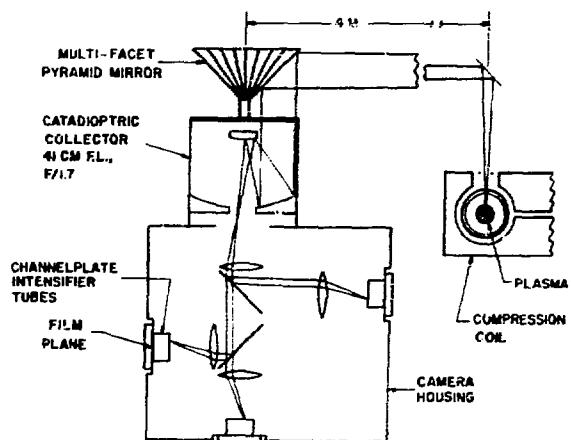
Fig. XI-4.

Schematic of 3-frame toroidal image intensifier framing camera.

optric collector, and this image is relayed by f/1.4 lenses and beamsplitters to three channel plate image intensifier tubes (ITT-18-mm format). The tubes are independently gated at selected times in the discharge. The output phosphors of the tube are fiber-optically coupled to the film plane (Polaroid type 57 sheet film is used). The plasma is viewed through slits in the compression coil. Two fiducial markers are placed across the slits at ~ 3.7-cm separation. They are back-lighted by plasma stray light.

A photograph of the system installed on Scyllac is shown in Fig. XI-5. The camera requires +28 V of external power and three low level triggers for gating the three tubes. All remaining electronics are internal to the camera.

The initial configuration of eight viewing locations on the derated sector is shown in Fig. XI-6. The remaining groove locations were not available for use. Sample data, obtained on discharge #7976, are shown in Fig. XI-7. Gate pulse width is 150 ns for all tubes and the timing of the three frames with respect to the magnetic field is shown on the monitor trace. The images are radially inverted, so that outward motion in the photographs corresponds to inward motion in the toroidal plane. The three frames show a predominant inward plasma motion in time. There is a strong toroidal variation of plasma position with maximum displacement occurring at a point somewhat clockwise of machine
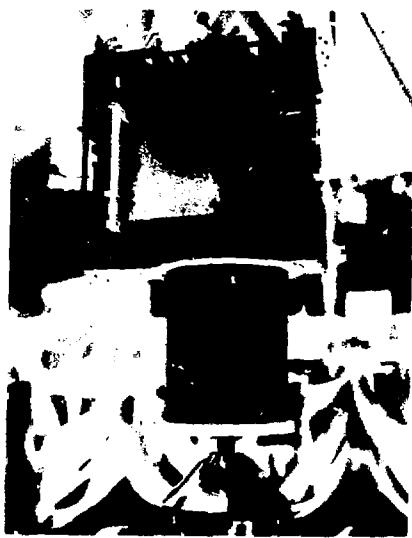
Fig. XI-5.

Toroidal mode structure framing camera installed on Scyllac.

Fig. XI-6.

Location of framing camera viewing slits on Scyllac derated sector.

center. Part of the plasma (near the clockwise end) even moves opposite to the main body.

Analyzed plasma position for the three frames is shown in Fig. XI-8. The error bar indicates a measurement accuracy of $\pm$ 3 mm. Part of this error is parallax in the system ($\pm$ 2 mm), which can be reduced by placing the fiducial markers closer to the plasma (e.g., on the discharge tube). For determining growth rates, this effect is eliminated by taking the difference between frames. The remaining error is due to resolution of the system ($\sim$ 10 Lp/mm), and the limited ability to visually locate the exact plasma center.

The measurement currently suffers from lack of a means to quickly read the large amount of data accumulating. Since only a number of x-y position measurements is required, it should be one of the less demanding tasks and will be one of early attempts of a new project on Automated Acquisition of 2-Dimensional Data.

E. HETERODYNE INTERFEROMETRY

An acousto-optic cell may be used to shift the light frequency in one arm of an interferometer so as to continually produce difference frequency beats when combined with the unshifted frequency of the other arm on the surface of a photodetector. A changing plasma density can be measured by detecting the small time shifts produced in the beat frequency when one arm traverses the plasma. The principle of the measurement is analogous to the coupled cavity interferometer and retains the advantage of fringe counting over the ambiguity associated with amplitude measurements. In addition, it has two primary improvements over the coupled cavity: a) fast fringe rates ($\sim$ 100 MHz) suitable for implosion measurements on a θ pinch can be produced, and b) multiple channels can be easily synchronized on a single experiment.

A Michelson interferometer configuration utilizing this technique was tested on the CTR-7, 0.9-meter resonant heating experiment.

This experiment specifically requires the fast time response and has line density just large enough for double pass measurements at 632.8 nm. The fairly compact optical system is shown in Fig. XI-9. The majority of the optical components are on a steel table of adjustable height and are in a plane below the discharge tube, thus allowing a simultaneous ruby holographic study (only small mirror M_6 blocks a portion of the expanded ruby beam). Large mirror M_7 is used simultaneously by both systems. Lens L_7 serves to focus the light on the acoustically driven lead molybdate crystal, and both the diffracted and zero-order beams are then recollimated by L_2.

The crystal is driven so that an acoustic grating continually moves in the direction of

132
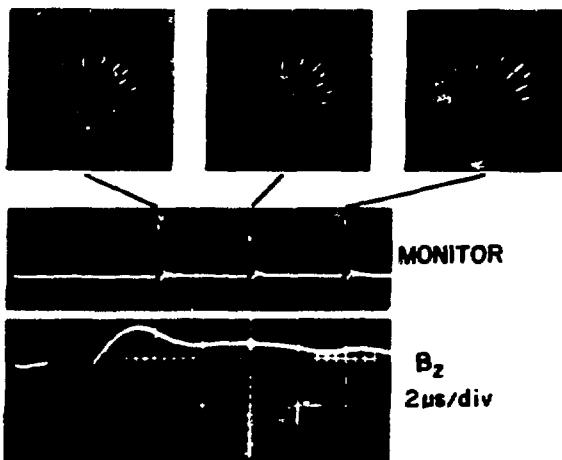
Fig. XI-7.

Toroidal mode structure framing camera data (Shot #7976).

Fig. XI-9

Plasma radial position vs. toroidal angle on Scyllac derated sector.

the diffracted beam, and this can be shown to result in an increase in frequency of the reference arm by the amount of the acoustic frequency (set at 80 MHz, tunable from 75 MHz to 125 MHz). The diffracted beam has an angular separation of 17 mrad and is picked off by M_3 to become the reference arm. The zero-order beam is passed through the plasma at a radius of 4.5 cm from the tube center in order to study rapid off-axis density changes. The two beams are recombined at a pellicle beam splitter in such a manner as to eliminate reflections back into the laser and associated coupled-cavity effects. The recombined beams are reflected to a detector positioned in the screen room. The detector is a Meret 528N photodetector module (w/ preamp). The module provides a fringe signal of 50 mV into 50 Ω at 80 MHz. The detector appears to have dropped off 3 or 4 dB (relative to low frequencies) at 80 MHz, but linearity is not as critical in this case as in the case of amplitude measurements.

Data were obtained with this technique at both 20-mTorr and 9-mTorr fill pressure, and the latter are shown in Fig. XI-10. The observation time on any single shot was about 250 ns, and its location with respect to the magnetic field waveform is shown by voltage spikes on the timing photo. The lower photo shows the fringes with plasma (data) on top and without plasma (reference) on bottom. The reference waveform is recorded several seconds after

the shot. The graph is a composite of several shots with various starting times for the observation interval.

The fringe shifts obtained are small, amounting to only 0.2 - 0.3 fringe total. For precise reading of the peaks and troughs, a measuring microscope was used, and this allowed a worst case phase resolution of ± 1/20 fringe. Analysis of a vacuum shot showed a rms phase resolution of 1/40 fringe. The data show the density rising to a peak and leveling off in 150 ns. No density sheath is observed passing by, indicating a buildup of the plasma column at this radius. The area density change obtained (1 fringe = 1.8 x 10^{17} cm^{-2}) may be converted to a local density change only if the axial profile is known. However, assuming an equivalent uniform length of 100 cm gives a density increment (at 4.5-cm radius) of ~ 5 x 10^{15} cm^{-3}. To obtain absolute density, this change must be added to the initial density established in the preionization phase.

Currently this technique is limited to very high speeds by the frequency of our acousto-optic modulator. Visible light modulators are generally limited to frequencies above 25 MHz in order to obtain good diffraction efficiencies in a single order (i.e., the Bragg region). This is in any case a desirable frequency range for studying the implosion phase. If lower frequency beats are required, another modulator in either arm would allow a tuning of beats to lower frequencies by subtracting the two light frequency shifts.
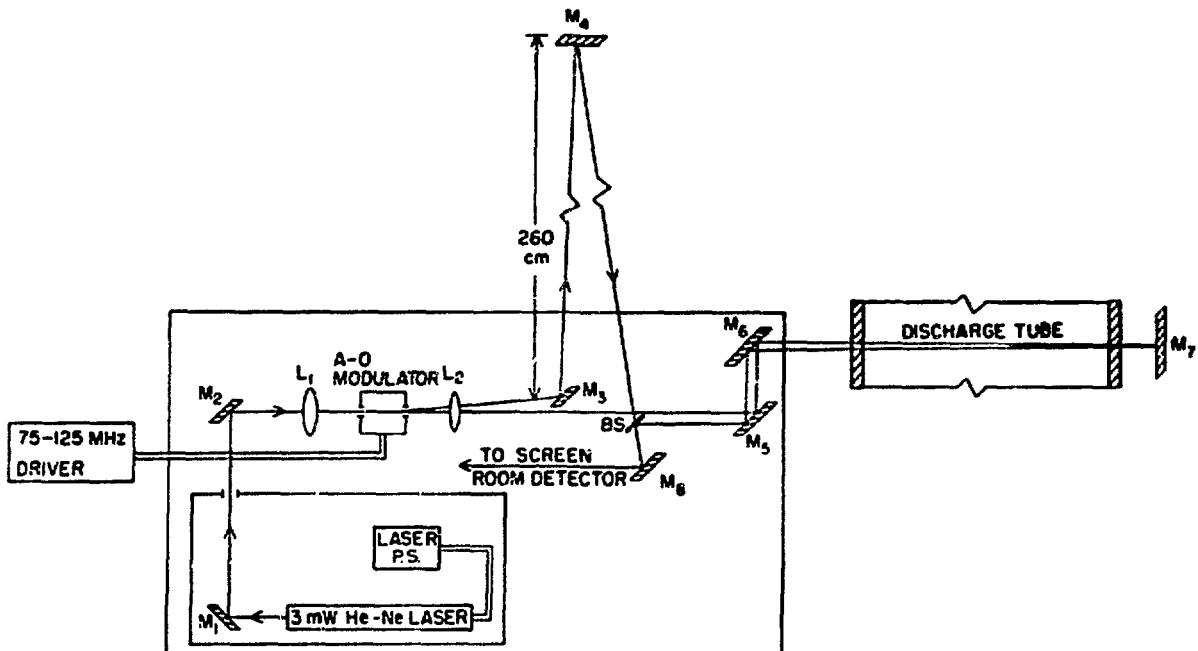
80 MHz MICHELSON HETERODYNE INTERFEROMETER

Fig. XI-9.

Schematic of optical system for laser heterodyne interferometer.

Attempts are under way to extend the technique also to the near infrared 3.39-μ wavelength and lower beat frequencies of the standard coupled-cavity interferometer. Arsenic trisulfide glass has been chosen as best suited for a single-cell modulator and will be driven by a lead molybdate transducer. Assuming equal intensity in the first-order and zero-order beams at 20 MHz and a 10% acoustic coupling efficiency requires a 40-watt R. F. power supply.

F. HF LASER HOLOGRAPHIC INTERFEROMETRY

HF interferometry (LA-6044-PR, p. 104) has been used to measure plasma density at a groove location on the Scyllac derated sector. Values obtained near peak field were in the range 2.7 - 4.7 x 10^{16} cm^{-3}, decreasing with increasing bias field, for filling pressures of $\sim$ 18 mTorr. Plasma radii obtained (1/e point) have been found to agree within 10% with those obtained from the luminosity measurement.

An attempt was made to make simultaneous measurements in both groove and land regions on the Scyllac full torus. It failed because of the inability of the interferometer to probe more than $\sim$ 2 cm off the discharge tube axis. This is a consequence of the off-axis cylindrical refraction, available optics, and required demagnification to evaporate the bismuth detector. The derated sector plasma is considerably less well centered than the previous high-temperature plasma in the full torus. The behavior in the land region, consisting of a strong helical oscillation and a large outward shift of the plasma away from the minor axis, makes it impractical to try the simultaneous density measurement with the existing capability.

The central problem in this measurement is insufficient energy. The energy available in a single line determines the allowed size of the exposure on the bismuth detector plate. This currently forces a severe demagnification (5 or 10:1) in the image size. This constraint, coupled with resolution and depth of field requirements, limits the field of view to $\sim$ 4 cm when using single-imaging lenses.

A new high-energy amplifier stage is under development. This unit is a linear scaleup by a factor of 5 in the discharge chamber cross section.
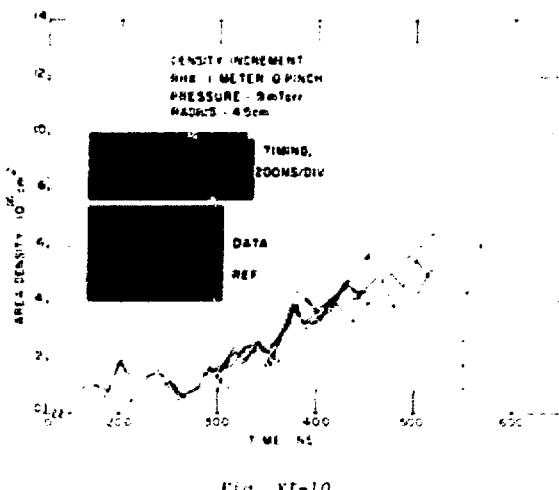
Fig. XI-10.

Heterodyne laser interferometer data on 0.9-meter
resonant heating experiment.

Thus, the active cross section is 10 cm x 20 cm with
a length of ~ 1 m. We are hoping for ~ 50 joules
(multi-line) from the new system. The laser head
is fed from a water line, which is to be pulse
charged to ~ 300 - 400 kV from an 8-kJ Marx bank.
The Marx bank has been designed and built, and is
currently being debugged. The discharge head has
been built and satisfactorily tested for mechanical
and vacuum integrity. The water line and connecting
parts are under construction.

G.   NEW LUMINOSITY APPARATUS

The 10-channel luminosity apparatus used pre-
viously on Scyllac has been expanded to 20 channels.
The magnification by the imaging optics has also
been modified, resulting in a √2 increase in both
the field of view and image resolution. The larger
field of view has been very helpful in observing
the derated sector plasma since excursions of the
plasma column are larger than in the torus. The
increased resolution has also improved the accuracy
of the profile measurements in the lands where the
plasma radius is small. A second (10-channel) ap-
paratus permits simultaneous operation in land and
groove locations.

Even with this increased resolution and field
of view, there are times when it is desirable to
sacrifice some resolution for yet more field of
view, and vice versa. The present apparatus is
inflexible and such changes cannot be made without

completely rebuilding the internal optics of the
device. Therefore, a new luminosity device, which
has a continually variable internal magnification,
has been designed.

The new device, which will first be used on
Scylla IV-P, allows the size of the plasma image at
the fixed detector array to be varied, while main-
taining image focus. This is accomplished by use of
a zoom lens to relay the plasma image formed by the
collimating optics onto the detector array. In the
old design the image was formed directly on the
detector. The focal length of the zoom lens can be
changed mechanically, thus changing the magnification
of the image over a factor three range. Image focus
is maintained by the simultaneous motion of an in-
ternal compensating element, which keeps the back
focus distance constant. The result is a continually
adjustable plasma image on the detector.

This modification will provide a high degree of
flexibility to the luminosity profile measurement.
Once the apparatus is positioned and focused, it
can be used for detailed profile measurements when
the plasma position is relatively constant. Alter-
natively, it can be used to follow a wide range of
plasma motion when highly resolved profile informa-
tion is not desired.

In addition to the use of the zoom lens, other
modifications have been made in the imaging system,
which should improve accuracy and reliability. For
instance, the beam splitter used to provide cali-
bration pulse light to the detector array has been
moved out in front of the objective lens, so that
the calibration light passes through the same optics
as does the plasma light. This had not been the
case in previous luminosity measurement systems.
Also, precise external controls of the zoom focal
length and the iris diameter have been provided
through the use of gear drives. External dials with
10-turn readout capability are used to vary the im-
age magnification and brightness. In addition, the
magnification control shaft is ganged with a 10-
turn potentiometer allowing remote computer sensing
of the image magnification and, therefore, channel
spacing in the plasma.

The light measurement system is also being
improved. New photomultiplier tubes (EMI 9798B)
are being used, which have a higher light gain and
broader spectral response (S-20) than the tubes

previously used. Also, a new line driver amplifier has been developed with a risetime of 2-5 ns for signal levels up to 10 volts. A new modular design is being used for the photomultiplier housing that will allow easy access for servicing and replacement of photomultiplier tubes *in situ*.

XII. MAGNETIC ENERGY TRANSFER AND STORAGE

*D. J. Blevins (Q-23), R. A. Haarman (P-14), C. G. Hoffman (L-4), T. I. Jones (CMB-6),
C. R. King, J. D. G. Lindsay, L. B. Lundberg (Q-23), G. A. Miranda, J. J. Petrovic
(CMB-5), J. D. Rogers, C. E. Swannack, W. C. Turner (Q-23), R. W. Warren (Industrial –
Westinghouse), J. D. Weldon, D. H. Whitaker, K. D. Williamson, J. J. Wollan*

A. SUMMARY

Significant progress was made in 1975 toward development of the superconducting magnetic energy transfer and storage (METS) system for use in future theta-pinch experiments. The technology being developed will have application to other CTR programs such as tokamak ohmic-heating systems and laser flash lamp power supplies. This work will culminate in a demonstration METS-SFTR coupled superconducting prototype system. The prototype is to be composed of three, 400-kJ superconducting energy storage coils stacked as a solenoid in an all-plastic non-conducting ℓHe dewar. The coils will be charged in 300 s to a field level of 2.5 T at 25 kA through continuous duty leads and discharged in 0.7 ms through special co-axial pulsed leads. The coils, charged in series with interconnecting switches or cryogenic disconnects, are first connected in parallel with respective inductive loads and shorting HVDC vacuum interrupters by opening the disconnects and then the energy is transferred by opening the interrupters. The energy transfer is efficient, being determined by the storage coil inductance – transfer capacitance – load inductance resonant circuit. Finally the energy is trapped in the load coil by a shorting crowbar switch for a 250-ms e-folding time decay period. During the past year, the simultaneous development of all the system components has resulted in the following accomplishments:

1. Successful interruption of 17 kA with standoff of 44 kV using a single 7-in. Westinghouse vacuum interrupter.

2. Development of two systems for measuring losses during discharge of the 300-kJ superconducting coils.

3. Successful production of Cu/CuNi/NbTi superconducting wire with a j_c of 2.5×10^5 A/cm^2 at 30 kG with a wire resistivity level of 10^{-12} ohm-cm.

4. The obtaining of mechanical property data for NbTi rod and further insight in the effect of impurities on the superconductor.

5. Testing of the IGC epoxy-fiber glass bronze mockup, 300-kJ coil and near completion of the MCA 300-kJ superconducting coil.

6. Completion of the 400-kJ coil design, the design of a simplified cryogenic disconnect utilizing Multilam; completion of pulsed lead and cable design; completion of design, fabrication, and testing of a 107-cm i.d. epoxy-fiber glass Dewar; and near completion of the installation drawings for the 700-W, 4.5-K refrigeration system. All of these are for the SFTR prototype system.

7. Completion of the SFTR conceptual design study.

8. Completion of the dielectric strength and voltage tracking studies in cryogenic helium and nitrogen.

9. Monitoring of the Westinghouse and University of Texas-EPRI funded study contract to design a 30-ms discharge time, 1-GJ homopolar machine and a 10-MJ prototype.

B. HVDC INTERRUPTER TESTS

1. Facility. The purpose of the facility is to provide experimental verification of successful current interruption using room temperature breakers and to test various components of the interrupter circuit. The facility became operational in November 1974. It successfully simulates the resonant energy transfer of the METS system for testing the HVDC vacuum interrupters and components with appropriate voltage (>40 kV) and current (>15 kA) characteristics. The facility is to be extended in its testing capacity to 60 kV and 30 kA. All hardware items for the upgrading were designed and are now available to make the modification. The crowbar as it will be used on the METS prototype, consisting of four type D ignitrons in series, has been designed, built, and tested to the present limit of the facility.

2. HVDC Interrupters. Testing has been completed on the 7-inch Westinghouse vacuum breakers with Ross actuators. Current interruption always occurs when the proper operating conditions are used.

One breaker has been operated up to 17 kA and 44 kV with no degradation. The interrupter circuit has been simplified by omission of the saturable reactor originally felt to be necessary to suppress the rate of change of current at I = 0 to increase the time for deionization. $\dot{I}$ values as high as 600 A/μs were encountered with successful current interruption.

Mechanical life tests were performed on the vacuum breaker bellows using the Ross Engineering actuator. Three interrupters were cycled 74 000, 10 900, and 10 400 times without damage.

Another 7-in. Westinghouse interrupter has been tested for use in switching the 300-kJ industrial coils. As such it has been ramped to carry current up to 10 kA over a 60-s period and then operated successfully through the current interruption cycle.

3. Flying Disk Interrupter. A fast breaker which opens under "no arc" conditions, with a gap opening velocity which exceeds the voltage rise waveform of the METS-SFTR circuit is being developed.

The aluminum mechanical prototype flying disk breaker was used for the first time to interrupt current. The best interruption was at 1.83 kA with a peak voltage of 2.1 kV. Since the breaker was operated in air, arc restrike occurred. To advance the development the next model will have to be one which provides for complete arc quenching.

C. 300-kJ TEST FACILITY

The 300-kJ test facility was used for additional tests on the LASL 300-kJ, 10-kA coil, for testing a bronze mockup of the IGC 300-kJ, 10-kA coil (Section F), and to complete the superconducting switch program (Section E).

1. Power Supplies. The 6-V, 18-kA homopolar power supply used to test the 300-kJ coils has been modified to eliminate undue brush noise. The slip ring was machined in place, the rotor balanced to within 1.0 g-cm; and pneumatically operated brushes installed. In addition, two d.c., 5-kA pass bank battery operated power supplies for charging coils have been built.

2. Continuous Duty 10-kA and 25-kA, 60-kV Cryogenic Electrical Leads. Two new 10-kA continuous duty current leads have been designed and fabricated for use with the three identical superconducting, 300-kJ storage coils. The leads are vapor cooled and similar to those already in use in the 300-kJ test facility. The lead insulation is a combination of Mylar and G-10 fiber glass and will withstand 60 kV.

Two 25-kA, 60-kV continuous current leads were also designed and fabricated. These leads will be used to test the cryogenic disconnect and the 400-kJ prototype coils.

3. Energy Loss Measurement Apparatus. The energy loss during pulsed operation of the 300-kJ superconducting coils is to be determined by measuring the gas evolved immediately after a pulse. A gas shroud to cover the coils was built to collect the gas. The shroud was calibrated by discharging a capacitor through the prototype bronze IGC coil. (Section F).

The gas collection-energy loss measuring system is augmented with an electronic system. In this system the total voltage across the storage coil minus the inductive part of the voltage as measured with a pickup coil is integrated and then plotted against the current in the storage coil. With a cyclic charge and discharge of the coil, the plotted curve is a loop whose area is proportional to the energy loss in the storage coil. Energy loss in the 300-kJ storage coil is expected to range from 0.03% to 0.3% of the stored energy and considerable care is needed to prevent extraneous voltage sources from masking the desired voltage.

D. SUPERCONDUCTING WIRE DEVELOPMENT

1. Industrial Status. The performance specifications for the 300-kJ energy storage coils require a current of 10 kA to be charged in 10 s and discharged in 0.002 s without going normal. The energy loss per cycle is to be below 0.3% of the stored energy. Conductor for the coils must be multistrand cable or braid and possibly made of multi-filament strands. To meet the large rate of change of field required without coupling between the individual Nb-Ti superconducting filaments, the superconducting filaments must be small, isolated electrically, and twisted or braided to yield low-energy losses.

The electrical coupling between filaments is minimized in the MCA coil wire by using an insulated 0.005-in. monofilament, Cu matrix wire that is cabled and braided into a 1224-strand conductor.

The electrical coupling between filaments is minimized in the IGC wire by putting Cu-Ni resistive barriers between the filaments in each wire as well as by cabling. Test samples indicate that the wire is excellent. This wire was produced using procedures and specifications worked out between LASL and industry.

2. *Wire Evaluation Program.* Evaluation of wire samples is being done in three major areas: short sample critical current (<1 kA), ac loss measurements, and metallurgical and mechanical studies of extrusion crops and starting materials as well as wire.

The critical current measurements are done on bifilarly wound coil samples approximately one meter in length. They provide data up to 500 A and 70 kG at wire resistivity levels less than 10^{-12} ohm-cm. Test samples of IGC wire for their 300-kJ coil have consistently yielded j_c's of 2.5 x 10^5 A/cm^2 at 30 kG and at a wire resistivity level of 10^{-12} ohm-cm. With refinements in the heat treating process, values as high as 2.8 x 10^5 A/cm^2 have been attained. The marked improvement in these j_c's is a result of using high-purity, well-annealed Cu-30Ni; helium-gas-quenched, recrystallized Nb-Ti rod; annealed Cu-10Ni cans; dense billets; and correct extrusion parameters.

The loss apparatus is capable of measuring static hysteresis losses up to 25 kG and dynamic losses up to $\dot{B}$'s of 3 x 10^7 G/s. Loss measurements have been made on two basic wire systems. The first system consisted of a set of wires with a CuNi-Cu matrix for sizes from 0.025 cm to 0.076 cm. Both hysteretic and pulsed losses were evaluated. Total losses were measured as a function of both wire diameter, twist pitch, maximum applied B, and $\dot{B}$. The hysteretic losses are dominant and the Cu-Ni barriers are effectively limiting the eddy current losses in the matrix. Second, a similar set of data was taken on a series of copper matrix wires as a function of the same parameters. In this case the coupling or eddy current losses in the matrix dominate; however, for some wire parameters the loss goes through a maximum as a function of $\dot{B}$.

The room temperature mechanical properties of NbTi rods comparable to those which have gone into extrusion billets for the LASL wire program have been studied. Eleven different specimen sets have been tested, and the data from these tests are pre-

sented in Table XII-I. All the rods were fabricated by Teledyne Wah Chang Albany (TWCA). So far, the highest J_c conductors have been made with the NbTi from heats 590548 and 590549. The former gave 2.5 x 10^5 A/cm^2, and the latter, 3 x 10^5 A/cm^2, both at 4.2 K, 3 T, and 10^{-12} ohm-cm. These rods exhibit high ductility, are recrystallized/helium-gas-quenched, and have the lowest titanium content of those tested.

The elastic modulus data shows a significant dependence on titanium content. This is consistent with Russian data.[1] There also appears to be a significant titanium content effect on the shape of the stress-strain diagram. As can be seen by comparing Figs. XII-1 and XII-2, an upper and lower yield point is found in the higher titanium alloys. This yield point phenomenon can cause complications in the wire drawing operation. The absence of the yield point phenomenon usually means easier wire drawing.

Strain-rate sensitivity studies were made on materials listed in Table XII-I. Both instantaneous strain rate change and stress relaxation were used to determine the strain rate sensitivity, m. According to Hart[2]

$$ m = (\partial \ln \sigma / \partial \ln \dot{\varepsilon})_\varepsilon = (\partial \ln \sigma / \partial \ln \dot{\sigma})_{\dot{\varepsilon}=0} \cdot $$

where σ = stress and ε = strain.

The data are compared with various metals in Table XII-II. It will be noted in this table that the strain rate sensitivity of the NbTi alloys in this composition range have intermediate values. The higher the value of m, the more uniform elongation a material will exhibit before the onset of localized necking (plastic instability). The strain-rate sensitivity tends to increase with temperature which probably helps explain why slowing extrusion rates and lowering the extrusion temperature have tended to give better superconductors.

3. *High-Critical-Current Testing Facility.* Tinning and epoxy potting procedures were developed to test the MCA braids and IGC cables. The conductors were reliably constrained by the potting systems used.

Two MCA braids, one rectangularly compacted IGC cable, and a major sub-bundle of wires from an uncompacted round IGC cable were tested. Both cables and the sub-bundle carried current well beyond the limiting current requirement for the 300-kJ

TABLE XII-I

TENSILE TEST DATA FOR NbTi .PERCONDUCTOR ROD

Heat Number	Rod Description	Wt% Ti	Wire[1] Cond.	0.2 Yield Strength[2] (MPa)	Ultimate Tensile Strength (MPa)	Young's Modulus (GPa)	Total Elongation (%)	Reduction in Area
590418	0.070-in. Hex	47.9	RX/SC	(3)	477 + 4	75.2 + 0.7	24 + 2	64 + 2
590418	0.143-in. Hex	47.9	CW	636 + 7	681 + 1	74.5 + 4.1	15 + 1	76 + 1
590486	0.078-in. Rnd	49.2	CW	608 + 8	643 + 4	69.0 + 2.0	7[4]	67 + 3
590486	0.151-in. Rnd	49.2	CW	577 + 10	592 + 10	69.0 + 2.0	9[4]	72 + 2
590486	0.151-in. Rnd	49.2	RX/GQ	(5)	449 (7)	72.2	28	7E
590549	0.125-in. Rnd	45.7	RX/GQ	498 + 3	521 + 12	82.0 + 0.7	20 + 1	71 + 1
590548	0.190-in. Rnd	45.6	RX/GQ	425 + 2	445 + 2	80.0 + 2.0	31 + 2	93 + 2
590548	0.190-in. Rnd	45.6	RX/GQ	443 + 1	458 + 1	80.0 + 1.0	28 + 3	90 + 2
590592	0.093-in. Rnd	(6)	RX/SC	480 + 9	488 + 8	83.3 + 0.6	23	81 + 1
590592	0.182-in. Rnd	(6)	RX/GQ	485 + 5	507 + 6	90.0 + 2.0	26 + 2	84 + 1
590663	0.126-in. Rnd	(6)	Unknown	480 + 0	500 + 0	90.0 + 4.:	23	64 + 0

(1) RX/SC = Recrystallized/slow cooled
    CW   = Cold worked
    RX/GQ = Recrystallized gas quenched

(2) + values are standard deviation of the means

(3) Upper yield point = 490 + 3 MPa
    Lower yield point = 461 + 3 MPa

(4) Estimated from load deflection curves

(5) Upper yield point = 463 MPa
    Lower yield point = 441 MPa

(6) Data not yet received.

(7) Data without standard deviations are for one sample only.
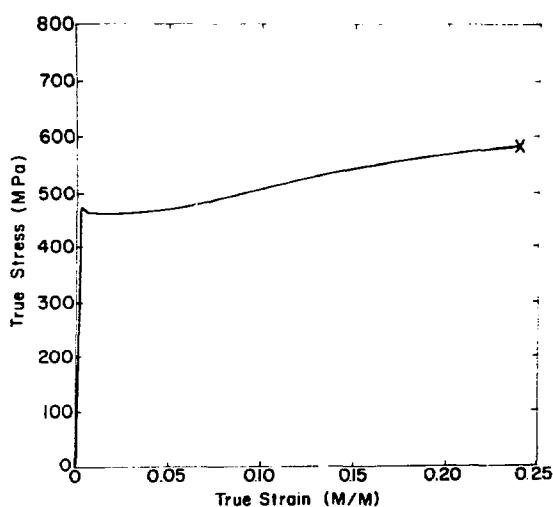
Fig. XII-1.

Typical room temperature stress-strain diagram for RX/SC Nb-48 wt. % Ti.
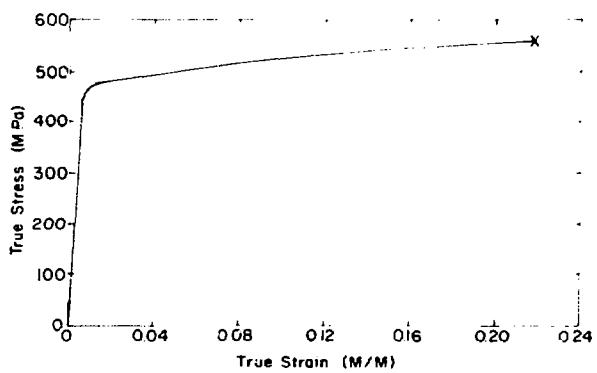
Fig. XII-2.

Typical room temperature stress-strain diagram for RX/GQ Nb-46 wt. % Ti.

TABLE XII-II

STRAIN RATE SENSITIVITY OF METALS AND ALLOYS
AT ROOM TEMPERATURE

Material	m
Nb-48Ti RX/SC, TWCA heat 590418	0.025
Nb-49Ti RX/GC, TWCA heat 590486	0.023
Nb-46Ti RX/GC, TWCA heat 590548	0.022
Nb-46Ti RX/SC, TWCA heat 490548	0.022
70 - 30 Brass	~ 0
Cu	0.006
Low-Carbon steels	0.010-0.015
Mo	0.06
Nb	0.12

coils. The coil specification calls for the 10-kA, 2.2-T operating condition to be exceeded by the limiting transport current as measured along the load line by 50%.

A new large-bore dipole magnet is designed for testing of large superconducting cables in fields up to 60 kG. The major design work is complete for the magnet structure windings, quench protection, and coil winding apparatus. Engineering of the mechanical structure is well under way and the drafting design is nearly complete. A copper wire of the same dimensions as the superconductor was ordered and is being used to build a mechanical mockup of the magnet to determine conductor tolerance accumulations and packing densities and to solve construction problems. This mockup is about half complete.

4. *Cabling and Epoxy Potting Development.*
Because of problems developed during cabling and cable compaction which caused insulation damage and shorting between wire strands for the 300-kJ industrial coils, an extensive program has been initiated to eliminate the insulation damage for the 400-kJ METS-SFTR prototype storage coils. The experimental work will examine a number of cable arrays, different types of insulation, means of removing the insulation without unwinding the cable, and varying degrees of cable compaction. Bronze will be used to simulate the superconductor.

The cabling work is to be followed with epoxy potting of stacked short lengths of cable wrapped in fiber glass to evaluate different epoxy systems for their structural and thermal cycling integrity as well as their compatibility with the wire insulation.

E. 10-kA SUPERCONDUCTING SWITCHES

The 4-ohm, 10-kA superconducting switches were completed and tested. These switches were of the parallel-element type; one containing ten modules of the sleeve braided element, the other, five modules of the accordion-type element connected in parallel. Test results are shown in Table XII-III. When the switches were connected to the storage coil, they were located about one meter from the storage coil. These fringing fields caused the lower current values for the coil-switch combination.

Additional 10-kA low-resistance superconducting switches were made with a single 121-wire braid wound as an accordion-type module. Resistance of the switches was 0.36 ohms and the switches reached 6 kA and 7 kA during testing. The low current was due to breakage of several wires when the switch was cast into a block of epoxy resin. No further superconducting switch work is planned. The need for these switches has been eliminated by the advance in HVDC interrupter and cryogenic disconnect developments and in circuit changes for the METS system.

F. COIL DEVELOPMENT PROGRAM

1. *Industrial 300-kJ Coils.* Three, 300-kJ superconducting energy storage coils are being built on contract with Intermagnetics General Corporation (IGC), Magnetic Corporation of America (MCA), and Westinghouse Electric Corporation. The IGC and Westinghouse coils have been delayed principally because of the inability of the original supplier to make an adequate amount of good copper-nickel, copper matrix superconductor on a timely basis; and the MCA coil was delayed because of difficulties encountered in braiding the conductor.

TABLE XII-III

TESTS ON COMPOSITE SWITCHES

Switch	SW-25	SW-26
Type	sleeve	accordion
Maximum Current, kA		
Switch alone	10.8	11.5
Switch and coil	9.0	10.2
Energy Switched, kJ	200	257
Maximum Voltage, kV	9	10

Tests were run on an IGC, epoxy, fiber-glass, bronze mockup coil to determine radial and axial moduli of elasticity, the extent of possible insulation damage the wires may have sustained during winding and compaction, and energy losses from different levels of pulsed energy. The MCA coil is very nearly complete and is to be delivered in January 1976. It will be followed in May by the Westinghouse coil and in June by the IGC coil.

G. SFTR PROTOTYPE METS SYSTEM

A prototype METS system is being designed to simulate one of the ten-coil, METS-SFTR modules. A proposal for the prototype was drafted, LA-5918-P, and a program evaluation was held in June 1975, with a DCTR review panel.

The prototype system will be built with three 400-kJ, 25-kA, 2.5-T superconducting energy storage coils stacked as a solenoid in an epoxy, fiber-glass ℓHe Dewar. To design the prototype system, individual coil designs have been made; the 25-kA superconducting cable has been designed; the pulsed 25-kA, 60-kV coaxial leads to the coils have been designed; and two alternative cryogenic disconnect designs to connect the coils in series during the charging cycle are being evaluated. A considerable effort has been undertaken to bring the ten-coil Dewar, pulsed leads, continuous leads, cryogenic disconnects, and actuator systems to a sufficiently advanced state of development that the stresses, displacements, deformations, forces, and dynamic response characteristics are well enough known to guide the prototype system design. The ten-coil analysis is complete and detailed drafting on the prototype remains to be done.

1. Storage Coil Design. A detailed engineering design of the prototype coil has been carried out. As in previous iterations of the design, the peak current is limited to 25 kA and the peak voltage to 60 kV. The maximum field at the winding is 2.5 T and the total energy stored in the three coupled coils is 1.2 MJ. The length of each coil is 60 cm and the radius is 31.2 cm. The winding is to be made of a single layer, edge wound cable of cross section 1.10 cm by 2.44 cm.

2. Energy Loss in the Storage Coil. Energy loss due to hysteresis and eddy currents in each

energy storage coil during fast discharge of the coil (0.7 msec) has been calculated to be 400 to 800 J. The exact number will depend on the matrix resistivity and superconducting wire diameter.

Energy loss in the Dewar radiation shield due to eddy currents has also been calculated and found to be negligible.

3. External Breaker. One method of reducing the requirements which the cryogenic disconnect must meet is to place an additional circuit breaker in the circuit outside each storage Dewar. Opening this breaker would cause current to transfer out of each cryogenic disconnect completing the circuit through the pulsed leads to the externally located HVDC vacuum interrupter. With little or no current in the cryogenic disconnect, arcing and shock waves would be eliminated when the disconnect is opened.

4. Cryogenic Disconnect. Effort was expended throughout the year toward development of a special, high-current electrical switch for service in liquid helium. This switch or cryogenic disconnect is to be mechanically actuated, will carry 25 kA, stand off 60 kV when open, and dissipate less than 24 W under full current load. In addition, the disconnect must be able to open in 30 ms. Progress toward development of the disconnect has been good.

A toggle-operated disconnect requiring high butt contact pressures has been built ready for testing. Cyclic tests for wear on the component parts and contact materials have been conducted. Resistivity measurements were made on the contact materials and values as low as 9 nohm/cm^2 at 4 K in ℓHe were obtained for silver on silver sheets. Force and acceleration calculations were made for the toggle disconnect for 30-ms opening times. Forces of the order of 67 500 N will be required to actuate the disconnect.

Priority effort has more recently been assigned to what can lead to a greatly simplified cryogenic disconnect design. A series of tests were performed to determine the electrical resistivity of a set of contacts utilizing a commercial product called "Multilam Strips". These strips are louvered stampings, fabricated from silver plated beryllium copper. Resistances as low as 1.6 μohms/cm^2 in ℓHe were observed. The Multilam contacts have high reproducibility of contact resistance, good cycle life, and require very low pressures.

5. *Cable and Lead Design.* The METS prototype
will require cabling between the superconducting
coils and vacuum interrupters capable of carrying a
current pulse of 25 kA at 60 kV for 0.1 second under
fault conditions. The cable must have low inductance
and a low-temperature rise per pulse. A Type 218/220
cable was designed to meet these requirements with
a seven-cable bundle per pulse lead from the coil
Dewar. Bids are on hand and orders for cables for
evaluation will be placed with at least two
manufacturers.

The design of a header to connect the super-
conducting coil pulsed lead to the seven-cable bundle
of Type 218/220 cables running to the vacuum inter-
rupter was completed. The coaxial header takes min-
imal Dewar lid space by routing the cables straight
up. The design allows each cable to be replaced
individually and provides for gaseous nitrogen purge
to prevent frost buildup. A schematic of the header
is shown in Fig. XII-3. The header inductance is
about 120 nH.

The temperature profiles of the inner and outer
conductors of the pulse lead have been calculated.
The computer program accounts for thermal conductiv-
ity, electrical resistivity, viscosity, and the heat
transfer coefficient as functions of temperature.
The pulse leads are cooled by the vapor boiled off
from the liquid helium surface due to the heat leak-
age of the lead itself. This is the self-cooled
case. The pulse lead was designed to operate suc-
cessfully for one transfer at 25 kA for 0.1 s with
no part of the lead exceeding about 400 K if vapor
cooling is restricted or stopped. The calculations
clearly indicate the need for a pulsed lead with
both inner and outer conductors graded or stepped
to have a larger cross-sectional area on the upper
ends. The computer program has been expanded to
handle design calculations for 25-kA continuous
duty leads.

6. *Plastic Dewar.* A vacuum-jacketed, fiber-
glass-reinforced epoxy Dewar large enough for test-
ing a single 400-kJ prototype superconducting coil
was designed, fabricated, and built during 1975.
Initial tests indicated a ℓN_2 heat loss of 21.3 W
and ℓHe heat loss of 10 W. Even though the heat
leak was acceptable, problems existed in the vacuum
jacket and the Dewar lid. The laminated Dewar lid
interlayer leaks were sealed by a vacuum impregnation
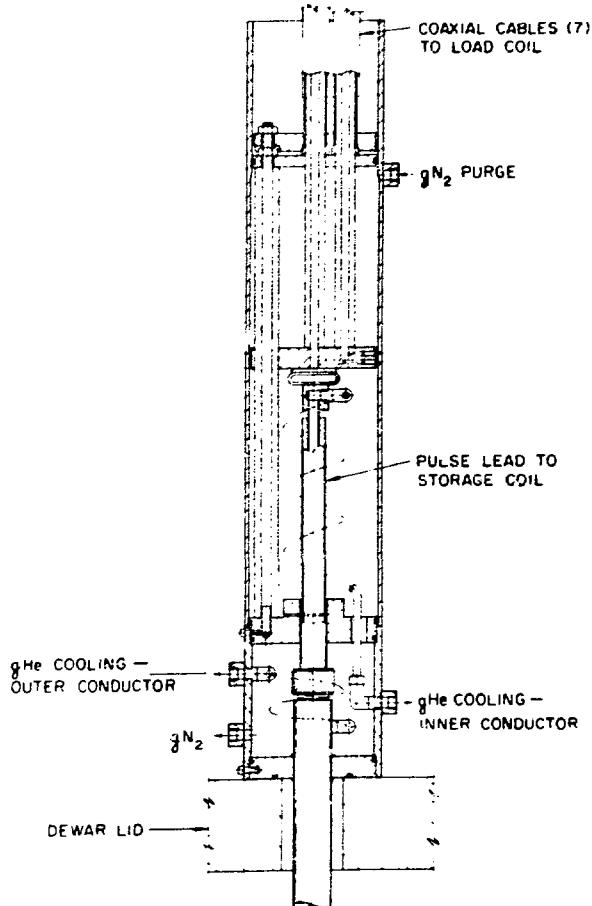
Fig. XII-3.
Pulsed Lead - Cable Connector.

operation. The vacuum jacket problem was solved by
coating the porous wall with epoxy. The seal at the
bell jar gasket was improved by installing a 50-
durometer bell jar gasket.

7. *Refrigeration System.* An engineering study,
a cost estimate, and engineering design study for
the installation of the 700-W, 4.5-K helium refrig-
eration system were initiated during the year. The
first two items were completed, and the installa-
tion drawings are nearly complete. An operating
procedure for the refrigerator was drafted and ac-
cepted by the contractor. Additional documentation
covering the check-out and start-up of the completed
system was also written. Construction of the 6.1-m-
deep pit to contain the refrigerator cold box and
experimental coil Dewar was completed. This

143

construction also included completion of the concrete floor as well as excavation and asphalt surfacing of the ℓN_2 and gHe trailer stations.

H.   SFTR CONCEPTUAL DESIGN STUDY

1. *Design Parameters.* The conceptual design of the METS-SFTR system was completed. The final design provides for 1280 superconducting energy storage coils, each with 381 kJ of stored energy to be transferred out to ambient temperature, copper, plasma-compression load-coils in 0.7 ms. The storage coils will operate at full current of 26 kA at 2.5 T with a peak circuit voltage of 60 kV at the half transfer period time. The energy transfer is initiated by first opening cryogenic disconnects connecting the coils in series in plastic Dewars, each containing ten coils, followed by the opening of HVDC vacuum interrupters external to the Dewars. The transfer is completed by shorting or crowbarring the energy in the load coils to create a 5.5-T compression field on the plasma by firing ignitrons followed in sequence with the closure of metal-to-metal switches. The e-folding decay time of the crowbarred compression coils is 250 ms. A complete cost analysis was made for the METS portion of the system.

2. *Circuit Fault Analysis.* A preliminary fault analysis of the METS circuit used for the SFTR has been carried out. This analysis was done by assuming that any component of the circuit could fail either by being short circuited or open circuited and then modeling the defective circuit with the NET-2 computer code. Some faults, such as short circuiting of a storage coil through a pulsed lead, cannot be protected against except by very conservative insulation design.

Other faults caused high voltage at points of the circuit which normally do not develop high voltage. These voltages can be minimized by connecting together appropriate nodes of the circuit with passive resistors.

Short circuits can cause unusually high-energy dissipation in circuit elements other than the one which is short circuited and in this way cause damage. Damage of this type can be eliminated in one case with a single triggered fuse in the vacuum breaker leg of the circuit.

I.   DIELECTRIC STRENGTH AND VOLTAGE TRACKING STUDIES

The program to study the dielectric strength of helium and nitrogen in both the liquid and gaseous state and to study voltage tracking along insulation surfaces in helium and nitrogen was completed.

A 60-kV pulse with a 500-μs rise time simulating the SFTR waveform was used for the tests. From the study it was concluded that gaseous helium is a poor dielectric relative to nitrogen, that plane-plane electrodes should be avoided in liquid cryogen applications because of the possible entrapment of bubbles, that the SFTR pulsed voltage application is more nearly equivalent to published ac or dc data than impulse voltage data, and that both the dielectric and tracking strength data vary widely, being dependent upon such parameters as the fluid environment, temperature, and pressure.

J.   EPRI HOMOPOLAR STUDY CONTRACT

LASL is acting as the technical coordinator of the University of Texas at Austin and Westinghouse to conduct an in-depth design of an energy storage homopolar machine capable of a 30-ms discharge time with low losses. Other contractual work includes a search for possible applications of homopolars other than the RTPR and a study of the ultimate limits of homopolars. In 1975 and 1976 the homopolar systems were optimized for theta-pinch applications. A 1-GJ, 30-ms discharge homopolar generator and a 10.7-MJ prototype were designed. These units will use superconducting field coils. The prototype will be used to examine peripheral rotor speeds up to 277 m/s, brush wear, brush collection systems with current densities up to 1.6 kA/cm^2, hydrogen atmosphere cooling, energy transfer and efficiency, bearing loading, and other machine characteristics.

Joint monthly meetings have been held by the three organizations and detailed minutes of the technical discussions held at these meetings were prepared by LASL. Progress reports on the work are submitted to EPRI.

K.   MISCELLANEOUS

1. *METS Application as a Laser Power Source.* A short study was conducted to establish the concept

of applying superconducting energy storage and a METS type circuit to the problem of coupling energy into flash lamps. The study shows that a factor of ten or more improvement in energy efficiency could be realized with the proper circuit design.

2. *Explosive Generator.* A design and computational parametric study was performed for a conceptual pulsed power generator with the idea of the generator being the primary source of the SFTR compression coil energy. The original idea came from M. Cowan of Sandia Laboratories.

Inertial energy of a moving conductor is converted to electrical energy in a load circuit by magnetic flux compression within a generator. The moving conductor (armature) is a metallic piston which enters a magnetic field region axially, excluding flux from its volume by eddy current shielding. Computationally the piston is modeled by a metallic liner exploding radially. Surrounding the field region is a solenoid which is coupled to the external load, and outside of the solenoid is a thick (long time constant) constant-flux shield. The initial magnetic field is supplied by a superconducting solenoid outside the flux shield. A sample calculation shows 80° transfer of 650 MJ into an SFTR like inductive load in 300 μs at 30 kV output voltage using a bias field of 26.5 kG from the superconducting coil.

3. *New "Mixed METS" Circuit Analyses.* Ten circuits were analyzed in detail. These use the storage capability of the transfer capacitors in addition to the superconducting energy storage. Power crowbarring was also analyzed.

Of the circuits considered, one in particular showed very impressive circuit simplification and cost reduction. In this circuit the total number of modules required by METS-SFTR could be reduced from 1280 to 320. The total superconducting plus capacitive storage size would be reduced from 725 MJ to 430 MJ, and the system cost would be cut by 50% to $32.6M for the components considered. The power crowbar energy source would be 20 modules of 50-MJ inertial capacitors (homopolars).

Since the SFTR Phase I conventional system has capacitor storage for one-half the total final system energy, the possibility of adding only sufficient METS storage coils to supply the other half of the energy and to use the capacitors both actively for storage and passively to transfer the inductively stored energy merits consideration.

REFERENCES

1. S. G. Fedotov, "Dependence of the Elastic Properties of Titanium Alloys on Their Composition and Structure," in *Titanium and Its Alloys*, Pub. No. 10, I. I. Kornilov, ed., Eng. Trans. U. S. Dept. of Comm., Springfield, VA, (1966) p. 199.

2. E. H. Hart, "Theory of the Tensile Test," Acta Met., 15, (1967) 351.

L. A. Booth, G. E. Bosler, J. M. Bunch, F. W. Clinard, Jr., D. J. Dudziak,
T. Frank, S. A. W. Gerstl, W. V. Green, G. M. Hale, J. G. Hoffman, G. F. Hurley,
R. A. Krakowski, D. W. Muir, T. A. Oliphant, D. M. Parkin, M. L. Simmons, W. F. Sommer

A. INTRODUCTION

The Fusion Technology task performs analyses and systems studies of conceptual fusion reactors based upon inertial and high-β magnetic confinement schemes. Progress in the areas of theoretical analysis (plasma and neutral-gas blanket models), specific reactor studies (toroidal and linear theta pinches, Z pinches, laser fusion) neutronic and nuclear data assessments, materials (metals and insulators) evaluation, and general engineering design is reported herein.

B. THEORETICAL ANALYSIS

The majority activity in the theoretical analysis task has centered on a more detailed analysis of the transient behavior of the neutral-gas blanket envisaged for the Reference Theta-Pinch Reactor[1] (RTPR). The use of neutral-gas layers for confinement or heat removal in prototype thermonuclear reactors has been considered by several authors.[2-4] The model applied to the RTPR[5] uses a short mean-free-path limit for thermal conduction and a quasi-steady assumption for the plasma and neutral-gas profiles. It has been shown[6,7] that correcting the former approximation makes quantitative but not qualitative difference. The latter approximation is, however, much more serious and has recently been brought into question.[3] The argument is made that if the charge-exchange transients which occur while a steady state is being set up are "properly" taken into account, the blanket may never establish without excessive first-wall damage caused by a transient burst of fast charge-exchange neutrals. To answer this question a transient theory of the neutral-gas layer development must be developed which takes proper account of charge exchange and the finite thickness of the plasma sheath. A preliminary indication that the quasi-steady layer could be formed has been given[7], but the amount of energy deposited at the wall by the charge-exchange neutrals was not reported. The more recent analysis[9] discusses an improved mathematical model and gives estimates of energy deposition at the first wall.

Since the main point being considered is the transient formation of the layer, the more long-term effects, such as charge-exchange with the alpha particles and over-all energy transfer, have not been considered.

The post-quench conditions used in the analysis[1] are $n = 10^{14}$ cm^{-3} and $T = 7$ keV, and the initial density and magnetic field profiles are as shown in Fig. XIII-1. The transient calculation was carried out for 16 μs, using time intervals of .05 μs. As the cold neutral gas reacts with the edge of the plasma, energy is removed specifically from the edge of the plasma, and a temperature profile is established. At later times the incoming neutrals react with the cooler edge of a plasma, and less energy is removed from the plasma per interaction. Because of this edge-cooling effect less energetic charge-exchange neutrals impinge on the wall, thereby causing less damage as time increases. Furthermore, since less and less energy for interaction is removed from the plasma, the shape of the plasma ion temperature profile changes more slowly with time, and a steady-state profile is established.
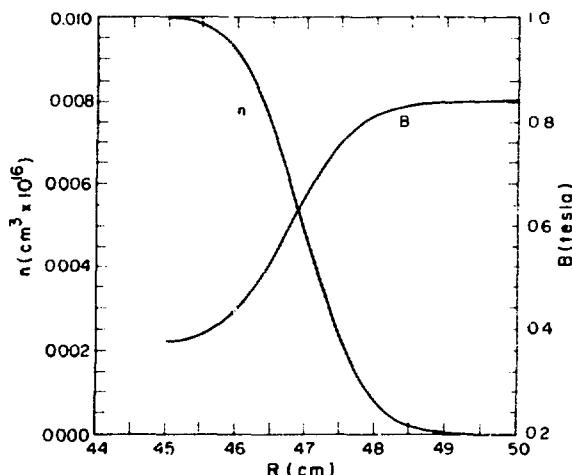
Fig. XIII-1.

Initial plasma density, n, and magnetic field, B, profiles for the plasma-sheath region immediately after quench. The first-wall radius is 50 cm.

The temperature and density profiles at 11 μs are shown in Fig. XIII-2; for the ensuing 50 μs no discernable change in the ion temperature and density profiles is found, except for a gradual increase in the height of the "foot" that developes at outer edge of the plasma.

The amount of energy deposited in the wall by charge-exchange neutrals normalized to the total latent heat of a 10-μm-thick Nb first wall is shown in Fig. XIII-3. The initial energy pulse reaches the first-wall within ~ 11 μs, after which energy from fast neutrals at the wall is negligible. Because of the smallness of the final value of this fraction it can be concluded first-wall melting is not a problem. Furthermore, the calculation demonstrates the establishment of a quasi-static profile after which essentially no further wall damage occurs as a result of fast charge-exchange neutrals. This transient model is being refined to incorporate both first-wall heat-transfer and sputtering models.

All aspects of the Theoretical Analyses Task, including the aforementioned neutral-gas layer model, must ultimately be incorporated into a general systems code that is used to study the potential operating regime of a fusion reactor based upon a prescribed high-beta confinement scheme. The generic name given to this code is the LASL Systems

RATIO OF TOTAL ENERGY DEPOSITED TO LATENT HEAT OF WALL

Fig. XIII-3.

Time dependence of energy deposited at the first-wall by charge-exchanged neutrals expressed as fraction of latent heat of a first-wall layer of 10 μm thickness.

Analysis Code (LASLSAC), and a block diagram of this code for the RTPR is shown in Fig. XIII-4. The status of LASLSAC is summarized below:

- IMPL (implosion heating model) - resonant heating model being developed and almost ready to incorporate into LASLSAC.
- STG (staging model) - not developed.
- COMP (adiabatic compression) - operational within LASLSAC for HETS power supply and time-dependent joule heating calculation.
- EQ/STAB (equilibrium/stability monitor) - operational within LASLSAC for $m \geq 1$ stability.
- FEEDBK (feedback power) - operational within LASLSAC for $\ell = 0$ or $\ell = 2$ (optional) time-dependent fast feedback of $m = 1$ modes.
- ENBAL (total energy balance) - operational within LASLSAC.
- GASBLK (neutral-gas blanket) - being developed.

Fig. XIII-2.

Plasma density, r, and temperature, T, profiles for the plasma-sheath region 11 μs after introduction of a neutral gas into the annulus between the plasma and the first wall (radius is 50 cm).
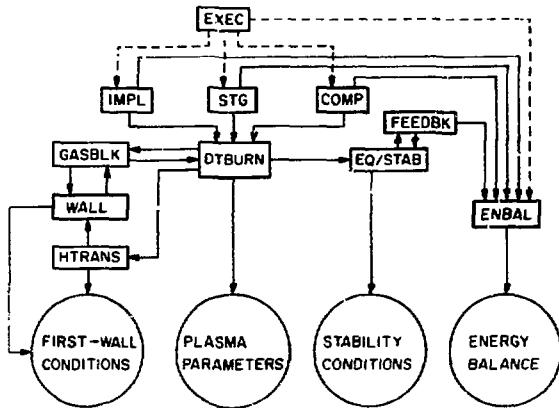
Fig. XIII-4.

Operations diagram of the LASL systems analysis code
(LASLSAC). Identity and function of each subroutine
is given in the text.

- WALL (first-wall evaporation and sputtering)
  not developed.
- HTTRANS (first-wall heat transfer) - opera-
  tional in LASLSAC.

Although the primary purpose of LASLSAC is the
performance of systems evaluation on the basis of
engineering Q-values and systems efficiency, a cost-
ing subroutine will ultimately be added.

C.   REACTOR DESIGN STUDIES

The reactor design studies have focused onto
three major areas: technology assessment and opera-
ting-point re-design of the RTPR, preliminary design
of a Linear Theta-Pinch Hybrid Reactor (LTPHR), and
exploratory reactor calculations of a Reverse-Field
Z-Pinch Reactor (RFZPR). Design activity in each
of these areas is continuing, and progress is sum-
marized below.

1.   Reference Theta-Pinch Reactor (RTPR).

a.   *Thermal-Mechanical Analysis of RTPR*

First-Wall. The blanket envisioned
for the Reference Theta-Pinch Reactor (RTPR)[1] is
inserted into an implosion heating coil which in
turn is surrounded by an adiabatic compression coil
(Fig. XIII-5). The blanket is structurally indepen-
dent of the nested magnet system, but must pass mag-
netic flux in a short time (~ 1.0 μs) and hold off
the induced azimuthal voltages (1-2 kV/cm). For
this reason the RTPR blanket is comprised of ~ 100,
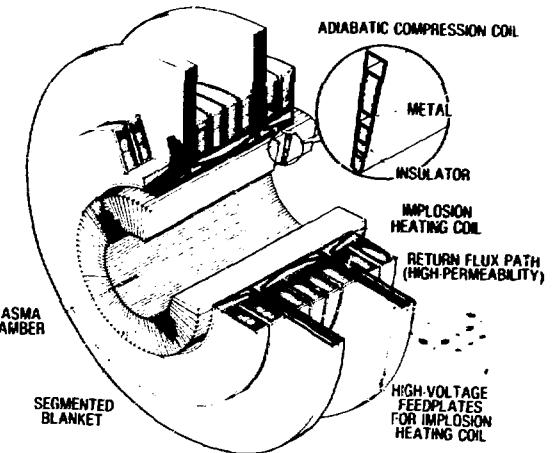
Fig. XIII-5.

Isometric view of RTPR blanket, implosion heating
coils, and adiabatic compression coils. Blanket is
structurally and electrically independent of the
magnet coils.

electrically insulated trapezoidal segments. The
electrical insulation must continue around a portion
of the leading edge (i.e., first wall) of each
blanket segment.

A number of first-wall configurations have been
proposed to alleviate the thermal shock[10] induced by
the (~ 0.1 s) plasma burn: (1) insulator/metal lam-
inates, (2) all-ceramic bodies, and (3) bumper-pro-
tected walls; Figure XIII-6 illustrates these first-
wall configurations. Although a large number of
insulator and insulator/metal materials are under
evaluation, the thermal/mechanical calculations
presented herein have used Al_2O_3, Al_2O_3/Nb-1Zr, and
Si_3N_4 as reference materials. Representative one-
dimensional and two-dimensional finite-element mod-
els of each first-wall concept have been used for
both dynamic heat-transfer[11] and stress[12] calcu-
lations. Figure XIII-7 illustrates the first-wall
stress response computed for the reference case,
the thin insulator case, and the bumper-protected
first wall. The two-dimensional finite-element
structural analysis of the blanket leading edge
considered four boundary conditions to study the
effects of inward curvature (Figs. XIII-5, 6) and
the means of attachment (rigid vs azimuthal flexure
vs radial fixture vs tapered insulator, Fig. XIII-8)
on the stress distribution. These two-dimensional
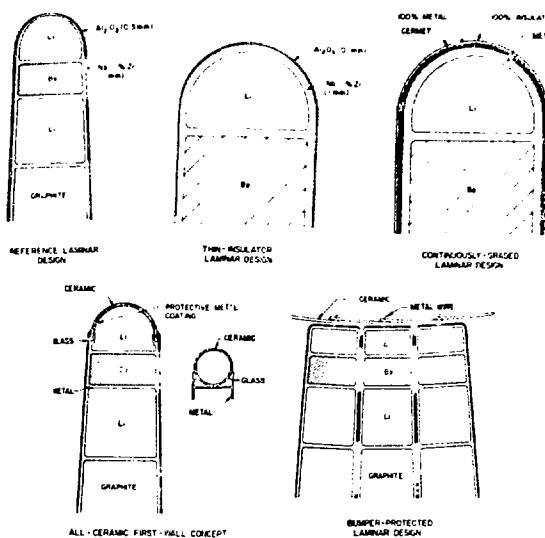
Fig. XIII-6.

Schematic diagrams of five first-wall concepts being studied for the RTPR. (Refer to Fig. XIII-5.)

Fig. XIII-8.

Graphical summary of boundary conditions used in the two-dimensional finite-element structural analyses of the RTPR first wall.

effects had little intrinsic effect on the computed stresses, as seen from the summary given in Table XIII-I, although the increased surface area associated with the rounded first-wall edge of the blanket segments reduces stresses by ~ 40%. The computed stresses are influenced strongly by the temperature dependences of physical properties and (for laminates) the relative thickness of each phase. For instance, either thinning the insulator or thickening the support metal for laminates results in appreciable decreases in tensile stresses generated within the ceramic phase; decreasing the insulator

Fig. XIII-7.

First-wall thermal-stress transient for, a) 0.3 mm Al_2O_3 (Ref. case[1]) laminate, b) 0.1 mm laminate, and c) bumper-protected first-wall.

thickness from 0.3 to 0.1 mm reduces the maximum tensile stress in the Al_2O_3 from 150 MPa to zero. These results are summarized in Table XIII-II and Fig. XIII-9.

Using published fracture mechanical data[13] and theories,[14] the static fatigue life of the Si_3N_4 all-ceramic first-wall was calculated. A flaw of length a_o is placed at a given location within the first-wall, and, using the calculated thermal and stress transient at that location, the flaw extension is numerically computed.[13,15] This procedure was repeated for a number of 10-s RTPR power cycles[1] until either the crack extended through the all-ceramic first wall (5-mm) or the stress intensity factor[14] exceeded a critical value (K_{IC} ~ 5 MPa m$^{1/2}$ for Si_3N_4).[13] The number of such cycles required to "fail" the first wall, i.e., the static fatigue life, for the thermal/stress transient given in Fig. XIII-10 is shown in Fig. XIII-11 as a function of stress-free reference temperature, flaw size, and flaw location. Initial flaw sizes in excess of ~ 200 μm (4% of the wall thickness) located at the

149

TABLE XIII-I

SUMMARY OF FINITE-ELEMENT STRUCTURAL ANALYSES FOR VARIOUS BOUNDARY CONDITIONS
REFER TO FIG. XIII-8 FOR THE BOUNDARY CONDITIONS USED.

End Condition	Al_2O_3/vacuum	Al_2O_3/Nb Bond in Al_2O_3	in Nb	Nb/Lithium
Case A (cylindrical)	-460	150	64	92
Case B (pinned)	-510	250	82	120
Case C (pinned)	-500	250	82	110
Case D (built-in)	-500	160	65	110
Case C (pinned with $T(\theta) = T(90°) \sin(\theta)$	-340	190	69	51

TABLE XIII-II

SUMMARY OF INFLUENCE OF MECHANICAL PROPERTIES ON FIRST-WALL STRESSES

	Nb-1Zr Modulus (MPA)	Al_2O_3/vacuum	Al_2O_3/Nb Interface in Al_2O_3	in Nb	Nb/Lithium
Time into burn is 105 ms, Case A end condition (Table XIII-I)	82700	-410	88	59	89
	50600	-350	150	46	66
	18600	-260	240	23	30
Time into burn is 60 ms, Case D end condition (Table XIII-I)	82700	-500	160	65	110
	18600	-330	320	26	39

outer first-wall radius (maximum tensile stress) are required to reduce the service life at 1000 K to less than one year ($\sim 2.5 \times 10^6$ pulses); flaws of this size should easily be detected by proof-testing measures.[16] Similar calculations were made for the Al_2O_3/Nb-1Zr laminates, using the Si_3N_4 crack-growth data but not specifying the critical stress intensity factor, K_{IC}. Figure XIII-12 gives the computed static fatigue life of the Al_2O_3/Nb-1Zr reference first wall in terms of K_C.

Interposing a sacrificial, radiatively-cooled bumper between the plasma and first wall reduces the thermal stress in the first wall by more than a factor of 10. The onus now is placed upon the bumper, which in principle can be made structurally non-supportive and must operate at relatively high temperatures. A thin (~ 1-mm) ceramic cloth or "macro-weave" that is loosely draped over the first wall is being considered for this purpose.

Reconfiguration of the RTPR represents one method to alleviate the pulsed thermal/mechanical problem. Two other approaches to this problem involve materials selection/re-engineering and changes in the RTPR operation (less implosion voltage, longer thermonuclear burn periods). The overall LASL approach (i.e., configuration, materials, and operation) to the RTPR first-wall design is summarized graphically in Fig. XIII-13.

b. *Fast Feedback Stabilization of m = 1 Modes.* As indicated by Fig. XIII-13, changing the RTPR operating point presents a means of alleviating the RTPR first-wall problem. Reducing the implosion heating voltage results in a lower initial plasma temperature and greater plasma compression for the same thermonuclear yield. The subsequent loss of wall stabilization of m = 1 MHD modes, therefore, necessitates the need for fast feedback stabilization. The feedback power requirement, therefore, has been assessed.
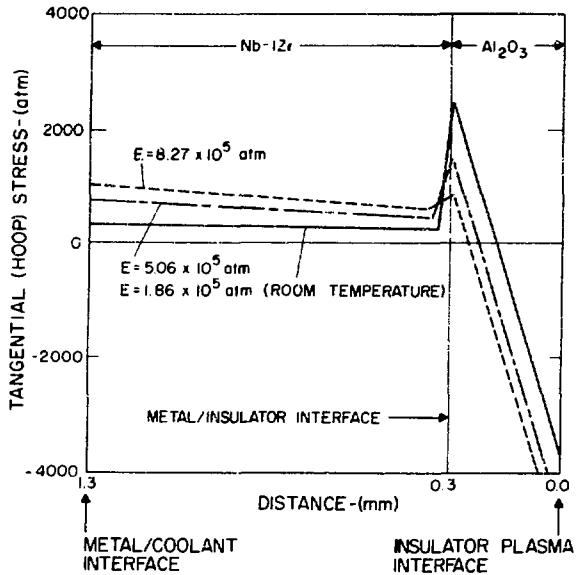
Fig. XIII-9.

Influence of metal substrate thickness on the stress profile generated in the RTPR reference first wall 60 ms into the burn (time of maximum stress).

Because of the large number of parameters and constraints associated with the optimization of RTPR feedback, this problem has been attacked on two levels. First, a feedback model was developed for average RTPR burn conditions. The stability and equilibrium parameters that result from this simple analysis are used by the thermonuclear burn code DTBURN to determine the time-dependent feedback power and total energy requirement.

Figure XIII-14 gives the dependence of the peak reactive feedback power $\hat{P}_{FB}(\ell=2)$, $b_1 = B(\ell=1)/B_0$, and helical wavelength λ for the RTPR reference
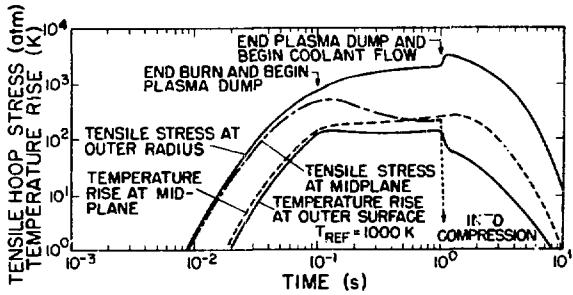
Fig. XIII-10.

Thermal and (hoop) stress transient in Si_3N_4 all-ceramic first wall used in fracture mechanical analysis of static fatigue life (Refer to Fig. XIII-11).
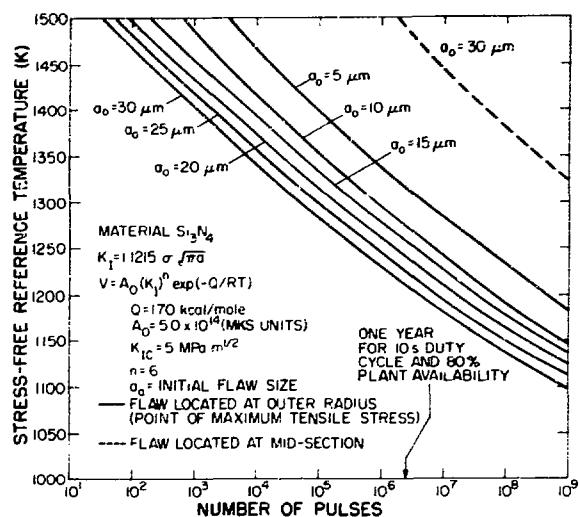
Fig. XIII-11.

Static fatigue life of a 5-mm-thick Si_3N_4 all-ceramic first wall as a function of stress-free reference temperature and initial flaw size.
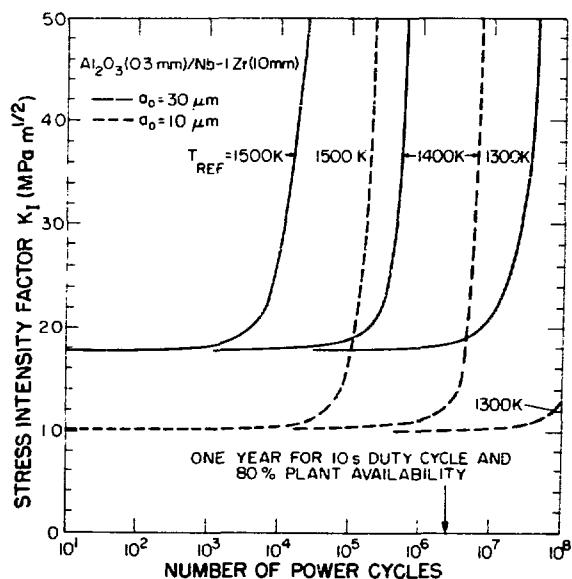
Fig. XIII-12.

Static fatigue life of reference Al_2O_3 (0.1 mm)/Nb-1Zr (1.0 mm) first wall as a function of initial flaw size and stress-free reference temperature. The crack growth data for Si_3N_4 was used (not available for Al_2O_3 in this temperature range), and K_{IC} for Al_2O_3 is expected to be 2-4 MPa $m^{1/2}$.

GENERAL CONSIDERATIONS
AND CONSTRAINTS

* Thermal-mechanical shock ——————➤ CTE, k/C$_p$, fracture toughness, bond integrity
* Chemical Stability ——————➤ REDOX, dissociation, vaporization
* Radiation Stability ——————➤ swelling, impurities, sputtering
* Electrical Stability ——————➤ electrical resistivity, dielectric strength
* Fabrication/repairability ——————➤ proof testing, maintenance, cost

SOLUTIONS

———————➤ * configuration
┌ * materials selection/re-engineering
* RTPR operation ——————

* Laminates
  -plasma arc spray ┐ · simple coating, reduced
  -enameling   │   thickness, tapered
  -CVD   │   insulator
  -sputter deposition ┘ · graded and/or
                         composite coating

* glass-impregnated (crystalline)
  ceramics

* graded cermets

* phase-graded ceramics

* decoupling (viscous) interlayer

* fibrous composites

* All-ceramic structure

  -hot pressing

  -reaction sintering of extruded,
   isostatically-pressed or
   slip-cast bodies

* Thin bumpers with either
  all-ceramic or laminate
  first-wall configurations

  -ceramic weaves or blankets

  -ceramic "macroweaves"

  -metal chevrons or "fenders"

* Increased number of RTPR
  blanket segments

* Reduce implosion heating voltage
  and use fast feedback
  stabilization

* Reduce instantaneous first-wall
  loading (Bremsstrahlung, plasma
  heat dump)

Fig. XIII-13.

LASL approach to the RTPR first-wall design.

case.[1] The peak neutron power, $\hat{P}_N$(20 MeV/n), has been used to normalize $\hat{P}_{FB}(\ell = 2)$, $\ell = 2$ feedback has been used, and the values of δ_1 are shown. For realistic values of δ_1 (2-3) and λ, the peak reactive feedback power can be kept a small fraction of $\hat{P}_N$. Since $\hat{P}_{FB}(\ell = 2)$ can be recovered with ~ 95% efficiency by a resonant LC feedback circuit,[17] the use of $\ell = 2$ feedback should present no serious drain on the re-circulating power loop for RTPR. Using the stability/equilibrium parameters given by point (a) on Fig. XIII-14 ($b_1 = 0.1$, hb = $2\pi b/\lambda = 0.1$), the time-dependence of $\hat{P}_{FB}(\ell = 2)$ was computed for three cases and is shown on Fig. XIII-15. These cases correspond to the optimum values of Q_E when the filling density P_A(mTorr) is varied. The dependence of Q_E on E_θ(kV/cm) and P_A is shown on Fig. XIII-16, as are the three feedback cases previously discussed. Although a high level of design effort is required before the technological viability of fast feedback for RTPR can be accurately assessed, these preliminary energy balance computations show great promise

for feedback stabilization of m = 1 modes in RTPR and, hence, the reduction of E_θ(kV/cm), the use of thinner blanket dielectric, and ultimately a reduction in the thermal stress developed in the RTPR first wall.

    c. Neutronic Design of RTPR Blankets. Neutronic system studies of RTPR have focused primarily on sensitivity and blanket thinning studies. Specifically, the effects of thinner graphite moderators, use of Mo and V in place of Nb, replacement of Be by BeO, varying the thicknesses of Be or BeO, and changing the ^{6}Li enrichment were studied. The influence of these changes on tritium breeding, radiation heating of coils, first-wall radiation damage (dpa) and coil (Cu) transmutation rate was resolved. Table XIII-III summarizes the effects of decreased graphite thickness. Surprisingly, the ~ 13-cm decrease in blanket thickness (27.7% reduction in coil area and stored energy requirement) which results from trimming the graphite did not reduce the tritium breeding below the reference

TABLE XIII-III

NEUTRONICS EFFECTS OF THINNING

THE GRAPHITE MODERATOR IN RTPR

Graphite Thickness (cm)	Tritium Breeding Ratio	Recoverable Energy (MeV/D-T Neutron)	Waste* Heat (MeV/D-T Neutron)	Copper Transmutations (ppm/y)
14.74 (ref)	1.062	19.42	0.94	418
11.05	1.060	19.00	1.39	484
7.37	1.069	18.45	2.00	707
3.68	1.063	17.68	2.85	1001
1.23	1.069	16.98	3.62	1257

*Waste heat could be recovered by redesign, i.e., use of high temperature, high-Z shield between blanket and coil.

value of 1.06 (actually 1.11 if resonance self-shielding is taken into account). The increased waste heat deposited into the magnet structure (Table XIII-III) is a clear drawback, although interposing a thin, high-Z, high-temperature shield between the thinned blanket and compression coil should increase the recoverable heat. Use o; a thinner blanket, even if the recoverable thermal energy is decreased, will result in increased values of the engineering Q-value, Q_E, because of the reduced magnetic energy storage and attendant transfer/joule losses. More detailed analysis of this aspect of the RTPR blanket design is being pursued. Sec. XIV.D.2 gives a more detailed discussion of these neutronic studies, *per se*.
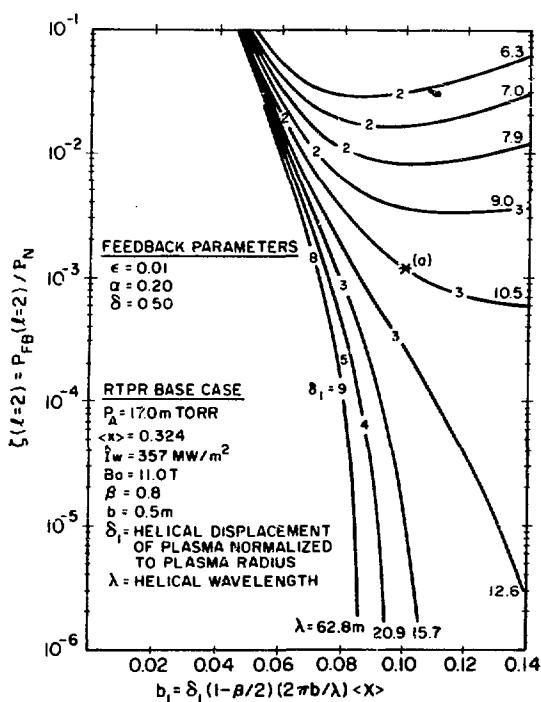
Fig. XIII-14.

Dependence of $\ell = 2$ feedback power $\hat{P}_{FB}(\ell = 2)$ relative to instantaneous neutron power $\hat{P}_N(20\ MeV/n)$ on δ_1 and λ for nominal[1] RTPR operating conditions ($b_1 = 0.1$, $2\pi b/\lambda = 0.1$) used for dynamic DTBURN calculation (Fig. XIII-15). Note the $\hat{P}_{FB}(\ell = 2)$ is the reactive feedback power, ~ 95% of which can be reversibly recovered.
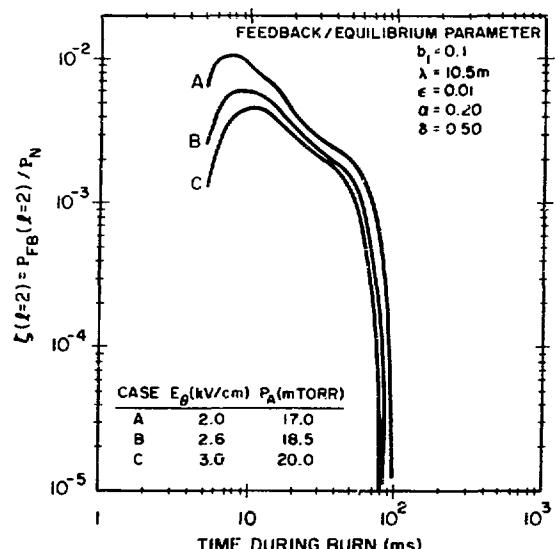
Fig. XIII-15.

Time dependence of $\ell = 2$ feedback power $\hat{P}_{FB}(\ell = 2$ relative to instantaneous neutron power $\hat{P}_N(20\ MeV/n)$ as determined by DTBURN for nominal[1] RTPR conditions. Note the $\hat{P}_{FB}(\ell = 2)$ is the reactive feedback power, ~ 95% of which can be reversibly recovered.
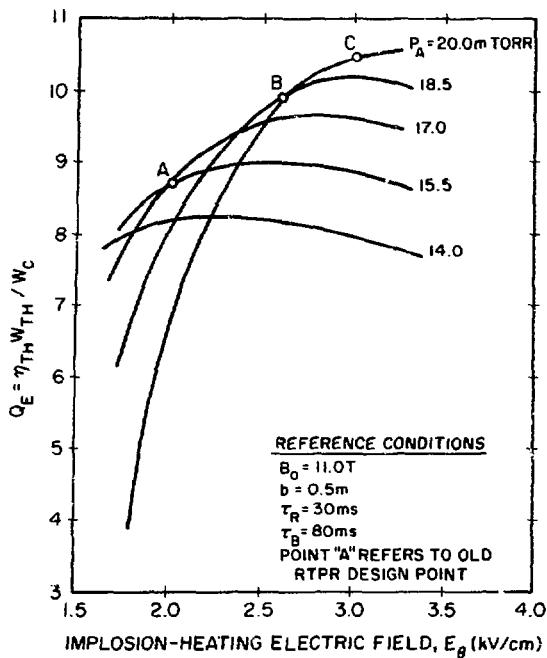
Fig. XIII-16.

Dependence of engineering Q-value, Q_E, on implosion field E_θ (kV/cm) and filling pressure P_A (20 MeV/n) as determined by DTBURN. The total recoverable thermal energy is W_{TH}, the circulating energy is W_C and the thermal conversion efficiency is η_{TH}. Refer to Fig. XIII-15 for cases A, B, and C.

2. *Linear Theta-Pinch Hybrid Reactor (LTPHR) Studies.* System studies of the LTPHR have dealt primarily with the power supply (HETS), neutronic aspects of the blanket, and generalized energy balance. The overall layout envisaged for the LTPHR is shown schematically in Fig. XIII-17. A capacitor driven implosion heating coil (IHC), a HETS driven adiabatic compression coil (ACC), and a "clam-shell" hemi-cylindrical blanket of the HTGR type are being considered. A generalized circuit diagram and operating scenario for the LTPHR is illustrated in Fig. XIII-18; the HETS is shown as a capacitor (C), and generally the flat-top time τ_{FT} is set to zero. All calculations assume free-streaming particle end loss. A brief summary of activity in the areas of blanket neutronics, power-supply design (HETS) and energy balance is given below.

a. *LTPHR Neutronic Studies.* A summary of three generic blanket designs for the LTPHR is given in Table XIII-IV. All neutronic studies considered
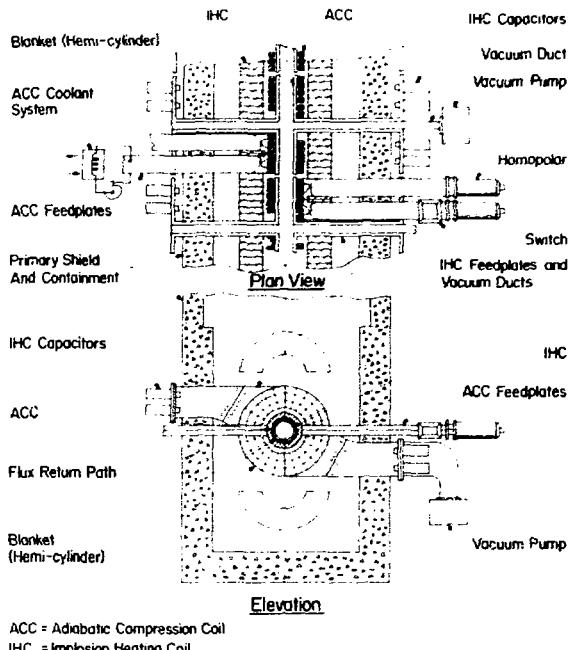
Fig. XIII-17.

Schematic layout of homopolar-driven LTPHR showing relative arrangement of implosion heating coil (IHC), adiabatic compression coil (ACC), HTGR blanket, vacuum system, and shielding.
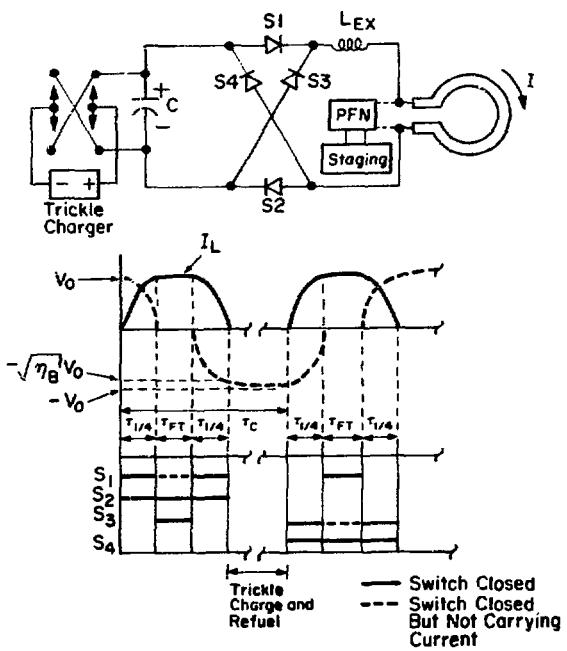
Fig. XIII-18.

Switching scheme envisaged for LTPHR using homopolar motor/generator power supply for ACC (shown as capacitor C) and solid-state switching.

TABLE XIII-IV
HYBRID BLANKETS BEING CONSIDERED FOR THE LTPHR

- CASE I : THORIUM FIRST REGION (E + E* ~ 450 MeV/n, E/E* = 10.4)
    - low neutron multiplication
    - low fast fission rate
    - most tritium comes from ^{6}Li
    - (n, Nn) on ^{232}Th leads to radiological problems
    - high fissile fuel inventory (~ 50 kg/m)

- CASE II : LITHIUM-7 FIRST REGION (E + E* = 477 MeV/n, E/E* = 10.1)
    - no neutron multiplication or fast fission in first region
    - tritium breeding in ^{7}Li
    - high neutron population for conversion and energy multiplication
    - lower fissile fuel inventory (18 kg/m)

- CASE III : URANIUM-238 FIRST REGION (under study)
    - high neutron multiplication
    - high fast fission rate
    - epithermal neutron spectrum in outer blanket
    - tritium breeding in ^{6}Li and ^{7}Li
    - lower fissile fuel inventory

only the HTGR ^{232}Th/^{233}U fuel cycle, although the as yet incomplete Case III blanket study envisions the use of a ^{238}U neutron multiplication region near the first wall. The major goal of the neutronic studies is the development of a fuel/moderator/multiplier/breeder configuration which gives high ^{233}U-breeding and maintains a tritium breeding ratio in excess of unity. Table XIII-V gives the dependence of key blanket parameters on the ^{233}U inventory I_{23} (kg/m), and presents an indication of the rate at which the moderate ^{233}U inventory could be "built-in" from a pure ^{233}Th blanket. The engineering Q-value Q_E, is shown as a function of I_{23} and LTPHR length ℓ(m). Although Q_E exceeds unity for all values of I_{23}, economic breakeven does not occur until I_{23} exceeds ~ 5 kg/m; this would take in excess of one year of operating the LTPHR with an initially unenriched ^{232}Th blanket. Although time-dependent burn-up calculations have been set up, results on the transient aspect of the blanket are not yet available. The ^{238}U neutron multiplier (Case III, Table XIII-IV) should enhance considerably the prospects for a low-enrichment blanket, although these calculations are not complete. Any ^{239}Pu produced by the Case III

blanket would be cycled internally and would not be directly incorporated in the LTPHR energy balance as virtual energy E* (MeV/n). Specific aspects of the neutronic results for LTPHR can be found in Sec. D.3.

b. *LTPHR Power Supply.* A variety of power supplies for the LTPHR ACC have been considered, some in more detail than others (Table XIII-VI). Because of the promise offered by the 30-ms-discharge homopolar energy transfer and storage (HETS) system proposed for the RTPR,[18] the possibility of applying this system to the 1-2 ms discharge requirement of LTPHR was investigated. The details of this design are reported elsewhere,[19] but Table XIII-VII gives a breakdown of efficiency and cost of a 2-ms discharging HETS. An overall transfer efficiency of 8.5% is marginally acceptable, although reassessment of the major loss component (joule losses in the HETS drum) may lead to increased efficiency. These encouraging results will lead to more detailed design activity for the fast discharging HETS system as applied to LTPHR.

c. *LTPHR Energy Balance.* The generalized LTPHR energy balance depicted in Fig. XIII-19 was

TABLE XIII-V

Case II blanket performance as a function of initial ^{233}U inventory. The real energy yield, virtual energy yield, fissile conversion ratio, tritium breeding ratio, and fissile breeding rate are, respectively, E, E^*, $[CV]$, $[BR]$, and R_{23}. For a given LTPHR length ℓ, the engineering Q-value Q_E is given.

EFFECT OF ^{233}U ENRICHMENT ON NUCLEAR RESPONSE OF 400-SERIES
BLANKET (^{7}Li FIRST REGION) FOR $I_W = 2.0$ MW/M^2

I_{23}(KG/M)	$E + E^*$(MeV/N)	E/E^*	$[CV]$	$[BR]$	R_{23}(KG/M Y)	I_{23}/R_{23}(Y)	$Q_E^{(C)}$		
							ℓ = 500m	750m	1000m
0	113(119)[B]	0.23	0.53	0.85	3.60	0.0	2.39	3.01	3.47
1	120(126)	0.30	0.53	0.85	3.60	0.28	2.52	3.17	3.66
5	154(163)	0.71	0.49	0.95	3.32	1.50	3.18	4.03	4.68
10	205(216)	1.93	0.42	1.07	2.85	3.51	4.12	5.26	6.13
15	288(304)	4.14	0.30	1.22	2.04	7.37	5.67	7.30	8.35
18[A]	454(477)	10.64	0.23	1.35	1.56	11.54	8.77	11.32	13.28

(A) Reference Case

(B) Extrapolated from $\Delta B = 0.015m$ to Zero Coil Thickness

(C) B = 25 T, E_θ = 4.0 kV/cm, ---- = economic breakeven

TABLE XIII-VI

Compression field power supplies considered for the LTPHR. The homopolar motor/generator appears most promising from a cost and efficiency viewpoint.

COMPRESSION FIELD POWER SUPPLIES CONSIDERED FOR LTPHR

SUPPLY	PROBLEMS/UNCERTAINTIES	ADVANTAGES
• CAPACITORS (electrostatic)	• HIGH COST • SIZE	• KNOWN TO WORK • ZERO CURRENT SWITCHING
• INDUCTIVE ENERGY STORAGE (Inductive)	• OPENING SWITCH • SIZABLE TRANSFER CAPACITOR	• LOW COST • HIGH ENERGY DENSITY
• HOMOPOLAR MOTOR/GENERATOR (mechanical inertia)	• RISE-TIME LIMITATION • LOW VOLTAGE	• LOW COST • COMPACT • ZERO CURRENT SWITCHING
• BATTERIES (& FUEL CELLS) (colombic)	• HIGH COST • POOR TRANSFER EFFICIENCY FOR FAST RISE PULSE • SHORT LIFE-TIME FOR DEEP DISCHARGE	• HIGH ENERGY DENSITY • EASE OF SWITCHING
• THERMIONIC EMITTERS (thermal inertia)	• LOW VOLTAGE • LOW EFFICIENCY	• HIGH CURRENT DENSITY • DIRECT DRIVE

---

used for the Case II (Table XIII-IV) blanket to generate parametrically the dependence of Q_E on length ℓ(m), maximum compression field B, and implosion heating voltage E_θ (kV/cm) for an optimized value of filling pressure P_A (mTorr). Figure XIII-20 illustrates this dependence. The dependence of Q_E on first-wall ACC thickness as determined by neutronic (decreased $E + E^*$) and mechanical strength considerations was determined[20] and is discussed below. Fig. XIII-21 shows the dependence of the total (real plus virtual) energy worth $E + E^*$ on the ACC thickness used in this analysis.

TABLE XIII-VII

SUMMARY OF HETS EFFICIENCY AND COST

Loss Component	Losses in percent of Total Stored Energy
Joule losses in drum	5.8
Return conductor	0.2
Brush voltage drop	0.6
Brush friction loss	1.3
Bearing (windage) loss	0.4
Refrigeration loss	0.02
Charging (power supply) loss	0.2
Total loss in HETS	8.5

Cost Component	Cost in percent of Total HETS
Superconductor	12.3
Refrigeration	4.4
Return conductor, drum	6.2
Current collection	17.4
Assembly	16.4

*All Power Expressed as MW/m

Fig. XIII-19.

Schematic diagram of LTPHR energy balance. The LTPHR with fissile conversion ratio [CV], ^{232}U inventory I_{23}, and sensible-heat generation $E(MeV)/n$, operates symbiotically with a fissile-fuel burner that uses $E^*(MeV/n)$ of virtual energy generated as bred fuel by the LTPHR. One of the total re-circulating power needs P_B, the fracture η_I goes to plasma heating, f_{BLK} as joule losses in the coil, and $f_I f_{EX}$ is lost externally.

The adiabatic compression coil (ACC) for a LTPHR[21,22] is designed as a multi-turn solenoid. Energy balance considerations require peak magnetic fields of ~20 T, which are pulsed roughly as half-sine waveforms of half-period ~1 ms and are repeated as often as four pulses per second. Hemi-cylindrical blankets are situated outside of and concentric with the compression coil, each hemi-cylinder being a self-contained core (Fig. XIII-17). The structural analysis of the high-field compression coil utilized the theory of elasticity solution for a thick-walled cylinder[23] and was made in conjunction with a detailed energy balance (Fig. XIII-19).

The dynamic model consisted of a mass, M_t, moving outward with the ACC as it expanded under the pulsed, internal magnetic pressure. The mass, M_t, may be either that of the ACC alone (uncoupled) or the blanket plus ACC (coupled). The strain energy for a coil of length ℓ, inner radius b, and thickness Δb, was determined, and the equivalent stiffness, k_r, for motion at the outer coil radius, $b + \Delta b$, was found to be of the form,

$$k_r = \frac{\pi \ell E \left[\left(\frac{\Delta b}{b} + 1 \right) - 1 \right]}{2 \left(\frac{\Delta b}{b} + 1 \right)^2} ,$$
$$\left[(1 - \nu) + (1 + \nu) \left(\frac{\Delta b}{b} + 1 \right)^2 \right] , \qquad (1)$$

where E is the Young's modulus and ν is Poisson's ratio for the composite (conductor/structure) material.

Using the principle of virtual work, the effective force acting at the outer ACC radius, $b + \Delta b$, was determined, and the dynamic equation[24] in the absence of damping was solved for a sinusoidal displacement function of period $T = 2\pi (M_t/kr)^{1/2}$. A shock-spectrum technique[24] was used to obtain the maximum dynamic amplification (attenuation) factor, α, as a function of the pulse duration, τ, and the mechanical period, T.

For a composite material of total cross section A, where only one component of area A_s contributes the fatigue strength and the other component carries the current, the maximum hoop stress in the composite material, $\sigma_{\theta max}$, is given by

$$\sigma_{\theta max} = \frac{A}{A_s} \alpha \frac{B^2}{2\mu_0} \frac{1 + (1 + \Delta b/b)^2}{(\Delta b/b + 1)^2 - 1} . \qquad (2)$$

The stress, $\sigma_{\theta max}$, may be taken either as the endurance limit (10^7 cycles) or as the yield strength (single pulse). The mechanical constraint imposed by Eq. (2) has been combined with neutronic and energy-balance constraints via a parametric systems analysis to determine an optimum ACC design.
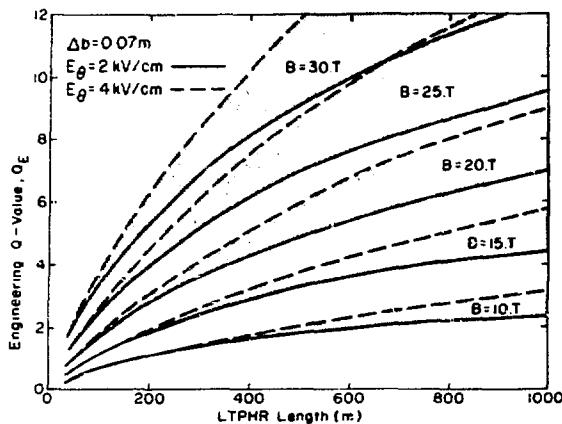
Fig. XIII-20.

Dependence of engineering Q-values, $Q_E = (P_E + P_\phi^*)/P_C$ (refer to Fig. XIII-19) on LTPHR length, implosion electric field $E_\theta (kV/cm)$, and compression field $B(T)$. The Case II blanket (Table XIII-IV) is used, and Δb is the first-wall coil thickness.

Fig. XIII-21.

Dependence of total energy worth (real, E, plus virtual, E*) of fusion neutron on LTPHR coil thickness and material. Case II (Table XIII-IV) blanket was used, and b is the inner radius of first-wall coil.

Figure XIII-22 shows the material constraint curves (dashed) for endurance (10.8 x 10⁸ Pa tension-tension or 7.6 x 10⁸ Pa tension-compression) and yield (16.3 x 10⁹ Pa) limits for an age-hardenable stainless steel (Custom 455) in composite form with a copper conductor and a structural material fraction, A_s/A, equal to 0.4. Figure XIII-22 pertains to a mechanically uncoupled ACC/blanket system; the case where the LTPHR blanket is tightly coupled to the ACC, increases the mechanical period from 0.23 to 0.70 msec. The solid line curves in Fig. XIII-22 show the compression field, B, required for a given energy multiplication, Q_E. Shown also in Fig. XIII-22 is the boundary for economic breakeven for the Case II (Table XIII-VI)[21] blanket system. Parametric variation of the structural fraction, A_s/A, indicates values in the range 0.4 to 0.5 are optimal; lower values of A_s/A limit the compression field, while higher values lead to unacceptable joule losses in the fixed thickness ($\Delta b = 0.1$) ACC.

The results of the foregoing spectral shock analysis are applicable to any system requiring pulsed solenoidal fields. Two regions of operation are identified, depending on the magnitude of τ/T. The characteristics of the LTPHR are such that operation in the long-pulse ($\tau/T > 2$, $\alpha \sim 1.0$) mode is ergonically favorable. A design that places the

ACC frequency response near the mechanical resonance (i.e., $\tau/T \sim 0.8$, $\alpha \sim 1.7$ for a sine pulse or $\tau/T \sim 1.0$, $\alpha \sim 1.7$ for a versed-sine pulse) is clearly to be avoided. For the characteristics indicated in Fig. XIII-22, energy breakeven and economic breakeven, within the constraints imposed by material limitations, occur at LTPHR lengths of 120 and 230 m, respectively.

3. Preliminary Studies of a Reversed-Field Z Pinch (RFZPR). The potential of the reverse-field Z pinch for fusion power production has been addressed by a number of studies.[25-29] Since a reverse-field Z-pinch reactor (RFZPR) would operate well above the Kruskal-Shafranov[30] limit, the tokamak-related constraints of low aspect ratio, low total plasma beta, and small ratios of poloidal to toroidal magnetic fields are not encountered. Because plasma confinement is primarily by poloidal fields, the RFZPR is conservative of magnetic energy, and, for comparable toroidal fields, the RFZPR portends larger ohmic heating rates at higher plasma densities than MHD constraints allow for tokamaks.

Although the questions of stability, preheating, and cross-field diffusion for the RFZPR are by no means answered, it seems prudent at this time to elucidate further the options and constraints associated with the technological and physics operating point. To this end, a "global"[31] plasma engineering computer code has been used to calculate the burn
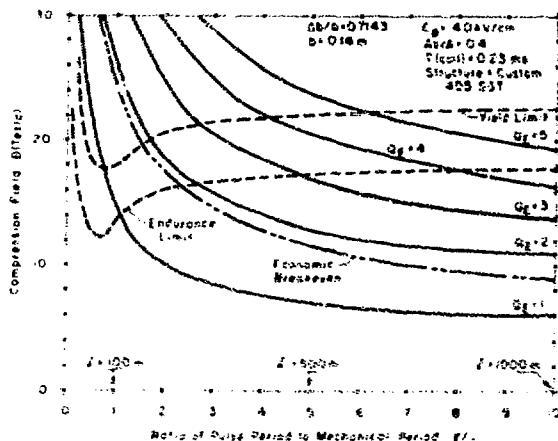
dynamics for a Z-pinch plasma that supports ideal
poloidal and toroidal field profile; alpha-particle
thermalization, radial particle diffusion, ohmic
heating and set-up of high shear equilibrium fields
are included. The major purpose of the global cal-
culation is threefold: a) to determine the plasma
set-up requirements that assure acceptable thermo-
nuclear yields for reasonable burn times, b) deter-
mine particle diffusion limits on energy balance,
and c) investigate the influence of alpha-particle
thermalization times on the energy-balance/burn-
time constraint. The global model used herein re-
presents the first stage of a general MHD model
being developed at LASL to study the effects of
field diffusion in a conceptual RFZPR.

The time dependence of the ratio Q_p of the sum
of neutron W_N, plasma W_{INT}, and bremsstrahlung W_{BR}
energies to the sum of set up W_{INT}^0 and ohmic-heating
W_{OHM} energies is shown in Fig. XIII-23 for two line
densities and a range of (constant) axial currents
I_z. The initial plasma temperature T_0 had no sig-
nificant effect on the Q_p vs t dependence, because
of the high efficiency of ohmic heating. The po-
loidal beta evaluated at the plasma surface $\beta_{\theta S}$
exceeds an assumed critical value of 0.4 before the
plasma expanded to the wall ($R_W = 0.6$ m), as indi-
cated by Fig. XIII-23. For all cases the plasma
was started with a radius of 0.4 R_W. Since an

"engineering" Q-value is expected to be ~ $Q_p/10$,
these results indicate viable RFZPR systems may be
possible for burn times in the range 0.1 - 1.0s and
for line densities on the order of 7.9 x 10^{23} (1/m^3).
Furthermore, if ohmic-heating currents in the range
20-30 MA can be induced in the plasma on a ~ 10-100
ms time scale, plasma set-up requirements may be
relatively modest. The dynamics of set-up, poloidal
field diffusion, and particle diffusion must, how-
ever, be addressed by a more detailed MHD model.

D.   THETA-PINCH NUCLEONIC STUDIES

1.   SFTR Shielding Studies. A comprehensive
shield design analysis for the SFTR has been per-
formed. The main results and conclusions are sum-
marized below.

A two-component shielding concept has been
adopted for the SFTR consisting of a 50-cm-thick
primary shield and 1.5-m secondary biological shield.
The primary shield is located immediately outboard
of the compression coil, and consists of annuli of
borated graphite, borated polyethylene, and a com-
mercially available lead-boron-polyethylene enclosed
in an aluminum structure. This shield composition
minimizes the induced activation and radiation dam-
age of the capacitors and structural materials and
also shields against gamma radiation from the coils

and coil structure. Exposure (dose) rates in the SFTR cell from the activated coils and structure are reduced to < 5 mrem/h at 1 day after a series of 1000 pulses (42 mrem/h at 1 h).

The secondary biological shield (a 1.5-m-thick ordinary concrete cell wall), in addition to the primary shield, was found to be sufficient to meet federal radiation exposure limits for personnel access areas outside the SFTR cell; i.e., a maximum total dose of 0.5 rem/y at the outer surface of the concrete wall. Air activation in the SFTR cell was also found to be within the limitations of federal regulations, so that no biological hazard is created by release of the cell air into the containment atmosphere or the environment.

Radiation effects which may change mechanical or chemical properties of materials were also considered. Energy production densities from neutrons and gamma rays are less than 1 MJ/m^3 per pulse, causing only negligible radiation heating rates. Likewise, the time-averaged 14-MeV (2.25-pJ) neutron wall loading on the first wall is only 2 x 10^{-4} MW/m^2, so radiation damage to metals will be inconsequential. Because of the small neutron fluence levels the transmutation effects at any location are below 1 ppm/y and cause no noticeable changes of mechanical or electrical properties in the copper coils or the Fe-Ni alloy (2 x 10^{-8} dpa/pulse or 2 x 10^{-5} dpa/y). The only remaining radiation effect which may impose a significant burden on the SFTR design is the radiation damage to organics being used as insulating and shielding materials.

Organic insulation may be used in the Fe-Ni alloy as well as the compression coil and the capacitors. The maximum dose to an organic insulator in the Fe-Ni alloy at r = 13.6 cm is 5 x 10^5 Gy/pulse and 3 x 10^3 Gy/pulse* to the compression coil insulator at r ≈ 17 cm. These doses may cause significant damage and impair the insulating properties of some organic materials if used as insulators at these locations.

The polyethylene in the primary shield is subject to a maximum physical dose of ~ 10 Gy/pulse at its location closest to the plasma. However, since there are no other than shielding requirements established for these polyethylene regions, an ab-

_____
*The gray (Gy) is an SI unit of physical dose, defined as 1 J/kg. Thus 1 Gy = 100 rads.

sorbed dose of 10 Gy/pulse is of no concern.

The maximum physical dose to the capacitor insulation is 1.5 Gy/pulse at R = 100 cm and falls off by over four decades to 8 x 10^{-5} Gy/pulse at R = 180 cm. Comparing this maximum dose of 1.5 Gy/pulse with a conservative radiation damage criterion of 10^3 Gy/y, it is seen that this criterion is almost met, even for the maximum value. It is concluded, therefore, that radiation damage to the capacitors is not expected to be a problem, but the presence of the primary shield is an absolute requirement to meet this objective.

2. RTPR Post-Design Nucleonic Assessment. A systematic review of key nucleonic parameters has been made for the Reference Theta-Pinch Reactor (RTPR). Blanket parameters considered include tritium breeding, energy deposition and spatial distribution, atom displacement and transmutation, etc. Effects on these responses due to structural material choice (V, Nb, or Mo), multiplier choice and thickness (Be, or BeO), graphite moderator thickness, and ^{6}Li enrichment were investigated. Calculations were performed by both repeated forward transport and perturbation methods. Thus, the study served not only as a blanket design sensitivity analysis, but also to define ranges of perturbation theory applicability.

Results for all facets of the study have been given in a detailed LASL report.[ ] Summarized below are some selected nucleonic effects as determined by repeated forward calculations, along with some quantitative accuracy information regarding SENSIT-1D perturbation calculations.

The major object of these post-design assessment studies was to provide basic data for a next iteration design of the RTPR. It is these iterations and continual feedback that will lead to the optimization of the reactor. Already this limited research has provided data on nuclear responses that could lead to significant improvement of the reference blanket design.

A secondary objective of determining the adequacy of using 25-group nuclear data was reached. In summary, it was found that 25-group calculations render total integral effects accurate to within 2% of the 100-group calculations. This accuracy is considered to be sufficient for computations pertaining to the change of nuclear effects caused by

design changes. Therefore, not only were computer time savings generated, but also the integrity of the answers was preserved.

The replacement of niobium with molybdenum resulted in an increase in parasitic absorption and subsequent decrease in tritium production of ~ 15%. In that the tritium breeding ratio of the reference case was 1.11, the decrease due to Mo would force the ratio to go below 1.0, an obviously undesirable effect. However, Mo does have the beneficial effect of a reduction in magnet coil heating of ~ 19%. This indicates that its presence in the blanket provides a better shield for the coils than an equivalent volume fraction of Nb. When vanadium was substituted for niobium as the structural metal, the tritium breeding ratio increased by 25%, while the coil heating increased by only ~ 2.5%. Thus, as far as tritium breeding and coil heating is concerned, the use of vanadium appears to be more advantageous.

Increases of the Be region thickness from 2.5 to 5.5 cm led to an increase in the tritium breeding ratio of ~ 10%. This provides a large margin to assure that the tritium breeding ratio can be kept above 1.0 after accounting for multidimensional effects. Also, as Be thickness increases, the flux is reduced in regions as far out as the outer graphite and copper coils; hence, advantageous effects such as the reduction in atom displacements and copper transmutation occur. Therefore, it appears that increases in the Be region thickness will increase the tritium production and also provide better shielding for the magnet coils. One possible drawback to such a design change is the limited availability of beryllium. However, considering the tenous basis for estimating resources, such conclusions are disputable.

The use of BeO as a neutron multiplier was found to be inadequate for the reference configuration. Because of its moderation properties, however, BeO is a potential superior neutron moderator; studies with BeO as the moderator should be initiated in a next iterative design of the RTPR blanket.

The graphite thickness study has the greatest potential impact on the RTPR blanket design. The blanket thickness can be decreased by removing ~ 13 cm of graphite, thus resulting in a reduction of stored magnetic energy and blanket joule losses,

having a negligible effect on tritium breeding. The detrimental effects of increase in coil damage and decrease in recoverable energy (Table XIII-III) appear to present no insurmountable problems. These effects could possibly be alleviated by the use of a gamma absorber at the periphery of the blanket. However, the potential capital savings in the cryogenic and energy storage systems, along with an improved energy balance, as a result of the decreased blanket thickness provide a strong incentive to redesign the RTPR blanket module.

Over a wide range, the degree of enrichment of ^{6}Li in the blanket showed little effect upon the tritium breeding. Hence, a savings in the cost of ^{6}Li can be realized. Copper transmutation increases are a minor effect. Future studies of the nuclear effects due to concurrent changes in the graphite thickness and ^{6}Li enrichment may provide more information on how much ^{6}Li enrichment cost can be saved.

The final purpose of this study was to determine the accuracy and limitations of the use of perturbation theory in the studies investigated. Perturbation theory was determined to be quite accurate (within 0.6% in the repeated forward calculations) in the Be and BeO studies. However, it was found that in the graphite study perturbation theory was invalid for decreases in the thickness by more than ∿ 1.0 cm. Perturbation theory assumes that the design change is small; hence, as an approximation, the unperturbed forward and adjoint fluxes are used in perturbation theory. However, in the graphite study, it was seen that if the outer graphite was decreased by more than ∿ 1.0 cm, perturbation theory was no longer applicable (i.e., such a design change must be considered a major perturbation). This confirms that when perturbation theory alone is used to calculate effects, one must carefully assure that design changes result in perturbations to the transport operator which are small in magnitude.

3. *LTPHR Neutronics Parameter Studies.* As a guide for the mechanical design of the magnet coils for the LTPHR, parametric neutronic sensitivity studies were performed to ascertain effects of coil thickness and materials. The reference blanket design (Case II, Table XIII-IV) was used for all regions outboard of the coil. Additional studies were made to determine the blanket energy production as a function of ^{233}U loading. From these latter

studies an estimate was made of the time required for "bootstrapping" a pure ^{232}Th LTPHR to a reference ^{233}U loading of 18.2 kg/m.

a. *Coil Material and Thickness Sensitivity.*

Three potential coil materials were examined: aluminum, copper, and molybdenum. In each case the coil thickness was varied from 0.1 to 10.0 cm. Figure XIII-21 shows the decrease of total blanket energy, E + E*, with coil thickness. In every case the coil is assumed to have 30 vol% He coolant. All results are normalized to their common value with no coil present. In all calculations the blanket region thicknesses were maintained constant at the reference design values. The shapes and magnitudes of the curves in Fig. XIII-21 reflect the neutron multiplication by (n,2n) reactions in competition with neutron parasitic absorption. Molybdenum, for example, has a much higher (n,2n) cross section at 14 MeV than copper (1.24 b vs 0.617 b), but generally exhibits higher parasitic absorption in the lower energy region. Hence, a thin molybdenum coil will rapidly reduce the blanket energy by parasitic absorption of neutrons reflected from the blanket. The molybdenum rapidly self-shields, however, and the curve (Fig. XIII-21) then is determined mainly by (n,2n) reactions, causing a relative flattening from about 1 to 5 cm, as compared to the other materials. At large coil thicknesses (> 5 cm) the neutron spectrum is softened sufficiently to reduce the effectiveness of the (n,2n) reaction, and epithermal capture again dominates. The spectrum of reflected neutrons from the blanket is predominantly epithermal (300-800 keV), where the molybdenum parasitic absorption cross section is over three times that of copper. Aluminum, despite its low parasitic absorption at neutron energies below ~ 6 MeV, has poor properties at higher energies; the (n,2n) cross-section threshold is above 13.5 MeV, and the parasitic absorption for neutrons above 6 MeV is greater than for copper or molybdenum.

Similar results for tritium breeding ratio, [BR], and fissile fuel conversion rate, [CV], are shown in Fig. XIII-24. Because of the loose neutronic coupling between the coil and the fertile seed, little difference in [CV] is found among the coil materials. The slight differences (indistinguishable on the curve) are mainly caused by slightly different 14-MeV neutron attenuation properties
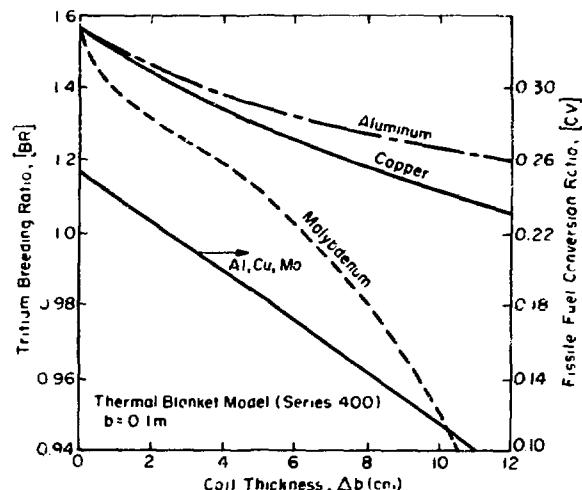
Fig. XIII-24.

Effect of LTPHR coil thickness and material on tritium breeding [BR], and fissile fuel conversion [CV], for the Case II blanket (Table XIII-IV).

of the coil materials. However, the ^{7}Li (99 at.%) region between the coils and fertile seed is strongly affected by the absorbing properties of the coil, as well as by the leakage spectrum from the coil. Tritium breeding is, therefore, enhanced by use of an aluminum coil with its low parasitic absorption at lower energies (i.e., at the peak in the neutron spectrum at the interface between coil and ^{7}Li regions).

b. *Parametric Studies of ^{233}U Loading in the LTPHR.*

As part of an assessment of material resource (especially fissile) requirements in the LTPHR, preliminary neutronic performance characteristics were studied for a range of initial ^{233}U loading. Again, the reference blanket design was used as a starting point. The production rate of ^{233}U in any blanket is given by

$$R \ (kg/m \cdot y) = 3.39 \ I_w[CV], \tag{3}$$

where I_w (MW/m^2) is the neutron wall loading and [CV] is the net conversion rate of ^{232}Th to ^{233}U. That is, [CV] is the production of ^{233}U from ^{232}Th (n, γ) reactions, minus the burning of ^{233}U, both per D-T neutron. For I_w = 2.0 MW/m^2, the production rate of ^{233}U in the pure Th/C blanket (i.e., no ^{233}U loading) is given by 6.78 [CV], or R = 3.05 kg/ m·y for [CV] = 0.45.

At this initial conversion rate, and assuming continuous removal of ^{233}U from the blanket, it would take about six years to produce the ^{233}U loading of 18.2 kg/m in the reference LTPHR design. In order to allow other possible fuel management schemes to be studied, especially ones with acceptable energy balances during the "bootstrapping" period, blanket neutronic responses were parameterized for arbitrary ^{233}U loadings. Capital and operating costs can then be estimated for the startup phase during the first few years of operation of the first reactor. Some of these costs may have to be charged to development of an LTPHR reactor system.

With two exceptions, all ^{233}U loadings considered were achieved by keeping the reference design configuration unchanged and independently varying the loadings of the two seed regions in the LTPHR blanket. Carbon-to-heavy metal (^{232}Th and ^{233}U) ratios were kept constant as the loading of ^{233}U in the heavy metal atom density varied from 1 at.% to 10 at.%. To achieve the two lowest loadings (4.42 and 1.92 kg/m), the outer seed outer radius was decreased to 76.5 cm. Also, the enriched ^{7}Li region was changed to 2 at.% ^{6}Li from the reference design value of 1 at.%.

Figure XIII-25 shows the variation of blanket energy, tritium breeding ratio, fissile conversion ratio, and specific total blanket power (normalized to a D-T source of 1 neutron per meter). The repeated changes of curvature in some of the curves is a result of the arbitrary partition of ^{233}U between the two seed regions, with no attempt made to optimize within any given loading. Only one serious constraint was identified by this study; the tritium breeding ratio is inadequate for the reference blanket configuration if ^{233}I < 9 kg/m. Therefore, further blanket design changes would be required during initial reactor operation if no external source of tritium were available.

E. NEUTRONICS

1. Quantitative Data Assessment. A computational method to determine neutron cross-section requirements for the neutronics analysis of any specific design has been developed. The theoretical basis for such analysis is a generalized perturbation theory that has been applied to sensitivity analysis. In order to provide a rational basis for
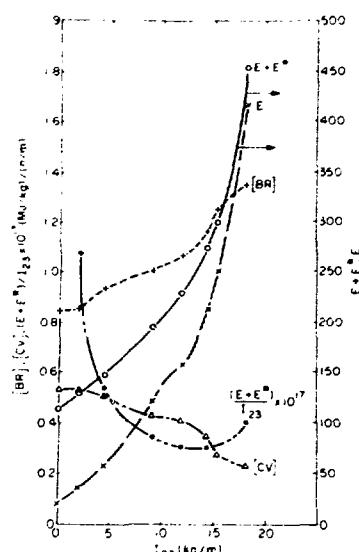
Fig. XIII-25.

Variation of total blanket energy (real + virtual) (E + E*), tritium breeding ratio [BR], fissile conversion ratio [CV], and specific blanket power,(per fusion neutron/m) on the fissile fuel inventory.

the priorities assigned to new cross-section measurements or evaluations, this method includes: quantitative estimates of the uncertainty of currently available data, the sensitivity of important nuclear design parameters to selected cross sections, and the accuracy desired in predicting nuclear design parameters. Linear perturbation theory is used to combine estimated cross-section uncertainties with calculated sensitivities to determine the variance of any nuclear design parameter of interest. These methods together with a typical application to the Tokamak Fusion Test Reactor (TFTR) are documented in detail.[53] Only the main conclusions of the study are reported here.

Nuclear data uncertainties have been analyzed to determine their effects upon activation of TFTR components. Because of the importance of accurately predicting dose rates in the reactor cell during maintenance operations, several important (dominant) activation reactions need to be considered. Errors in predicted activation rates depend upon both errors in transport cross sections and in the response (activation) cross sections themselves. These studies have been limited in scope by the availability of cross-section error information, an area in

which continuing effort is being placed. The results in the bottom lines of Table XIII-VIII can be directly compared with the design criteria for biological dose rates adopted for the TFTR, i.e., the total personnel exposure rate inside the reactor cell, E^P, must be less than 100 mrem/h 2 h after shutdown (for 1 pulse operation) and less than 10 mrem/h 1 day after shutdown (for 1 y of operation). The maximum allowable uncertainty in such calculated personnel exposure rates is set to $\pm$ 50%.

This analysis predicts an uncertainty in the calculated maximum allowable personnel dose rate of 41.4% for the steel TFTR structure (compare Table XIII-VIII) and 44.8% when aluminum structures are chosen.

These uncertainties result from cross-section uncertainties only. Comparing this result with the accuracy requirement of < 50%, we conclude that all neutron transport and activation cross sections are adequately known for this TFTR activation analysis. It is possible, however, that other activation reactions or radiation streaming effects which were not considered in the present analysis may cause additional uncertainties in calculated personnel dose rates, and the confidence limit specified above could be, therefore, exceeded. To make a final conclusion on the adequacy or inadequacy of all nuclear data for TFTR needs, this analysis must be extended to incorporate additional nuclear design criteria which may involve other radiation effects; e.g., radiation damage to insulators or biological dose rates due to direct radiation outside the test cell at operating conditions.

2. CCCC Code Interfaces and Cross Section Processing. Preliminary investigations have been made into the CTR applicability of coding standards established by the Committee on Computer Code Coordination (CCCC). A position paper recommending CTR participation in future code standardization efforts was prepared. Some study was given to modifying existing CCCC standards for more complete CTR compatibility, and proposals were made for further discussion by the CTR neutronics community.

An ongoing effort is being made to expand and improve LASL neutron and photon cross section and response function data sets for CTR system studies. Existing cross-section sets are being updated, documented, and conveniently stored to provide the CTR

neutronics staff with more automated access. When possible, missing data for some isotopes are calculated and added to the sets. Other data are included as they become available from sources such as RSIC.

3. Review of Lithium Sphere Experiment. Measurements of space-dependent neutron spectra and tritium breeding in lithium spheres have been performed in German laboratories (Karlsruhe) as well as at LASL. However, transport calculations by the Karlsruhe group in an attempt to analyze their experiment show unexplained discrepancies between calculations and measurements. The resolution of this problem is important because of implications with respect to fusion reactor systems analysis if numerical methods currently used in the CTR neutronics community are deficient. Also, the measurements were performed in a simple and clean geometry so that the experiment could be ideally suited as a benchmark for fast neutron transport in lithium.

In a recent visit to Karlsruhe the measurements and their analyses were discussed with the German group. The Karlsruhe group had repeated their measurements and refined their computational tools in an effort to explain and eliminate the existing discrepancies. This new analysis shows almost perfect agreement between measurements and calculation. The original discrepancies could be traced back to errors in both the measurements as well as the attempted computational analysis. This result gives confidence in the codes and data used for CTR neutronics analyses in lithium.

F. INSULATOR STUDIES

Insulator studies were directed toward structural, chemical, and electrical effects, with and without radiation. Methods for simulating 14-MeV neutron damage in ceramics were also investigated. Emphasis was placed on problems associated with the first-wall liner of the RTPR; however, information from these studies is also applicable to other insulator uses in fusion reactors.

1. Structural Effects. Studies of ceramics irradiated at elevated temperatures in the EBR-II fission reactor as part of an earlier LASL project[34] have been performed. Primary emphasis has been placed on transmission electron microscopy (TEM) analyses. Evaluations of Al_2O_3 and Y_2O_3, in progress

TABLE XIII-VIII

PREDICTED ABSOLUTE UNCERTAINTIES IN CALCULATED RADIATION EXPOSURE RATES
DUE TO ALL CROSS-SECTION UNCERTAINTIES - TFTR DESIGN WITH STEEL STRUCTURE

Radio nuclide i	$T_{1/2}$		Production Mechanism	Production Rate, R_i (atoms per fusion neutron)	Exposure Rate $E_i \pm \Delta E_i$ After			
					1 Pulse and 2 h		1 y and 1 d	
					E_i (rem/h)	ΔE_i (rem/h)	E_i (rem/h)	ΔE_i (rem/h)
^{54}Mn	313	d	$^{54}Fe(n,p)$	1.35 E-3	7.05 E-4	3.63 E-4	4.38 E-1	2.26 E-1
^{54}Mn	313	d	$^{55}Mn(n,2n)$	4.80 E-4	2.49 E-4	1.10 E-4	1.72 E-1	7.60 E-2
^{56}Mn	2.6	h	$^{56}Fe(n,p)$	3.32 E-3	5.11 E+0	2.28 E+0	6.31 E-3	2.82 E-3
^{58}Co	71	d	$^{58}Ni(n,p)$	2.30 E-3	6.16 E-3	2.92 E-3	1.67 E+0	7.92 E-1
^{62}Cu	9.8	m	$^{63}Cu(n,2n)$	9.89 E-3	6.94 E-1	4.64 E-2	< E-10	< E-10
^{60}Co	5.2	y	$^{63}Cu(n,\alpha)$	1.03 E-3	2.30 E-4	1.61 E-4	2.19 E-1	1.53 E-1
^{64}Cu	12.7	h	$^{65}Cu(n,2n)$	9.55 E-3	6.66 E-1	4.29 E-1	4.26 E-1	2.75 E-1
^{65}Ni	2.6	h	$^{65}Cu(n,p)$	2.69 E-4	1.53 E-1	1.13 E-1	1.91 E-4	1.41 E-4

Total Exposure Rate (unshielded): 6.53 rem/h, 3.22 rem/h, 2.90 rem/h, 1.20 rem/h

$$E = \sum_i E_i, \quad \Delta E \text{ includes correlations among } \Delta E_i$$

Total Personnel Exposure (shielded): 22.5 mrem/h, 11.1 mrem/h, 10.0 mrem/h, 4.14 mrem/h

$$(E^P \pm \Delta E^P) = 3.45 \times 10^{-3}(E \pm \Delta E)$$

last year, were completed,[35] and additional investigations of Y_2O_3-stabilized ZrO_2 carried out. The latter ceramic had earlier been shown to exhibit significant swelling ($\sim$ 2 vol%) after irradiation to 3-4 x 10^{21} n/cm² (E_n > 0.1 MeV) at 875 K, but were found to be dimensionally stable at 650 and 1025 K (Fig. XIII-26).[34] The intermediate-temperature material was found to contain aligned "pores" (Fig. XIII-27) similar to those seen earlier in irradiated Al_2O_3. Samples irradiated at the low and high temperatures showed only dislocations, loops and defect clusters. It is important to note that the temperature range for swelling in this ceramic is lower than that for typical metals, when expressed as a fraction of the absolute melting point; the range for metals is usually $\sim$ 0.3-0.5 T_m, while the ZrO_2 irradiation temperatures were 0.22, 0.30, and 0.36 T_m. These results indicate that ZrO_2 is above its swelling temperature range at first-wall operating temperatures, at least under EBR-II irradiation conditions.

It is of critical importance to identify the "pores" observed in the above studies in order to understand radiation damage in ceramics. Hobbs and Hughes[36] have pointed out that in such materials these defects may be voids (as in metals), cation aggregates, or anion aggregates. Nuclear magnetic resonance studies using the Knight shift have been made to determine whether colloidal aluminum is present in irradiated polycrystalline Al_2O_3. Resonant absorption data show that this is apparently the case. The amount of "metallic" aluminum present (calibrated by use of a known mass of aluminum power) was found to be 2.1 $\pm$ 1%, which compares with a "pore" content of 1.6% estimated by TEM and a measured macroscopic swelling value of 2.4%.[35] Unexpectedly, a control sample of the same polycrystalline Al_2O_3 showed an apparent metallic aluminum content of $\sim$ 0.5%; unirradiated single-crystal sapphire exhibited perhaps 10% of this amount.
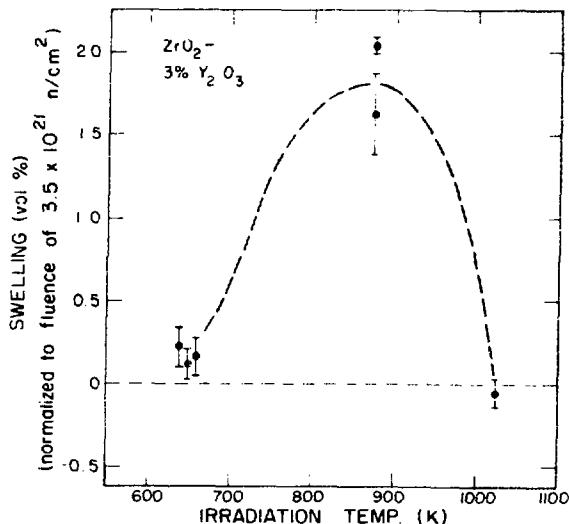
Fig. XIII-26.

Swelling of Y_2O_3-stabilized ZrO_2 after irradiation in EBR-II at three temperatures.

Fig. XIII-27.

Aligned "pores" in Y_2O_3-stabilized Zr_2O_3 after irradiation in EBR-II at 875 K. (150 000 X)

Studies are continuing, to improve the precision of the data and to understand the behavior of the control polycrystalline sample. To check the possibility that "pores" observed in Al_2O_3 or other irradiated ceramics may be high-pressure anion bubbles, a residual gas analysis apparatus has been modified to allow evaluation of gas release from fractured specimens; these tests are in progress.

RTPR first-wall re-design studies have been carried out. (Sec. XIV. C.1). A number of configurations were analyzed for thermal and stress response to the pulsed heat throughputs characteristic anticipated for the RTPR. Several first-wall concepts show significant improvement over the reference design.[1] This work is more completely described in Section XIV. C.1.

Thermal and stress behavior of the first-wall insulator is strongly dependent on thermal conductivity, which can be degraded by neutron irradiation.[37] A pulsed light source conductivity apparatus has been constructed to measure this property in samples which have been irradiated at elevated temperatures in a fission reactor (EBR-II). Measurements will begin after samples removed from EBR-II in January 1976 are returned to LASL. In support of this work, calculations on the effect of lattice defects on thermal conductivity are being

carried out in conjunction with Prof. Paul Klemens, consultant from the University of Connecticut.

The reference first-wall design for the RTPR[1] calls for Al_2O_3 laminated onto Nb-1%Zr. Bonding and diffusion studies of this system have been carried out, in part to determine Al_2O_3/Nb sample thicknesses for the EBR-II irradiation now in progress. Complex interdiffusion reactions were observed. Bonding appears satisfactory with polycrystalline alumina, but is marginal with single-crystal sapphire.

Si_3N_4, a high-strength structural ceramic, is being considered as a first-wall insulator. For an electrical application, porosity must be kept low, and for maximum strength, grain-boundary phases must be highly refractory. A program is under way in cooperation with CMB-6 to hot-press and evaluate Si_3N_4 made from amorphous powder and varying amounts of Y_2O_3 sintering aid. Early results are promising; it appears that a high-density, high-strength product can be made.

2. Chemical Effects. A high-density polycrystalline Al_2O_3 probe subjected to a large number of shots in an experimental theta-pinch device (Scylla 1-B) has been evaluated for evidence of degradation in surface structure and resistivity. Table XIII-IX summarizes the estimated exposure of this probe to plasma. Examination by scanning electron microscopy showed that the probe, which had protruded into the plasma, underwent surface melting to a thickness of ~ 1 μm (Fig. XIII-28), and studies utilizing solution chemistry revealed that partial reduction had occurred in this area. Surface electrical

TABLE XIII-IX
SUMMARY OF (ESTIMATED) EXPOSURE OF A HIGH-DENSITY Al_2O_3 PROBE TO SCYLLA I-B PLASMA

Parameter	minimum value	Average or most probable value	maximum value
H, number of discharges	1000	1800	2000
n, measured plasma density (ions/cm³)	1.0×10^{15}	3.0×10^{15}	5.0×10^{15}
$T_i + T_e$, measured ion + electron temperature (keV)	0.40	0.40	0.75
T_i, estimated ion temperature (keV)	0.30	0.30	0.55
T_e, estimated electron temperature (keV)	0.10	0.10	0.20
τ, duration of discharge (μs)	2.0	2.5	3.0
ϕ, plasma flux to probe, $\sim n\,[k(T_e + T_i)/m_i]^{1/2}$ (1/cm² s)	1.4×10^{22}	4.1×10^{22}	9.4×10^{22}
t, total exposure time (ms)	2.0	4.5	6.0
ϕt, total dose per discharge (1/cm²)	2.8×10^{19}	1.8×10^{20}	5.6×10^{20}
F_0, peak energy flux (J/cm² s)	8.96×10^5	8.9×10^5	1.68×10^6
ϕtN, total dose (1/cm²)	2.8×10^{22}	3.24×10^{23}	1.12×10^{24}
ΔT, calculated surface temperature rise (K)[a]	1222	1366	2805

[a]For a semi-infinite slab geometry, the temperature rise is given by $\Delta T = (2F_0/k)\sqrt{\kappa t/\pi}$, where F_0 is the peak flux, t is the duration of the pulse, k is the thermal conductivity (.3720 W/cm K for Al_2O_3 at 300 K) and κ is the thermal diffusivity (0.1010 cm²/s for Al_2O_3 at 300 K).

resistivity, however, was virtually unchanged from that of an undamaged control sample. Calculated temperature rises (Table XIII-IX) indicated surface melting only for the maximum heat fluxes, and analyses could not determine if the sample underwent single or repeated phase changes. The extent of observed damage is far beyond that expected in the RTPR, since that machine will make use of a neutral gas blanket to protect the insulator, and the first wall will not be in direct contact with the plasma.

Since the first-wall insulator in the RTPR is protected by a gas blanket, it is anticipated that the major source of chemical attack will be neutral atomic hydrogen. A residual gas analyzer with an atomic hydrogen source has been constructed to investigate chemical erosion, and preliminary tests are being conducted to increase detection sensitivity. Studies have also been conducted in a high-temperature furnace utilizing tungsten mesh heaters as an atomic hydrogen source, where evaporation and chemical erosion were measured by a weight-loss technique. Results indicate that in vacuum,

evaporative loss rates for Al_2O_3 would be acceptable up to ~ 1800-1900 K. The presence of atomic hydrogen increased the rate of weight loss; the magnitude of this effect is still under evaluation.

3. Electrical Effects. Calculations of degradation in electrical properties of insulators under ionizing radiation (bremsstrahlung and background gamma) have been carried out.[38]

The calculation treats both short-term ionization effects (free and trapped electrons and holes) and long-term gross damage effects (transmutation products and various lattice defects). The following processes were considered: (1) delayed electronic conductivity 10 sec after prompt ionization by bremsstrahlung, (2) prompt electronic conductivity from delayed (gamma-induced) ionization, (3) electronic breakdown, (4) thermal breakdown, (5) enhanced electronic conductivity, and (6) enhanced ionic conductivity. It was concluded that none of the first five processes is likely to result in electrical failure of the first-wall insulator, unless structural changes under irradiation cause a
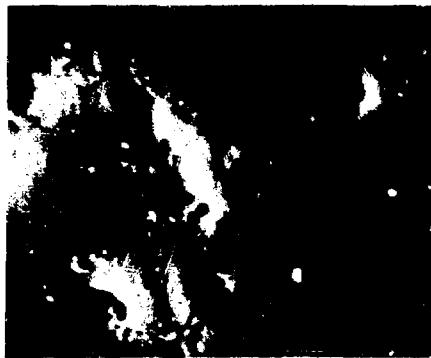
Fig. XIII-28.

Surface structure of Al_2O_3 probe after repeated exposure to plasma in Scylla 1-B. Estimated ion exposure is ~ 0.30 keV. (750 X)

significant decrease in dielectric properties. Ionic conductivity represents a major uncertainty.

Perhaps the most important single parameter for the first-wall insulator is dielectric breakdown strength (Dbs). Studies are under way at LASL and other CTR insulator laboratories to measure dbs of candidate materials, evaluate breakdown mechanisms, and determine the effect of radiation damage. To correlate data obtained from these studies a standard dbs test for use by all laboratories is under evaluation. Voltages up to 20 kV can be repeatedly applied to the test specimen, with rise and decay times of 2 μs and an adjustable plateau of from 0 to 10 μs. Results are obtained in the form of voltage and current vs time data. Pulses are short enough to simulate approximately first-wall pulse times (~ 0.1 μs) and to avoid thermal breakdown with resulting ambiguity in test results for low-resistivity materials.

4. *Radiation Damage Simulation.* The use of protons of energies between 5 and 15 MeV to simulate 14-MeV neutron damage has been evaluated both experimentally and theoretically. Earlier studies utilized the increase in optical absorption of irradiated sapphire as a measure of the nature and amount of damage per particle. A comparison of absorption spectra, their annealing characteristics, and damage per incoming particle between material irradiated with 14-MeV neutrons and 15-MeV protons showed good correlation, while lower energy protons gave a less-successful simulation. In the latest work[39] recoil energy spectra were calculated and converted

to damage energy spectra by use of the Lindhard efficiency factor. These results were integrated to yield damage per particle, agreement being good between 15-MeV protons and 14-MeV neutrons, with poorer agreement at lower proton energies.

Heavy ion bombardment can be used to generate high damage levels in a short time and to simulate the intense pulsed damage rates characteristic of RTPR. Since it is likely that rate effects in pulsed reactors will be important, these studies are necessary for a complete understanding of damage phenomena. Preliminary investigations on the use of oxygen ions for this purpose have been conducted. An apparatus has been constructed to allow ion bombardment at elevated temperatures, and calibration runs have been made with sapphire at 1075 K. Beam intensities of ~ 0.5 μA/cm² (~ 3 x 10¹² ions/ cm² s) have been achieved for times of several hours, corresponding to a first-wall neutron fluence of ~ 4 x 10²⁰ n/cm² at maximum penetration depth. Preliminary examinations of irradiated samples by TEM have been conducted.

A major effort has been directed toward irradiation of a variety of ceramic, glass, and laminated insulator/metal samples in EBR-II. The purpose of this study is to allow evaluation of a large number of materials of varying composition and microstructure after fast neutron irradiation at elevated temperatures to damage levels roughly equivalent to those expected for a one year first-wall exposure under RTPR conditions.[1] While irradiation conditions do not fully simulate first-wall conditions (e.g., with respect to transmutation-induced gas formation), valuable comparative and base-line information will be obtained. Three sample-containing capsules were placed in the reactor. A vacuum gap-regulated Dewar assembly was designed to hold samples at ~ 1025 K. This capsule was removed in January 1976, after six weeks in the reactor. Fluence was ~ 3 x 10²¹ n/cm² (E_n > 0.1 MeV). Two other assemblies are heat-pipe regulated at 925 and 1100 K, and will be removed about December 1976, after a one-year exposure (∿ 2 x 10²² n/cm²). Control samples are being held at test temperatures without irradiation, at LASL. Test materials are: Al_2O_3, BeO, Si_3N_4, SIALON, SiO_2, $Al_2O_3 \cdot MgO$, $nAl_2O_3 \cdot mY_2O_3$, $Y_2O_3 \cdot MgO$, Si_2ON_2, vitreous SiO_2, and two barium-aluminum-silicate enamels. Included are

monocrystals; polycrystals; CVD, sputter-deposited, and plasma-sprayed materials; and laminar insulator/metal structures. After irradiation these samples will be evaluated for defect content, dimensional changes, mechanical properties, dielectric strength, thermal conductivity, and interface effects in bonded samples.

G. ALLOY RESEARCH

The objective of the alloy research task is to determine the limits of metals in future fusion power reactors. The intense neutron irradiation will displace atoms, produce hydrogen, helium, and heavy impurity atoms all by nuclear reactions. Constant and cyclic stresses will also be present. Void formation induced by neutrons will cause high-temperature embrittlement. Facilities to simulate the combination of cyclic stress, elevated temperature and neutron irradiation do not exist so effort has been focused on developing appropriate facilities.

1. Cyclic Stress and Temperature. The first wall of a theta-pinch reactor is a layered composite with an insulator facing the plasma and a metal backing facing the Li blanket structure. Cyclic thermal tensile stresses will occur in the metal backing. Thermal fatigue damage will result and limit metal life. Earlier results were obtained on molybdenum at 1200 K under cyclic stressing. Niobium or its alloys were not evaluated because they are so highly reactive at elevated temperatures that existing facilities could not prevent reaction during elevated-temperature testing. Progress was made towards high-temperature mechanical testing of niobium alloys, however.

An ultrahigh vacuum system has been assembled. Initial use produced vacuum pressure lower than 10^{-8} torr. The system includes a helium expansion cryo-pump, an ion pump, a sorption pump for roughing, and a double-walled stainless steel bell jar with water cooling and provision to heat it for outgassing. A residual gas analyzer has been selected and ordered.

Elevated-temperature testing will be carried out inside the bell jar. Several options exist. An Instron closed-loop mechanical tester is scheduled to arrive at LASL in March 1976. It is an electro-hydraulic system which can be programmed to produce almost any load time cycle desired. As an alternate to Instron loading, cyclic temperature excursions could be produced in test niobium materials inside the bell jar by resistance heating or by electron-beam heating. An electron-beam thermal-shock power supply was built for other work at LASL. It is available to thermal fatigue refractory metals or even RTPR-like Al_2O_3/Nb-1%Zr layered composites.

Professor R. A. Yeske at the University of Illinois has an ultrahigh vacuum system similar to the LASL system, which is mounted in the load frame of a mechanical testing machine. The bell jar is fitted with a heater. A consultant agreement has been established wherein cyclic-stress tests will be performed on 15-Nb and 15-Nb-1 Zr samples. Each test requires about one week of effort. Heating for 60 h at 1093 K ($0.4\ T_m$) produced no change of oxygen content or sample appearance. Residual gas pressures for O_2, CO, NO, CO_2 and H_2O were all below 8×10^{-10} Torr. Strength level of wrought Nb was high relative to published data for annealed material, but consistent with published data for cold-worked Nb. Samples will be annealed to produce a known initial state. The results of this effort will be published as soon as they become available.

Dr. A. Pant and Professor L. M. Lidsky of Massachusetts Institute of Technology contend that many temperature spikes of 100-200°C called for in RTPR might produce property changes after many cycles of operation. They simulated the Nb-1% Zr cyclic thermal shock by resistance pulse heating Nb-1% Zr samples 100-200 K in a 10^{-3} torr vacuum at 1350-1500 K. Room-temperature mechanical testing after temperature pulsing established that a ductility loss resulted. The samples of Nb-1% Zr that were temperature cycled at MIT have been analyzed by us at LASL. Scanning electron microscopy, oxygen analysis and x-ray diffraction studies were carried out. The results of these analyses are summarized in Table XIII-X.

The control sample was annealed without temperature cycling and was not exposed to as much oxygen contamination as the cycled samples; the average oxygen content of the control sample was only slightly above the "as-received" oxygen content, whereas the cyclic samples showed large oxygen increases over the "as-received" value. A carbide phase was present on the surface of the "annealed

TABLE XIII-X

Sample	Post-Temperature Cycling Fracture Mode at Room Temperature	Surface Phase	Ave. wt/o Oxygen Content Before Surface Cleaning*	Ave. wt/o Oxygen Content After Surface Cleaning*
Control	Ductile-fracture fracture face enlarged voids	Nb	0.02%	---
Annealed at 1273 K for 604 ks**	Ductile but less than as-received control	NbC	0.077%	0.073%
10^5 cycles of temperature from 1350 to 1500 K	Embrittled fracture face shows some voids	NbO_2	0.2%	0.193%
3×10^5 cycle as above	Cleavage fracture. No ductility.	NbC_2	0.43%	0.422%

*
Determined by neutron activation.

**This time equals the time required to achieve 10^5 cycles.

---

only" control; a vapor phase containing significant oxygen would reduce NbC and replace it with an oxide phase. A sliding O-ring seal was used by the MIT group to accommodate the thermal expansion and contraction associated with the temperature cycling, each temperature cycle apparently introducing additional oxygen. The observed difference in the kind of surface contamination between cycled and isothermal annealing invalidates the contention made by the MIT group that impurity diffusion from the surface cannot be important because the isothermal annealed showed no serious ductility loss.

The surface phases were removed from the samples so that interstitial impurity contents could be determined in the bulk material. The oxygen contents in the cycled samples increase with increasing number of cycles; decreased room-temperature ductility is expected with increasing contamination. Even if only the surface of the sample is contaminated sufficiently for cleavage to be nucleated at the surface, a crack, once nucleated, could propagate through otherwise ductile metal. The oxygen analyses of samples that have the surface phase removed are included in Table XIII-X; the oxygen content of the bulk metal is as catastrophically high as that found for the samples which included the surface layer. Clearly, all specimens tested by the MIT group were grossly contaminated, the sliding O-ring seal probably being a major source of oxygen impurity.

The loss of ductility observed by Pant and Lidsky cannot be assumed to result from thermal cycling, as the oxygen contamination is sufficient in itself[40] to cause the observed ductility loss. The presence of thick surface phases, NbC in one case and NbO_2 in other cases, indicates that the MIT group observed an atmosphere effect and not redistribution of impurities to grain boundaries (as suggested by them). The surface phase formed was, in fact, so thick that x-ray diffraction patterns showed very little diffraction pattern of base niobium metal. It would be unwise to accept the conclusion proposed by the MIT group that the ductility loss is a result of cyclic temperature effects. The additional results all indicate that impurity diffusion from the surface caused the ductility loss.

2. *LAMPF*. Simpler creep-testing methods have been devised for neutron irradiations at LAMPF. All stringer and experiment insertion and retractions will be made during scheduled beam-off periods of at least one day. Problems and costs associated with remote handling are thereby greatly reduced. The stringers will be disposable if they become too radioactive. New experiments will be mounted on a stringer, bench-top tested and the entire unit placed in the stringer housing. Remote position detectors and adjustment for remote connection will not be required.

Short-stepped stringers were made for reasons

of improved shielding. The new stringer is only half as long as the first version. Alignment of the stringer housing on opposite sides of the remote disconnect pit is easily achieved with the shortened stringer. Umbilical lines will connect utility lines to the stringer back end with simple plug-in connectors. No tooling holes are required in the decking, and a transfer cart will not be used. Radioactive experiments will be removed directly into a cask at the end of the north stringer housing. The experimental fatigue tester will be sheared off the stringer at this location.

Recent calculations show that a lead neutron reflector will yield higher neutron flux than a nickel reflector. A lead reflector has been designed and was installed in the radiation damage cavity.

Figure XIII-29 shows the neutron spectrum computed for the so-called $90°$ location where the flux intensity is greatest, compared to the $135°$ location. The flux intensity at $90°$ will be 1.3×10^{14} n cm^{-2} s^{-1} per 1 mA (1 mA will be full-beam intensity). The $90°$ results are new results.

The LAMPF neutron irradiation facility at the beam stop is now ready for high-current operation. This is scheduled for the current run cycle. The facility has a useful irradiation volume of a few liters. The next major objectives of the LAMPF effort will be more extensive irradiations of materials at ambient temperature and the full development of high-temperature irradiation and mechanical testing capability. The i_ _ tion of materials at ambient temperature with _ pro riate physical properties evaluation will be _ _ ied out with ERDA-DPR support. A decision whethe_ _ not to develop high-temperature capability wil _ made after LAMPF beam current expectations are e_ lished and after an evaluation of methods on mea _ ent of irradiation enhanced creep in materi_ _ s completed.

3. *Radiation Damage Analysis*. Spectrum-averaged parameter cross sections using four parameter functions were calculated for Al, Cu, and Nb. In addition to the damage-energy function e(T), the following parameter functions were used:

(a) Total recoil energy
$$t(T) = T, \qquad (4)$$

(b) radiation-hardening parameter
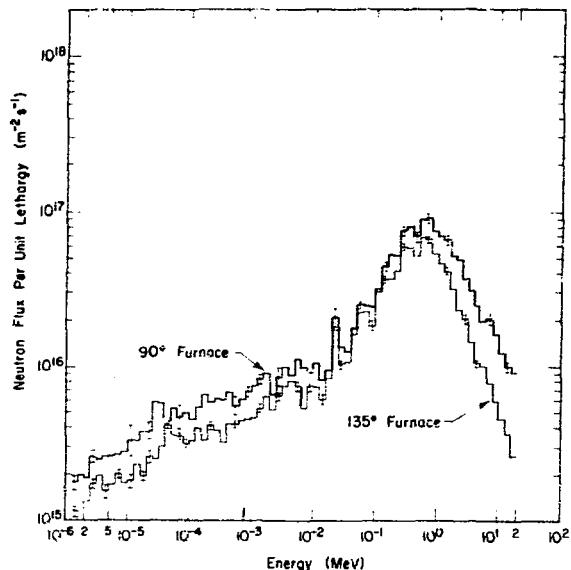
$$h(T) = \begin{cases} 0 & T \leq T_\ell \\ T - T_\ell & T_\ell \leq T \end{cases}, \qquad (5)$$

(c) Robinson-Torrens model 3 (Ref. 41)
$$r(T) = e(T)/(58 + 1.22 \times 10^{-3} e(T)). \qquad (6)$$

Equation (5) for h(T) is based on the computer calculations of Beeler,[42] and on the damage function results of Odette and Ziebold[43] for changes in yield stress in Fe. The function h(T) represents the relative probability of producing a defect cluster of sufficient size during the displacement cascade to act as an obstacle to dislocation motion. It has been found by Mitchell et al.[44] to compare favorably with the measured relative hardening rate for reactor neutrons and 14-MeV neutrons incident on Cu.

The Robinson and Torrens model-3 formula, r(T), (Eq. (6)), is derived from the results of computer simulation of displacement cascades in Cu. Their expression indicates that the number of Frenkel pairs produced is not directly proportional to damage energy. The calculations upon which r(T) is based covered a damage-energy range up to 10 keV whereas in the calculations of Parkin and Green[45] and the present calculations, r(T) has been extended to damage energies in the MeV range. Although this

may be a foolhardy extrapolation into an untested recoil-energy region, for the present interests r(T) has been used since it provides a parameter function similar to damage energy for low-recoil energy and extrapolates to values less than the damage energy at high-recoil energies.

We can compare t(T), h(T), and r(T) using the damage-energy-parameter function as a reference. t(T) and r(T) are similar to damage energy at low-recoil energy whereas at high-recoil energy they diverge, t(T) becoming greater than and r(T) less than the damage energy. h(T) is less than the damage energy at low-recoil energy and greater than the damage energy at high-recoil energy.

For nine neutron spectra the spectrum-averaged parameter cross sections for the four parameter functions normalized to their respective values in the EBRII-7 spectra are given in Table XIII-XI. The first five spectra are fission-type spectra whereas the last four have significant high-energy-neutron components.

One general observation based upon the data in Table XIII-XI is that in the four reactor spectra, the results are essentially independent of the parameter function used, and further that the relative cross sections are similar for all three materials. These similarities point out a difficulty in using only reactor irradiations to study material and spectral-dependent radiation damage.

Results for the remaining five spectra on the other hand are sensitive not only to the choice of parameter function, but to material as well. The sensitivity to parameter function increases as the high-energy component in the neutron spectrum increases, the maximum variations occurring at "14 MeV."

The largest variations as a function of material are seen in the two damage-energy-dependent models, e(T) and r(T), whereas the recoil-energy models t(T) and h(T) give more similar results. This difference is due to the inclusion of electronic losses in the damage-energy function. The most striking example of this effect is found in Al. Using r(T) we find almost no spectral dependence in the damage.

For a given material the largest difference (2-10) occurs between h(T) and r(T) or e(T). The last two represent simple Frenkel-pair production,

while h(T) is used here to represent radiation hardening. Both e(T) and h(T) have been used in comparative analyses of irradiation experiments performed in reactor-neutron spectra and in a 14-MeV neutron flux.

H. FEASIBILITY AND SYSTEMS STUDIES OF APPLICATIONS OF LASER FUSION

1. Introduction. Feasibility and systems studies are being done to assess the technical feasibility and the economic incentives of various commercial applications of laser fusion. Emphasis is placed on systems studies of the direct production of electricity in central-station generating stations. The general objectives of these studies are: the conceptualization and preliminary engineering analyses of laser-fusion reactor and generating-station concepts, the development of parametric computer models of generating-station subsystems for economic and technology trade-off and comparison studies, and the identification of problems requiring long-term development efforts. Studies of such potential commercial applications of laser fusion as the production of fuel for fission reactors and providing high-temperature process heat are also included.

2. Power Plant Engineering Analyses.

a. Magnetically Protected Laser Fusion Reactor Concept. Several laser-fusion reactor concepts are being considered for possible use in central-station generating stations. The two concepts currently being evaluated at LASL, the wetted-wall and the magnetically protected designs, were described previously.[46]

Studies of the magnetically protected laser-fusion reactor concept are continuing. The cavity is cylindrical with laser-initiated pellet microexplosions occurring at the geometric center. Erosion of the cylindrical walls and damage to the mirrors that focus the laser beams into the reactor cavity from energetic ionized particles produced by pellet microexplosions are avoided by diverting these particles with magnetic fields to energy sink regions in the ends of the cavity.

A computer program is being developed for numerical simulation of the time-dependent dynamics of collisionless finite-β plasmas interacting with applied and self-generated magnetic fields. The

TABLE XIII-XI
NORMALIZED PARAMETER CROSS SECTIONS

	Damage Energy	Recoil Energy	Radiation Hardening	Modified Damage Energy
Nb (1164)				
HFIR	0.8	0.8	1.0	0.6
LPTRE-1	1.0	1.0	1.1	0.9
EBRII-7	1.0	1.0	1.0	1.0
EBRII-2	1.4	1.5	1.6	1.3
U235	2.6	2.7	3.6	2.1
M-LAMPF	2.0	2.3	3.0	1.3
BENCH	3.4	3.9	5.3	1.8
30 MeV	8.6	10.3	15.1	3.5
"14 MeV"	9.7	11.5	16.9	3.7
CU (1087)				
HFIR	0.8	0.8	0.9	0.6
LPTRE-1	1.0	1.0	1.1	0.8
EBRII-7	1.0	1.0	1.0	1.0
EBRII-2	1.4	1.4	1.6	1.3
U235	2.6	2.8	3.4	1.9
M-LAMPF	1.8	2.2	2.7	1.2
BENCH	3.1	3.80	4.7	1.6
30 MeV	8.0	10.5	13.8	3.1
"14 MeV"	8.4	11.2	14.5	3.0
Al (1193)				
HFIR	0.6	0.7	0.8	0.5
LPTRE-1	0.9	1.0	1.0	0.8
EBRII-7	1.0	1.0	1.0	1.0
EBRII-2	1.3	1.4	1.5	1.2
U235	1.9	2.5	2.8	1.5
M-LAMPF	1.2	2.0	2.2	1.0
BENCH	1.7	3.5	3.9	1.1
30 MeV	3.2	8.9	10.2	1.4
"14 MeV"	3.4	10.5	12.0	1.5

model, based on particle-in-cell techniques, is two-dimensional with radial and axial variables. Initial calculations have been made with this program for a subregion of the reactor cavity. Ionized particles from a 100-MJ pellet microexplosion, represented by 50 000 simulation particles, and an applied magnetic field of 0.2 T were used in the calculation. It was found that the high-energy alpha particles expand initially, interact with the magnetic field, and are captured in gyro-orbits.

The denser and lower energy debris, consisting of deuterons, tritons, and low-energy alpha particles, expand in a football shaped shell, excluding the magnetic field. This expansion proceeds smoothly until pressure balance occurs between the magnetic field and the expanding plasma and is followed by a partial collapse of the plasma until collective plasma pressure increases enough to cause a subsequent expansion.

These calculations have confirmed analytic

predictions of the behavior of expanding fusion-pellet microexplosions in magnetic fields. The computer program is now being expanded to include the energy sink regions and to provide detailed temporal histories of incident particle fluxes on reactor cavity structures.

b. *Stress Analyses for Spherical Reactor Concepts.* Neutron energy deposition occurs for the most part in liquid-lithium blanket regions for reactor concepts now being considered and results in heating and expansion of the lithium. Because energy deposition in the lithium has a radial gradient, pressure waves result that travel between structural components. If evaporation of a protective layer from the interior surface of the cavity wall occurs (e.g., the wetted-wall concept), an impulse will be transmitted to the cavity structure from the recoil momentum. Secondary gamma-ray energy is deposited primarily in high-density structural components. Thermal gradients in structural regions due to energy deposition and the effects of coolant flow result in thermal stresses. Because of the pulsed operation of laser-fusion reactors, the most likely failure mode for cavity and blanket structures is fatigue failure.

Studies of structural responses and of the associated stresses generated have been made for a spherical reactor based on the wetted-wall concept. The cavity radius was assumed to be 2 m and the fusion pellet yield to be 100 MJ. The blanket region includes three structural shells enclosing two lithium regions. The total lithium thickness is 0.9 m and is divided by a middle structural shell into 0.7- and 0.2-m-thick regions. The structural materials considered were niobium, molybdenum, and stainless steel. Neutron and gamma-ray transport calculations were performed to determine the temporal and spatial dependence of energy deposition in the blanket. The results of these calculations were used to calculate pressure profiles in the liquid-lithium regions due to thermal expansion. As a worst case, the impulse that could be delivered to the cavity wall by ablated material was maximized with respect to the mass and temperature of this material.

The responses of structural shells were determined with finite-difference, wave-propagation computer programs. It was determined that shell thick-

nesses of 0.03, 0.03, and 0.02 m, respectively, for the inner, middle, and outer shells are approximately optimum for providing adequate structural strength with minimum total metal inventory, essentially independent of the structural material used. The results of typical calculations of hoop stresses in the inner wall as functions of time after the pellet microexplosion are shown in Fig. XIII-30. Damped ringing hoop stresses for a niobium inner structural shell with damping factors of 1, 2, and 4 are shown in Fig. XIII-31. A damping factor of 4° is believed appropriate; however, if the damping factor is as low as 1°, the stresses will be damped in ~ 0.1 s.

c. *Radioactive Waste Output from Laser-Fusion Generating Stations.* A preliminary assessment of radioactive waste output from laser-fusion generating stations during normal operations was made. Tritium is the only radioactive product of concern as a potential hazard to the public. Large tritium inventories will be necessary for plant operation; however, leakage rates can be reduced to acceptable or even to essentially zero levels by appropriate engineering designs.

Structural materials and impurities in the lithium coolant will become activated in the intense neutron flux in a laser-fusion reactor. These activated materials will be an operational problem not a radioactive effluent problem. Radiation protection is tractable because these materials are solid and immobile, and the radiation can be attenuated by appropriate shielding.

Tritium readily diffuses through most structural materials at elevated temperatures. In a laser-fusion generating station that uses lithium as a single-loop reactor coolant, the main tritium leakage paths are through reactor blanket enclosures, primary heat-transfer loop piping walls, and the steam generators. Permissible tritium leakage rates depend on the ultimate disposition of the tritium (e.g., whether in air or cooling water) and on characteristics of the plant site such as prevailing wind directions and velocities, population densities, etc. The very conservative goal of limiting total tritium leakage to 2 Ci per day appears to be attainable for laser-fusion generating stations without significant increases in power production costs and was adopted for this study.

The wetted-wall laser-fusion-reactor concept
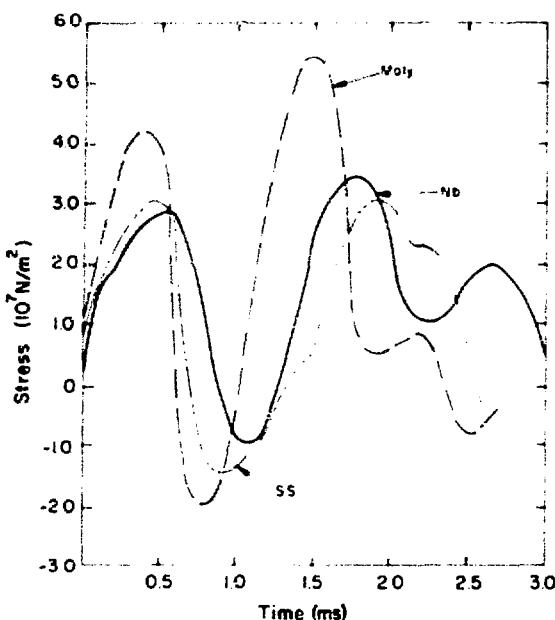
Fig. XIII-30.

Ringing hoop stresses in inner structural wall of wetted-wall reactor concept.

Fig. XIII-31

Damping of ringing hoop stresses in inner structural wall of wetted-wall reactor.

is more completely defined with respect to struc-
tural material masses and dimensions than others at
this time, and the evaluations included in this
study were for generating stations based on this
concept. Typical 1000-MWe laser-fusion generating
stations include from 20 (high-temperature, refrac-
tory metal structure) to 26 (low-temperature, stain-
less steel structure) reactors and have net effi-
ciencies in the range 28 to 36%.

Parameter studies were made of the effects on
the cost of producing electric power of various
engineering options for controlling tritium leakage.
The dependent parameter in these studies was the
cost of separating tritium from lithium to concen-
trations that are low enough to meet the tritium
discharge goal. The possibility of using semiper-
meable-membrane technology for tritium separation
from lithium is being assessed and computer models
of such separation systems were included in the
analyses.

The heat exchange loop that was modeled for
inclusion in the systems analysis program for these
studies is shown schematically in Fig. XIII-32. The
regenerative heat exchanger was incorporated as an

option to permit higher temperatures in the tritium
separator and thus reduce the required separator
membrane area. Variations in plant design included
a range in turbine inlet temperature from 600 to
1100 K. The appropriate energy conversion system,
selected from models described in Section XIV.H.3
was used for each part of the turbine inlet tempera-
ture range.

Niobium and vanadium were evaluated for use as
permeable membranes in lithium-tritium separators.
Several materials were considered for fabricating
the steam generators, including molybdenum and
tungsten-clad stainless steel. Niobium, molybdenum,
and stainless steel were evaluated for use as hot
piping both as bare pipes and as pipes inside plena
with cold aluminum walls.

Selected preliminary results are given in
Table XIII-XII for 1000-MWe generating stations.
The total tritium leakage, i.e., through the steam
generators and directly to the atmosphere through
the reactor blanket enclosures and the hot piping,
was limited to 2 Ci per day. Several combinations
of materials of fabrication for the hot piping, the
tritium-lithium separator membrane, and the steam
generator are included. The ranges of reactor out-
let and turbine inlet temperatures are such that
the value of a regenerator is illustrated and com-
parisons between low-temperature steam and high-
temperature potassium-steam binary conversion cycles
can be made.

The results of this study indicate that

TABLE XIII-XII

LITHIUM HEAT EXCHANGER AND TRITIUM SEPARATION LOOP CHARACTERISTICS FOR 1000-MWe LFR GENERATING STATIONS[a]

Structural Materials			Temperatures		Tritium Concentration in Hot Lithium (ppm)	Regenerative Heat Exchanger	Relative Cost of Generating Power
Hot Piping	Separator Membrane	Steam Generator	$T_r(K)$[c]	$T_t(K)$[d]			
SS,Al[b]	V	Mo	773	723	63	No	1.0
Mo	V	Mo	773	723	108	No	0.98
Mo	Nb	Mo	773	723	108	No	0.98
Nb,Al	V	Mo	875	723	4.6	Yes	1.30
Mo	V	Mo	875	723	36	Yes	1.22
Mo	V	SS,W[e]	875	723	45	Yes	1.28
Mo	V	Mo	900	839	20	Yes	1.05
Mo	V	Mo	1150	1100	0.70	No	0.95

a - Total tritium leakage limited to 2 Ci per day.
b - Stainless steel piping in aluminum plenum.
c - Lithium temperature at reactor outlet.
d - Turbine inlet temperature.
e - Tungsten-clad stainless steel.

molybdenum is the preferred material for hot piping and steam generators. The case resulting in minimum power cost utilizes the potassium-steam binary conversion cycle with a turbine inlet temperature of 1100 K and does not include a regenerator. Separation of tritium from lithium using semipermeable membrane techniques has not been demonstrated on a large scale for the conditions assumed, and achievable lower limits of tritium concentration in practical systems are not known. Thus, those cases for which allowable tritium concentrations are in the few ppm range are viewed with some skepticism at this time.

3. Systems Studies

a. *Energy Conversion Cycles*. Computer models have been developed for a potassium Rankine topping cycle, a high-temperature steam cycle, and a low-temperature steam cycle. Maximum turbine inlet temperatures for these cycles are 1100, 835, and 723 K, respectively. The potassium Rankine topping cycle is used with the high-temperature steam cycle to form a binary cycle. The high-temperature cycles require that refractory metals be used for reactor and heat-transfer loops, whereas stainless steel structures can be used in conjunction with the low-temperature steam cycle.

Plots of the percent change in power costs from nominal 1000-MWe generating stations are shown as functions of maximum turbine inlet temperatures in Fig. XIII-33. The increases in power cost corresponding to the transition temperature from low-temperature to high-temperature steam cycles is due to the increase in capital cost of refractory-metal structures compared to stainless steel structures. The systems analysis computer program specifies a generating station of minimum size that has a net power output at least as large as a specified value, 1000 MWe in this case. The discontinuity in power cost for the magnetically protected reactor concept and the binary conversion cycle is due to a change in total power output resulting from an increase in net efficiency and a decrease in the number of reactors required to produce at least 1000 MWe.

b. *Cooling Tower Options*. Computer simulation models of three types of cooling towers have been incorporated as options in the systems analysis computer program. The three types of cooling towers are: wet mechanical draft, wet natural
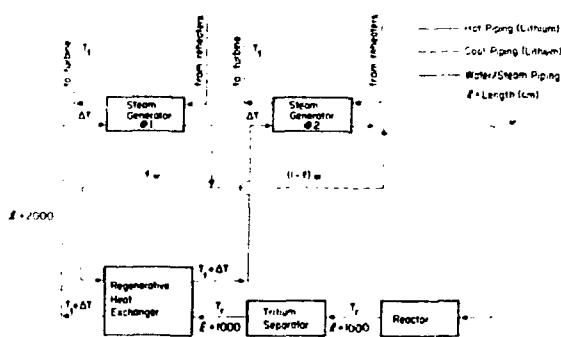
Fig. XIII-32.

Heat exchange loop for laser-fusion generating station.

Fig. XIII-33.

Percent changes in net power costs for laser-fusion generating stations based, respectively, on the wetted-wall and the magnetically protected reactor concepts as functions of turbine inlet temperature.

draft, and dry mechanical draft. Included in operating costs are water costs, as well as fan and pumping power costs.

Relative power costs for 1000-MWe LFR generating stations are given in Table XIII-XIII for various cooling tower options. The wet mechanical draft cooling tower is economically attractive compared to the other two. The use of dry mechanical draft cooling towers results in a significant increase in the cost of generating power compared to other options; however, the growing scarcity of water, particularly in the arid west, may result in a change in these relative economics in the future.

   c. *Electric Generating Station Concept.*
The specification of components for a generating station concept based on the magnetically protected reactor design and CO_2 laser technology was completed. Four reactors with a thermal power output of ~ 1250 MW each are included in the station. The net electrical output is ~ 1165 MW with a low-temperature (723 K turbine inlet temperature) conventional steam conversion cycle and ~ 1500 MW with a high-temperature (839 K turbine inlet temperature) steam cycle. Both the laser power amplifiers and the pulse forming networks, including capacitive energy storage, for the lasers are centralized and 100% redundancy of laser power amplifiers is included. A rotating mirror is provided to direct laser beams to successive reactor cavities. Single-loop heat-transfer systems are used between the reactors and the steam generators and semipermeable-membrane lithium-tritium separators are included in the lithium loops.

Plan and elevation drawings of the generating station are shown in Figs. XIII-34, XIII-35, and XIII-36. The reactors, heat exchangers, lithium-tritium separators, control room, and energy conversion equipment are located on the first level of the station. Separate heat-exchanger and lithium-tritium separator systems are provided for each reactor.

The pulse-forming networks are located on the second level and the main laser power amplifiers on the third level. There are sixteen laser power amplifiers, eight of which would be operated at one time to provide eight laser beams for quasi-symmetric illumination of fusion pellets. Selector mirrors are used to direct the laser beams from operating laser power amplifiers to the rotating mirror, also located on the third level. The required rotational velocity of the mirror is ten revolutions per second. For the design laser-beam length, the laser-beam focal spot travels only ~ 1 x 10⁻⁴ mm during a 1.0-ns pulse; thus, the focused beam will not move significantly off a millimeter-size target during the arrival time of a laser pulse. A laser-power-amplifier and pulse-forming-network maintenance area is located on the third level which is

177

TABLE XIII-XIII

EFFECTS OF THE USE OF COOLING TOWERS ON POWER
PRODUCTION COSTS FROM 1000-MWe LASER-FUSION-REACTOR
GENERATING STATIONS

Cooling Tower Type	Total Circulating Power Fraction	Turbine Exhaust Temperature (K)	Relative Power Cost
None	0.26	306	1.0
Wet Mechanical Draft	0.28	319	1.04
Wet Natural Draft	0.28	232	1.10
Dry Mechanical Draft	0.32	330	1.20

serviced from ground level by a freight elevator.

The front-end system, i.e., the oscillator and preamplifiers, is located on the top level. Differences in beam path length from the laser power amplifiers to the reactor cavity centers are compensated by corresponding differences in path lengths in the front-end system so that amplified laser pulses arrive at the cavity centers simultaneously.

All levels are serviced by a personnel and small component elevator. Shielding of the reactor enclosures and hot-cell maintenance areas is provided by thick concrete walls. Each reactor can be isolated from the system for service without affecting the operation of the remainder.

Comparisons were made between the arrangement of laser system components used in this station and an arrangement whereby each reactor is provided with a complete laser-power-amplifier system but the pulse forming networks for the lasers are centralized. The costs of power were estimated to be about 10% less for the case with totally centralized laser system components than for the case with partially centralized laser systems.

4. Alternative Commercial Applications of Laser-Fusion Reactors.

a. *Laser-Fusion Hybrid Reactor Studies.* The initial objective of the hybrid reactor studies is to define reactor designs for the production of ^{233}U from neutron irradiation of ^{232}Th. Reactor blanket designs for this concept consist of spherical shells with the following material compositions: (1) a liquid-lithium-cooled region of stainless-steel-clad rods of $^{238}UO_2$ and $^{239}PuO_2$ adjacent to the reactor cavity and (2) a region of stainless-steel-clad ThC rods, also cooled by liquid lithium.

The mixed oxide region contains the equilibrium concentration of $^{239}PuO_2$. The plutonium is continuously recycled in the fuel fabrication and processing cycles and serves only to amplify the neutron population and to produce thermal power.

Leakage neutrons from the oxide region are captured in the ThC region for breeding ^{233}U. The ^{233}U concentration will increase in this region until it either reaches an equilibrium value or the blanket is processed. It is anticipated that economic considerations will require that the ^{233}U breeding region be reprocessed after the ^{233}U concentration has reached a few percent, much lower than the equilibrium concentration. Tritium breeding occurs in both regions of the reactor blanket.

The overall reactor design is based on the wetted-wall reactor concept with outward radial flow of the coolant from the cavity wall. Essentially all of the fusion power is deposited in the mixed oxide region and essentially all of the fission power is produced in this region, especially immediately after reprocessing of the ^{233}U breeding region. Thus, most of the increase in coolant temperature will occur in the mixed oxide region and it will require careful design and analysis to ensure that performance goals are met. The following constraints and values of design parameters were adopted for the mixed oxide region:

● The fuel rods are contained in 37-rod bundles in stainless steel cans with hexagonal cross sections.
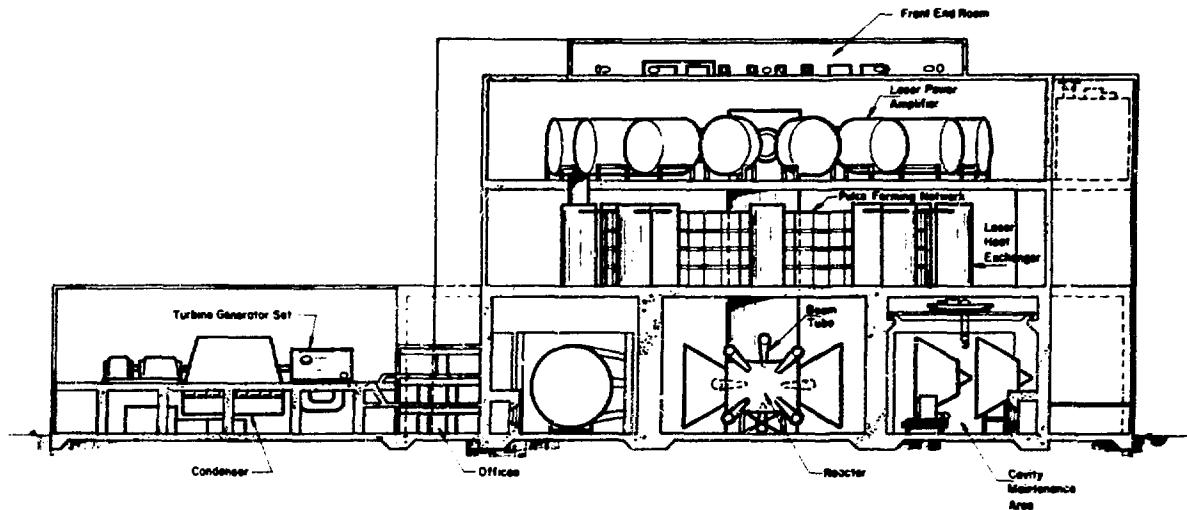
Fig. XIII-34.

Electric generating station based on magnetically protected laser fusion reactors and CO_2 laser technology, cross-section elevations as indicated in Figs. XIII-6 and 7.

- The fuel rods are constant-diameter cylinders that diverge in radial directions from the cavity wall.
- The minimum pitch-to-diameter ratio of the clad fuel rods is 1.05.
- Transient center-line fuel temperatures are constrained to less than 2700 K, and the thermal stresses in the fuel shall not exceed the cladding fatigue stress limit.
- The stainless steel cladding thickness is 0.38 mm for fuel rods 13 mm in diameter or less.
- The lithium coolant temperature is 673 K at the inlet and 973 K at the outlet.

In addition, the neutron multiplication factor of the systems was constrained to less than 0.95 with or without coolant present.

The reactor cavity diameter is 4 m and the radial thicknesses of the mixed oxide and ^{233}U breeding regions are 0.30 and 0.40 m, respectively. These regions are separated by appropriate structural walls and the reactor is enclosed by a lithium plenum 0.10 m thick. The mixed oxide region is 57.0% fuel, 16.3% stainless steel and 26.7% lithium. The ^{233}U breeding region is 60.0% ThC, 11.2% stainless steel and 28.8% lithium.

The performance of the system immediately after processing of the ^{233}U breeding region is given in Table XIII-XII. For the assumed fusion-pellet micro-

explosion repetition rate and yield, this reactor and associated auxiliary equipment would produce ~ 700 MW of electric power and would have a ^{233}U production rate of ~ 1.4 kg per day. The ^{233}U production rate would decrease and the power level would increase as the concentration of ^{233}U increases in the ThC region. Additional studies of this concept will include studies of end-of-cycle conditions.

b. *Unique Applications of Laser-Fusion Energy.* Although the primary, long-range goal of the laser-fusion program is the production of economically competitive electric power, there are other, perhaps even more important, potential applications of laser-fusion energy. Among the several classes of specialized application of laser fusion energy are radiolysis (e.g., the production of synthetic fuel) and industrial applications such as providing high-temperature process heat.

The unique energy forms characteristic of laser-fusion reactors using the DT-fuel cycle are x rays, hot ionized plasmas, and high-energy neutrons. It is conceptually possible to utilize all of these energy forms in special applications; however, the most straightforward engineering designs are based on the utilization of the neutron and gamma-ray energy, and initial investigations have been restricted to such
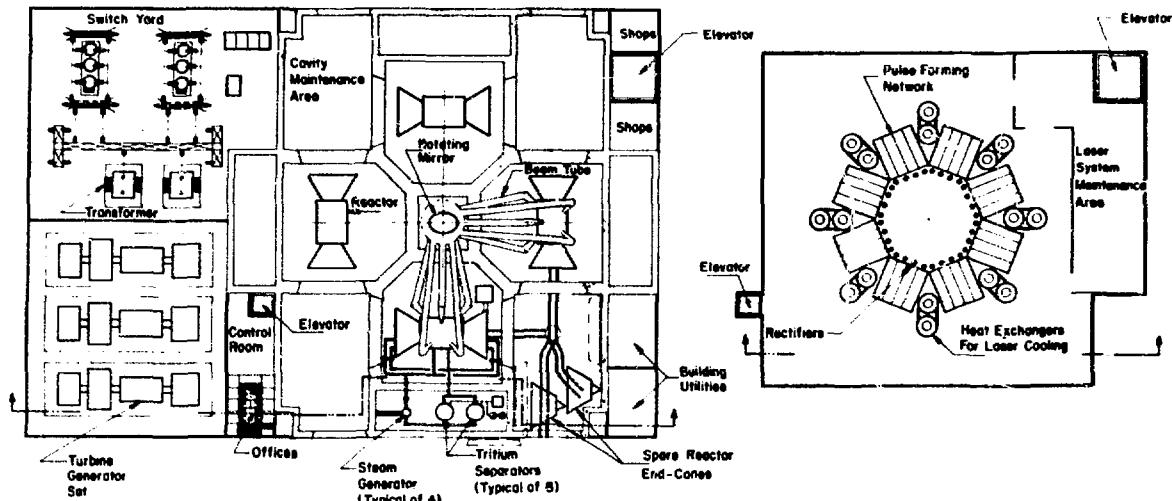
Fig. XIII-35.

Electric generating station based on magnetically protected laser-fusion reactors. (a) First level, reactor and energy conversion systems area, plan view. (b) Second level, power supply room, plan view.

concepts. Approximately 80% of the total energy produced in typical laser-fusion reactor designs is available for use free of cavity restraints. This is a unique characteristic of fusion reactors.

There has been considerable interest in the potential of fusion reactors for producing synthetic fuel by radiolytic decomposition of H_2O or CO_2. A preliminary examination of such energy conversion processes indicates that the efficiency of conversion via radiolysis is not high enough to compete economically in dedicated reactors. In fact, the cost of producing 14-MeV neutrons ($ per unit energy) is comparable to the cost of producing synthetic fuels ($ per unit energy content) by alternate routes (e.g., coal gasification), based on current economics. Thus, it appears that the production of synthetic fuel by radiolysis from laser-fusion reactors can at best only be economic as a topping cycle in a multi-purpose reactor unless radical changes in relative economics should occur.

A more attractive near-term special application of laser-fusion energy is to produce high-temperature process heat. For such a concept, the blanket region is replaced by a refractory material in which neutron and gamma-ray energy is deposited, and energy transfer from this region to an adjacent region of process fluid or chemical reactants is

accomplished by radiation. A significant advantage of laser-fusion reactors for process heat applications, compared to fission reactors, is the absence of high-temperature limitations due to fuel element distortion or melting and fission product release.

The feasibility of conceptual radiation sources that include carbon and a material with a high-absorption cross section for thermal neutrons as the principal energy deposition materials is being investigated. Initial calculations have been done for systems with two regions in the blanket, a pure carbon region next to the reactor cavity followed by a region of 90 vol% carbon and 10 vol% boron carbide. Boron carbide was selected because of its high melting temperature, its large thermal neutron absorption cross section, and because thermal-neutron capture in boron is exoergic with 2.5 MeV deposited locally by charged particles.

Temperature distributions have been calculated in the carbon and boron carbide for several cases of blanket thickness, type of carbon, and radiative power level. Maximum blanket temperatures were limited to 4000 K which is approximately the sublimation temperature of carbon.

Several interesting designs have been identified with radiation surface temperatures in excess
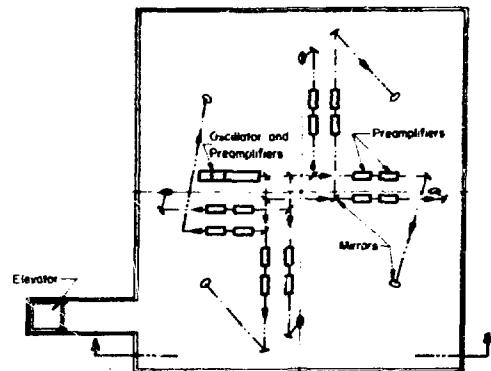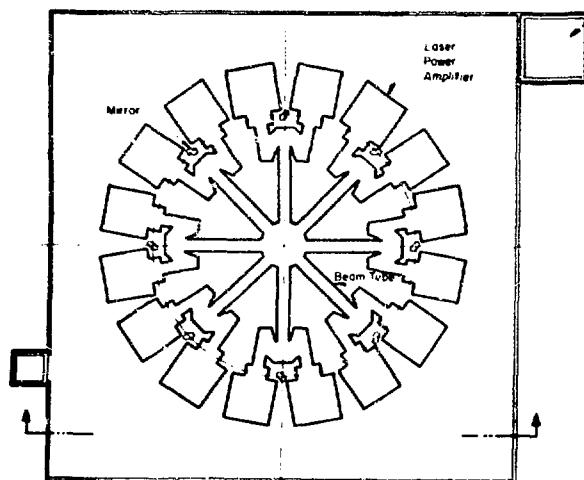
Fig. XIII-36.

Electric generating station based on magnetically protected laser-fusion reactors. (a) Third level, laser power amplifier room, plan view. (b) Fourth level, front-end room, plan view.

of 2000 K and radiation power levels in the range of 50 to 100 MW.

REFERENCES

1. R. A. Krakowski, F. L. Ribe, T. A. Coultas, A. J. Hatch, "An Engineering Design for a Reference Theta-Pinch Reactor (RTPR)," Los Alamos Scientific Laboratory report LA-5336/ANL-8019, March 1974.

2. B. Lehnert, Nucl. Fusion 8, 173 (1968).

3. S. G. Alikhanov, et. al., Nucl. Fusion 10, 13 (1970).

4. G. K. Verboom, J. Rem. Nucl. Fusion 13, 69 (1973).

5. T. A. Oliphant, Nucl. Fusion 13, 521 (1973).

6. T. A. Oliphant, J. Nucl. Mater. 53, 62 (1974).

7. T. A. Oliphant, Proceedings of the First Topical Meeting on the Technology of Controlled Nuclear Fusion, April 16-18, 1974, p. 667.

8. F. R. Chang and D. J. Rose, private communication.

9. T. A. Oliphant, G. E. Gryczkowski, T. Kammash, "Transient Change Exchange in a Neutral Gas Layer," to be published in Nucl. Fusion (1976).

10. F. W. Clinard, Jr., J. M. Bunch, J. C. Hoffman, G. F. Hurley, R. A. Krakowski, J. M. Dickenson, "Electrical Insulators for the First Wall of an Implosion-Heated Theta-Pinch Fusion Reactor," submitted to the High-Beta Pulsed Reactor Workshop, Leningrad, USSR (September 23-26, 1975).

11. R. G. Lawton, "The AYER Heat Conductor Computer Program," Los Alamos Scientific Laboratory report LA-5613-MS, May 1974.

12. R. G. Lawton, "PLACID: A General Finite-Element Computer Program for Stress Analysis of Plane and Axisymmetric Solids," Los Alamos Scientific Laboratory report LA-5621-MS, May 1974.

13. D. P. H. Hasselman, E. P. Chan, C. L. Ammann, J. E. Doherty, C. G. Nessler, "Failure Prediction of Thermal Fatigue of Silicon Nitride," J. Amer. Ceram. Soc. 58, (11), 513 (1975).

14. R. C. Bradt, D. P. H. Hasselman, F. F. Lange (eds.), Fracture Mechanics of Ceramics, Plenum Press, N. Y., (1974).

15. R. Badaliance, D. A. Krohn, D. P. H. Hasselman, "Effects of Slow Crack Growth on the Thermal-Stress Resistance of an $Na_2O - CaO - SiO_2$ Glass," J. Am. Ceram. Soc., 57, (10), 432, (1974).

16. W. H. Dukes, "Brittle Materials: A Design Challenge," Mech. Eng., p. 42, November 1975.

17. R. R. Bartsch, private communication, LASL (1975).

18. K. I. Thomassen, (ed.), "Fast Discharge Homopolar Machines for Fusion Devices," 6th Monthly Progress Report, EPRI project number RP-469-2, (Oct. 23, 1975 - Jan. 15, 1976).

19. H. F. Vogel, M. Brennan, B. Dase, K. Tolk, W. Weldon, "Energy Storage and Transfer with Homopolar Machine for a Linear Theta-Pinch Hybrid Reactor," US ERDA Rept. to be published (1976).

181

20. R. J. Bartholemew, R. A. Krakowski, R. L. Hagenson, "Structural Endurance Constraints for High-Field Theta-Pinch Coils," Trans. Amer. Nucl. Soc., 22, 20 (1975).

21. K. I. Thomassen, R. A. Krakowski, T. A. Oliphant, G. E. Bosler, and D. J. Dudziak, "Prospects for Converting ^{232}Th-^{233}U in a Linear Theta-Pinch," Trans. Am. Nucl. Soc., 19, 6 (1974).

22. R. A. Krakowski, D. J. Dudziak, T. A. Oliphant, and K. I. Thomassen, "An Engineering Design of a Linear Theta-Pinch Hybrid Reactor (LTPHR)," Trans. Am. Nucl. Soc., 21, 61 (1975).

23. S. Timoshenko and J. M. Goodier, Theory of Elasticity, 2nd ed., Chap. 4, p. 60, and Chap. 6, p. 178 (prob. 3), McGraw-Hill Book Co., NY (1951).

24. C. M. Harris and C. E. Crede, Eds., "Shock and Vibration Handbook," Chap. 8, p. 8-3, p. 8-21, and p. 8-24, McGraw-Hill Book Co., NY (1961).

25. H. A. B. Bodin, T. E. James, A. A. Newton, "A Pulsed Fusion Reactor Based on the Toroidal Pinch," Proc. BNES Nucl. Fus. Reactor Conf., 255, Sept. (1969).

26. H. A. B. Bodin, E. P. Butt, R. Carruthers, T. E. James, A. A. Newton, G. Rostagni, "The Pulsed Reverse Field Pinch Reactor," Plasma Physics and Controlled Nuclear Fusion Research, paper CN-31/Gr, IAEA, Vienna (1975).

27. D. A. Baker, L. C. Burkhardt, J. N. Di Marco, P. R. Forman, A. Haberstich, R. B. Howell, H. J. Karr, J. A. Phillips, A. E. Schofield, "Plasma Parameters and Stability of the ZT-1 Pinch Experiment," Fifth Conference of Plasma Physics and Controlled Nuclear Fusion Research, IAEA CN-33/E3, Tokyo, Japan,11-15 November 1974.

28. R. Carruthers, "Some Considerations of the Toroidal Diffuse Pinch," International School of Fusion Reactor Technology, Sept. 8-20, 1974, Enrice (Trapani, Sicily) Italy.

29. D. A. Baker, R. C. Davidson, J. N. Di Marco, "Overview of the LASL Z-Pinch Program," presented at the High-Beta Study Group Meeting, July 28-31, 1975, Los Alamos Scientific Laboratory, Los Alamos, New Mexico.

30. L. A. Artsimonich, "Tokamak Devices," Nucl. Fusion, 12, 215 (1972).

31. W. M. Stacey, Jr., "Global Plasma Models Low Tokamak Engineering Studies," Trans. Amer. Nucl. Soc., 22, 267 (1975).

32. E. L. Simmons, D. J. Dudziak, S. A. W. Gerstl, "Reference Theta-Pinch Reactor (RTPR) Nucleonic Design Sensitivity Analysis by Perturbation Theory," Los Alamos Scientific Laboratory report LA-6272-MS, April 1976.

33. S. A. W. Gerstl, D. J. Dudziak, D. W. Muir, "Application of Sensitivity Analysis to a Quantitative Assessment of Neutron Cross Section Requirements for the TFTR - An Interim Report," Los Alamos Scientific Laboratory report LA-6118-MS (November 1975).

34. "Quarterly Report on the Space Electric Power R&D Program," Los Alamos Scientific Laboratory report LA-5113-PR, November 1972.

35. F. W. Clinard, Jr., J. M. Bunch, and W. A. Ranken, "Neutron Irradiation Damage in Al_2O_3 and Y_2O_3," presented at the International Conference on Radiation Effects and Tritium Technology for Fusion Reactors, Gatlinburg, TN., October 1975. Proceedings to be published.

36. L. W. Hobbs and A. E. Hughes, "Radiation Damage to Diatomic Insulators at High Doses," presented at the Annual Meeting of the American Ceramic Society, Washington, DC, May 1975.

37. W. H. Reichelt, W. A. Ranken, C. V. Weaver, A. W. Blackstock, A. J. Patrick, and M. C. Chaney, "Radiation-Induced Damage to Ceramics in the EBR-II Reactor," presented at the 1970 Thermionic Conversion Specialists Conference, Miami, Fla., October 1970.

38. V. A. J. van Lint, J. M. Bunch, and T. M. Flanagan, "The Effects of Ionizing Radiation on Electrical Properties of Refractory Insulators," op. cit., Ref. 35.

39. D. W. Muir and J. M. Bunch, "High-Energy Proton Simulation of 14 MeV Neutron Damage in Al_2O_3," ibid.

40. H. E. McCoy and D. A. Douglas, "Effect of Various Gaseous Contaminants on the Strength and Formability of Columbium," In Columbium Metallurgy. Edited by D. L. Douglas and F. W. Kunz, Interscience, NY, 1961, p. 93.

41. M. T. Robinson and I. M. Torrens, Phys. Rev. B9, 5008 (1974).

42. J. R. Beeler, Jr., J. Appl. Phys. 37, 3000 (1966).

43. G. R. Odette and T. O. Ziebold, Nucl. Sci. Eng. 49, 72 (1972).

44. J. B. Mitchell, R. A. Van Konynenburg, D. M. Parkin,and C. J. Echer, "DT Fusion Radiation Strengthening of Copper and Niobium," op. cit., Ref. 35.

45. Don M. Parkin and W. V. Green, "Neutron Energy Dependence of Defect Production Cross Sections in Copper and Aluminum," Bull. Am. Phys. Soc. 20, 351 (1975).

46. F. L. Ribe, (Compiler), "LASL Controlled Thermonuclear Progress, January-December 1974," Los Alamos Scientific Laboratory report LA-6044-PR, August 1975.

R. J. Bartholomew
R. A. Krakowski
R. L. Hagenson

"Structural Endurance Constraints for High-Field Theta-Pinch Coils"

Trans. Amer. Nucl. Soc., 22, 20 (1975)

D. J. Dudziak
S. A. W. Gerstl

"Shielding and Activation of a Scyllac Fusion Test Reactor (SFTR)"

Trans. Am. Nucl. Soc. 21, 29 (1975)

S. A. W. Gerstl
D. J. Dudziak
D. W. Muir

"A Quantitative Basis for Cross-Section Requirements for a Fusion Test Reactor"

Trans. Am. Nucl. Soc. 21, 68 (1975)

R. A. Krakowski
D. J. Dudziak
T. A. Oliphant
K. I. Thomassen

"An Engineering Design for a Linear Theta-Pinch Hybrid Reactor (LTPHR)"

Trans. Am. Nucl. Soc. 21, 61 (1975) (invited paper)

R. Kristal

"Pulsed HF Laser Holographic Interferometry"

Applied Optics, Vol. 14, No. 3, p. 628, March 1975

E. L. Simmons
D. J. Dudziak
S. A. W. Gerstl

"Nucleonic Design Sensitivity Analysis of the Reference Theta-Pinch Reactor (RTPR)"

Trans. Am. Nucl. Soc. 22 43 (1975)

M. L. Simmons
D. J. Dudziak

"High-Energy Neutron Spectra at the LAMPF Radiation Effects Facility"

Trans. Am. Nucl. Soc. 22, 171 (1975)

D. W. Muir
D. R. Harris
D. G. Foster, Jr.
R. W. MacFarlane
W. A. Reupke
W. B. Wilson

"Cross-Section Uncertainty Analysis"

Am. Nucl. Soc. 22, 794 (1975)

G. E. Bosler
T. G. Frank

"Energy Deposition Rates in a Laser-Fusion Reactor"

Trans. Am. Nucl. Soc. 21 (1975)

J. N. Downing
M. Eisner

"Dynamics of the Dense Plasma Focus as Determined From An Analysis of Laser Scattering Spectra"

Phys. Fluids 18, 991 (1975)

R. B. Howell
H. J. Karr

"Spectroscopic Measurements of the Plasma Temperature in the 7T-1 Toroidal Pinch"

accepted for publication in Physics of Fluids

A. N. Goland, Jr.
D. M. Parkin
R. B. Theus

"Use of Li(d,n) Neutrons for Simulation of Radiation Effects in Fusion Reactors"

IEEE Trans. Nucl. Sci. NS-22, 1776 (1975)

C. L. Snead, Jr.
D. M. Parkin

"The Effects of Neutron Irradiation on the Critical Current of Nb_3Sn at High Field"

Trans. Am. Nucl. Soc. 22, 157 (1975)

M. L. Simmons
D. J. Dudziak

"CTR Neutron Spectra Simulation at the LAMPF Radiation Effects Facility"

Nucl. Tech. (to be published)

D. M. Parkin
A. R. Sweedler

"Neutron Irradiation at Nb_3Sn and NbT Multifilamentary Composites"

IEEE Trans. Mag. MAG-11, 166 (1975)

D. M. Parkin
A. N. Goland

"Calculation of Radiation Effects as a Function of Incident Neutron Spectrum"

to be published in Radiation Effects

C. L. Snead, Jr.
D. M. Parkin

"The Effects of Neutron Irradiation on the Critical Current of Nb_3Sn at High Field"

to be published in Nuclear Technology

D. M. Parkin
L. Thompson
A. Sosin

"$I_D - I_E$ Recovery in Electron Irradiated Copper. I. Experimental"

Radiation Effects 25, 217 (1975)

D. A. Freiwald
R. A. Axford

"Approximate Spherical Blast Theory Including Source Mass"

J. Appl. Phys. V. 46, 1171-4 (1975)

A. C. Smith, Jr. C. E. Swannack H. H. Fleischmann D. A. Phelps	"Energy Losses from Strong Electron Rings Trapped in RECE-Berta"	Nuclear Fusion, 15, No. 3 June 1975
G. E. Bosler	"Implications to the CTR Community of Standardization in Nuclear Analysis Codes"	Trans. Am. Nucl. Soc. 22 (1975)
G. E. Bosler	"Energy Deposition in a Two-Dimensional LFR Model"	Trans. Am. Nucl. Soc. 22 (1975)
S. A. W. Gerstl	"Sensitivity Analysis in Shielding--An Overview"	Trans. Am. Nucl. Soc. 22, 719 (1975)(invited paper)
K. F. McKenna R. Kristal E. L. Zimmerman	"Radial Plasma Structure During a Theta-Pinch Implosion: Flute instabilities"	Phys. of Fluids, Vol. 18, No. 10 (1975)
G. Miller	"Motion of a Plasma Column in a Perturbing Magnetic Field"	Phys. Fluids, 18, No. 12 (1975) p. 1704
W. R. Ellis	"CTR Applications of the High-Density Linear Theta Pinch"	Nucl. Fusion 15, 255 (1975)
G. Miller	"Motion of a Plasma Column in a Perturbing Magnetic Field"	Phys. Fluids 18, 1704 (1975)
R. C. Davidson	"Synchrotron Radiation Spectrum for a Relativistic Plasma Column"	Phys. Fluids 18, 1143-1150 (1975)
G. Berge J. P. Freidberg	"MHD Stability of the Scyllac Configuration"	IAEA-CN-33/E 1-1, Vienna (1975)
R. A. Gerwin	"Energy Loss of a Relativistic, Finite Electron Beam in a Plasma"	Phys. Fluids 18, 614 (1975)
S. Peter Gary R. A. Gerwin D. W. Forslund	"Electromagnetic Current Instabilities"	submitted to Physics of Fluids
J. Enoch	"Pressure Profiles in a Thermonuclear Plasma Sheath Containing Energetic α-Particles"	Nuclear Fusion 15, (1975)
J. P. Goedbloed	"Spectrum of Ideal Magnetohydrodynamics of Axisymmetric Toroidal Systems"	Phys. Fluids 18, 1258 (1975)
J. P. Freidberg R. A. Gerwin	"Stability of a Closed-Line Scyllac Configuration"	Nuclear Fusion 15, 605 (1975)
D. D' Ippolito R. C. Davidson	"Hybrid-Kinetic Model for High-Beta Plasmas"	submitted to Physics of Fluids for publication 3-13-75
R. C. Davidson N. T. Gladd	"Anomalous Transport Properties Associated with the Lower-Hybrid-Drift Instability"	Phys. Fluids 18, 1327 (1975)
R. C. Davidson J. M. Ogden	"Electromagnetic Ion Cyclotron Instability Driven by Ion Energy Anisotropy in High-Beta Plasmas"	Phys. Fluids 18, 1045 (1975)
G. Berge J. P. Freidberg	"Stability of a Diffuse, High-β, ℓ = 1 System"	Phys. Fluids 18, 1362 (1975)
B. M. Marder	"Straight ℓ = 1 Equilibrium and Stability"	submitted to Physics of Fluids for publication 11-11-75
J. P. Freidberg W. Grossman	"Magnetohydrodynamic Stability of a Sharp Boundary Model of Tokamak"	Phys. Fluids 18, 1494 (1975)

N. T. Gladd	"The Lower Hybrid Drift Instability and the Modified Two Stream Instability in High Density Theta-Pinch Environments"	Plasma Physics 18, 27 (1976)
R. Y. Dagazian	"Nonlinear Coupling of Kink Modes in Tokamaks"	submitted for publication in Nucl. Fusion May 1975
J. P. Freidberg H. Weitzner	"Endloss from a Theta Pinch"	Nucl. Fusion 15, 217 (1975)
A. G. Sgro	"The Collision of a Strong Shock with a Gas Cloud: A Model for Cassiopeia A"	The Astrophysical Journal 1197, 621 (1975)
H. R. Lewis C. W. Nielson	"A Comparison of Three Two-Dimensional Electrostatic Plasma Simulation Models"	J. Comp. Physics 17 (1975)
C. W. Nielson H. R. Lewis	"Particle-Code Models in the Nonradiative Limit"	Methods in Computational Physics, Chapter 1, Vol. 16 (Academic Press, Inc.) (1975)
J. U. Brackbill	"Numerical Magnetohydrodynamics for High-Beta Plasmas"	Methods in Computational Physics (Academic Press, Inc.) (1975)
D. Winske D. W. Hewett	"Flute Instabilities in Two-Dimensional Simulations of Strongly Inhomogeneous Theta-Pinch Plasmas"	Phys. Rev. Lett 35, 937 (1975)
A. G. Sgro C. W. Nielson	"Hybrid Model Studies of Ion Dynamics and Magnetic Field Diffusion During Pinch Implosions"	submitted to Physics of Fluids for publication, 7-22-75
D. W. Hewett C. W. Nielson D. Winske	"Vlasov Confinement Equilibria in One Dimension"	submitted to Phys. of Fluids for publication, 9-15-75

D. A. Baker J. N. Di Marco	"The LASL Reversed-Field Pinch Program Plan"	Los Alamos Scientific Laboratory report LA-6177- MS, (December 1975)
D. A. Baker L. C. Burkhardt R. S. Dike J. N. Di Marco P. R. Forman A. Haberstich H. J. Karr L. W. Mann J. A. Phillips A. E. Schofield	"Design of the ZT-1 Toroidal Pinch Experiment"	Los Alamos Scientific Laboratory report LA-6173- MS (December 1975)
A. W. DeSilva	"Ion Temperature Measurement by Laser Scattering at 2.8 μ"	LA-5895-MS (1975)
W. R. Ellis	"LTPF: A Linear Theta-Pinch Neutron Source"	LA-6032-MS (1975)
F. C. Jahoda R. Kristal W. E. Quinn	"Toroidal Mode Structure in the Scyllac Full Torus"	LA-5853-MS (1975)
G. Miller	"A Two-Step Model of Scyllac Equilibrium"	LA-6204-MS (1975)
K. Sugisaki	"Origin of Axial Current in Scyllac"	LA-6178-MS (1975)
T. M. York K. F. McKenna	"Laser-Plasma Interactions in the Scylla I-C Experiment: Preliminary Analysis"	LA-5957 (1975)
G. Miller	"A Two-Step Model of Scyllac Equilibrium"	LA-6204-MS
T. E. McDonald W. C. Nunnally	"Proposal for the Construction of the Staged Scyllac Prototype"	Los Alamos Scientific Laboratory report LA-5966-P (December 1975)
G. P. Boicourt	"XPECT -- A Monte Carlo Program to Predict the Expected Time to Next Failures in CTR Systems"	Los Alamos Scientific Laboratory report LA-5980 (April 1975)
R. Gerwin	"The Vlasov-Fluid Model with Electron Pressure"	Los Alamos Scientific Laboratory Report LA-6130-MS (November 1975)
F. C. Jahoda R. Kristal W. E. Quinn	"Toroidal Mode Structure in the Scyllac Full Torus"	LA-5853-MS (February 1975)
J. D. Rogers K. D. Williamson, Jr.	"Proposed METS-FTR Coupled Superconducting Prototype System"	LA-5918-P (April 1975)
R. A. Krakowski D. J. Dudziak T. A. Oliphant K. I. Thomassen G. E. Bosler F. L. Ribe	"Prospects for Converting Th-232 to U-233 in a Linear Theta-Pinch Hybrid Reactor (LTPHR)"	USERDA Report ERDA-4 Conceptual Fusion-Fission Energy System (1975) pp. 249-320
F. W. Clinard, Jr.	"Ceramics for CTR Systems"	Presented at the conference on Critical Needs and Opportunities in Funda- mental Ceramics Research, Cambridge, Mass., January 1975. Summary published as ERDA Report No. ERDA-9.

R. A. Axford   "Integration Methods for Uncoupled and Coupled Thermo-elastic Problems"   Los Alamos Scientific Laboratory Report LA-6071 (1975)

R. A. Axford   "Direct Evaluation of Transient Surface Temperature and Heat Fluxes"   Los Alamos Scientific Laboratory Report LA-6051 (1975)

D. J. Dudziak
D. W. Muir   "Analysis of a Benchmark Calculation of Tritium Breeding in a Fusion Reactor Blanket -- The United States Contribution"   D. Steiner, editor Oak Ridge National Laboratory Report ORNL-TM-4177 (1975)

S. A. W. Gerstl
D. J. Dudziak
D. W. Muir   "Application of Sensitivity Analysis to a Quantitative Assessment of Neutron Cross-Section Requirements to the TFTR -- An Interim Report"   Los Alamos Scientific Laboratory Report LA-6118-MS (1975)

E. L. Simmons
D. J. Dudziak
S. A. W. Gerstl   "Reference Theta-Pinch Reactor (RTPR) Nucleonic Design Sensitivity by Perturbation Theory"   Los Alamos Scientific Laboratory Report (to be published)

D. R. Harris
W. A. Reupke
W. B. Wilson   "Consistency Among Differential Nuclear Data and Integral Observations -- The ALVIN Code for Data Adjustment, for Sensitivity Calculations, and for Identification of Inconsistent Data"   Los Alamos Scientific Laboratory Report LA-5957 (1975)

A. A. Husseiny
Z. A. Sabri
D. R. Harris   "Slowing-in Distribution of Fast Particles Released in Maxwellian Plasma"   Los Alamos Scientific Laboratory Report LA-5988 (1975)

C. Philis
P. G. Young   "Evaluation des Sections Efficaces des Reactions $^{93}_{41}$Nb $(n,2n)$ $^{92}_{41}$Nb du Seuil A 20 MeV"   Service de Physique Nucleaire - Centre d' Etudes de Bruyeres-le-Chatel report CEA-R-4676 (1975)

P. G. Young   "Nuclear Models and Data for Gamma-ray Production"   Conference on Nuclear Cross Sections and Technology, NBS Special Publication 425, p. 149 (1975)

J. S. Gilbert
E. A. Kern   "Analysis of Homopolar Generators and Superconducting Inductive Energy Storage Systems as Power Supplies for High Energy, Space Based Lasers"   Los Alamos Scientific Laboratory Report LA-5837-MS (1975)

J. S. Gilbert
R. E. Stapleton   "Electrical Requirements of Xenon Lasers"   Los Alamos Scientific Laboratory Report LA-5815-MS (1975)

R. E. Howell H. J. Karr P. R. Forman	"Ion Temperature Measurements on the ZT-1 Reversed-Field Pinch"
A. Haberstich D. A. Baker J. N. Di Marco L. W. Mann S. Ortolani	"Stability and Diffusion of the ZT-1 Reversed-Field Pinch"
R. K. Linford T. A. Oliphant K. I. Thomassen	"Scyllac Fusion Test Reactor Design"
R. K. Linford J. N. Downing R. F. Gribble A. R. Jacobson D. A. Platts K. S. Thomas	"Staged Theta Pinch Experiments"
I. Henins J. E. Hammel T. R. Jarboe J. Marshall A. R. Sherwood	"Implosion Measurements in a High-Voltage, Large-Diameter, Medium-Density Theta Pinch"
K. F. McKenna E. L. Zimmerman K. B. Freese	"Laser-Plasma Interaction in the Scylla I-C Theta Pinch"
K. B. Freese F. C. Jahoda R. Kristal F. T. Seibel R. E. Siemon	"Optical Diagnostics on Scyllac"
G. Miller	"A Dynamic Model of Gross Plasma Motion in Scyllac"
R. C. Davidson J. P. Freidberg	"Review of Toroidal Theta-Pinch Theory"
R. C. Davidson R. A. Gerwin N. T. Gladd	"Post-Implosion Anomalous Transport Properties Associated with the Lower Hybrid-Drift Instability"
J. P. Freidberg J. P. Goedbloed	"Equilibrium and Stability of High-Beta Diffuse Tokamaks"
D. W. Hewett D. Winske	"Numerical Simulation of the Lower Hybrid Drift Instability"
J. U. Brackbill M. T. Menzel D. C. Barnes	"Numerical Studies of the Linear Theta Pinch"
H. R. Lewis L. Turner	"Stability Analysis of Sharp-Boundary Vlasov-Fluid Screw-Pinch Equilibria"
A. G. Sgro C. W. Nielson	"Hybrid Model Studies of Magnetic Field Diffusion in High-Beta Pinches"
J. U. Brackbill D. C. Barnes	"Time-Dependent Calculations of Equilibrium and Stability Problems in Scyllac and Tokamak Geometries"

D. A. Freiwald   "Laser Fusion Sources for CTR Surface and Bulk Damage Testing"
E. A. Kern

C. E. Swannack   "Superconducting Magnetic and Intertial Energy Pulsed Power Systems"
K. D. Williamson

G. P. Boicourt   "Capacitor Requirements for Controlled Thermonuclear Experiments and Reactors"
P. S. Hoffman

E. L. Cantrell   "Scyllac Derated Feedback Sector Experiments"
W. R. Ellis
B. L. Freeman
K. B. Freese
R. F. Gribble
W. D. Gutscher
F. C. Jahoda
K. J. Johnson
R. Kristal
K. J. Kutac
J. R. McConnell
G. Miller
W. E. Quinn
R. E. Siemon

R. K. Linford   "Staged Theta Pinch Experiments"
J. N. Downing
R. F. Gribble
A. R. Jacobson
D. A. Platts
K. S. Thomas

E. L. Cantrell   "Scyllac 'Derated' Feedback Sector Experiments"
W. R. Ellis
B. L. Freeman
K. B. Freese
R. F. Gribble
W. D. Gutscher
F. C. Jahoda
K. J. Johnson
R. Kristal
K. J. Kutac
J. R. McConnell
G. Miller
W. E. Quinn
R. E. Siemon

J. P. Goedbloed   "Magnetohydrodynamic Stability of Toroidal High-Beta Systems"

D. A. Baker   "Stability and Temperature Measurements on ZT-1"
L. C. Burkhardt
J. N. Di Marco
P. R. Forman
A. Haberstich
R. B. Howell
H. J. Karr
S. Ortolani
A. E. Schofield

E. L. Cantrell W. R. Ellis B. L. Freeman R. F. Gribble W. D. Gutscher K. J. Johnson K. J. Kutac G. Miller W. E. Quinn	"Scyllac Feedback Stabilization Experiments"
G. Miller	"A Dynamic Model of Gross Plasma Motion in Scyllac"
K. F. McKenna E. L. Zimmermann K. B. Freese	"Laser-Plasma Interaction in the Scylla I-C Theta Pinch"
W. R. Ellis	"The Linear Theta Pinch as a 14-MeV Neutron Source"
W. R. Ellis R. A. Krakowski	"High-Density Linear Systems for Fusion Power"

INTERNATIONAL CONFERENCE ON RADIATION EFFECTS AND TRITIUM TECHNOLOGY FOR FUSION REACTORS

GATLINBURG, TENN.

OCTOBER 1975

D. W. Muir J. M. Bunch	"High-Energy Proton Simulation of 14-MeV Neutron Damage in Al_2O_3"
J. B. Mitchell R. A. Van Konynenburg D. M. Parkin C. J. Echer	"DT Fusion Radiation Strengthening of Copper and Niobium"
D. M. Parkin A. N. Goland	"Analysis of Radiation Damage in Fusion-Simulation Neutron Spectra"
F. W. Clinard, Jr. J. B. Bunch W. A. Ranken	"Neutron Irradiation Damage in Al_2O_3 and Y_2O_3"
V. A. J. van Lint J. M. Bunch T. M. Flanagan	"The Effects of Ionizing Radiation on Electrical Properties of Refractory Insulators"
D. W. Muir J. B. Bunch	"High-Energy Proton Simulation of 14 MeV Neutron Damage in Al_2O_3"
D. M. Parkin C. L. Snead, Jr.	"The Effects of Reactor Neutron 14-MeV Neutron and Energetic-Charged-Particle Irradiations on the Critical Current in Nb_3Sn"
A. R. Sweedler C. L. Snead L. Newkirk F. Valencia T. H. Ceballe R. H. Schwall B. T. Matthias E. Corenswit D. M. Parkin	"High-Energy Neutron Irradiation of Superconducting Compounds"

J. W. Lillberg
G. I. Chandler
F. T. Seibel
"Scylla IV-P Computer Based Control and Data Acquisition System"

C. E. Swannack
R. A. Haarman
J. D. G. Lindsay
D. M. Weldon
"HVDC Interrupter Experiments for Large Magnetic Energy Transfer and Storage (METS) Systems"

J. D. G. Lindsay
"10-kA Low-Resistance Superconducting Switch"

R. K. Linford
W. C. Nunnally
K. I. Thomassen
"Imploding Heating in the Scyllac Fusion Test Reactor"

I. Henins
J. Marshall
A. R. Sherwood
"A Simple, Versatile System for Digitizing and Reducing Data in Photograph Form"

L. C. Burkhardt
R. S. Dike
J. N. Di Marco
R. A. Haarman
"A High Voltage, High-Current, Pulsed Energy Source Having dI/dt's of 2×10^{13} A/s"

C. F. Hammer
K. S. Thomas
W. H. Borkenhagen
R. S. Dike
J. J. Banta
R. F. Gribble
R. K. Linford
"System Design of the Los Alamos Scientific Laboratory Staged Theta Pinch"

A. G. Bailey
M. D. Machalek
"Scylla IV-P Linear Theta Pinch, a Design and Construction Overlook"

R. K. Linford
W. C. Nunnally
K. I. Thomassen
"Implosion-Heating System Design for the SFTR"

K. J. Kutac
R. W. Kewish
R. F. Gribble
G. Miller
E. L. Kemp
R. R. Bartsch
A. S. Rawcliffe
"The Final Installation and Testing of the Feedback Power Amplifier for the Scyllac Feedback Experiment"

W. D. Gutscher
K. J. Johnson
"Scyllac Experiment Reliability Analyses"

G. P. Boicourt
"Some Properties of Castor Oil Affecting Its Performance as a Capacitor Impregnant and Their Significance to Future Impregnant Research"

L. D. Hansborough
C. F. Hammer
K. W. Hanks
T. E. McDonald
W. C. Nunnally
"Engineering Prototypes for Theta-Pinch Devices"

W. C. Nunnally
W. H. Borkenhagen
R. F. Gribble
L. D. Hansborough
R. K. Linford
J. G. Melton
"Multichannel Spark-Gap Technology for Staged Theta-Pinch Machines"

G. P. Boicourt   "The Diagnosis of Underlying in Paper Castor Oil Capacitors"

SEVENTH CONFERENCE ON NUMERICAL SIMULATION PLASMAS
COURANT INSTITUTE, NEW YORK, NY
JUNE 1975

B. L. Buzbee   "A Numerical Method for Approximating the Eigenfrequency Spectrom for Vlasov
H. R. Lewis   Problems"
G. H. Golub

M. Menzel   "A Two-Dimensional Magnetohydrodynamic Calculation of a Proposed Wall Stabilization
J. Brackbill   Experiment"

J. Brackbill   "Three-Dimensional Algorithms for Toroidal MHD Problems"
D. C. Barnes

D. W. Hewett   "Inhomogeneous Vlasov Equilibria for PIC Simulations"
C. W. Nielson
D. Winske

C. W. Nielson   "Nonradiative Electromagnetic Particle Simulation"
H. R. Lewis

1975 ANNUAL MEETING ON THEORETICAL ASPECTS OF CONTROLLED THERMONUCLEAR RESEARCH
WASHINGTON, DC
April 1975

R. C. Davidson   "Anomalous Transport Properties Characteristic of the Post-Implosion Phase of
R. Gerwin   High-Density Pinch Experiments"
N. T. Gladd

J. P. Goedbloed   "Equilibrium and Stability of High-Beta Diffuse Tokamaks"
J. P. Freidberg

J. U. Brackbill   "Nonlinear Magnetohydrodynamic Calculations Applied to Controlled Thermonuclear
Research"

D. C. Barnes   "Toroidal MHD Computations"
J. U. Brackbill

S. Ortolani   "Minimum Energy Reverse-Field Configurations"

R. C. Davidson   "Kinetic and Fluid-Numerical Studies of High-Beta Plasmas"
B. H. Hui
P. C. Liewer
S. Hamasaki
M. Z. Caponi
C. B. Batchelor
D. D'Ippolito
J. M. Ogden

H. R. Lewis   "Stability Analysis of Sharp-Boundary Vlasov-Fluid Screw-Pinch Equilibria"
L. Turner

D. W. Hewett   "Vlasov Confinement for High-Beta Plasma"
C. W. Nielson
D. Winske

A. G. Sgro   "Hybrid Model Studies of Magnetic Field Diffusion Studies"
C. W. Nielson

SECOND INTERNATIONAL CONGRESS ON WAVES AND INSTABILITIES IN PLASMAS
INNSBRUCK, AUSTRIA
March 1975

J. P. Goedbloed   "The Continuous Spectrum of Ideal Magnetohydrodynamics in Toroidal Geometry"

J. P. Goedbloed   "Equilibrium and Stability of High-Beta Diffuse Tokamaks"
J. P. Freidberg

J. P. Goedbloed   "Spin, Parity, and the Spectrum of Ideal Magnetohydrodynamics"

OTHER CONFERENCES

D. J. Blevins   "Design and Performance of Two 10 kA Superconducting Switches," 1975 IEEE
J. D. G. Lindsay   International Conference on Plasma Science, Ann Arbor, Mich., May 14-16, 1975.

W. E. Quinn   "Nuclear-Based Energy Resources: Fusion Technology," Proc. Conference on Magnitude
R. R. Buntzen   and Deployment Schedule of Energy Resources (Portland, Ore., July 21-23, 1975),
E. Kintner   Oregon State University, Sept. 1975.

L. A. Booth   "Engineering Concepts for Laser-Fusion Reactor Applications," presented at 10th
T. G. Frank   Intersociety Energy Conversion Engineering Conference, Newark, Delaware, August
F. T. Finch   18-22, 1975.

A. N. Goland   "The Dependence of Radiation Damage Analysis on Neutron Dosimetry," to be
D. M. Parkin   published in Proc. 1st ASTM-EURATOM Symposium on Reactor Dosimetry: Developments
    and Standardization.

S. A. W. Gerstl   "The Application of Sensitivity Analysis to Nuclear Data Assessment," Proc.
D. J. Dudziak   Specialists Meeting on Sensit. Studies and Shielding Benchmarks, Paris, France
D. W. Muir   (1975).

D. A. Baker   "Reversed-Field Toroidal Z-Pinch Experiments," American Phys. Soc. Meeting,
    Washington, DC (April 28, 1975) (Invited paper).

D. M. Parkin   "The Effects of Reactor Neutron, 14-MeV Neutron and Energetic-Charged-Particle
C. L. Snead, Jr.   Irradiations on the Critical Current in Nb_3Sn," to be published in Proc.
    International Conference on Fundamental Aspects of Radiation Damage in Metals.

F. T. Seibel   "Data Acquisition and Process Control Computers at Los Alamos CTR," abstract of
J. W. Lillberg   paper presented at IEEE Conference on Plasma Science, Ann Arbor, MI, May 1975.
R. C. Amsden

F. C. Jahoda   "Optical Diagnostics of the 'Scylac' CTR Device: A Case Study," abstract of
    invited paper presented at the Optical Society of American meeting, Boston, MA,
    October 1975.

R. A. Haarman   "Electrical Breakdown and Tracking Characteristics of Pulsed High Voltages in
K. D. Williamson   Cryogenic Helium and Nitrogen," 1975 Cryogenic Engineering Conference, Kingston,
    Ontario, Canada, July 22-25, 1975.

D. J. Dudziak   "Spectrum Calculations Applied to Fusion and Fission Reactor Structural Material
R. G. Palmer   Dosimetry," Proc. ASTM-EURATOM Symp. on Reactor Dosimetry, Petten.Netherlands
    (1975) (invited paper).

G. E. Bosler   "Energy Deposition Rates in a Laser-Fusion Reactor," 21st Annual Meeting of
G. Frank   American Nuclear Society, New Orleans, LA, June 8-13, 1975.

S. A. W. Gerstl   "A Quantitative Assessment of CTR Cross-Section Needs," Proc. Conf. on Nucl. Cross
D. J. Dudziak   Sections and Technology, Washington, DC (March 1975).
D. W. Muir

P. D. Soran   "Application of Bondarenko Formalism to Fusion Reactors," Proc. Conf. on Nucl.
D. J. Dudziak   Cross Sections and Technology, Washington, DC (March 1975).

W. E. Quinn   "Scyllac and Isar Toroidal Theta-Pinch Experiments," Proceedings of the High Beta Workshop (Los Alamos, July 28-August 1, 1975) ERDA-76/108.

K. F. McKenna   "Implosion Heating Studies in Scylla I-B," Proceedings of the High Beta Workshop (Los Alamos, July 28-August 1, 1975) ERDA-76/108

W. E. Quinn   "Linear Theta-Pinch Experiments," Proceedings of the High Beta Workshop (Los Alamos, July 28-August 1, 1975) ERDA-76/108.

W. R. Ellis   "Reactor Scaling of Linear Theta Pinches," Proceedings of the High Beta Workshop (Los Alamos, July 28-August 1, 1975) ERDA-76/108.